



HAL
open science

Ultrafast optical response of complex plasmonic nanoparticles

Tadele Otomalo

► **To cite this version:**

Tadele Otomalo. Ultrafast optical response of complex plasmonic nanoparticles. Plasmas. Université Paris Saclay (COMUE), 2019. English. NNT : 2019SACLC102 . tel-03092306

HAL Id: tel-03092306

<https://theses.hal.science/tel-03092306>

Submitted on 2 Jan 2021

HAL is a multi-disciplinary open access archive for the deposit and dissemination of scientific research documents, whether they are published or not. The documents may come from teaching and research institutions in France or abroad, or from public or private research centers.

L'archive ouverte pluridisciplinaire **HAL**, est destinée au dépôt et à la diffusion de documents scientifiques de niveau recherche, publiés ou non, émanant des établissements d'enseignement et de recherche français ou étrangers, des laboratoires publics ou privés.

Ultrafast optical response of complex plasmonic nanoparticles

Thèse de doctorat de l'Université Paris-Saclay
préparée à CentraleSupélec

École doctorale n°573 Interfaces : approches interdisciplinaires,
fondements, applications et innovation

Spécialité de doctorat : Physique

Thèse présentée et soutenue à Gif-sur-Yvette, le 20 Décembre 2019, par

Monsieur Tadele Orbula OTOMALO

Composition du Jury :

Pierre-Michel Adam Professeur des Universités, Université de Technologie de Troyes	Rapporteur
Aurélien Crut Maître de Conférences, Université Claude Bernard – Lyon 1	Rapporteur
Céline Fiorini Chercheuse, CEA, Saclay	Examinatrice
Alessandra Paladini Chercheuse, Consiglio Nazionale delle Ricerche, Rome, Italie	Examinatrice
Olivier Pluchery Professeur des Universités, Sorbonne Université	Président du jury
Bruno Palpant Professeur des Universités, CentraleSupélec	Directeur de thèse

To my late parents

Acknowledgments

First and foremost, I thank God for being my shepherd during these times of my stay away from family and friends.

It is a blessing to be supervised by a person like Prof. Bruno Palpant. He is one of the most kind and diligent people that I have worked with. Our first acquaintance was during my masters study in ENS Cachan where he taught me a course of Plasmonics. I immediately joined his team for the master thesis internship. We then agreed to pitch this Ph.D. subject for a grant at the annual Concours of the INTERFACES doctoral school. I thank him for believing in me and allowing me to pursue this Ph.D. under his supervision. He doesn't only show me the way to know more but also takes his time to let me internalize them through discussion. He thoroughly reads any document that I prepare for a publication or conference (including this thesis) and provides his valuable comments and suggestions. His ideas and directions have always brought me into the appropriate point when I run into a problem. Without his guidance, encouragement and persistent help this thesis would not have been possible. So, thank you.

I would like to thank the CentraleSupélec and ENS Paris-Saclay for the funding and for permitting me to spend my three year Ph.D. research in their facilities. Let me take this opportunity to especially thank Prof. Isabelle Ledoux, the director of LPQM, for her quick and kind responses for every request that I have made to her office. I thank the physics department of CentraleSupélec for allowing me to take part in the teaching duties. Especially, I would like to express my very great appreciation to Thomas Antoni, Pierre-Eymeric Janolin, and Jean-Michel Gillet for assigning me for the duties.

I am grateful to our colleagues Cyrille Hamon, Doru Constantin and Claire Goldmann of Laboratoire de Physique des Solides (LPS) in Orsay. They have provided me with the samples that I have required for my experiments without any hesitation. I also thank them for the fruitful discussions that we had on the results. I am also greatly indebted to our colleagues in the group of ultrafast processes in materials (FLASHit) Alessandra Paladini, Daniele Catone, Patrick O'Keeffe, Faustino Martelli, Lorenzo Di Mario, Stefano Turchini and Valentina Utrio Lanfaloni from the Istituto di Struttura della Materia (ISM), CNR, Rome. They fully availed their experimental setup for the experiments on my samples and participated in the work as well. My collaboration with them since 2017 was the most fruitful one. A special thanks to Fabrice Mayran de Chamisso from CEA-LIST, for allowing me to use his FDTD code in my research.

My thanks to Khanh-Van Do, a research engineer of our group for her support, advice and great friendship. She has even taken her time to accompany me to Rome for conducting the experiments.

I would also like to take this chance to acknowledge the great impact that my fellow Ph.D. students had on this research work. Big thank you to Timothée, Vita, Andrea, and Syrine for their good friendship and the nice working environment that we have had together.

I would like to thank the jury members of my thesis defense Pierre-Michel Adam, Aurelien Crut, Celine Fiorini, Alessandra Paladini, and Olivier Pluchery. Particularly, I am grateful to the rapporteurs Pierre-Michel and Aurelien for allowing me to take enough time while organizing this final manuscript.

Finally, I would also like to thank my close family members [Mamo (Gashe), Meselech (Kola), Arba, Karcho, Mengistu, Hamuse (Kurate), Kalita, Adane Kumbi, Kututa Gewadho, Abebech (Tate), Bekalu, Argachew, Atalelech, Mulunesh, Selamawit (Selam), Binyam (Abi) and Debora] who have unconditionally loved, supported and inspired me since my early childhood. I am also fortunate to have friends like Aman Zaid and his wife Abeba, Paméla Didier, Sivaramakrishnan, Getaneh Diress and Eyassu Dilla who have always been there whenever I needed them.

Abstract

The remarkable properties associated with the localized plasmon resonance (LSPR) in noble metal nanoparticles (NPs) make plasmonics an important topic with multiple applications. When NPs are illuminated by ultrashort laser pulses they undergo a rapid dynamics of energy exchanges which leads to the ultrafast variation of their optical properties, associated with other effects such as broadband photoluminescence, hyperlocalized heat release, electron photoemission, production of reactive oxygen species and nano-cavitation. The design of complex hybrid nanostructures can enable us to tailor the plasmonic properties as to optimize the applications. We have studied some hybrid nanostructures by broadband pump-probe absorption spectroscopy and a dedicated modeling: AuNP-decorated silica fibers and core-shell Au-Ag NPs. Their stationary and transient optical responses are analyzed depending on the NP morphology.

In the developments evoked above the enhanced near field around plasmonic NPs plays a key role. However, the study of the ultrafast transient modulation of the near field is limited by the inability of the conventional numerical tools to catch the small variations of the NP permittivity. Here, a complex-conjugate pole-residue pair based FDTD method is successfully implemented to simulate the time-dependence of the plasmonic near-field topography. Beyond, the LSPR mode can be resonantly coupled with a photonic mode in a hybrid microcavity for conceiving optically-controlled photonic functionalities. The coupling of a 2D array of parallel gold nanorods with the defect mode of a 1D photonic crystal cavity is investigated theoretically. The optical anisotropy enables us to play with several degrees of freedom like field polarization. The ultrafast modulation of the optical response that is predicted in such hybrid nanostructures opens the possibility of their future optimization for designing time-resolved sensors.

Keywords: plasmonics, nanoparticles, ultrafast, near-field

Résumé

Les propriétés remarquables associées à la résonance plasmon localisée (LSPR) dans les nanoparticules (NP) de métaux nobles font de la plasmonique un sujet aux applications multiples. Lorsque les NP sont éclairées par des impulsions laser ultracourtes, une dynamique rapide d'échanges d'énergie conduit à la variation ultrarapide de leurs propriétés optiques, accompagnée d'autres effets comme la photoluminescence, l'échauffement hyperlocalisé, la photoémission électronique, la production de radicaux libres, la nano-cavitation. La conception de nanostructures hybrides complexes permet d'adapter les propriétés plasmoniques pour optimiser les applications. Nous avons étudié certaines nanostructures hybrides par spectroscopie d'absorption pompe-sonde large bande et une modélisation dédiée : fibres de silice décorées de NP d'or, NP cœurs-coquilles Au-Ag. Leurs réponses optiques stationnaire et transitoire sont analysées en fonction de la morphologie des NP.

Dans les développements évoqués ci-dessus, l'exaltation de champ proche autour des NP plasmoniques joue un rôle clé. Cependant, l'étude de la modulation transitoire du champ proche est limitée par l'incapacité des outils numériques usuels à saisir de faibles variations de la permittivité des NP. Nous mettons en œuvre une méthode FDTD basée sur les paires pole-résidu complexes-conjugués pour pouvoir simuler l'évolution temporelle de la topographie du champ proche plasmonique. Au-delà, le mode LSPR peut être couplé à un mode photonique dans une cavité hybride pour concevoir des fonctionnalités photoniques optiquement contrôlées. Le couplage d'un réseau 2D de nanobâtonnets d'or parallèles avec le mode de défaut d'une cavité d'un cristal photonique 1D est étudié théoriquement. L'anisotropie optique permet de jouer avec plusieurs degrés de liberté comme la polarisation du champ. La modulation ultrarapide de la réponse optique prédite dans de telles nanostructures hybrides ouvre la possibilité de leur optimisation future pour la conception de capteurs résolus en temps.

Mots-clés: plasmonique, nanoparticules, ultrarapide, champ proche

Contents

Acknowledgments	ii
Abstract	iv
List of Figures	xi
List of Tables	xvii
Acronyms	xix
Introduction	1
1 Optical response of noble metal nanoparticles: background and tools	5
1.1 Introduction	5
1.2 Optical properties of bulk noble metals	6
1.2.1 Electronic structure and properties	6
1.2.1.1 Conduction electrons	7
1.2.1.2 Involvement of the <i>d</i> -band electrons	8
1.2.2 Heat capacity of the metal ionic lattice	9
1.2.3 Dielectric function of noble metals	11
1.2.3.1 Interband dielectric function contribution (Rosei model)	11
1.2.3.2 Intraband dielectric function contribution (Drude-Sommerfeld model)	12
1.2.3.3 Total dielectric function	14
1.3 Stationary regime optical response of noble metal nanoparticles	17
1.3.1 Spherical nanoparticles	17
1.3.2 Non-spherical nanoparticles: the case of nanorods	19
1.3.2.1 Gans-Mie theory	21
1.3.3 Ensemble of nanoparticles	22
1.3.3.1 Extended Maxwell-Garnett model	23
1.3.3.2 Yamaguchi model	24
1.4 Numerical approaches	26
1.5 Optical response of noble metal nanoparticles in the transient regime	27
1.5.1 Time resolved pump-probe experiment	29
1.6 Summary	31
2 Transient optical response of silica nanowires decorated by gold nanoparticles	33
2.1 Introduction	33

2.2	Sample preparation	34
2.3	Experimental results	35
2.3.1	Stationary regime LSPR	35
2.3.2	Pump-probe experiment	36
2.4	Theoretical modeling	38
2.4.1	Modeling the AuNP decorated SiO ₂ NWs in the stationary regime	38
2.4.2	Modeling the transient regime optical response	40
2.4.2.1	The effect of shape distribution of the sample	42
2.5	Discussion	44
2.6	Summary	48
3	Ultrafast transient optical response of nonspherical gold and core-shell, gold-silver nanoparticles	51
3.1	Introduction	51
3.2	Synthesis of the nanoparticles	53
3.2.1	Gold nanorods	53
3.2.2	Silver coating	53
3.3	Experimental study	55
3.3.1	Stationary regime optical response of the nanoparticles	55
3.3.2	Pump-probe investigation results	57
3.3.2.1	Transient regime spectral signature of the nanoparticles	58
3.3.2.2	Electron-phonon relaxation time in the nanoparticles	62
3.4	Theoretical analysis	64
3.4.1	Modeling the stationary optical response of the nanoparticles	65
3.4.2	Modeling the ultrafast transient optical response of the nanoparticles	69
3.5	Discussion	75
3.6	Summary	79
4	Ultrafast transient near field variation in and around a gold nanoparticle: investigation by FDTD	81
4.1	Introduction	81
4.2	Complex-conjugate pole-residue pair based (CCPRP) FDTD	83
4.2.1	Principle of the method	83
4.2.2	Validation of the end-to-end accuracy of the method	84
4.3	Modeling the ultrafast transient near-field	87
4.3.1	Transient dielectric function of the AuNP determined by the 3TM	87
4.3.2	Transient near field variation in and around the AuNP	89
4.4	Summary	95
5	Plasmonic-photonic coupling: gold nanorods in a 1D microcavity	97
5.1	Introduction	97
5.2	The uncoupled sub-systems	98
5.2.1	Choosing a plasmonic nanocomposite layer	98
5.2.2	The 1D photonic crystal	100
5.3	Stationary regime optical response of the plasmonic-photonic hybrid microcavity	102
5.3.1	Coupling between the defect mode and the LgSPR	102

5.3.1.1	Monitoring the coupling regime: vacuum-field Rabi splitting . . .	104
5.3.2	Coupling between the defect mode and the TrSPR	106
5.3.3	Absorptance of the hybrid cavity compared to that of a bare thin plasmonic film	107
5.4	Transient optical response of the hybrid structure	109
5.5	Summary	112
Conclusion		115
A Rosei Model		119
B Synthesis of NPs and the reactants used		123
C Heaviside step function based equation for electron dynamics fitting		125
Bibliography		127

List of Figures

1	Periodic table of plasmonic nanoparticle shapes, as reported in Ref. [34].	2
1.2	Fermi surface (yellow) within the first Brillouin zone of (a) Ag and (b) Au [75]. (c) First Brillouin zone of the noble metals with high symmetry points [75]. Γ is the center of the Brillouin zone. The X and L points occupy the centers of the square and the hexagonal surfaces, respectively.	7
1.5	Schematic representation of the displacement of the conduction electrons from the ionic core of a spherical NP in response to an applied external electromagnetic field.	17
1.6	Near-field enhancement factor F calculated inside and outside of a gold nanosphere with radius $R = 10$ nm in water, excited by a light wave tuned to its LSPR at 520 nm. The directions of the incident electric field \mathbf{E} and the wave vector \mathbf{k} are indicated [71].	20
1.8	The axes of spheroidal shapes, oblate if $c < a$ (left) and prolate if $c > a$ (right). The z axis is the symmetry axis for both cases (from Wikipedia).	22
1.9	Aspect ratio dependent spectra of a prolate shaped AuNR as calculated by Gans-Mie theory. The green arrow indicates the AR dependent red shift of the LgSPR mode.	22
1.10	Scheme of a composite medium consisting of randomly dispersed anisotropic NPs in a 3-D dielectric host medium.	23
1.11	Schematic representation of the dipole moments p and p' of NPs and their mirror images, receptively. The induced local field experienced by the particle \mathbf{E}_{loc} which is the sum of the external applied field \mathbf{E}_{ext} , the field created by the image dipole p'_j and the field created by all other dipoles p_j is also shown. Taken from Ref. [121].	24
2.2	Experimental absorbance spectrum of the AuNP decorated SiO ₂ NW array.	36
2.3	The pump-probe experiment setup of the group of Ultrafast processes in materials (FLASHit) in Instituto di Struttura della Materia (ISM).	37
2.4	Experimental spectral dependence of the transient absorption for different delay times between pump and probe pulses. ΔA is defined as the absorbance difference of the sample after and before pump excitation.	38
2.6	The calculated stationary optical properties: the left y axis (black) shows the absorption coefficient of the effective medium (randomly oriented oblate AuNPs with AR = 2.25 dispersed in the air-silica mixture) and the right y axis (blue) shows the absorption cross-section of an oblate AuNP with AR = 2.25.	39
2.7	The geometrical representation of the model required for the thermal dynamics calculation: designed in COMSOL Multiphysics.	41

2.8	Calculated spectral dependence of the pump-induced variation of the absorption coefficient ($\Delta\alpha$) at different delay times for oblate AuNPs of AR = 2.25.	42
2.11	Time evolution of the negative minimum of the absorption modification corresponding to the plasmon bleaching, as calculated for three NPs with AR = 1.75 (black), 2.25 (red), and 2.75 (blue), respectively.	45
2.13	Effective relaxation time of the transient optical signal as a function of probe photon energy, as extracted from the dynamics calculated for two NPs with AR = 1.75 (black) and 2.75 (red), respectively. The dashed vertical lines denote the spectral location of the corresponding LSPR mode.	47
2.14	Position of the main minimum in the ΔA measurements (black squares) and in the $\Delta\alpha$ calculation (red dots) as a function of the delay time between pump and probe pulses.	48
3.2	A cartoon showing the Ag overgrowth process.	53
3.4	Stationary regime extinction spectra of free AuNRs and of the AuNR@Ag NPs in water. The data are normalized by their respective maximum values. The L and T labels indicated on the AuNR@Ag 8eq resonances represent the longitudinal and transverse modes, respectively. Subscripts of L and T denote the mode types that are present for each field polarization: 0 subscript denotes a dipolar mode while the subscripts 1, 2 and 3 represent the higher order modes. Unlike the others, the AuNR@Ag 2eq sample presents five resonances which are indicated here with the red arrows. The blue arrow indicates the progressive blue shift of the T_0 TrSPR mode of the AuNR-core as the Ag:Au ratio increases.	56
3.6	(a) Extinction of the AuNR sample determined by UV-VIS spectrophotometry exhibiting the TrSPR and LgSPR bands. (b) Color chart of the time and spectral dependence of the absorbance variation (in mOD) of the AuNRs measured via pump-probe spectroscopy. (c) Spectral dependence of the differential absorbance at different delay times as extracted from (b). The vertical dashed lines indicate the spectral position of the two plasmon resonance modes of the AuNRs.	59
3.7	Same as Fig. 3.6 but for AuNR@Ag 0.8eq.	59
3.8	Same as Fig. 3.6 but for AuNR@Ag 2eq. The green arrow in (c) shows the bleaching peak formed around the T_0 mode.	60
3.9	Same as Fig. 3.6 but for AuNR@Ag 4eq. The green arrow in (c) indicates the fifth bleaching peak associated with the weak T_0 mode which is hidden in the T_1 band in (a).	60
3.10	Same as Fig. 3.9 but for AuNR@Ag 8eq.	61
3.12	Pump energy dependent e-ph relaxation time representing the recovery lifetime of the different bleaching peaks. The connected blue and red symbols in each panel represent the pump power dependent e-ph relaxation time (ps) of each sample pumped at 380 nm and at their respective dipolar LgSPR, L_0 . Panel (a) for AuNR@Ag 0.8 eq, (b) for AuNR@Ag 2eq, (c) for AuNR@Ag 4eq and (d) for AuNR@Ag 8eq. . . .	64

3.13	Stationary optical response of the bare AuNRs. Black: experimental extinction of the AuNR solution. Red: extinction cross-section of a AuNR with AR = 2.9 calculated by the BEM. Both data are normalized by their respective values at 384 nm. The green arrow points at a shoulder in the TrSPR band of the experimental data, originating from a small population rounded cuboids of gold in the solution.	65
3.14	Near field map (modulus of the field) of the bare AuNR determined by the BEM: taken (a) at its longitudinal resonance (680 nm, \mathbf{E} parallel to the NR) and (b) at its transverse resonance (514 nm, \mathbf{E} perpendicular to the NR).	66
3.15	Schematic representation of the AuNR@Ag NPs with (a) thin Ag shell and (b) thick Ag shell. The degree of rounding of the edges and corners can be seen.	66
3.16	Modeling the stationary optical response of the AuNR@Ag NPs using the BEM. From (a) to (d), the black curves denote the experimental extinction data while the red ones represent the modeled data. Both the experimental and the calculated data are normalized against their respective maximum value which is at the L_0 mode. The green square highlights the presence of a weak mode in that region.	67
3.17	Effect of the rounding of a silver nanocuboid as calculated using the DDA taken from Ref. [163]. p is a parameter in a super-ellipsoid equation which can be used to control the sharpness of the edges and the corners of a cuboid model. $p = 0.01$ corresponds to a nanocuboid with sharp edges and corners while $p = 1$ produces a shape that is similar to an ellipsoid.	68
3.18	Modulus of the near field of AuNR@Ag 8eq NP taken (a) around its longitudinal resonance mode [515 nm] and around its transverse resonance modes [(b) 427 nm, (c) 378 nm and (d) 341 nm], as determined by the BEM.	69
3.19	(a) Calculated stationary regime extinction cross-section of a bare AuNR with AR = 2.9. (b) Its simulated transient optical response (variation of the time dependent extinction cross-section from the stationary one) at different delay times after 50-fs pump pulse absorption. The inset shows the dynamics around the TrSPR mode. The vertical dashed lines indicate the spectral positions of the LgSPR and TrSPR of the AuNR in the stationary regime.	72
3.20	Same as Fig. 3.19 but for AuNR@Ag 0.8eq.	72
3.21	Same as Fig. 3.19 but for AuNR@Ag 2eq. The green arrow in (c) shows the bleaching peak formed around the T_0 mode.	73
3.22	Same as Fig. 3.19 but for AuNR@Ag 4eq. The green arrow in (b) indicates the fifth bleaching peak associated with the very weak T_0 mode.	73
3.23	Same as Fig. 3.22 but for AuNR@Ag 8eq.	74

- 3.24 Break down of the calculated extinction cross-section of the AuNR@Ag NPs into its contributing components for the two extreme samples AuNR@Ag 0.8eq (thin Ag shell) and AuNR@Ag 8eq (thick Ag shell). The top panels show the effects of scattering and absorption cross-sections for (a) AuNR@Ag 0.8eq and (b) AuNR@Ag 8eq. The orange colored full lines are the total extinction cross-section curves while the olive and wine colored full lines represent the absorption and scattering cross-sections, respectively. The longitudinal, LgPol (dash-dotted curve), and transverse, TrPol (dotted curve), polarization excitation contributions to the absorption (olive color) and the scattering (wine color) cross-sections are also shown in the top panels. The bottom two panels depict the overall polarization dependent contributions to the total extinction cross-section (c) for AuNR@Ag 0.8eq and (d) for AuNR@Ag 8eq. 76
- 3.25 Contributors to the transient extinction cross-section of the AuNR@Ag 0.8eq (thin Ag-shell) sample at 2.5 ps delay. The scattering [the black line in (a)] and absorption [the black line in (b)] cross-section contributions to the transient extinction [the black line in (c)] spectral signature are also shown. The purple and olive colored lines in (a), (b) and (c) correspond to the transverse- (TrPol) and longitudinal-polarization (LgPol) excitation components of the corresponding optical properties. The blue and red colored lines in panel (d) are the scattering and absorption contributors to the total extinction (black line). 77
- 3.26 Same as Fig. 3.25 but for AuNR@Ag 8eq (thick Ag shell). 78
- 3.27 (a) Imaginary and (b) real parts of the complex dielectric functions of Au and Ag plotted together. The vertical gray lines indicate the spectral positions of the four dominant resonances as modeled for the AuNR@Ag 8eq sample. 79
- 4.1 Dielectric function of gold as a function of photon energy. Solid lines: experimental values obtained from [85]; dashed lines: curves fitted with the CCPRP method with (a) 2 and (b) 4 poles, obtained by the vector fitting. 84
- 4.5 (a) Sketch of the flow chart of the steps followed and (b) top view of the FDTD simulation layout to calculate the ultrafast variation of the near field enhancement around a 20 nm AuNP. The distances are given in pixels (1 px = 1 nm). 90
- 4.7 Comparison of the transient near-field intensity enhancement variation (TNFIEV) of the 20 nm AuNP in air observed at its very center (a) calculated with the Mie theory and (b) obtained by our FDTD simulation, for different delay times (500 fs, 2 ps, 4 ps, and 7 ps) after irradiation with an ultrashort laser pulse having the same characteristics as in Fig. 4.4. Horizontal and vertical scales are identical. 92
- 4.8 Field intensity enhancement spectrum $|\mathbf{E}|^2$ simulated by FDTD at $d = 27$ nm away from the AuNP in both the stationary (connected red dots) and transient (at 2 ps, connected black dots) regimes. The blue dash-dot vertical line indicates the stationary LSPR energy. The green arrows indicate the red-shift of the enhancement peak for both the stationary and transient near-field intensities. 93

- 4.9 Upper panel: color mapping of the time evolution (up to 7 ps) of the relative variation of the transient near-field intensity enhancement spectrum (from 1.5 to 3.5 eV) after initial pulsed excitation at three different distances, d , away from the AuNP surface along the y axis [(a) $d = 7$ nm, (c) $d = 27$ nm and (e) $d = 47$ nm] simulated by FDTD. The lower panel shows the relative variation of the near-field intensity enhancement observed at the delay times of 2 ps and 6 ps after the passage of the laser pulse, as are extracted from the upper panel plots [(b) from (a), (d) from (c) and (f) from (e)]. The inset in (b) shows a close-up of the additional artifact features that can be observed in the transient signal (numerical noise in the photon energy range from 1.9 eV to 2.2 eV) due to the proximity of the observation point to the AuNP surface and its pixelized interface with air. 94
- 5.5 Electric field intensity enhancement $|\mathbf{E}|^2$ inside the plasmonic-photonic hybrid microcavity for p -polarized light in the stationary regime. The structure is designed such that the LgSPR of the plasmonic nanocomposite layer and the defect mode of the PC cavity are perfectly coupled at 608 nm. (a) Wavelength and position dependent $|\mathbf{E}|^2$ distribution in the hybrid device. The arrows indicate the constituents of its defect layer: the plasmonic nanocomposite layer (with 0.1% Au) and the two Al_2O_3 layers. H and L designate the alternating high and low refractive index layers, respectively, that make up the Bragg mirrors. (b) $|\mathbf{E}|^2$ distribution along the device taken at the LgSPR (608 nm) of the nanocomposite layer. The green vertical dashed lines indicate the interfaces between the H and L layers. 104
- 5.7 Angle of incidence θ dependent transmittance spectra of the plasmonic-photonic hybrid cavity. The green vertical dashed lines indicate the spectral locations (527 nm and 608 nm) of the modes of the hybrid cavity as a result of the coupling between the guest plasmonic nanocomposite thin layer of 0.1% Au concentration and the defect mode of the host PC. They can be observed at $\theta = 64^\circ$ (s -polarization) and $\theta = 0^\circ$ (p -polarization), respectively. 107
- 5.8 Schematic representation of a bare thin film (equivalent to the defect layer of the hybrid cavity). 108
- 5.9 Comparison of the absorptance of the hybrid cavity (full lines) and a thin bare nanocomposite film (dashed lines). The red and black curves correspond to the excitation of the TrSPR (s -pol. light at 64°) and LgSPR (p -pol. light at 0°) modes of the nanocomposite layer, respectively. The absorptance of the bare film is magnified 50 and 10 times for the TrSPR and LgSPR mode excitation, respectively. 108
- 5.11 Schematic representation of the calculation process for the transient optical response of the 1D plasmonic-photonic hybrid cavity. 110
- 5.12 Pump induced relative change of the transmittance of the hybrid structure after absorption of a 100-fs laser pulse: (a) Case (1), when pumped at TrSPR in s -polarization (527 nm, 2.35 eV) and probed with p -polarized light, and (b) Case (2), when pumped at LgSPR (608 nm, 2.04 eV) in p -polarization and probed with s -polarized light. 111

5.13	Relative change of the absorption coefficient of the nanocomposite layer 3 ps after the absorption of a 100-fs laser pulse with $I_0 = 1 \text{ GW/cm}^2$. Red curve: for case (1), i.e, when pumped at TrSPR (547 nm , 2.35 eV) in s -polarization and probed with a light polarized parallel to the AuNRs. Black curve: for case (2), i.e, when pumped at LgSPR (608 nm, 2.04 eV) in p -polarization and probed with light polarized perpendicular to the AuNRs. The red and black arrows highlight the $\Delta\alpha_{eff}/\alpha_{eff}$ values at 2.04 eV and 2.35 eV, respectively.	111
5.14	Transient transmittance spectrum of the hybrid plasmonic-photonic cavity probed at normal incidence (excites the LgSPR of the AuNRs) after excitation by a 100-fs laser pulse at 527 nm (2.35 eV), case (1).	112
5.15	Same as Fig. 5.14 but pumped at 608 nm (2.04 eV) and monitored by a s -polarized probe light at $\theta = 64^\circ$ exciting the TrSPR of the AuNRs, case (2).	112
A.1	The parabolic band structure of Rosei model around the (a) L point of Ag and the (b) L & (c) X points of Au Brilluoin zone, taken from Ref. [96]. The origin is taken to be the Fermi level E_F	119

List of Tables

1.1	Lattice parameter \tilde{a} , Fermi energy E_F and Fermi temperature T_F of Cu, Ag and Au [73].	6
1.2	Values of the conduction electron density n_c and the γ parameter in the relation $C_e(T_e) = \gamma T_e$ [76].	8
1.3	The band energy and relative oscillator strength values, $\eta_{i \rightarrow f}^{X,L} = \left M_{X,L}^{i-f} \right ^2 / \left M_L^{d-p} \right ^2$, of Au and Ag that are used in this work as compared to the ones reported in Ref. [99]). The origin of the energies is set at E_F	16
2.1	Thermal parameters of the media involved in the two sub-systems.	42
3.1	Dimensions of the cuboidal AuNR-Ag bimetallic NPs estimated from the analysis of their TEM images.	55
3.2	Spectral positions of the resonant modes of the anisotropic AuNR@Ag nanoparticles depending on the Ag:Ag molar ratio (eq) value.	56
3.3	Dimensions of the cuboid-shaped AuNR@Ag bimetallic NPs obtained by adjusting the BEM simulation as to match the experimental stationary optical spectra.	68
3.4	Thermal properties of bulk Ag and Au at ambient temperature (300 K) as reported in Ref. [174].	70

Acronyms

Acronym	Meaning
LPQM	Laboratoire de Photonique Quantique et Moléculaire
LPS	Laboratoire de Physique des Solides
CNR	Consiglio Nazionale delle Ricerche
ISM	Istituto di Struttura della Materia
FLASHit	Division of Ultrafast Processes in Materials at CNR-ISM
UTT	Université de Technologie de Troyes
Au	Gold
Ag	Silver
Cu	Copper
SPR	Surface plasmon resonance
SPP	Surface plasmon polariton
LSPR	Localized surface plasmon resonance
SERS	Surface enhanced Raman spectroscopy
NP	Nanoparticle
AuNP	Gold nanoparticle
AgNP	Silver nanoparticle
CuNP	Copper nanoparticle
AuNR	Gold nanorod
AgNR	Silver nanorod
LgSPR	Longitudinal surface plasmon resonance
TrSPR	Transverse surface plasmon resonance
LgPol	Longitudinal polarization
TrPol	Transverse polarization
DOS	Density of states
JDOS	Joint density of states
EDJDOS	Energy distribution of joint density of states
AR	Aspect ratio
fcc	face-centered cubic
E_F	Fermi level
T_F	Fermi temperature
T_e	Electron temperature
T_l	Lattice temperature

DFT	Density functional theory
EMT	Effective medium theory
MG	Maxwell-Garnett
DDA	Discrete dipole approximation
BEM	Boundary element method
MNPBEM	Metal NanoParticle Boundary Element Method
TMM	Transfer matrix method
FDTD	Finite difference time domain
3TM	Three temperature model
NW	Nano-wire
SiO ₂	Silicon dioxide (silica)
PECVD	Plasma enhanced chemical vapor deposition
VLS	Vapor-liquid-solid
SEM	Scanning electron microscopy
TA	Transient absorbance
FTAS	Femtosecond transient absorption spectrometer
TEM	Tunneling electron microscopy
UV	Ultra-violet
VIS	Visible
IR	Infrared
OD	Optical depth
eq	Ag: Au molar ratio equivalent
AuNR@Ag	AuNR-core, Ag-shell nanoparticle
CTAB	Hexadecyltrimethylammonium bromide
CTAC	hexadecyltrimethylammonium chloride
AgNO ₃	silver nitrate
HAuCl ₄ ·3H ₂ O	Hydrogen tetrachloroaurate trihydrate
AA	ascorbic acid
NaBH ₄	Sodium borohydride
MUDOL	(1-mercaptoundec-11-yl)hexa(ethyleneglycol)
C ₇ H ₆ O ₃	Salicylic acid
CCPRP	Complex-conjugate pole-residue pair
CPU	Central processing unit
PML	Perfectly matched layer
TE	Transverse electric
TM	Transverse magnetic
TNFIEV	Transient near field intensity enhancement variation
GDM	Green dyadic method

Introduction

The interest of working with nanoscale noble metals (gold, silver and copper) has increased owing to their fascinating optical property called the *Surface Plasmon Resonance* (SPR). The SPR is a collective oscillation of the conduction electrons of the metal driven by an electromagnetic radiation when the frequency of the latter matches the eigenfrequency of the electron gas in the metal. SPR has two principal domains, *Surface Plasmon Polaritons* (SPP) [1] and *Localized Surface Plasmon Resonance* (LSPR) [2], both of them gaining a firm understanding in the early of 1900 [3]. The former deals with plasmon modes propagating along a bulk metal-dielectric interface while the latter concerns about a plasmon oscillation localized in a nanoparticle (NP) the size regime which is small against the wavelength. Despite of being one of the youngest disciplines in the field of optics, plasmonics is yet among the fastest developing ones. Its wide range of applicability, its high sensitivity for optical characterization, the availability of fabrication techniques and the advancements in computing power and speed make it easy to work with [3].

Noble metal NPs are characterized by their strong absorption of light due to the LSPR. The LSPR frequency and/or its spectral width can be tailored by varying the size, shape and composition of the metal NPs [4]. For instance, for a gold nanorod (AuNR), two LSPR modes can be observed that correspond to the light polarization along its longitudinal (LgSPR) or transverse (TrSPR) dimension. The LgSPR mode is the most acute resonance of the two and can be tuned from the visible to near the IR by modifying the NP shape, while the TrSPR is damped and spectrally blue-shifts only weakly from the sphere LSPR. Figure 1 highlights the progress in the preparation/synthesis of NPs of different shapes. Changing either the environment in which the NPs are placed and/or the gap between the NPs (coupling) can strongly alter the spectral position, the number of LSPR modes appearing and their width [5–7]. Moreover, plasmonic NPs are also well known for enhancing the incident electromagnetic field tuned to the resonant frequency near their surface [6, 8–11]. These rich properties of noble metal NPs have made them of great interest for multiple applications in the stationary regime, biological and biomedical applications [12–18], plasmon-enhanced fluorescence [19–24], surface enhanced Raman scattering (SERS) [25–27], photothermal therapy [28–30] and manipulation of nanobjects and/or light at the nanoscale [31–33] being some.

Beyond, when these NPs are illuminated by ultrashort laser pulses, they undergo a rapid dynamics of energy exchanges. First, the LSPR of the NPs is excited, then the exchange process begins with the redistribution of the absorbed energy within the electron gas by electron-electron collisions, which lasts for a few hundred femtoseconds [35–37]. This is then followed by the energy exchange between the electron gas and the metal lattice, hence heating the NP. The heat is finally

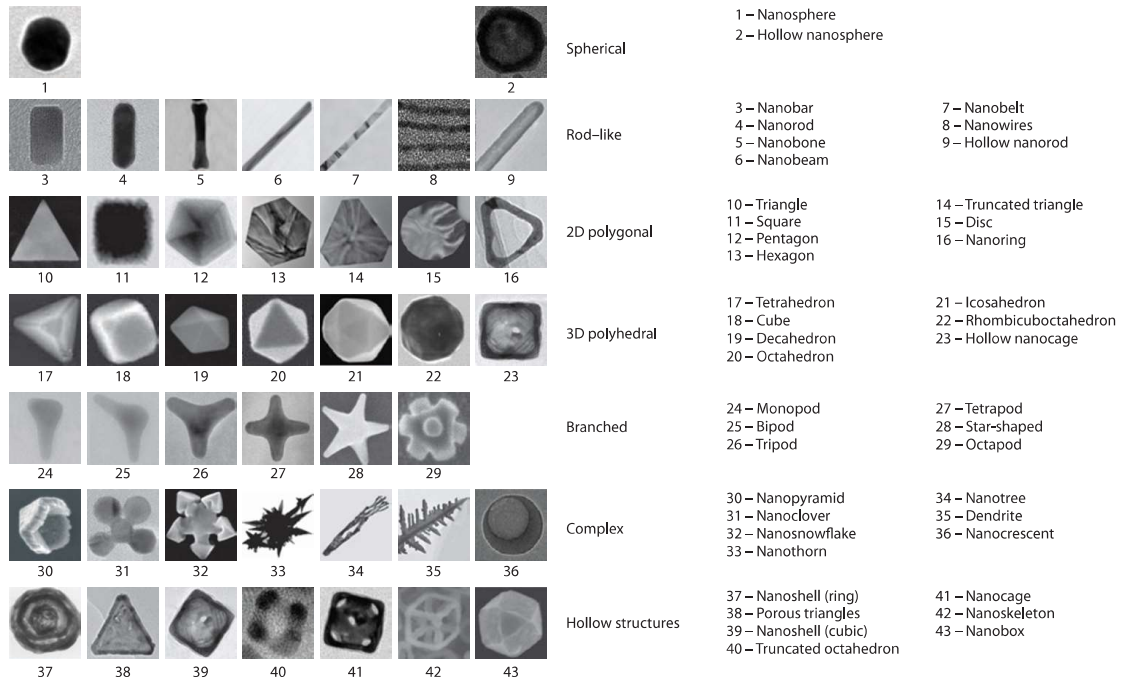


Figure 1 – Periodic table of plasmonic nanoparticle shapes, as reported in Ref. [34].

transferred toward the surrounding environment at the interface by phonon-phonon scattering which lasts from tens up to hundreds of picoseconds depending on the laser pulse intensity, size of the NP and heat transport properties of the host medium [38]. These ultrafast energy exchanges prompt the variation of the electron distribution within the NPs and consequently, the resulting dielectric function variation drives the transient modulation of their optical properties, which can be monitored both temporally and spectrally by pump-probe spectroscopy [39–41]. The laser-induced transient modulation of the optical properties of NPs, which has been extensively studied [35–37, 40–46], has helped to explain the various phenomena that occur in recent developments like electron photoemission [47, 48], photoluminescence [49], plasma generation around nanoparticle [50], nano-cavitation [51] or production of reactive oxygen species in aqueous media [52]. In most of these developments, the ultrafast modulation of the plasmonic near field enhancement plays a role. It is then vital to study the physics behind the optical response of metal NPs depending on their morphology, selected for unique functionalities.

The transient spectral signature of the NP optical response strongly depends on their shape [40, 41]. Consequently, in an ensemble of NPs, the shape distribution is a key parameter to be accounted for in the analysis. Beyond, working with monometallic NPs limits the spectral region of significant transient signal. For instance, AuNPs display their LSPR in the visible or near IR while AgNPs demonstrate their LSPR in the near UV. These two metals can be coupled together such that their molar ratio can also be used as a LSPR tuning parameter in addition to the conventional ones (size, shape, and hosting environment) [7, 53–57]. This may be achieved, either in the form of a homogeneous alloy [58], or in the form of a core-shell arrangement. Several spectral and temporal features have been observed by using core-shell bimetallic NPs. In the transient regime, they demonstrate low frequency acoustic vibration modes (phonon dynamics) which are very sensitive to the amount of the material being deposited onto the core. This has

been studied both experimentally and theoretically, leading to a possible application of these NPs as nano-balances for mass sensing [59–62]. However, for the study of the ultrafast electron dynamics of anisotropic metal-metal (core-shell) configurations, most of the works reported to date are experimental [57,63]. The unavailability of theoretical investigations for these cases may be due to the complexity of the theoretical treatment of the heat transport at the metal-metal interface which requires a careful consideration of the interface shape and the different thermodynamic properties of the metals.

As has been mentioned earlier, most of the applications of the transient optical response of plasmonic NPs depend on the near-field topography around the NPs which undergoes a transient variation by itself. This ultrafast transient modulation of the plasmonic near field can be used to develop time resolved sensors, based on the same considerations as for the stationary plasmon enhanced fluorescence or SERS. Beside, by coupling the LSPR with a resonant mode of an electromagnetic cavity one can benefit from several optically controlled photonic functionalities. In the stationary regime, near field enhancement and confinement as well as absorbance increase were demonstrated by exploiting the coupling of spherical NPs with photonic crystals [64, 65]. Beyond, our team could achieve an efficient signal modulation on a picosecond timescale by optimizing this plasmonic-photonic coupling when inserting spherical gold NPs in a microcavity [66, 67]. More complex configurations can be envisaged, playing with NP shape and light polarization to generate new functionalities. In addition, the strong near field and the possibility to modulate it at an ultrafast timescale may open outlooks for developments based on the near-field energy transfer from a plasmonic NP coupled to a cavity to other neighboring objects being light-responsive. Therefore, for all these developments, studying the space- as well as time-dependent near-field variations [68,69] inside and around NPs is vital. Unfortunately, catching these small variations of a NP's optical properties along their dynamics cannot be achieved by using the conventional phenomenological models that are applied in most of numerical approaches for modeling the dielectric function of dispersive media like metals. This may explain the absence, in the literature, of studies assessing numerically the ultrafast transient near field topography of plasmonic nanostructures.

This Ph.D. work aims at addressing, to some extent, the issues that we have evoked above, the overall goal being to understand the physical processes involved in the ultrafast response of plasmonic materials that incorporate noble metal NPs. The work contains the interpretation of both experimental (obtained by time-resolved pump-probe spectroscopy) and theoretical results. The general structure of the dissertation is as follows.

All the theoretical foundations that have been used for this study will be summarized in the first chapter. The chapter will begin by presenting the optical properties of noble metals in their bulk form, by taking a closer look at their electronic band structure and pointing out the main contributors (interband and intraband transitions) to their frequency-dependent dielectric function. Based on this, we then calculate the dielectric functions of Au and Ag that fit well with their experimental data. Following that, the LSPR properties of their NPs will be described based on a simple electrostatic approximation. The discussion starts with the case of a symmetric spherical NP and extends the idea to nanorods and ensembles of NPs. This chapter will also highlight about the three-temperature model (3TM) which is suited for the theoretical study of thermal dynamics in plasmonic structures over "long" times where both the initial non-thermal regime is completed and the energy exchange with the surrounding medium enters into play. It enables us to calculate

the electron and metal lattice temperatures inside a NP and the heat dissipation into its host environment. From these temperature dynamics, the transient optical response can be determined through the calculation of the time evolution of the NP dielectric function. Finally we will present the basic principles of time-resolved pump-probe spectroscopy.

In the second chapter, both the stationary and transient optical responses of silica nanowires decorated by nonspherical AuNPs will be presented. The experimental results will be reproduced theoretically and the ultrafast transient spectral dynamics of the sample will be interpreted by invoking the influence of the shape distribution of NPs in the sample and the LSPR coupling with interband transitions close to their threshold. This work has been achieved in close collaboration with partners from ISM-CNR, Rome.

The third chapter will be devoted to the study of the optical response of cuboidal AuNR@Ag (core@shell) NPs elaborated by our partners from LPS laboratory in Orsay. Both the stationary and the ultrafast transient responses will be studied depending on the Ag-shell thickness. The results will be analyzed by relying on theoretical calculations which satisfactorily reproduce the experimental data. This study also strongly involves our colleagues from Italy.

In chapter four, a complex-conjugate pole-residue pair (CCPRP) based FDTD method will be used to calculate the spatial, temporal and spectral dependence of the field inside and around a spherical AuNP. The ultrafast modulation of the near field will be analyzed by accounting for the influence of the different contributors to the near field (propagating or non-propagating). This work has been achieved in collaboration with a partner from CEA-LIST, a former master student in the team.

Finally, in the fifth chapter, we will prospectively investigate plasmonic-photonic coupling by theoretical means. We will consider an anisotropic configuration in which AuNRs have been used to investigate polarization-controlled photonic functionalities. Both the stationary and transient responses will be explored.

Chapter 1

Optical response of noble metal nanoparticles: background and tools

Contents

1.1 Introduction	5
1.2 Optical properties of bulk noble metals	6
1.2.1 Electronic structure and properties	6
1.2.2 Heat capacity of the metal ionic lattice	9
1.2.3 Dielectric function of noble metals	11
1.3 Stationary regime optical response of noble metal nanoparticles	17
1.3.1 Spherical nanoparticles	17
1.3.2 Non-spherical nanoparticles: the case of nanorods	19
1.3.3 Ensemble of nanoparticles	22
1.4 Numerical approaches	26
1.5 Optical response of noble metal nanoparticles in the transient regime	27
1.5.1 Time resolved pump-probe experiment	29
1.6 Summary	31

1.1 Introduction

Contrary to their bulk counterpart, noble metal nanoparticles (NPs) possess a fascinating optical property called surface plasmon resonance (SPR) which arises from the electromagnetic-field driven collective oscillation of their conduction electrons as a result of their dielectric confinement. This dissertation aims at studying both the stationary and transient optical responses of plasmonic nanoparticles, focusing on gold and silver. Hence, understanding the electronic characteristics of these metals and their interaction with electromagnetic radiation is crucial. The purpose of this first chapter is therefore to highlight the theoretical fundamentals by first focusing on the dovetailed optical response of noble metals in their bulk form, and then proceed to the specific properties that

appear when these metals are confined to the nanoscale. The theoretical foundations for gold have already been discussed in the preceding four dissertations [70–73] which were supervised by Bruno Palpant. Here we present an improved version of the former model that better describes the optical properties of silver and gold. Finally, the fundamental principles of pump-probe experiments, which enable to investigate the ultrafast transient optical properties of the noble metal NPs, will be presented.

1.2 Optical properties of bulk noble metals

1.2.1 Electronic structure and properties

In physics, definition of noble metals require the d -bands of the electronic structure be completely filled. Hence, copper (Cu), silver (Ag) and gold (Au) being the only three metals which fulfill this criteria since their d -bands are filled and do not cross the Fermi level (E_F). Their less-bound electron configuration has 5 filled d -bands (also called *valence bands*) and a half-filled s and p -states (also termed *conduction band*). In normal conditions of pressure and temperature they are organized in a monovalent face-centered cubic (fcc) crystalline structure and therefore have very similar band structures too (see Fig. 1.1). The electrons in the partially-filled conduction band are quasi-free and therefore responsible for the most electronic and thermal transport properties, while the ones in the bound valence bands contribute a few for this. Table 1.1 summarizes the main characteristics of the lattice structure and the Fermi energy, E_F and temperature, T_F values for each of the three noble metals.

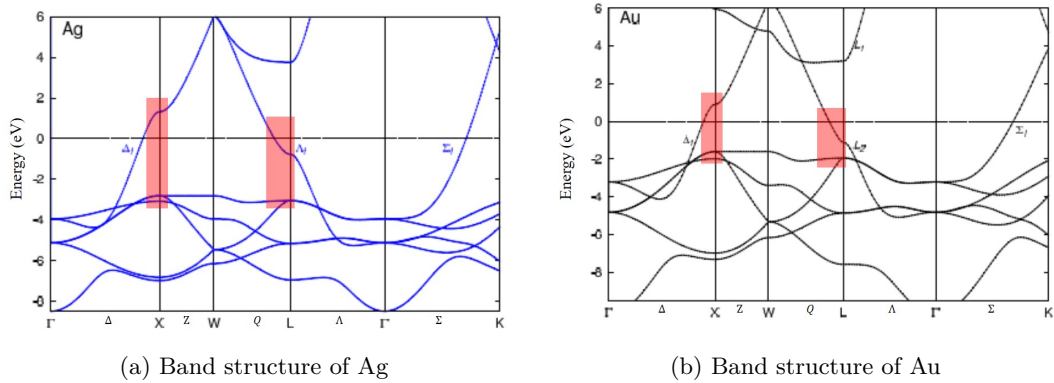


Figure 1.1 – Band structure of (a) silver and (b) gold along their high symmetry points and lines, taken from Ref. [74]. The dashed zero line indicates the Fermi level E_F (shifted to the zero energy). The red bars indicate the most probable zones for vertical electron transitions between the valence and conduction bands, close to their threshold.

Metal	\tilde{a} (Å)	E_F (eV)	T_F (K)
Cu	3.61	4.67	54400
Ag	4.08	5.49	63800
Au	4.07	5.53	64200

Table 1.1 – Lattice parameter \tilde{a} , Fermi energy E_F and Fermi temperature T_F of Cu, Ag and Au [73].

Cu is the less chemically stable noble metal among the three, making it difficult to control its size and shape during the synthesis of its NPs (CuNPs) as it is highly prone to oxidation. This makes it difficult to apply in the domain of plasmonics. Au is the most stable noble metal and is mostly used as a support for the preparation of anisotropic NPs. The spectral domain in which we will be focusing extends from near UV to near IR, i.e., for photons with energies between about 1 eV and 4 eV. These energies are too low to be able to excite electrons from the bands below the d -bands. Therefore, only the d -valence bands and the s - and/or p -conduction band govern the optical response of the noble metals for this spectral domain.

1.2.1.1 Conduction electrons

As we have pointed out above, the conduction electrons that populate the sp -band are delocalized over the entire crystal. The Fermi surface is defined as a surface in the reciprocal \mathbf{k} -space separating the occupied and unoccupied levels of the conduction bands at zero temperature. The lattice structure of noble metals being fcc, it takes the form shown in Fig. 1.2(a) for Ag and in Fig. 1.2(b) for Au.

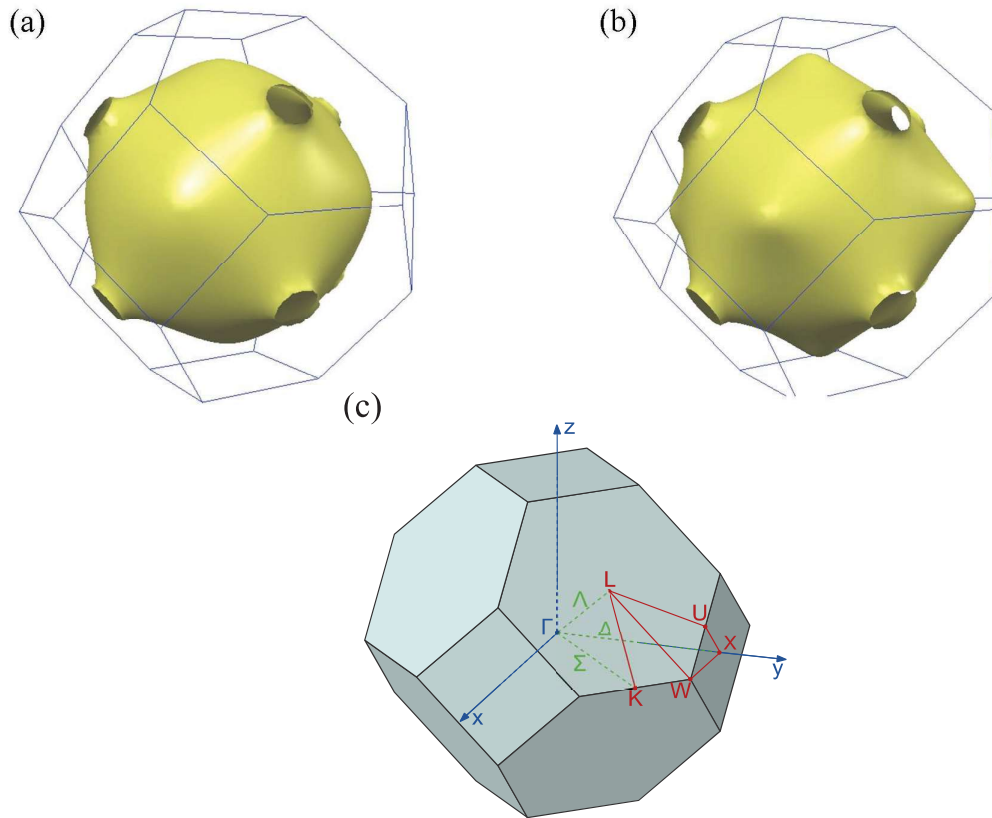


Figure 1.2 – Fermi surface (yellow) within the first Brillouin zone of (a) Ag and (b) Au [75]. (c) First Brillouin zone of the noble metals with high symmetry points [75]. Γ is the center of the Brillouin zone. The X and L points occupy the centers of the square and the hexagonal surfaces, respectively.

As can be seen, the Fermi surfaces of Au and Ag are roughly spherical –the perfect sphere corresponding to the case of a free electron gas– except at the L and X points of their Brillouin zone due to the weak ionic potential [76]. Conduction electrons can therefore be considered almost

free and hence are also termed as "quasi-free" electrons, which gives noble metals the well-known high thermal and electrical conductivities. Their dispersion law can then be considered as quasi-parabolic and the following dispersion relation can be employed [76]:

$$E(\mathbf{k}) = \frac{\hbar^2 \mathbf{k}^2}{2 m^*}, \quad (1.1)$$

where E , \mathbf{k} and m^* are the energy, wave vector and effective mass of the conduction electrons and \hbar is the reduced Planck constant. The use of effective mass also allows to write the density of electronic states $\rho(E)$ in the conduction band in a form similar to that of a free electron gas with mass m^* [76]:

$$\rho(E) = \frac{1}{2\pi^2} \left(\frac{2m^*}{\hbar^2} \right)^{3/2} \sqrt{E} \approx \frac{1}{2\pi^2} \left(\frac{2m}{\hbar^2} \right)^{3/2} \sqrt{E}. \quad (1.2)$$

For a quasi-free electron gas at internal equilibrium of temperature T_e (thermal regime), the occupancy probability density (or electron distribution) at energy E , $f(E)$, is given by the Fermi-Dirac statistics [76]:

$$f(E) = \frac{1}{1 + \exp\left(\frac{E - E_F}{\kappa_B T_e}\right)}, \quad (1.3)$$

where κ_B is the Boltzmann constant. Eq. 1.3 is established based on the assumption that the chemical potential $\mu(T_e)$ is equal to E_F [71, 73]. This condition complies well at temperatures $T_e \ll T_F$, see Table 1.1.

Besides, the free electron gas heat capacity is a linear function of temperature [76]:

$$C_e(T_e) = \frac{\pi^2}{2} \frac{T_e}{T_F} n_c \kappa_B = \gamma T_e, \quad (1.4)$$

where n_c is the density of conduction electrons. The heat capacity can therefore be put in the form $C_e(T_e) = \gamma T_e$, with $\gamma = \pi^2 n_c \kappa_B / 2 T_F$. Table 1.2 specifies the values of n_c and γ for the noble metals.

Metal	n_c ($\times 10^{28} \text{ m}^{-3}$)	γ ($\text{J m}^{-3} \text{ K}^{-2}$)
Cu	8.47	71
Ag	5.86	65
Au	5.9	66

Table 1.2 – Values of the conduction electron density n_c and the γ parameter in the relation $C_e(T_e) = \gamma T_e$ [76].

1.2.1.2 Involvement of the d -band electrons

As has been shown before experimentally [77, 78], Eq. 1.4 is no more valid for high electron temperature conditions ($\kappa_B T_e \geq 0.26$ eV for Au and $\kappa_B T_e \geq 0.43$ eV for Ag). Indeed, in this

case $f(E)$ is significantly less than 1 when the energy levels E corresponding to the d -bands are involved [79]. The calculation of $C_e(T_e)$ and the resulting properties must therefore take into account the presence of d electrons. Lin *et al.* [79] have calculated the density of states $\rho_{tot}(E)$ of metals by the density functional theory (DFT) by taking the d -band electrons into account. They then obtained $C_e(T_e)$ at high electron temperature by storing the T_e -dependent total number of electrons per unit volume, denoted by n_e :

$$n_e = \int_{-\infty}^{\infty} f(E, \mu(T_e), T_e) \rho_{tot}(E) dE . \quad (1.5)$$

Fig. 1.3 is extracted from Lin's work [79]. It displays the energy-dependent electron DOS and the T_e -dependent heat capacity for gold and silver.

As shown in Fig. 1.3, the high values of $\rho_{tot}(E)$ in the d -bands lead to a strong rise of $C_e(T_e)$ with T_e whereas the development of Sommerfeld would have predicted the opposite since it is based on a linear temperature dependence of the electron heat capacity and temperature independent electron-phonon coupling constant. The values of $C_e(T_e)$ are deduced by applying the definition of heat capacity to each energy level, then integrating over all weighted energy levels of the density of states $\rho_{tot}(E)$ [79]:

$$C_e(T_e) = \frac{\partial \langle E \rangle}{\partial T_e} = \int_{-\infty}^{\infty} \frac{\partial f(E, \mu(T_e), T_e)}{\partial T_e} \rho_{tot}(E) E dE . \quad (1.6)$$

Recently, Brown *et al.* [80] have applied a more rigorous (relativistic) approach to calculate electronic band structures accurately. They have provided the electron temperature dependent parameters [$C_e(T_e)$ and $G_{e-ph}(T_e)$] of noble metals which would have helped us with a better evaluation of the optical response of Au and Ag. However, Brown's work has appeared in the literature in a time which was too late for us to include their considerations in our calculation.

Hence, the linear relationship $C_e(T_e) = \gamma T_e$ (Eq. 1.4) is valid only at low electron temperatures up to about 3000 K for Au and 5000 K for Ag ($k_B T_e \sim 0.25 - 0.43$ eV). Beyond that, the heat capacity increases with electron temperature faster than in Eq. 1.4.

High electronic temperatures have an influence on other thermodynamic and electronic quantities, too [77,79]. In this work, we will study the heat transfer in metals by using the electron-phonon coupling parameter G values [79] that take this influence into account.

1.2.2 Heat capacity of the metal ionic lattice

Phonons are involved in many of the physical properties of the atomic structure of the metal, such as the ability to propagate sound, conduct and store heat [81]. This concept is also provided by the Debye model, which makes it possible to define a temperature T_D , called Debye temperature, above which all vibration modes can be thermally excited. In the regime where the ionic lattice temperature T_l is greater than T_D , the heat capacity of the lattice C_l therefore takes a constant

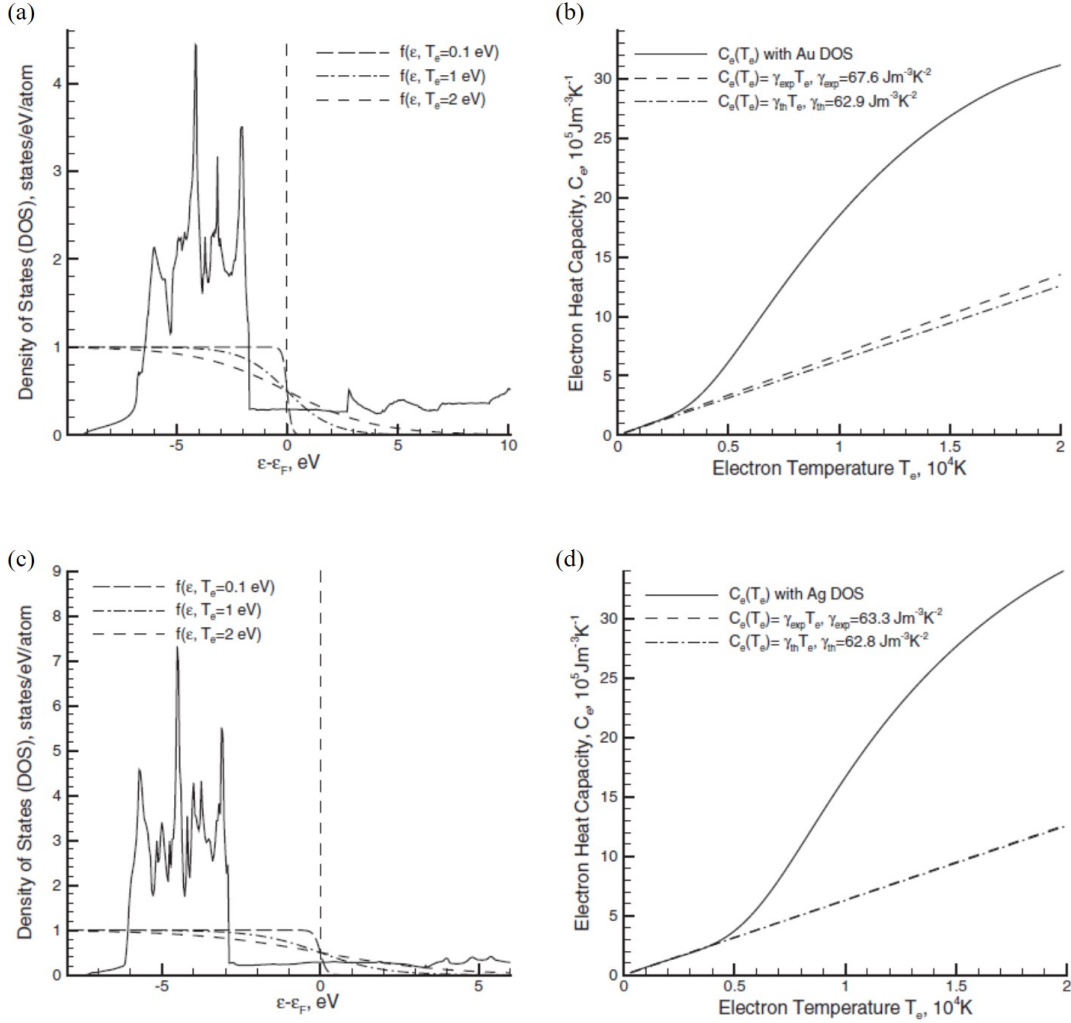


Figure 1.3 – Properties of the electron gas in Au and Ag as calculated by Lin *et al.* [79] by a DFT-based approach. (a) Solid line: density of electronic states of gold, ρ_{tot} , including the d -band electrons, as a function of the electron energy (E_F is considered as the origin). Dashed and dash-dotted lines: electronic distribution f according to Fermi-Dirac statistics for various values of T_e (1 eV corresponds to 11000 K approximately). (b) Electron heat capacity of gold as a function of the electron temperature. Solid line: calculation with the density of electronic states ρ_{tot} . Dashed and dash-dotted lines: calculations according to Sommerfeld's development with two different values of γ . (c) same as (a) and (d) same as (b) but for silver. All taken from Ref. [79].

value described by Dulong & Petit law [76]:

$$C_l = 3 n_{at} k_B \quad (1.7)$$

where n_{at} is the density of atoms per unit volume. Noble metals being monovalent, $n_{at} = n_c$. Debye's temperature is 170 K for Au and 215 K for Ag [76]. We will therefore consider in all the following that $T_l > T_D$, which results in $C_l \approx 2.49 \times 10^6 \text{ J m}^{-3} \text{ K}^{-1}$ for both Au and Ag [82].

1.2.3 Dielectric function of noble metals

The optical response of a noble metals is characterized by a (angular) frequency ω dependent complex relative dielectric function (also called the permittivity) $\varepsilon(\omega) = \varepsilon_1(\omega) + i\varepsilon_2(\omega) = 1 + \chi(\omega)$, where χ is the dielectric susceptibility of the material. The imaginary and real parts, $\varepsilon_2(\omega)$ and $\varepsilon_1(\omega)$, are interrelated by the Kramers-Kronig relations [83]:

$$\begin{aligned}\varepsilon_1(\omega) &= \frac{1}{\pi} \text{P} \int_{-\infty}^{\infty} \frac{\varepsilon_2(\omega')}{\omega' - \omega} d\omega', \\ \varepsilon_2(\omega) &= -\frac{1}{\pi} \text{P} \int_{-\infty}^{\infty} \frac{\varepsilon_1(\omega') - 1}{\omega' - \omega} d\omega'\end{aligned}\tag{1.8}$$

where P denotes the Cauchy principal value.

The frequency dependence of ε originates from the fact that the polarizability doesn't respond instantaneously to the applied field due to inertia of charge carriers. By definition, in a linear and isotropic environment, ε connects the electric displacement \mathbf{D} to the electric field \mathbf{E} according to:

$$\mathbf{D} = \varepsilon_0 \mathbf{E} + \mathbf{P} = \varepsilon_0 \mathbf{E} + \varepsilon_0(1 + \chi)\mathbf{E} = \varepsilon_0 \varepsilon \mathbf{E},\tag{1.9}$$

where ε_0 is the vacuum permittivity and \mathbf{P} the polarization in the metal. $\varepsilon(\omega)$ can also be expressed as the square of the complex optical index: $\varepsilon = \tilde{n}^2 = (n + i\kappa)^2$, where n is the refractive index and κ the extinction coefficient.

Dielectric function of noble metals have been experimentally determined by several authors [84–88], the most commonly used being those reported by Johnson & Christy [84] and those compiled by Palik [85]. In this work, we are interested in studying the details of the processes which rule the value of $\varepsilon(\omega)$ as well as their dependence on the electron and the lattice temperatures. More precisely, we are interested in the response of gold and silver to a light wave in the near UV to near IR (approximately from 1 to 4 eV). In this range of photon energy, the dielectric functions is constituted of two contributions [71, 73]. The electron transitions within the conduction band, s and/or p , (termed as "intraband" transitions) and the transitions between the valence bands, d and the s - and/or p -bands (termed as "interband" transitions). Hence, the dielectric function is therefore the sum of an interband contribution ε^{ib} and an intraband contribution χ^D , Eq. 1.10. The superscript D in χ^D denotes the fact that the intraband contribution can be characterized via the Drude-Sammerfeld model.

$$\varepsilon(\omega) = \varepsilon^{ib}(\omega) + \chi^D(\omega) = \varepsilon_1^{ib}(\omega) + i\varepsilon_2^{ib}(\omega) + \chi_1^D(\omega) + i\chi_2^D(\omega).\tag{1.10}$$

Now, we are in a position to discuss the details of these contributors that make up the complex dielectric function $\varepsilon(\omega)$ of Au and Ag noble metals.

1.2.3.1 Interband dielectric function contribution (Rosei model)

The interband transitions occur between the valence and conduction bands. We call the minimum energy difference between the top of the d -bands and the first empty electronic level of the s -

and/or p -bands (for a direct vertical electron transition) the "interband electron transition threshold", $\hbar\omega_{ib}$. A photon with energy higher than $\hbar\omega_{ib}$ can be absorbed for promoting an electron from d -band to the s - and/or p -bands. ε_2^{ib} [Eq. 1.10] is then equal to zero for photon energies below $\hbar\omega_{ib}$. The interband transition contribution can only be described by a quantum approach [89–93]. For this, we use the dielectric function expressions based on the Lindhard's theory [94] in the work of Y. Guillet [73].

The band structure of Au and Ag are shown in Fig. 1.1. The d -bands lie a few eV below the Fermi level (see the zero line) and the sp -band crosses E_F level in the vicinity of the points X , L and along the direction of Σ of the Brillouin zone. For the spectral zone extending from near UV to near IR, the X and L points provide the main contributions to interband transitions in noble metals. However, the transitions around the L point have a greater oscillator strength than the X point one. Beyond, in the ultrafast transient optical response of gold in the visible and near IR spectral domain, the contribution of the transitions around the L point are significantly larger than the one around the X point, and have usually been considered only [40, 71, 73, 95]. For the spectral zone of our interest (1 to 4 eV), considering the involvement of both the L and X point transitions [the red regions in Fig. 1.1(b)] is required for fitting the dielectric function of gold. For silver, consideration of only the L point transitions [the red region in Fig. 1.1(a)] is enough for a satisfying fit of its dielectric function. The interband transition threshold values are, respectively, $\hbar\omega_{ib}^{L,Au} \sim 2.4$ eV and $\hbar\omega_{ib}^{X,Au} \sim 1.9$ eV for the transitions around the L and X points for Au while $\hbar\omega_{ib}^{L,Ag} \sim 3.9$ eV for Ag for the transition around the L point.

The band structures are modeled based on the work of Rosei [90–93]. The X and L points are high symmetry points in the vicinity of which the electron energy bands exhibit a quadratic dependence on \mathbf{k} [96]. Thus, parabolic band structures are locally assumed in each direction [73, 89–93, 96]. The Rosei model is only valid for photons energies not too far from interband transition threshold. For our calculation of the interband transition contribution to $\varepsilon(\omega)$, we adopt the same approach as the one of the team of F. Vallée and N. Del Fatti in Lyon as detailed in [96]. Details are given in Appendix A.

1.2.3.2 Intraband dielectric function contribution (Drude-Sommerfeld model)

We have established the framework that helps to obtain the interband contribution to the dielectric function. In this section we deal with the remaining intraband contribution so that we have a complete model for the dielectric function calculation. For this, the properties of the quasi-free electrons in the conduction band are described by the classical model developed by Drude and Sommerfeld. Assuming an electron with effective mass m^* and charge $-e$ interacting with an external electric field $\mathbf{E}(t)$, its motion (displacement vector \mathbf{r}) can be described according to the Newton's second law [73, 76, 96]:

$$m^*\ddot{\mathbf{r}} = -m^*\Gamma\dot{\mathbf{r}} - e\mathbf{E}(t) , \quad (1.11)$$

τ being the characteristic collision time, its counterpart in energy is $\Gamma = 1/\tau$. Γ is then the phenomenological scattering constant that accounts for all the scattering processes experienced by the electrons. The electron displacement creates a dipole moment $\mathbf{p} = -e\mathbf{r}$. Hence, assuming that all electrons behave the same way and are independent, the polarization is deduced at the

mesoscopic scale:

$$\mathbf{P} = n_e \mathbf{p} , \quad (1.12)$$

and since the \mathbf{P} and \mathbf{E} are interrelated via the susceptibility,

$$\mathbf{P} = \varepsilon_0 \chi^D(\omega) \mathbf{E} . \quad (1.13)$$

The Drude dielectric function ε^D can then be expressed as

$$\varepsilon^D = 1 + \chi^D(\omega) = 1 - \frac{\omega_p^2}{\omega(\omega + i\Gamma)} , \quad (1.14)$$

where $\omega_p = \sqrt{\frac{n_e e^2}{m^* \varepsilon_0}}$ is the plasma frequency. The plasma frequency of Au and Ag is $\hbar\omega_p = 8.984$ eV.

As can be seen in Eq. 1.14 the determination of the phenomenological scattering constant Γ is the core of this section to establish the variations of $\chi^D(\omega)$ with f and T_l . For the NP size range and temperature values of our interest here, Γ is the sum of two main contributions [73]:

$$\Gamma = \Gamma_{e-e} + \Gamma_{e-ph} , \quad (1.15)$$

where Γ_{e-e} is the rate of electron-electron scattering and Γ_{e-ph} the rate of electron-phonon scattering. The first was calculated by R. Gurzhi [97] as part of Landau's theory of Fermi liquids in the case where an electronic temperature T_e can be defined, in the thermal regime [97]:

$$\Gamma_{e-e}(\hbar, \omega, T_e) = \frac{(k_B T_e)^2}{\hbar^2 \omega_p} \left[1 + \left(\frac{\hbar\omega}{2, \pi \kappa_m B}, T_e \right)^2 \right] . \quad (1.16)$$

In the hypothesis of quasi-free electrons (parabolic dispersion relationship), assuming that the phonon energies involved are negligible compared to those of photons, Chin-Yi Tsai *et al.* [98] calculated Γ_{e-ph} using the Fermi golden rule at the second order. It is given as [73]:

$$\Gamma_{e-ph}(\hbar\omega) = \frac{G_{e-ph}}{\hbar\omega} \int_0^\infty \sqrt{E} \sqrt{E + \hbar\omega} f(E) [1 - f(E + \hbar\omega)] dE , \quad (1.17)$$

where G_{e-ph} is an electron-phonon coupling "parameter" not to be confused with the coupling "constant". Earlier in this chapter (see §1.2.1.2), we have discussed about the dependence of C_e on T_e [79]. We will evoke this issue in chapter 2 where we will take the contributions of d -band electrons into account for the calculation of the dielectric function of Au. For the $T_l > T_D$ case

(§1.2.2), $G_{e-ph} \propto T_l$, which leads to the equation [98]:

$$\Gamma_{e-ph}(\hbar\omega) \propto \frac{T_l}{\hbar\omega} \int_0^\infty \sqrt{E} \sqrt{E + \hbar\omega} f(E)[1 - f(E + \hbar\omega)] dE . \quad (1.18)$$

At room temperature, $\Gamma_{e-e} \ll \Gamma_{e-ph}$ [73]. However, the T_e values may sometimes reach several thousand kelvins. Γ_{e-e} can then no longer be neglected in the establishment of Γ . For example, for $T_e = 5000$ K, $\hbar\Gamma_{e-e}(1 \text{ eV}) = 23 \text{ meV}$ and $\hbar\Gamma_{e-ph}(1 \text{ eV}) = 77 \text{ meV}$ [71]. So, both contributions have to be considered in this case. Finally, for the photon energies below the interband threshold, the proportionality constant in Eq. 1.18 is evaluated by adjusting it to the experimental values at room temperature.

1.2.3.3 Total dielectric function

In this manuscript, we model the experimental dielectric function data of Palik [85] for Au and of Johnson & Christy [84] for Ag, both being good at predicting the spectral characteristics of the SPR. As shown in Fig. 1.4(a) and (b), a very satisfactory agreement can be achieved with the experimental data reported in Ref. [85] for Au. For this, in addition to the intraband transition contribution (Drude model), the interband transitions from $d \rightarrow p$ and $p \rightarrow s$ are considered at the L point of the Brillouin zone while a $d \rightarrow p$ transition was considered at the X point. Fig. 1.4(c) and (d) confirm that considering only the L point interband transitions ($d \rightarrow p$ and $p \rightarrow s$) is enough for a satisfying modeling of the the experimental dielectric function of Ag from Ref. [84].

For the simulation of the dielectric functions, the parabolic band parameters (for the interband transitions) of both Au and Ag are implemented as reported in Ref. [99]. Values of the effective masses for both Ag and Au are directly used as reported in Refs. [96,99]. However, the parameters of Au that have been used in this work are slightly different from what can be read in Ref. [99], because different experimental data of Au are considered by this work and Ref. [99]. Besides, there is no difference between the band energy values that we have implemented for Ag and the ones reported in Ref. [99]. Table 1.3 summarizes the relative oscillator strength, $\eta_{i \rightarrow f}^{X,L} = \left| M_{X,L}^{i-f} \right|^2 / \left| M_L^{d-p} \right|^2$ and the band energy values (eV) that are considered in this work for both Au and Ag and compares them with the ones reported in Ref. [99].

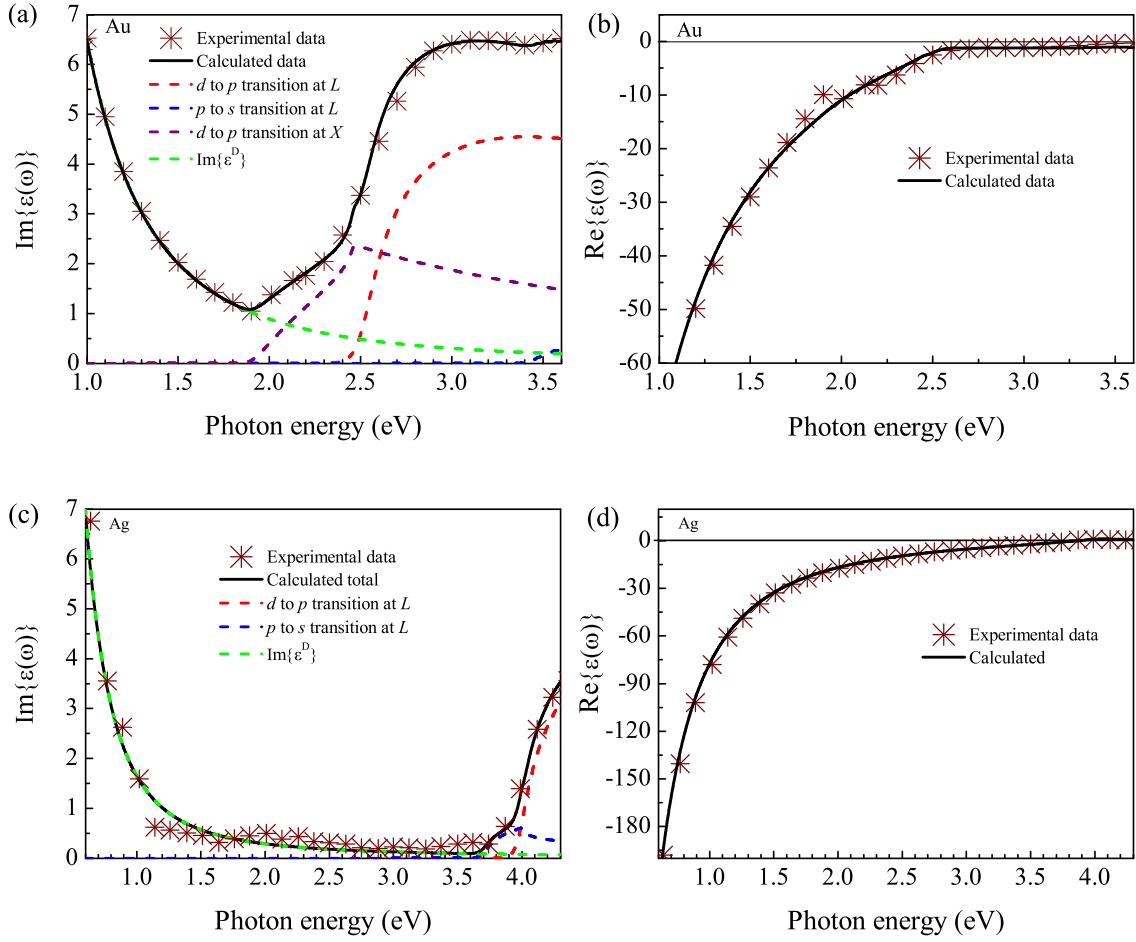


Figure 1.4 – Comparison of the calculated stationary dielectric functions of Au and Ag with the experimental data of Palik [85] and Johnson & Christy [84], respectively. (a) The calculated imaginary part of the dielectric function of Au (solid black line) is compared to the experimental data (symbols). The interband (around both L and X points of the Brillouin zone) and intraband (Drude part) transition contributions are indicated with dashed lines. (b) The real part obtained by the Kramers-Kronig relation (Eq. 1.8) from the calculated imaginary part [shown in (a)] as compared to the real part of Palik’s experimental data. (c) Same as (a) but for Ag (interband transitions at L point are considered only) as compared to the imaginary part of the dielectric function reported by Johnson & Christy. (d) same as (b) but for Ag.

Element	Band	Energy (eV)		$\eta_{i \rightarrow f}^{X,L}$
		This work	Ref. [99]	
Au	$L_{4+} (s)$	+3.414	+3.414	$\eta_{d \rightarrow p}^L = 1$ $\eta_{p \rightarrow s}^L = 0.24$ (= 0.272 in Ref. [99]) $\eta_{d \rightarrow p}^X = 0.29$ (= 0.32 in Ref. [99])
	$L_{4-} (p)$	-1.550	-1.368	
	$L_{5++6+} (d)$	-2.055	-2.055	
	$X_{6-} (p)$	+640	+573	
	$X_{7-} (d)$	-2.460	-1.763	
Ag	$L_{4+} (s)$	+3.684	+3.680	$\eta_{d \rightarrow p}^L = 1$ $\eta_{p \rightarrow s}^L = 0.35$ (= 0.478 in Ref. [99])
	$L_{4-} (p)$	-0.310	-0.320	
	$L_{5++6+} (d)$	-3.942	-3.940	

Table 1.3 – The band energy and relative oscillator strength values, $\eta_{i \rightarrow f}^{X,L} = |M_{X,L}^{i-f}|^2 / |M_L^{d-p}|^2$, of Au and Ag that are used in this work as compared to the ones reported in Ref. [99]). The origin of the energies is set at E_F

1.3 Stationary regime optical response of noble metal nanoparticles

For a metal particle of size much smaller than the wavelength of the incoming light, the conduction electrons experience a homogeneous field and oscillate collectively on either side of the ionic core lattice (Fig. 1.5). This oscillating system has a natural eigenfrequency and gives rise to a resonance phenomenon, the LSPR. When the frequency of the applied wave matches the LSPR frequency of the particle, there is a maximum energy transfer from the electromagnetic wave to the particle. The energy is dissipated either non-radiatively ($e-e$ and $e-ph$ scattering) or radiatively. The damping of this oscillator is described by Γ , the total electron collision rate introduced in the previous section in which the radiative damping is negligible (§1.2.3.2). In the following, we begin from the simplest case of spherical NPs and proceed to the more complex case of anisotropic NPs.

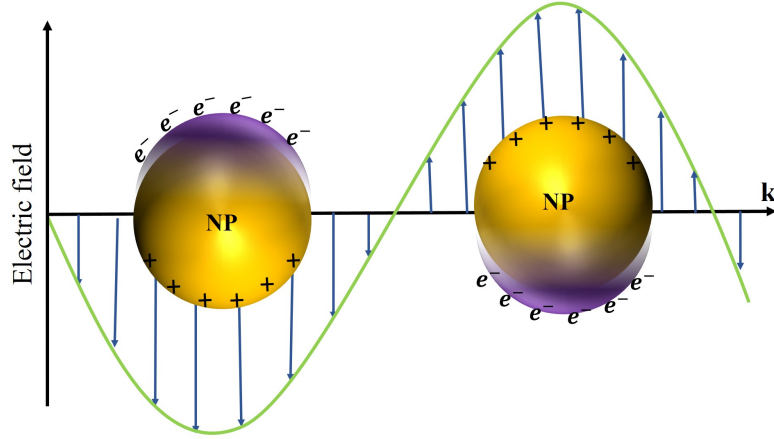


Figure 1.5 – Schematic representation of the displacement of the conduction electrons from the ionic core of a spherical NP in response to an applied external electromagnetic field.

1.3.1 Spherical nanoparticles

Considering a homogeneous spherical particle of radius $R \ll \lambda$, placed in an isotropic host medium of dielectric constant ε_d , under the electric field $\mathbf{E}_0 e^{-i\omega t}$, where λ and ω are respectively the wavelength and the angular frequency of the incident field. The optical response of the system can be calculated by solving Maxwell equations, either based on the pioneering work of Mie (multipolar expansion) [2] or the analytic and/or numerical developments that followed. However, we present here the simplest case which is based on the electric dipole approximation where the NP response is assimilated as that of a dipole, \mathbf{p} . So, the dipole moment induced in the NP by the incident field can be written as:

$$\mathbf{p} = \alpha(\omega)\mathbf{E}_0. \quad (1.19)$$

$\alpha(\omega)$ is polarizability of the particle. The total field \mathbf{E}_{tot} inside the metal is given by the sum of the incident field and the induced field (also called depolarizing field):

$$\mathbf{E}_{tot} = \frac{3\varepsilon_d(\omega)}{\varepsilon(\omega) + 2\varepsilon_d(\omega)} \mathbf{E}_0. \quad (1.20)$$

The extinction σ_{ext} and scattering σ_{sca} cross-sections can be obtained from the scattering field radiated by the dipole. The power radiated by this dipole moment, which is also the power scattered by the particle, is given by [70]:

$$\mathcal{P}_{ray} = \frac{\omega^4}{12\pi\pi\varepsilon_0c^3} |\mathbf{p}|^2. \quad (1.21)$$

Hence, σ_{ext} and σ_{sca} of the system can be deduced from the Eqs. (1.19) and (1.21):

$$\sigma_{sca}(\omega) = \frac{\kappa^4}{6\pi} |\alpha(\omega)|^2. \quad (1.22)$$

$$\sigma_{ext}(\omega) = \kappa \text{Im}[\alpha(\omega)], \quad (1.23)$$

where κ is the wave vector of the incident field.

In the dipolar approximation, if we neglect the radiative correction (which is valid when $\kappa R \ll 1$), $\alpha(\omega)$ of the spherical particle is given by [83]:

$$\alpha(\omega) = 4\pi\varepsilon_0\varepsilon_d(\omega)R^3 \frac{\varepsilon(\omega) - \varepsilon_d(\omega)}{\varepsilon(\omega) + 2\varepsilon_d(\omega)}. \quad (1.24)$$

The effective absorption cross-section ($\sigma_{abs} = \sigma_{ext} - \sigma_{sca}$) is then given as [70, 71]:

$$\sigma_{abs}(\omega) = 9\frac{\omega}{c}\varepsilon_d(\omega)^{3/2}V \frac{\varepsilon_2(\omega)}{[\varepsilon_1(\omega) + 2\varepsilon_d(\omega)]^2 + \varepsilon_2(\omega)^2}. \quad (1.25)$$

Eq. 1.25 tells us that in the case where $\varepsilon_2(\omega)$ is small or weakly dispersed, σ_{abs} reaches its maximum value when the condition $\varepsilon_1(\omega) = -2\varepsilon_d(\omega)$ is satisfied. For $\Gamma \ll \omega$ ($\hbar\Gamma \sim 100$ meV in the visible domain), we can deduce:

$$\omega_{SPR} = \frac{\omega_p}{\sqrt{\varepsilon_1^{ib}(\omega_{SPR}) + 2\varepsilon_d(\omega_{SPR})}}. \quad (1.26)$$

Let us now summarize some properties of LSPR and its dependence upon a few key parameters of the system.

1. LSPR band spectral profile

As for the case of spherical AgNPs, if ω_{SPR} is far below the interband transition threshold, the LSPR spectral profile can be approximated as quasi-Lorentzian. This is not the case for spherical AuNPs whose ω_{SPR} and interband transition threshold overlap [96].

2. Influence of the surrounding medium

From Eqs. 1.25 and 1.26 we can see that when ε_d increases, the LSPR shifts to the red and its amplitude increases. Hence, the characteristics of LSPR are sensitive to the refractive index of the surrounding medium.

3. Near-field enhancement

At LSPR resonance, the local electromagnetic field is enhanced in and around the NP. This can be characterized by a value of the near-field enhancement factor $F = \frac{|E_{tot}|}{|E_0|} > 1$ inside the NP. For the case of spherical NPs, the enhancement factor is given by $F(\omega) = \left| \frac{3\varepsilon_m(\omega)}{\varepsilon(\omega) + 2\varepsilon_m(\omega)} \right|$ inside the metal (see Eq. 1.20). However, the field enhancement extends to the vicinity of the nanoparticle. It is maximum at the interface (in the polarization direction of the wave) and for small enough NPs it decreases as $\frac{1}{r^3}$ with the distance r from the center of the NP [Fig. 1.6]. In chapter 4, we will study its modulation in response to the absorption of a femtosecond laser pulse by a spherical NP.

4. Influence of the NP size

Particle size also has an important influence. On the one hand, for aggregates of a few hundred atoms ($R \leq 2$ nm), their optical properties can no longer be described by using the dielectric function of the bulk noble metal due to several quantum electronic effects, comprising the modification of the mean free path of electrons [97, 100, 101]. On the other hand, from the Eqs. 1.22, 1.27 and 1.25 we can notice that $\sigma_{abs} \propto R^3$ and $\sigma_{sca} \propto R^6$, which then allows one to neglect the scattering term for sufficiently small particles. This is actually the case for most of the samples that we will study in this dissertation except the ones in chapter 3. Indeed, in the third chapter, we will see that σ_{sca} has a significant influence on the optical response of bigger NPs. Multipolar effects start to play an important role in the optical properties of NPs the size of which exceeds about 30 nm [96].

1.3.2 Non-spherical nanoparticles: the case of nanorods

LSPR is also very sensitive to the shape of the NP [102]. Many studies have been devoted to the shape dependent optical response of noble metal NPs starting from the simple rod-like (nanorods) [40, 103, 104] to the more complex star-shaped ones (see Fig. 1) [105]. For example, nanorods (NRs) are characterized by their aspect ratio (AR) which is the ratio of the longest axis dimension to the shortest one. The symmetry lowering compared to the sphere induces the appearance of two LSPR modes that can be excited depending on the polarization of the incident light [104]. For the other shapes (Fig. 1), the lower the symmetry, the larger the number of resonance modes. With a linearly polarized incident light, if the NR is oriented perpendicular to the field polarization then the incident wave excites an electron oscillation perpendicular to the major axis of the particle [Fig. 1.7(a)]. This resonance mode is called *transverse* (TrSPR). The corresponding absorption band appears as the small peak (designated by T) appearing around 2.5 eV of the red curve in Fig. 1.7(b) where the absorption spectrum of a gold nanorod with random orientation (AuNR) is displayed together with the one of a gold nanosphere of equivalent volume. On the contrary, if the AuNR is parallel to the polarization, the electrons oscillate parallel to

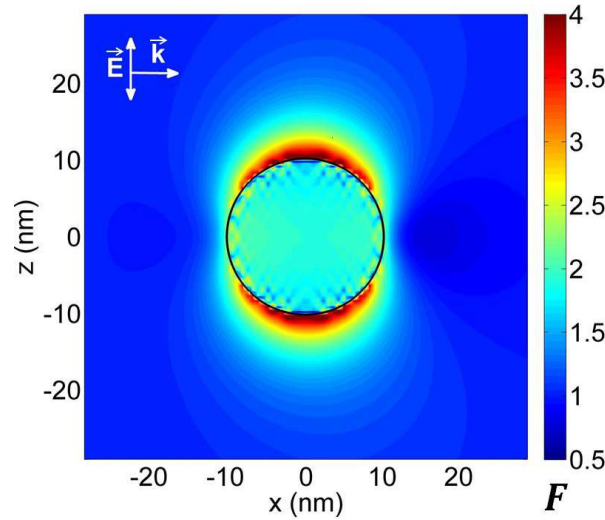


Figure 1.6 – Near-field enhancement factor F calculated inside and outside of a gold nanosphere with radius $R = 10$ nm in water, excited by a light wave tuned to its LSPR at 520 nm. The directions of the incident electric field \mathbf{E} and the wave vector \mathbf{k} are indicated [71].

the major axis. The corresponding LSPR mode is called the *longitudinal* mode (LgSPR). This mode manifests itself as the large absorption peak appearing in the red curve of Fig. 1.7(b) which is designated by L . The transverse resonance frequency (ω_{SPR}^T) is close to that of a sphere [the black curve in Fig. 1.7(b)] and shifts only weakly with the AR of the NR. On the other hand, the longitudinal resonance frequency (ω_{SPR}^L) shifts to the infrared [see 1.7(b)] as the AR of the NR increases [106]. Hence, the 3-fold degeneracy of the LSPR that can be observed in spherical NPs due to their symmetry is partially lifted for the case of NRs. So, after averaging over all possible orientations of the AuNR with respect to the polarization direction, the extinction spectrum exhibits two resonance bands [see the red curve in Fig. 1.7(b)].

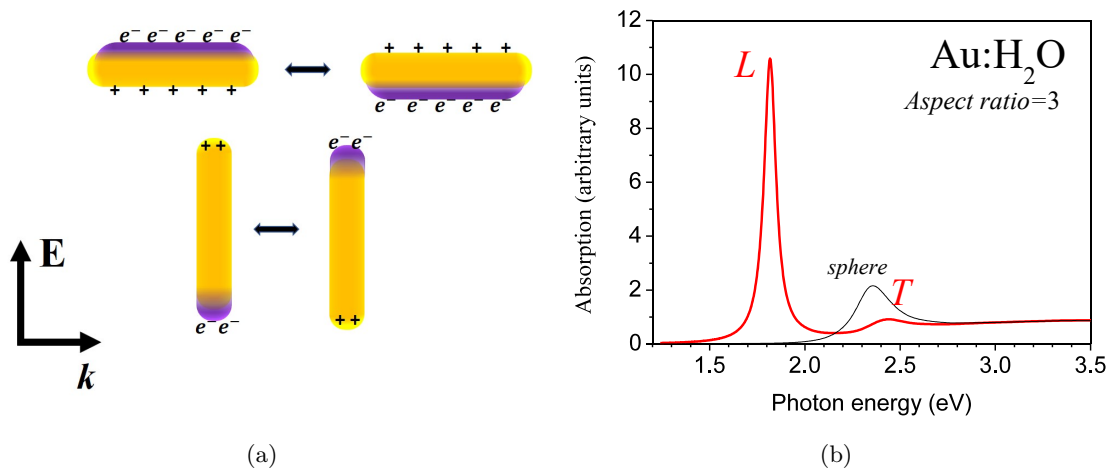


Figure 1.7 – (a) Cartoon depicting the principle of the interaction of a linearly polarized light wave with a AuNR. \mathbf{E} : direction of the electric field polarization. \mathbf{k} : wave vector. e^- : electron. (b) The calculated absorption spectra of a spherical AuNP (black) and a AuNR (red) with AR = 3 having the same volume, in water, with a randomly-polarized incident field [72].

Finally, we would like to stress that there is no straight analytic method for modeling the optical properties of complex non-spherical NPs (Fig. 1). Usually, numerical approaches (§1.4) are employed for such kind of plasmonic nanostructures. It is however possible to describe the optical properties of ellipsoidal NPs using the analytic method developed by R. Gans [107], which is an extension of Mie theory [2] using ellipsoidal coordinates. As we will deal with AuNRs in some of the following chapters, and as the optical response of AuNRs can be assimilated, to some extent, to the ones of ellipsoids [108], let us now present this approach. In the following discussions, we will assume (for simplicity) that the dielectric environment is weakly dispersed and therefore $\varepsilon_b(\omega)$ can be expressed as ε_d .

1.3.2.1 Gans-Mie theory

The Gans-Mie theory [107, 109], also called the *extended Mie theory*, was developed to characterize the optical response of spheroidal particles (oblate and prolate), Fig. 1.8. Following the electric dipole approximation method that we have developed for spherical nanoparticles (§1.3.1), a general formula of extinction cross-section for spheroids (ellipsoids with semi-axes: $a = b$ and c) can be deduced using the quasi static approximation ($a = b$ and $c \ll \lambda$) [83, 107, 110–112]. The polarizability of an ellipsoid (analogues to Eq. 1.27) when an electric field is applied parallel to one of its x , y or z directions can be shown to be [83]:

$$\alpha_{x,y,z}(\omega) = \frac{4\pi}{3} abc \frac{\varepsilon(\omega) - \varepsilon_d}{\varepsilon_d + L_{x,y,z}[\varepsilon(\omega) - \varepsilon_d]}, \quad (1.27)$$

where $L_{x,y,z}$ is the depolarization factor that depends on the geometry of the ellipsoid and is characterized by the possible polarization directions. One can show, by solving the Maxwell equations in a system of ellipsoidal coordinates [83], that the depolarization factor along the long axis, L_z , for a prolate spheroid ($a = b < c$, Fig. 1.8-right) is given by

$$L_z = \frac{1 - e^2}{e^2} \left[-1 + \frac{1}{2e} \ln \frac{1 + e}{1 - e} \right]. \quad (1.28)$$

For the long axis of an oblate spheroid, $L_x = L_y$ ($a = b > c$, Fig. 1.8-left), we can express it as [113]:

$$L_x = L_y = \frac{(1 - e^2)^{1/2}}{2e^3} \left[\frac{\pi}{2} - \arctan \left(\frac{(1 - e^2)^{1/2}}{e} \right) \right] - \frac{1 - e^2}{2e^2} \quad (1.29)$$

where $e^2 = 1 - (1/\text{AR})^2$ is the eccentricity, expressed in terms of the particle's aspect ratio $\text{AR} = c/a$. Then the geometrical factor expressions for the short axis are given by $L_y = L_x = (1 - L_z)/2 > 1/3 > L_z$ and $L_z = (1 - 2L_{x,y}) > 1/3 > L_x = L_y$ for prolate and oblate shapes, respectively. For light polarized along the i direction parallel to x , y or z , the particle absorption cross section σ_{abs} averaging over all possible polarizations is given by [112, 113]

$$\sigma_{abs}(\omega) = \frac{\omega}{3c} \varepsilon_d^{3/2} V \sum_i \frac{\varepsilon_2(\omega)/L_i^2}{\left[\varepsilon_1(\omega) + \left(\frac{1 - L_i}{L_i} \right) \varepsilon_d \right]^2 + \varepsilon_2(\omega)^2} \quad (1.30)$$

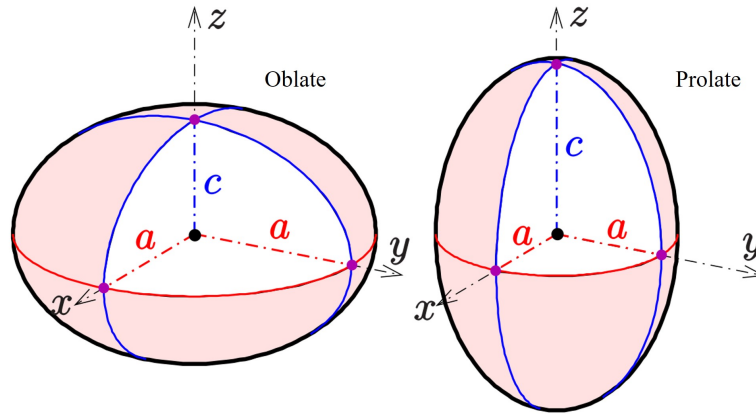


Figure 1.8 – The axes of spheroidal shapes, oblate if $c < a$ (left) and prolate if $c > a$ (right). The z axis is the symmetry axis for both cases (from Wikipedia).

where V is the volume of the spheroid.

AR dependent spectra calculated for prolate AuNRs by use of Eqs. 1.28 and 1.30 are shown in Fig. 1.9. As expected, the LgSPR red shifts with the increase of AR. The LgSPR resonance magnitude increases with increasing AR because of: (i) the increase of the volume of the NP since the short axis is kept constant ($a = 10$ nm) and the long axis c is varied, and (ii) the LgSPR mode decouples more and more from interband transitions.

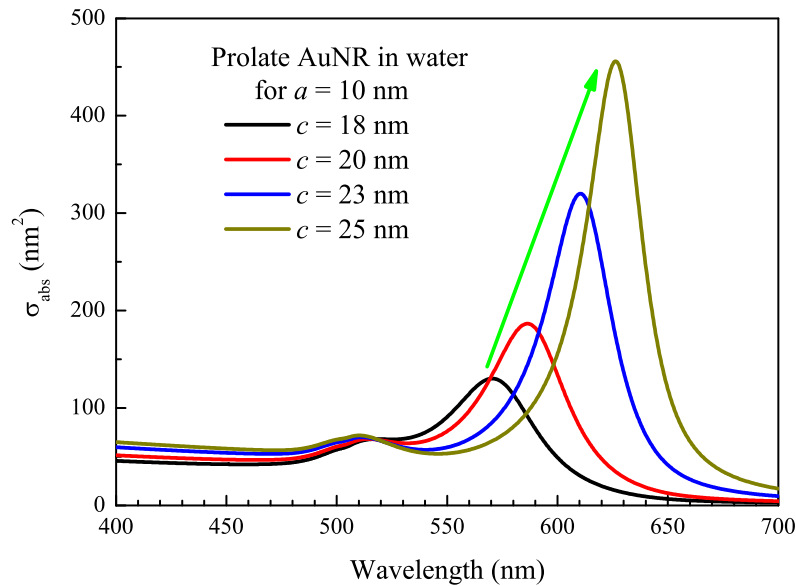


Figure 1.9 – Aspect ratio dependent spectra of a prolate shaped AuNR as calculated by Gans-Mie theory. The green arrow indicates the AR dependent red shift of the LgSPR mode.

1.3.3 Ensemble of nanoparticles

There exists analytical approaches to model an ensemble of nanoparticles that are dispersed in a continuous host of dielectric medium. A general approach called effective medium theory (EMT) is used to describe the mesoscopic behavior of the electromagnetic field propagating in

such kind of complex media, like plasmonic nanocomposite thin films. It consists in replacing the inhomogeneous medium by a fictitious homogeneous medium characterized by an effective dielectric function, ε_{eff} , such that the electromagnetic field propagation has the same properties as in the actual medium. In this work we are interested in studying two- or three-dimensional nanocomposites which are made up of non-spherical metal nanoparticles distributed in a dielectric medium. Hence, this section will be devoted to the models that have been used in our study, i.e., the extended Maxwell-Garnett [114, 115] and Yamaguchi [116] models. The former is particularly suitable for a totally random three-dimensional distribution of NPs while the latter is applicable for a two-dimensional distribution of NPs in a dielectric host medium. They are both based on a mean field approach.

1.3.3.1 Extended Maxwell-Garnett model

The extended Maxwell-Garnett (MG) model, as its name suggests, is an extension of the original Maxwell-Garnett model [114, 115] which was developed to estimate the effective dielectric function of a medium consisting of spherical particles randomly dispersed in a volume of dielectric host material. Hence, the extended MG model is applicable for inclusions of ellipsoidal NPs. This model has proven to be very useful for calculating the optical properties of 3-D media containing a low density of metallic inclusions (Fig. 1.10). Indeed, as the interactions between NPs are disregarded in this model, it is valid for metal volume fractions lower than $\sim 15\%$ in the visible spectral domain [117]. The effective dielectric function, ε_{eff}^{MG} , of a composite medium containing a small fraction of metal NPs is related to the dielectric functions of the dielectric host medium and of the metal via [118]:

$$\varepsilon_{eff}^{MG}(\omega) = \varepsilon_d \frac{1 + \frac{3L_{x,y,z} + 2q}{3} \frac{\varepsilon - \varepsilon_d}{\varepsilon_d}}{1 + \frac{3L_{x,y,z} - q}{3} \frac{\varepsilon - \varepsilon_d}{\varepsilon_d}} \quad (1.31)$$

where ε_d and ε are the dielectric functions of the host medium and the bulk metal, respectively, and q is the volume fraction of the spheroidal inclusions. The L_i are given by Eqs. 1.28-1.29.

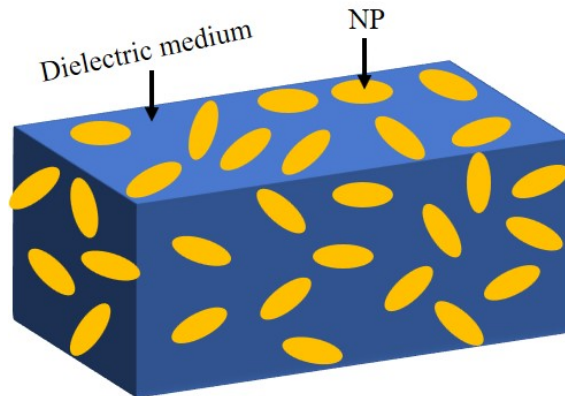


Figure 1.10 – Scheme of a composite medium consisting of randomly dispersed anisotropic NPs in a 3-D dielectric host medium.

1.3.3.2 Yamaguchi model

Contrary to the volumic distribution of inclusions (Fig. 1.10) that we have discussed just now, one may also encounter with samples that present an in-plane (two-dimensional) distribution of NPs [Fig. 1.12(a)]. In this case, the Yamaguchi model can give good predictions [116, 119, 120]. Let us consider identical NPs distributed on a substrate of dielectric function ϵ_{sub} and having a height of h above the substrate. We denote the dielectric function of the external environment in which the NPs are embedded by ϵ_{ext} to be consistent with Fig. 1.11. The electric field induced by each particle and its mirror image due to the external applied electric field, \mathbf{E}_{ext} , are in opposite direction.

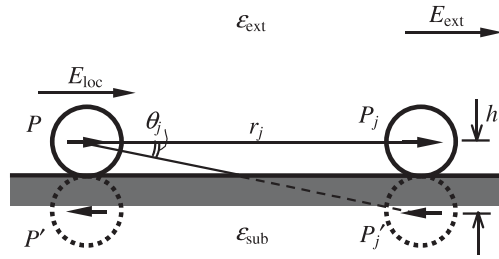


Figure 1.11 – Schematic representation of the dipole moments p and p' of NPs and their mirror images, receptively. The induced local field experienced by the particle \mathbf{E}_{loc} which is the sum of the external applied field \mathbf{E}_{ext} , the field created by the image dipole p'_j and the field created by all other dipoles p_j is also shown. Taken from Ref. [121].

The induced total local electric field that is acting on each particle, \mathbf{E}_{loc} , is then the sum of the external field, the field produced by the mirror image \mathbf{E}_{img} and the field by the surrounding particles \mathbf{E}_{sur} [121]:

$$\mathbf{E}_{loc} = \mathbf{E}_{ext} + \mathbf{E}_{img} + \mathbf{E}_{sur}. \quad (1.32)$$

\mathbf{E}_{img} is given by [121]:

$$\mathbf{E}_{img} = -\frac{1}{4\pi\epsilon_0\epsilon_{ext}h^3}p' = \frac{1}{4\pi\epsilon_0\epsilon_{ext}h^3}\frac{\epsilon_{sub} - \epsilon_{ext}}{\epsilon_{sub} + \epsilon_{ext}}p \quad (1.33)$$

where $p' = \frac{\epsilon_{sub} - \epsilon_{ext}}{\epsilon_{sub} + \epsilon_{ext}}p$. A spherical coordinate system can be introduced to calculate the contributions of the surrounding particles and their mirror images. If we consider that the distance between the neighboring particles $r_j \gg h$, then $\theta_j \cong 0$ hence p'_j and p_j can be replaced by an effective dipole moment p''_j [121]:

$$p''_j = p_j - p'_j = \frac{2\epsilon_{ext}}{\epsilon_{sub} + \epsilon_{ext}}p_j. \quad (1.34)$$

\mathbf{E}_{sur} is given by [121]:

$$\mathbf{E}_{sur} = -\frac{1}{4\pi\varepsilon_0\varepsilon_{ext}} \frac{2\varepsilon_{ext}}{\varepsilon_{sub} + \varepsilon_{ext}} \sum_j \frac{3\cos^2\phi'_j - 1}{r_j'^3}, \quad (1.35)$$

where ϕ'_j is the angle between r_j and p_j'' . From Eqs. 1.33 and 1.35 the induced electric field \mathbf{E}_{loc} can be written as [121,122]:

$$\mathbf{E}_{loc} = \frac{\mathbf{E}_{ext}}{1 + \varepsilon_0\varepsilon_{ext}\alpha\beta}, \quad (1.36)$$

where α is the polarisability of the NP while β is the parameter that accounts for all the interactions. β carries all the information regarding to the interaction of a NP with the neighboring NPs and also with the image dipole created inside the substrate at a distance of h from its center. It is given by [122]:

$$\beta = \frac{1}{4\pi\varepsilon_0\varepsilon(\omega)h^3} \frac{\varepsilon_{sub} - \varepsilon_{ext}}{\varepsilon_{sub} + \varepsilon_{ext}} - \frac{C}{4\pi\varepsilon_0\varepsilon(\omega)}. \quad (1.37)$$

C is a parameter that accounts for the shape distribution of a sample and it is given by [122]

$$C = \sum_j \frac{3\cos^2\phi_j - 1}{r_j^3} + \frac{\varepsilon_{sub} - \varepsilon_{ext}}{\varepsilon_{sub} + \varepsilon_{ext}} \sum_j \frac{3\cos^2\phi'_j - 1}{r_j'^3} \quad (1.38)$$

where r_j and r'_j are the distances between the reference dipole p and another dipole p_j (located at j) and its mirror image (p'_j), respectively (see Fig. 1.11). If the particles are identical or homogeneous, C becomes [122]:

$$C = \int_{r=0}^{\infty} \int_{\phi=0}^{2\pi} \frac{3\cos^2\phi - 1}{r^3} N(r) r dr d\phi + \frac{\varepsilon_{sub} - \varepsilon_{ext}}{\varepsilon_{sub} + \varepsilon_{ext}} - \frac{1}{4\pi\varepsilon_0\varepsilon(\omega)} \int_{r=0}^{\infty} \int_{\phi'=0}^{2\pi} \frac{3\cos^2\phi - 1}{r^3} N(r) r dr d\phi \quad (1.39)$$

where $N(r)$ stands for the number of particles per surface area $r dr d\phi$ at a distance r and angle ϕ . Eq. 1.39 can be simplified to:

$$C = \frac{2\varepsilon_{ext}}{\varepsilon_{sub} + \varepsilon_{ext}} \frac{\pi d}{\Lambda} \quad (1.40)$$

where d is defined to be the particle density, Λ is the distance between the first neighbors and

$$N(r) = \begin{cases} 0 & \text{if } r < \Lambda, \\ d & \text{if } r \geq \Lambda. \end{cases} \quad (1.41)$$

In this study, we are interested in spheroidal NPs whose depolarization factors $L_{x,y,z}$ are given by Eqs. 1.28 and 1.29. For a square lattice distribution of NPs, we can find the effective depolarization

factor $F_{x,y,z}$ to be [122]:

$$F_{x,y,z} = \frac{\varepsilon_0 \varepsilon_{ext}^2}{\varepsilon(\omega) - \varepsilon_{ext}} \alpha \beta + L_{x,y,z} (1 + \varepsilon_0 \varepsilon_{ext} \alpha \beta). \quad (1.42)$$

Hence, for a particle filling factor q , the effective dielectric function ε_{eff}^Y is found to be [121, 122]:

$$\varepsilon_{eff}^Y = \varepsilon_{ext} \left(1 + \frac{q[\varepsilon(\omega) - \varepsilon_{ext}]}{\varepsilon_{ext} + F_{x,y,z}[\varepsilon(\omega) - \varepsilon_{ext}]} \right). \quad (1.43)$$

Fig. 1.12(b) displays the q dependent effective absorption coefficient whose effective dielectric function values were obtained using Eq. 1.43 for identical prolate AuNPs (AR = 3) arranged on a Al_2O_3 ($\varepsilon_s = 2.75$) substrate as a square lattice ($\Lambda = 120$ nm). The external environment ε_{ext} is considered to be the same as the substrate. The magnitude of both the TrSPR and LgSPR modes increases with the filling factor due to the rise of metal amount.

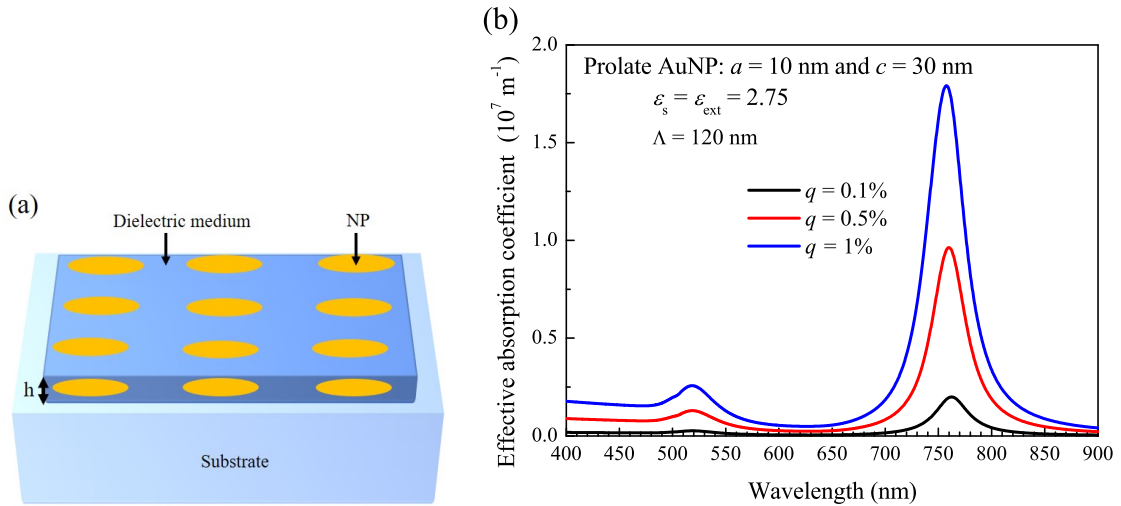


Figure 1.12 – (a) Schematic representation of a 2D distribution of identical parallel spheroidal NPs on a substrate and embedded in an external dielectric medium. (b) NP filling factor dependent effective extinction coefficient of a nanocomposite thin film made of identical prolate AuNRs dispersed in a square lattice arrangement in which Al_2O_3 acts as both the substrate and the external environment.

1.4 Numerical approaches

The problem of the interaction between metal nanoparticles of complex shapes and an electromagnetic wave, for which there is no analytic way of solving, can be investigated using a variety of numerical methods that have been developed so far. Among them, the *Discrete Dipole Approximation* (DDA), the *Boundary Element Method* (BEM), the *Transfer Matrix Method* (TMM) and the *Finite-Difference Time-Domain* (FDTD) methods being very famous in the community.

DDA was initially developed by E. M. Purcell & C. R. Pennypacker [123]. It allows to calculate the absorption and scattering of a plane wave by particles of arbitrary shape or by periodic structures [124, 125]. It also calculates the local field enhancement factor [126]. The method is

based on the discretization of a particle by a finite and large number of point dipoles. In response to the incident electric field, the dipoles acquire a dipole moment; then the DDA calculates both the polarization (resulting from the interaction of the dipole with all the other dipoles and with the incident field) and the local field at each point. One then obtains σ_{abs} and σ_{sca} from the local field and all the calculated polarizations.

The FDTD method, which was developed by Yee [127], is based on solving the Maxwell equations for an electromagnetic field propagating in the computational space (domain) of interest. The entire computational space is discretized into a differential time and space grid. The field at the successive nodes of the grid are accumulated, hence giving the whole movie-like propagation of the field (both in space and time) inside the domain of interest. This makes it the best choice for theoretically demonstrating the real time effects of light matter interaction. However, FDTD requires a fine discretization of time and space for best results which makes working with it very expensive in terms of memory space and time consumption.

BEM is based on solving the Maxwell's equations by considering the charges and currents distributed on the boundaries and surfaces of the nanostructures of interest. This approach, which was invented by Garcia de Abajo & Howie [128], allows one to obtain the absorption, scattering and field enhancement due to the interaction of plasmonic nanostructures (sitting in a uniform dielectric medium) with electromagnetic field. In this approach, each region is assigned with a local dielectric function and the boundary conditions are handled by surface integrals between the different media. It is therefore perfectly suited for the study of the LSPR of metallic nanostructures [129, 130]. It can be also applied to a coupled nanoparticle systems [131].

TMM, originally formulated by P. C. Waterman [132], also allows to calculate optical response of particles. It can be applied to rotationally symmetric geometries to calculate the absorption and scattering of light by nanoparticles [133, 134]. Beside, it is also a simple technique to calculate electromagnetic wave propagation through layers of media. The transmittance, reflectance, absorbance and field distribution can be calculated by accumulating the fields at the interfaces into a "transfer matrix" as the incident light passes through the entire material.

A number of other numerical methods can be found elsewhere besides the aforementioned ones. However, the ones listed above are the most used ones for the study of the optical response of plasmonic nanostructures. We will use some of these numerical approaches in this work in addition to the analytical Gans-Mie theory (§1.3.2.1). In chapter 3, we will use the BEM to simulate the optical properties of AuNRs and bimetallic AuNR-Ag, core-shell colloidal nanoparticles. In the 4th chapter, the FDTD method will be used to study the dynamics of the near field enhancement topography around a spherical NP subject to absorption of a femtosecond laser pulse. Finally, in the 5th chapter, the TMM will be implemented to study the optical response of plasmonic-photonic hybrid micro-cavities.

1.5 Optical response of noble metal nanoparticles in the transient regime

As described earlier, when a NP is excited with an ultrashort laser pulse at its plasmon resonance, the energy absorbed by the NP is mainly released as heat to the surrounding environment.

This occurs via a series of rapid energy exchange processes, as illustrated in Fig. 1.13 [38]. It begins with the excitation of the coherent oscillation of the electrons (plasmon mode). However, this coherence disappears in a few femtoseconds. The energy input is then spread over a fraction of electrons. The electron distribution is then out of equilibrium. This phase is called the athermal regime. Theoretical modeling of the electron response in this regime requires the resolution of Boltzman equation for the electron distribution. This regime lasts for a few hundreds of femtoseconds and will be disregarded in the following chapters as our interest is to study the optical response of NPs over a longer time. Hence, a thermal model has been used that we are going to discuss about below.

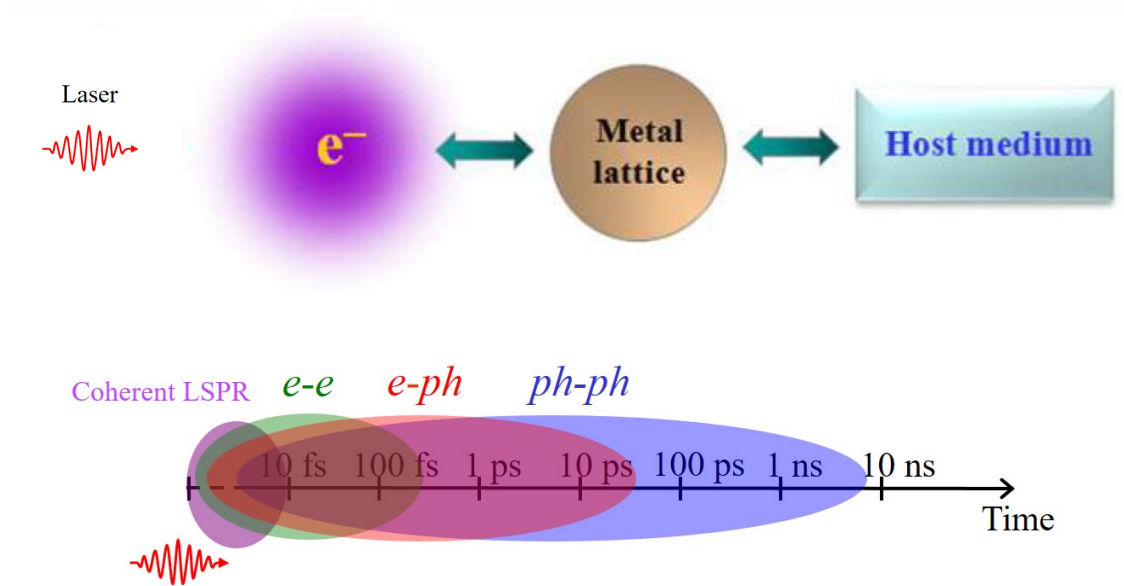


Figure 1.13 – Diagrams representing the energy exchange processes in a plasmonic NP after excitation by an ultrashort laser pulse [38] as well as their typical time scales.

Along the athermal regime, the energy absorbed redistributes within the electron gas via $e - e$ collisions, which leads to its internal thermalization after a few hundred femtoseconds. Once this internal equilibrium is recovered, the electronic distribution follows the Fermi-Dirac statistics with a temperature T_e higher than the initial temperature, T_0 . This phase is called the thermal regime. $e - ph$ collisions ensure the energy exchange between the electron gas and the metal ionic lattice. The electron energy is therefore converted into lattice vibrations which induce heating of the NP. The typical time of $e - ph$ scattering is in the order of a few picoseconds. The heat is then transferred to the surrounding environment by $ph - ph$ collisions at the interface, which leads to the cooling of the NP while heating of the host environment that is in contact. Depending on the thermal transport properties in the host medium, as well as the interface thermal conductivity, the characteristic time of this process can vary from a few picoseconds to a few nanoseconds. Finally, the heat is evacuated mainly by diffusion in the host environment.

We have seen earlier that the dielectric function of noble metals depends on T_l , T_e and $f(E)$ and therefore we expect it to evolve with the energy exchange processes. Hence, this is accompanied by a rapid evolution of the optical properties of the noble metal NPs. In this thesis, we will focus on the ultrafast variation of optical properties over a long time scale. Therefore, we briefly present

the three-temperature model (3TM) that we will carry out to study the ultrafast optical response of anisotropic NPs that are in colloidal solution form, suspended on dielectric fibers, or coupled with an optical resonator. This model has already been used formerly in the team in X. Wang's thesis [72].

In this model, three subsystems are considered: the metallic lattice having a temperature T_l , the electron gas with temperature T_e and the surrounding environment possessing a temperature T_m . We assume that the electron gas is in internal thermal equilibrium at all times. The electron distribution is therefore ruled by the Fermi-Dirac statistics at $T_e(t)$. Evolution of the temperatures T_e , T_l and T_m can be described by the following three equations:

$$C_e(T_e) \frac{\partial T_e}{\partial t} = -G(T_e)(T_e - T_l) + P_{abs}(t) \quad (1.44)$$

$$C_l \frac{\partial T_l}{\partial t} = G(T_e)(T_e - T_l) - \frac{H(t)}{V} \quad (1.45)$$

where $P_{abs}(t)$ is the instantaneous power density absorbed at the instant time t , $C_e(T_e)$ and C_l are the thermal capacities of the electron gas and the metal lattice, respectively, and $G(T_e)$ is the electron-phonon coupling parameter. The behaviors of C_e and G differ from those at low temperatures when T_e reaches a few thousand Kelvin (§1.2.1.2). V is the volume of the particle and $H(t)$ correspond to the instantaneous heat release into the surrounding environment through the interface. Considering a perfect interface between a spherical nanoparticle and its surrounding matrix, the second term in the right-hand side of Eq. 1.45 can be expressed as:

$$\frac{H(t)}{V} = \frac{S}{V} \kappa_m \left. \frac{\partial T_m}{\partial r} \right|_{r=R}. \quad (1.46)$$

S is the surface area of the particle while κ_m is the thermal conductivity of the host medium. Given D_m , the thermal diffusion constant of the medium, its heat capacity is $C_m = \frac{\kappa_m}{D_m}$ and the heat equation inside the medium writes (Fourier law):

$$\frac{\partial T_m}{\partial t} = D_m \nabla^2 T_m. \quad (1.47)$$

Therefore, Eq. 1.47 together with Eqs. 1.44 and 1.45, make up the 3TM model. Thus, the 3TM can be used to calculate the evolution of T_e , T_l and T_m over a "long" time.

Let us mention that the possible thermal interface resistance, disregarded here, could be easily accounted for in the equations [135, 136].

1.5.1 Time resolved pump-probe experiment

In the previous sections, we have presented the theoretical methods that we use to investigate the transient optical response of the NPs. We have also discussed the physical processes that a plasmonic nanostructure undergoes upon its interaction with a subpicosecond laser pulse. It begins with the formation of an out-of-equilibrium electron gas whose characteristic time (duration of the athermal regime) is a few hundreds of femtoseconds and ultimately reaches an equilibrium

where the temperatures of the electron gas and the metal lattice of the NP, as well as that of the surrounding matrix at the interface, finally become equal which lasts hundreds of picoseconds (thermal regime). So, to understand the underlying physics, we need to discriminate between the different physical processes involved based on their characteristics time (before the whole system returns to the equilibrium). Therefore, we need a time resolved experimental technique that can allow to temporally separate these processes and study the overall dynamics of the system until the equilibrium condition is attained. Hence, we devote this section to introduce the pump-probe experimental technique that has widely been used to study such kind of physical process.

In a pump-probe setup, two pulses are required, the pump and the probe [see Fig. 1.14(a)]. The former sets the system out of equilibrium (perturbation). It is intense enough to excite non-linearities. The time at which the peak of the pump pulse crosses the material (to create excitation) is considered as the origin $t = 0$ for the probe pulse. Then the latter is sent on to the sample. Its role is to monitor the modifications that are induced in the material by the pump. A high-precision mechanical linear translation stage with a control feedback is used to vary the delay between the pump and the probe pulses over a time range of several nanoseconds and with femtosecond resolution [see Fig. 1.14(b)]. In our experiments, the probe beam is a white-light supercontinuum in order to record the dynamics over a broad spectral range [see Fig. 1.14(a)]. The probe intensity must be low enough not to induce any change in the optical properties of the sample.

For this, each initial pulse emitted by the laser output has to be split into an intense part ensuring pumping and a weak one for probing, the delay between both being varied by elongating the optical path difference between both in order to reconstruct the relaxation dynamics [see Fig. 1.14(b)]. The weak part (the probe) is focused onto a dispersive transparent medium (sapphire for example) to generate a white-light supercontinuum beam. The probe intensity after crossing the sample is then measured as a function of wavelength with a spectrometer coupled to a detector [see Fig. 1.14(b)]. The quantity which is monitored as a function of pump-probe delay time and probe wavelength is then the differential transmission, $\frac{\Delta T}{T} = -\Delta OD$, which represents the relative variation of the sample transmittance induced by the pump and experienced by the probe.

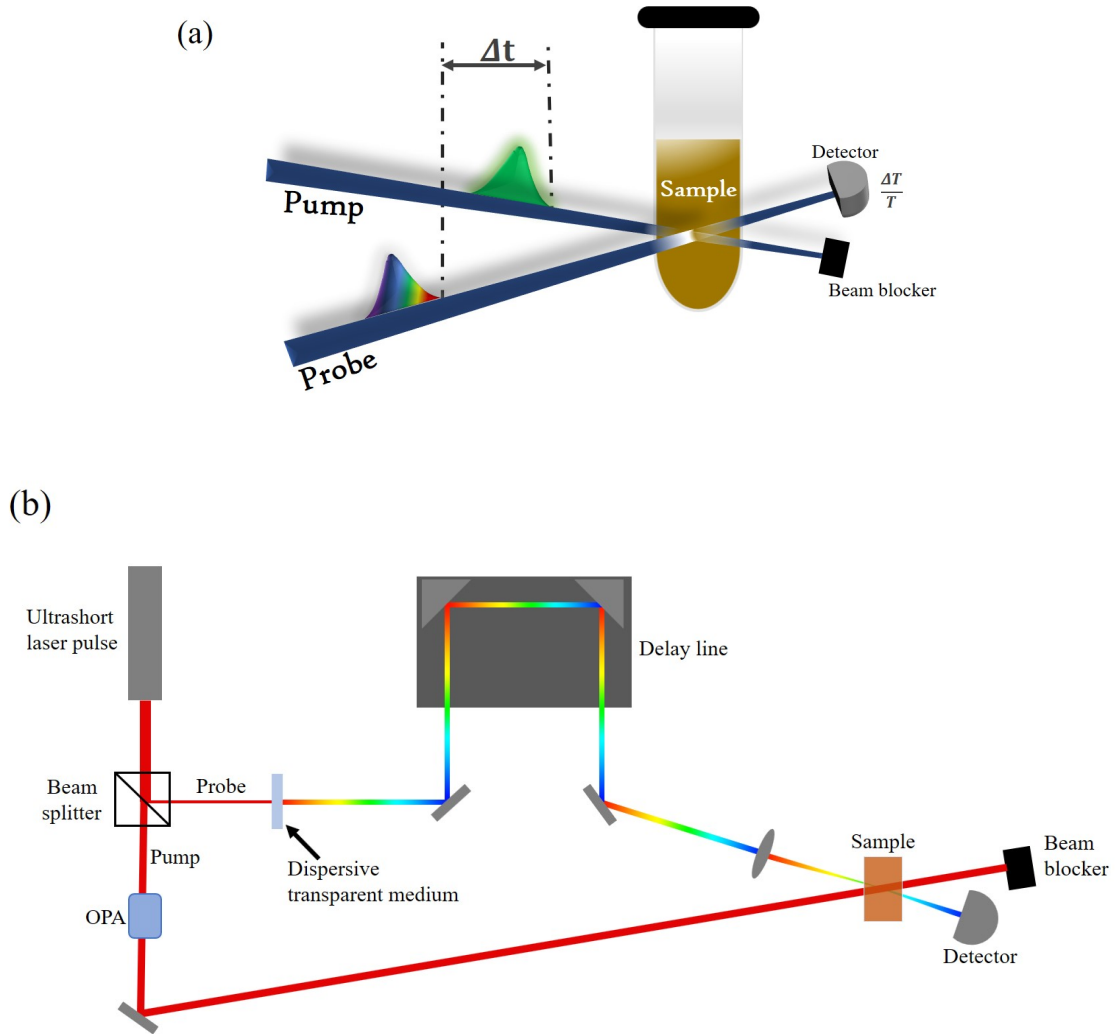


Figure 1.14 – Illustrations of the principle of our pump-probe experiments: (a) At the sample level. The pump and probe spatially overlap inside the sample, Δt is the time delay between the pump and probe pulses and $\frac{\Delta T}{T}$ is the relative variation of the transmittance of the sample. (b) Scheme of pump-probe experimental setup principle for the measurement of the broadband ultrafast transient optical response of a sample.

1.6 Summary

In this chapter, we have presented an overview of the theoretical and numerical tools that we will use to calculate the optical properties of noble metals, first in the bulk form and then reduced at the nanometric scale. In addition to the analytic approaches, we have pointed out the numerical methods that can help to simulate the optical properties of complex shaped NPs because of the inability of analytic approaches to address most of the non-spherical morphologies. Effective medium theories (Maxwell-Garnett and Yamaguchi models) that can be used to calculate the optical responses of an ensemble of NPs dispersed/embedded either in 2D or 3D in a dielectric medium have also been presented. For the case of the interaction of NPs with ultrashort laser pulses, a series of energy exchanges takes place between the incident photons and electrons (transitions), electrons with each other ($e - e$), electron and metal ionic lattice ($e - ph$), metal lattice and host environment ($ph - ph$). This induces an ultrafast temporal variation of the dielectric function of the NP and hence a subsequent change in its optical properties. These variations can therefore

be modeled by coordinating the 3TM, the intraband (Rosei model) and interband (Drude model) contributions to the dielectric function, and the numerical/analytic methods for the calculation of the optical response of the NP. The broadband pump-probe spectroscopy technique can then be used to experimentally assess the temporal dynamics of the NP optical response after femtosecond laser pulse absorption.

Chapter 2

Transient optical response of silica nanowires decorated by gold nanoparticles

Contents

2.1	Introduction	33
2.2	Sample preparation	34
2.3	Experimental results	35
2.3.1	Stationary regime LSPR	35
2.3.2	Pump-probe experiment	36
2.4	Theoretical modeling	38
2.4.1	Modeling the AuNP decorated SiO ₂ NWs in the stationary regime	38
2.4.2	Modeling the transient regime optical response	40
2.5	Discussion	44
2.6	Summary	48

2.1 Introduction

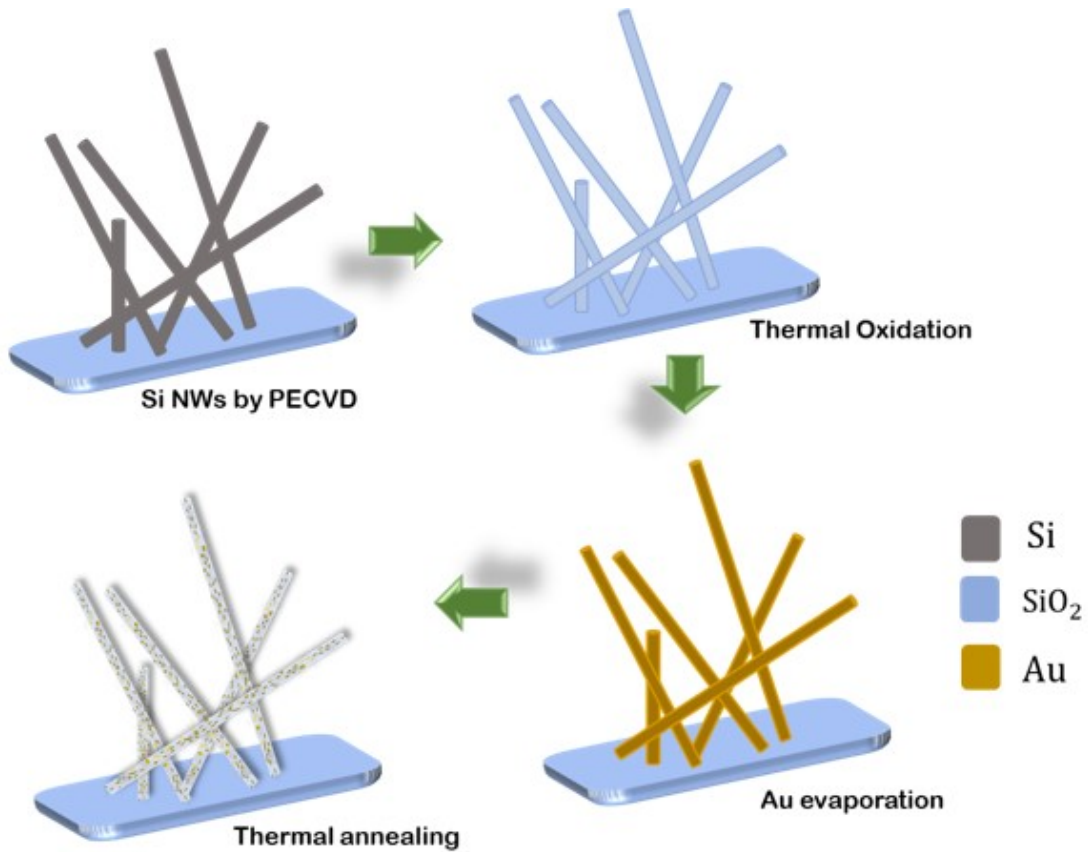
As we have seen in the preceding chapter, the ultrafast response of plasmonic nanostructures is a complex phenomenon that involves a sequence of several energy exchange processes, with different time scales, from a few femtoseconds to hundreds of picoseconds. Understanding the physics behind the processes and how each of them is affected by size, shape, and composition of the NPs and by their environment is essential to fully exploit the NPs in many applications. For isolated NPs dispersed in liquids or on a flat glass support, the ways the different dynamic processes depend on the shape and size of the NPs have been extensively studied [137] see Hartland, "*Optical studies of dynamics in noble metal nanostructures*" and the references therein. Moreover, for most applications, the metal NPs have to be combined with other materials and the fabrication processes can strongly limit the control over the NP morphology.

One-dimensional nanostructures and in particular nanowires (NWs) can be easily exploited as support structures for metal NPs. In fact, they can be synthesized in dense arrays, by carefully controlling their morphology and orientation with respect to the substrate. Such controlled fabrication allows us to obtain samples that may increase the accessibility of NPs to molecules in gas or liquids, and hence the potential sensitivity of devices. Studies have been reported where semiconductor NWs have been decorated with metal NPs and exploited as a substrate for surface enhanced Raman scattering spectroscopy [138, 139]. Oxide NWs functionalized with metal NPs have also been used for many applications like optical sensing [140] and catalysis [141–144].

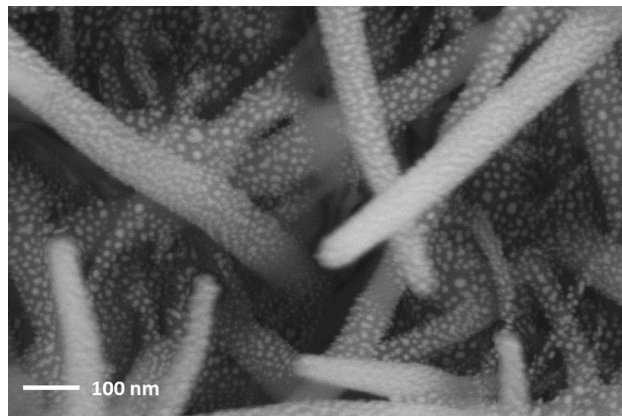
In this chapter, the stationary and transient optical responses of silica NW arrays decorated by AuNPs are presented. This study has been carried out in partnership with colleagues from ISM-CNR in Rome. The silica NW arrays have been fabricated via thermal oxidation of Si NWs grown on a quartz substrate. The structures fabricated are an excellent support for metal NPs owing to their large surface area to attach the NPs, providing at the same time a macroporous framework that enables easy access to liquids or gases thus giving an efficient interaction with the environment [145]. Our arrays are fully transparent in the visible to near-UV region of the spectrum, thus allowing transmission measurements. Additionally, the strong light trapping typical of the nanowire arrays [146] increases the light absorption by the NPs thus enhancing the optical sensitivity of the 3D-arrays to the environment [145]. A two-step, three-temperature model, developed to reproduce and interpret the experimental results, is also presented that allows for the correlation of several features of the stationary and transient optical responses to the shape and shape distribution of the AuNPs in the arrays.

2.2 Sample preparation

The Au-decorated SiO₂ NW arrays have been fabricated by our partners from ISM-CNR in Rome, as schematically shown in Fig. 2.1(a). Si NWs have been first grown by plasma enhanced chemical vapor deposition (PECVD) on top of a flat quartz substrate, using Au NPs as seeds in a vapor-liquid-solid (VLS) process [146]. The NW arrays have been then oxidized to obtain SiO₂ NWs, and further covered with a thin layer (5 nm nominal thickness) of Au by thermal evaporation [145]. For this work, a thermal annealing at 500 °C for 1 hour has been used to obtain the AuNPs from the dewetting of the thin film. A scanning electron microscopy (SEM) image of a typical array fabricated for this work is reported in Fig. 2.1(b). A NW length around 2 μm has been selected in order to obtain the best compromise between a large surface area to attach the AuNPs and a good transparency of the whole structure to perform optical measurements in transmission. A dense and disordered ensemble of AuNPs has been obtained at the end of the fabrication process. An average particle size of about 15 nm in the direction parallel to the NW growth axis has been estimated by averaging over hundreds of NPs using SEM images. As for the axis perpendicular to the NW surface, the analysis of the SEM images is not a suitable way to estimate the NP size due to the difficulty in identifying the NPs with the suitable orientation for accurate measurements. On the other hand, the SEM images clearly show a low contact angle between the NPs and the NW surface suggesting that the NP shape can be well approximated by an oblate ellipsoid.



(a) Sample preparation process



(b) SEM image of the sample

Figure 2.1 – (a) Schematic representation of the fabrication process of Au-decorated silica NW arrays. (b) Representative SEM image of an Au-decorated silica NW array.

2.3 Experimental results

2.3.1 Stationary regime LSPR

The stationary absorbance spectrum of the sample have been obtained by measuring both transmission and reflection in the visible range with a Perkin-Elmer spectrophotometer, equipped with an integration sphere to collect all the light scattered by the SiO₂ NWs. The absorbance of the NP/NW array in the visible range is shown in Fig. 2.2. Due to the transparency of the SiO₂

NW array in the explored energy range, the spectrum only represents the AuNP optical response, with a well-defined LSPR band peaked at 2.3 eV superimposed on a rising absorption starting from ~ 2.0 eV, due to interband electronic transitions.

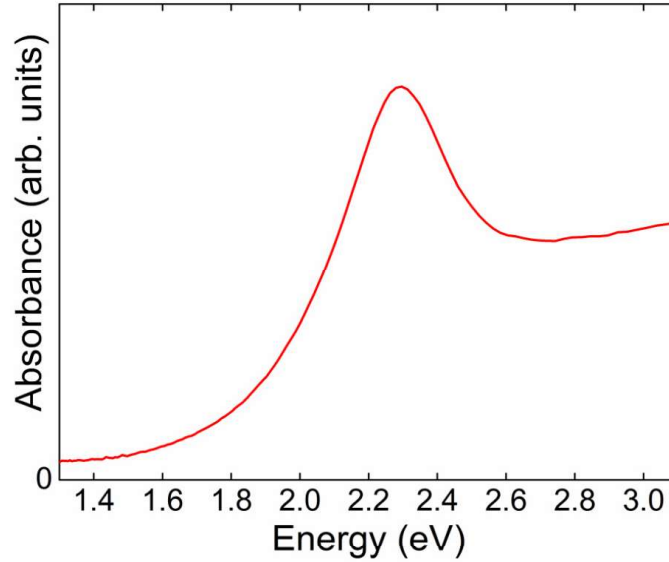


Figure 2.2 – Experimental absorbance spectrum of the AuNP decorated SiO₂ NW array.

2.3.2 Pump-probe experiment

The pump-probe experiments were done at the Istituto di Struttura della Materia (ISM), CNR, Rome, in the group of ultrafast processes in materials (FLASHit). Their setup is equipped with a Ti:Sapphire laser (COHERENT[®]) operating with a Mode-Locked Oscillator - Vitara-T, Regenerative Amplifier - Legend Elite HE+ and Optical Parameter Amplifier - OPerA-Solo (see Fig. 2.3).

For the transient absorption (TA) spectroscopy measurements, the optical pump consists of the second harmonic of the Ti:Sapphire laser at 405 nm with a pulse length shorter than 50 fs and a repetition rate of 1 kHz. Under these conditions, after pump excitation, a complete dissipation of the heating induced by the pump occurs prior to the subsequent pulse. A white light supercontinuum generated in a femtosecond transient absorption spectrometer (FTAS) of IB Photonics (FemtoFrame II) has been used as the probe. The probe wavelengths ranged between 330 and 750 nm, while the pump-probe delay time lasted up to 500 ps, with an overall temporal resolution of around 50 fs. The measurements have been performed using four different pump peak intensities (0.4, 0.8, 2, and 4 GW cm⁻²).

Using the white light supercontinuum as probe for the TA spectroscopy measurements, the variation of the absorbance (ΔA) of the sample after the pump pulse excitation depends on both the probe wavelength and the delay time between pump and probe. For the sake of clarity, the TA results are shown and discussed separating the spectral and the temporal dependencies. Figure 2.4 shows the spectral dependence of the TA of the Au-decorated SiO₂ NW array, for different pump-probe delays, acquired with a pump peak intensity of 2 GW cm⁻². Similar behaviors have been obtained for the different pump intensities. Three main features characterize the spectra: a

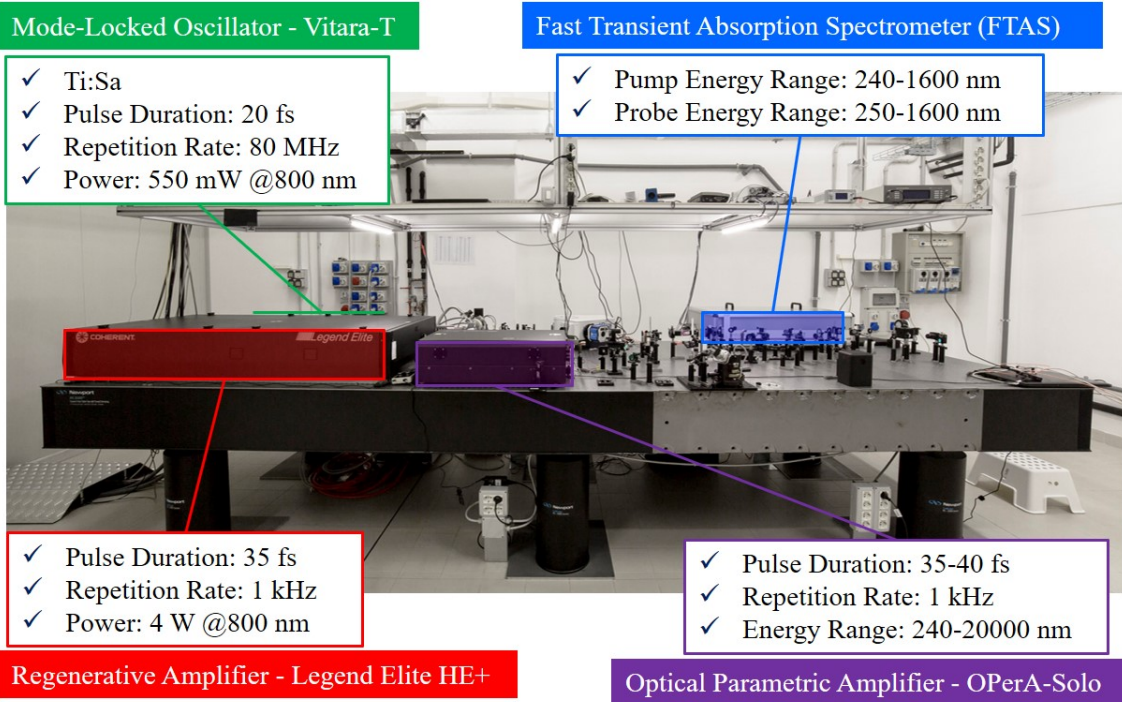


Figure 2.3 – The pump-probe experiment setup of the group of Ultrafast processes in materials (FLASHit) in Istituto di Struttura della Materia (ISM).

negative minimum of the signal peaking at the LSPR location, and two positive signals at both wings of the LSPR. This is the typical signature of the bleaching of the plasmon resonance. The main effect of the ultrafast light absorption is the increase in the electron temperature T_e (or internal energy) with the ensuing broadening of the plasmon band. This leads to a transient reduction of the absorption near the plasmon maximum and to a transient absorption increase in the wings of the band [147]. At short delays, the positive wings have different magnitudes, presenting an evident asymmetry that disappears for time delays longer than 10 ps. Furthermore, a blueshift of the bleaching of the LSPR can be observed for the first 20 ps.

The temporal dependence of the TA at different probe energies close to the LSPR energy is reported in Fig. 2.5(a) for time delays up to 10 ps. All the probe energies in this range show similar dynamics, which can be described by single exponential decays, indicating that a single process is dominant in this time range: the electron-phonon coupling. The dynamics becomes slower for increasing probe photon energy, as it will be discussed below. This is consistent with the observation of a blue shift of the minimum during the first picoseconds. Fitting the time decay at 2.3 eV, corresponding to the stationary LSPR, it is possible to determine the electron-phonon coupling characteristic time from the relaxation time constant. However, data from single pump pulse intensity are not sufficient, since the relaxation time depends on the excitation intensity. Indeed, the effective relaxation time is not only dependent on the electron-phonon scattering, but also is affected by the electron gas heat capacity, C_e which increases as the initial energy input increases. The standard approach to extract the electron-phonon scattering time consists in performing measurements with different pump intensities and plotting the relaxation times obtained as a function of that intensity as shown in Fig. 2.5(b). The electron-phonon coupling time can then be extrapolated by performing a linear fit of the data and looking at the zero power

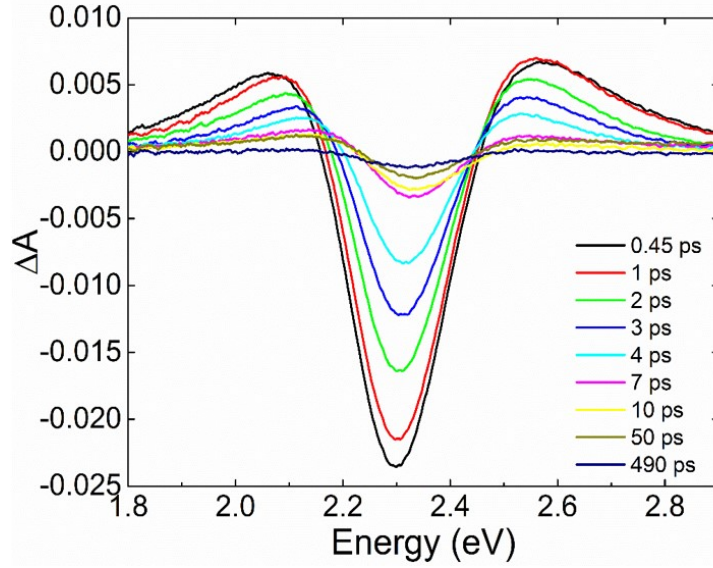


Figure 2.4 – Experimental spectral dependence of the transient absorption for different delay times between pump and probe pulses. ΔA is defined as the absorbance difference of the sample after and before pump excitation.

intercept [148]. The fit gives a value of the electron-phonon coupling time constant for our Au NPs array of $\tau_{e-ph} = 0.95 \pm 0.06$ ps, in agreement with what is expected for our NP size [149].

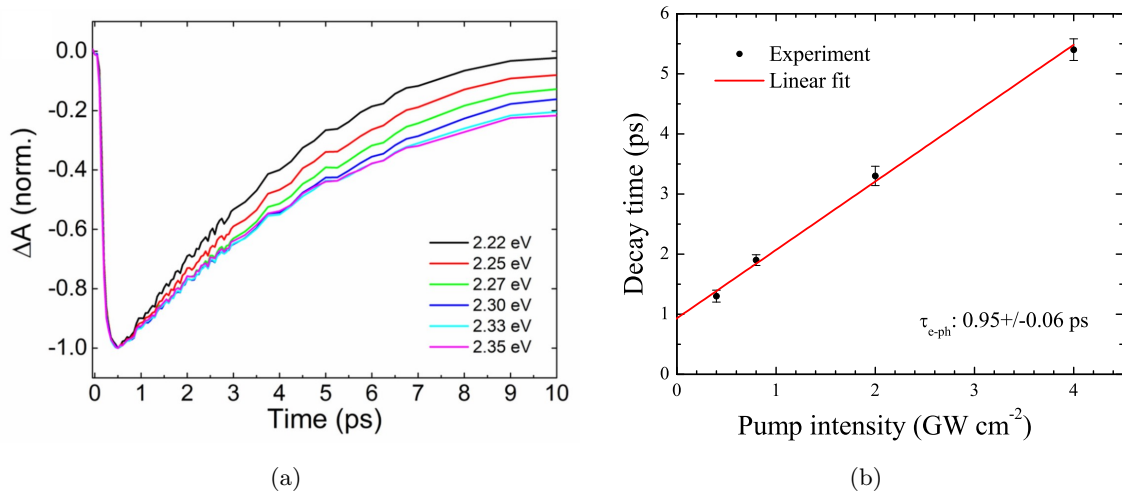


Figure 2.5 – (a) Experimental time dependence of ΔA at different probe energies. (b) Decay time of ΔA at the energy of the minimum as a function of the pump peak intensity.

2.4 Theoretical modeling

2.4.1 Modeling the AuNP decorated SiO₂ NWs in the stationary regime

Both the stationary and transient optical responses of the arrays have been simulated. Based on the SEM images that indicate that the NPs have a spheroidal shape, rather than a fully symmetrical (sphere) one, we have used oblate ellipsoids to describe the NPs. As the NPs are spread randomly on the SiO₂ NWs and present a random orientation relative to the incident

field polarization direction, the Maxwell-Garnett effective medium approach extended for oblate-shaped NPs has been used to estimate the effective dielectric function $\varepsilon^{eff}(\omega)$. Thus, a fictitious homogeneous host medium embedding the NPs has been considered (see Fig. 1.10 in chapter 1), the dielectric function of which (ε^{hm}) is evaluated as the surface-area-weighted average value of those of air (ε^{air}) and SiO_2 (ε^{silica}):

$$\varepsilon^{hm} = q\varepsilon^{silica} + (1 - q)\varepsilon^{air}, \quad (2.1)$$

where q is the fraction of the NP surface in contact with the NW; from the observation of SEM images and NP shape, its value is estimated to be $q \sim 1/3$.

Using an aspect ratio (AR) of 2.25, the simulated stationary LSPR matches then one that is determined experimentally (2.3 eV), as shown in Fig. 2.6. In Fig. 2.6, the right y axis shows the stationary optical absorption cross-section spectrum as calculated using the Gans-Mie theory [109]. For comparison, the stationary effective absorption coefficient of the whole medium (AuNPs in the air-silica mixture) has also been calculated (left y axis) for a volume filling fraction $p = 0.02$. This value is chosen somehow arbitrarily as in the following the absolute magnitude of the absorption coefficient and its transient variation will not be compared directly with experimental data. It is chosen to be sufficiently small to avoid any significant mean-field effect in the width and location of the plasmon band. In both cases, the stationary dielectric function of Au (ε_{ω}^0) has been taken from the experimental data reported by Palik [85].

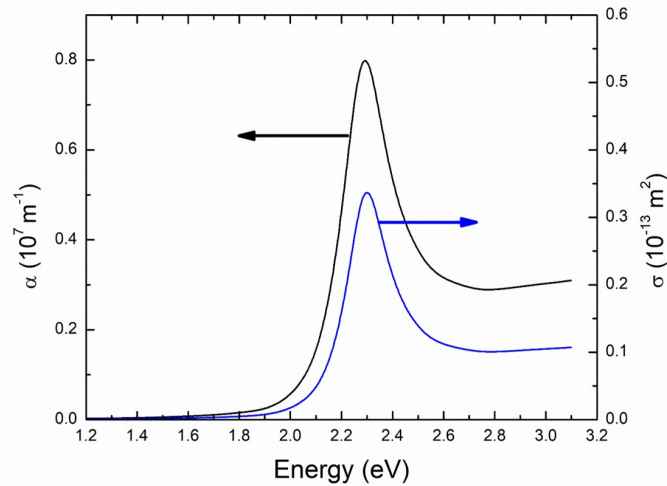


Figure 2.6 – The calculated stationary optical properties: the left y axis (black) shows the absorption coefficient of the effective medium (randomly oriented oblate AuNPs with AR = 2.25 dispersed in the air-silica mixture) and the right y axis (blue) shows the absorption cross-section of an oblate AuNP with AR = 2.25.

The calculation is performed by integrating over all the possible NP orientations relative to the fixed field polarization direction in order to match the actual sample morphology [see Fig. 2.1(b)]. Hence, two absorption bands are expected to appear in the spectra, corresponding to the two LSPR modes (polarization parallel or perpendicular to the oblate NP). However, for the chosen AR = 2.25 (and also for the other ARs that will be considered later), the two individual resonance peaks

are not decoupled enough. Moreover, the oscillation strength associated with the field polarization along the short axis is very small and it results only in the broadening of the effective resonance peak, which mainly stems from the twofold degenerate in-plane resonance mode. This explains why the stationary absorption spectrum (Fig. 2.6) exhibits a single LSPR band peaking at 2.3 eV, just as in the experimental stationary data.

2.4.2 Modeling the transient regime optical response

As has been discussed in the first chapter, the 3TM is a convenient method to model the response of NPs over times longer than, say, one picosecond. Indeed, it disregards the athermal regime (that happens within the first hundreds of fs). The transient optical response has been calculated by solving the coupled differential equations of the 3TM by a finite element method, FEM (using the optimization software COMSOL Multiphysics). Indeed, the geometry of the virtual AuNPs that we are considering here is non-spherical (as has been described in §2.4.1 above) and therefore the 3TM model cannot be implemented directly. The FEM approach of solving the 3TM nonlinear equations have been described in depth in the Ph.D. dissertation of Xiaoli Wang [72]. So, let us discuss here only a few points of the approach here. The computational geometry involves building a big volume-matrix ($600 \times 600 \times 600 \text{ nm}^3$ in our case) around the NP which is located at the center (Fig. 2.7). Both the electron cloud and metal ionic lattice (phonons) of the NP are considered to have the same geometry as the NP. The initial electron and lattice temperatures, T_0 , are taken to be the same, 300 K, and the temperature at the edges of the volume-matrix is considered to be equal to T_0 as it is big enough. Hence, two coupled computational sub-systems are created in COMSOL for the energy exchange calculation in which the volume-matrix plays both the role of virtual and real surrounding matrices.

- The electrons exchange against a virtual matrix (as they don't interact directly with the physical matrix).
- The phonons exchange against the surrounding physical matrix (there exists a direct contact between the two).

The electron (virtual) matrix was offered a very small thermal conductivity value ($10^{-10} \text{ Wm}^{-1}\text{K}^{-1}$) to ensure that the electron gas is not losing its thermal energy in any other case than the electron-phonon interaction. It has also been demonstrated that the value of the electron matrix conductivity does not influence the result of the overall thermal dynamics [40, 72]. On the contrary, a very high thermal conductivity value is assigned for the electron and phonon media making them isothermal [72]. This is done to neglect any thermal gradient within the NP as it is very small and hence ensuring that the ultrashort laser power absorption is homogeneous. The source term in the 3TM was calculated by considering a pump peak intensity of 2 GW cm^{-2} with all its parameters being kept the same as in the pump-probe experiment (§2.3.2). Table 2.1 shows the thermal parameters of the media involved in the two sub-systems.

As the heat generated in the NPs by electron-phonon collisions is released to the host medium through the contact interface, the corresponding thermal conductivity and the heat capacity of the fictitious medium, involved in the 3TM equations, are evaluated as the surface-area-weighted average values, in the same way as the dielectric function of the host medium ϵ^{hm} was calculated using Eq. 2.1. The individual thermal properties of silica and air are taken from Refs. [150] and [151], respectively, as presented in Table 2.1. The dependence of the electron-phonon coupling

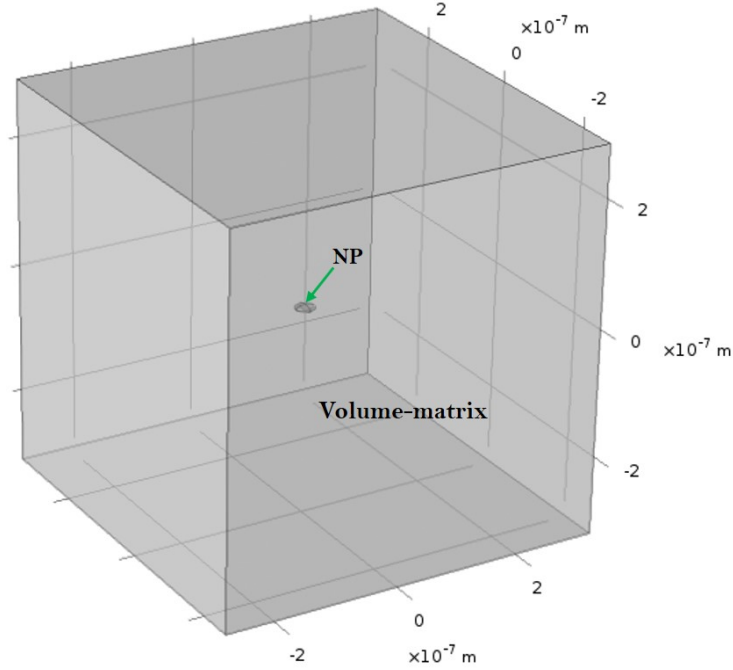


Figure 2.7 – The geometrical representation of the model required for the thermal dynamics calculation: designed in COMSOL Multiphysics.

constant G on the electron temperature T_e in the high T_e regime, due to the involvement of the d-band electrons, has been taken into consideration. Indeed, as has been discussed in the first chapter, following Ref. [79], at higher T_e (~ 3000 K) the value of electron gas heat capacity C_e departs from the simple quasi-free electron approach owing to the non-negligible influence of d-band electrons on the electron density of states of gold. The time-dependent temperatures obtained in this way have then been used to calculate the variation of the dielectric function of Au at each angular frequency ω due to the contributions from interband $[\varepsilon^{ib}(\omega)]$ and intraband $[\varepsilon^D(\omega)]$ electron transitions. The absorption cross-section value, which was used to determine the instantaneous absorbed power, has been obtained by using the Gans-Mie theory at 405 nm (experimental pump wavelength).

Fig. 2.8 shows the calculated transient optical absorption for a collection of AuNPs with AR = 2.25 in the fictitious homogeneous environment. First of all, it should be noted that the use of the 3TM at short times ($t < 1$ ps) is only a rather approximate approach as the athermal regime for the electron gas cannot be described by a pure thermal model [50,152]. Nonetheless, the computed spectral signature and its evolution with time depicted in Fig. 2.8 have strong similarities with the experimental results. However, some differences can be seen in both stationary and transient spectra: (i) the theoretical profiles are narrower than the experimental ones, (ii) a very small blue shift observed for the single AR AuNP; it is much smaller than the experimental one of about 50 meV, always being less than 5 meV (hardly visible in Fig. 2.8), and (iii) the balance of the right and left positive wings of the theoretical curve is more asymmetric than in the experimental results. We emphasize the fact that the actual sample presents a quite broad dispersion in NP shape, as shown by the SEM image [Fig. 2.1(b)]. As the LSPR mode energy depends on this shape, we have investigated the influence of a nonuniform NP shape distribution on the stationary and transient optical responses.

	Sub-system 1		Sub-system 2	
	Electrons	Virtual matrix	Phonons	Surrounding matrix
Thermal conductivity (W m ⁻¹ K ⁻¹)	10 ⁶	10 ⁻¹⁰	10 ⁶	SiO ₂ : 1.4 (Ref. [150]) Air: 0.026 (Ref. [151])
Mass heat capacity (J Kg ⁻¹ K ⁻¹)	For $T_e \leq 3000$ K: γT_e $\gamma = 66 \text{ J m}^{-3} \text{ K}^{-2}$ For $T_e > 3000$ K: Ref. [79]	1	2.49×10^6 Ref. [72]	SiO ₂ : 1.8 (Ref. [150]) Air: 10^3 (Ref. [151])
Volume power of source term	$P_{Vol} + G(T_l - T_e)$ For $T_e \leq 3000$ K: $G = 3 \times 10^{16} \text{ W m}^{-3} \text{ K}^{-1}$ For $T_e > 3000$ K: Ref. [79]	0	$T_e \leq 3000$ K: $-G(T_l - T_e)$ $T_e > 3000$ K: Ref. [79]	0

Table 2.1 – Thermal parameters of the media involved in the two sub-systems.

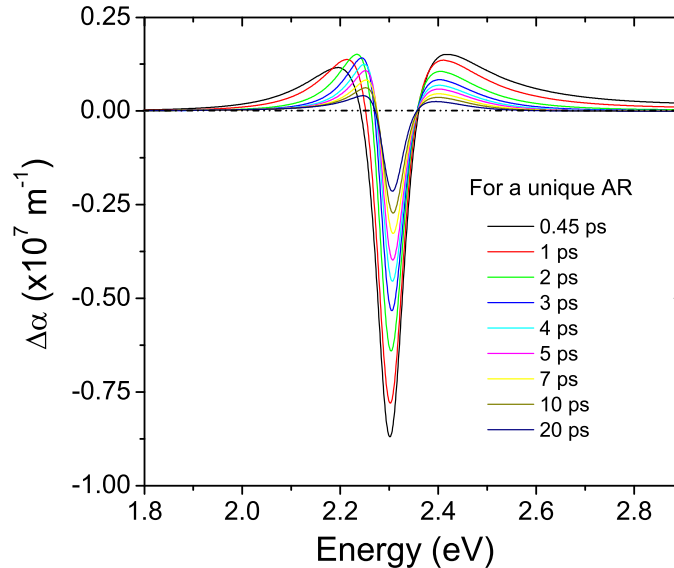


Figure 2.8 – Calculated spectral dependence of the pump-induced variation of the absorption coefficient ($\Delta\alpha$) at different delay times for oblate AuNPs of AR = 2.25.

2.4.2.1 The effect of shape distribution of the sample

In order to understand the role of the broad shape distribution of the sample [see SEM image on Fig.2.1(b)] on the transient signature, we have considered four additional oblate Au nano-spheroids (keeping the NP volume constant) with equally spaced ARs, around the central value of 2.25 (1.75, 2.00, 2.25, 2.50, and 2.75) [see Fig. 2.9(a)], following the method reported in Ref. [152]. It should be noted that the goal was not to reproduce exactly the experimental findings by accounting for the actual shape distribution of the array, but rather to qualitatively demonstrate the effects of a shape distribution on the characteristics of the optical response. Fig. 2.9(b) shows the stationary optical absorption spectra obtained for the five different ARs taken into account and their average value. Lower energies for the LSPR maximum correspond to higher ARs, as expected considering the increase of the length of the long axis of the NP [153]. The LSPR band of the average stationary

spectrum is centered around 2.3 eV, in agreement with the experimental spectrum, and it has a broader linewidth compared to the spectra obtained for individual ARs. Figure 2.9(c) shows the spectral dependence of the differential absorption coefficient for the five different ARs and their average value, at 4 ps delay time after the pump pulse maximum. The spectra show that the asymmetry of the two positive wings can be modified when accounting for the shape distribution. In addition, the spectral profile of the average is broadened and damped by the effect of the shape distribution, just as observed in the stationary absorbance. The shape-averaged calculated spectrum is closer to the experimental spectrum than that calculated for a single AR in terms of both the balance between the two positive wings and the width of the spectral profile.

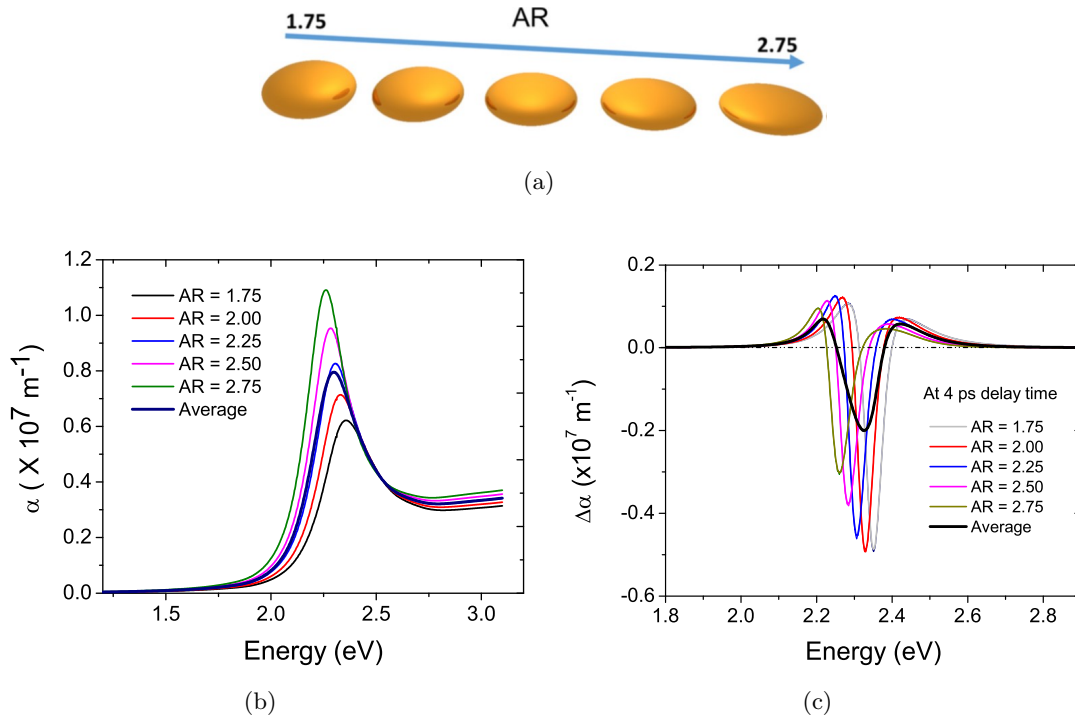


Figure 2.9 – (a) Graphic representation of the five ARs (1.75, 2.00, 2.25, 2.50, and 2.75) considered for the oblate Au NPs. (b) Calculated spectra of the absorption coefficient for NPs with different ARs and their average value. (c) Calculated spectral dependence of $\Delta\alpha$ for NPs with different ARs and their average value at 4 ps delay following pump pulse absorption.

The variation of the shape-averaged spectrum with the delay time is reported in Fig. 2.10(a). The shape-averaged spectra can reproduce the shift of the minimum observed experimentally. A zoom into the minima of the spectra [Fig. 2.10(b)] clearly shows the blue shift of the minimum as the delay time increases, which was almost not observed when considering a single AR. A closer look at the two positive wings [Fig. 2.10(c)] demonstrates that the model better reproduces the experimental time evolution when the shape average of different ARs is introduced.

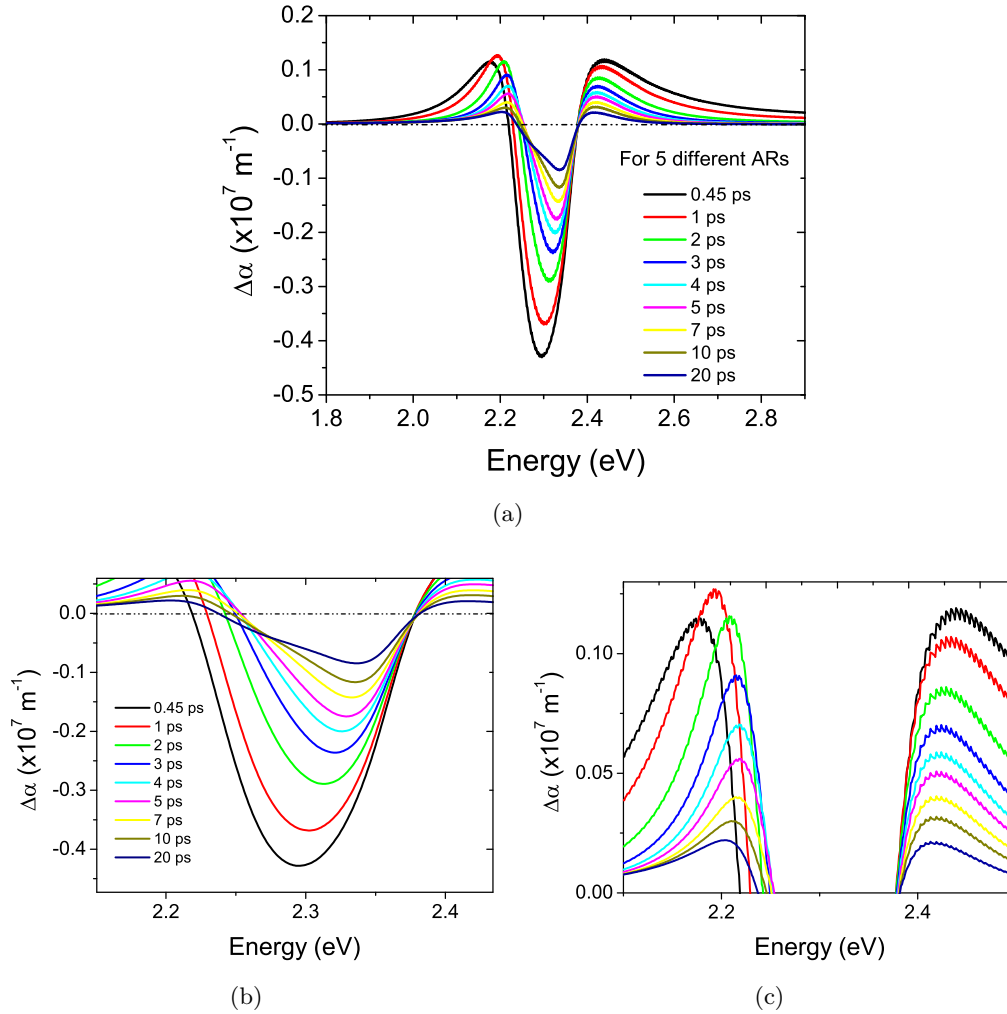


Figure 2.10 – (a) Spectrum of the pump-induced absorption coefficient variation at different delay times, calculated as the average value over five arbitrary ARs. (b) Close-up of the minimum, which clearly shows the blue-shift with increasing delay time. (c) Close-up of the two positive wings, which shows the time evolution of the symmetry between the two peaks.

2.5 Discussion

Examination of the stationary optical response of the array (Fig. 2.2) reveals that the position and linewidth of the LSPR can be correlated with the size and shape of the NPs. It should be noted that a given relative variation of the NP shape has a larger effect on the LSPR position than a similar relative variation of the NP size [153]. The calculations performed [Figs. 2.6(a) and 2.9(b)] show that the LSPR position can be accurately reproduced considering AuNPs with the shape of oblate ellipsoids and an AR of 2.25. The broader linewidth of experimental spectrum can be explained by taking into account a distribution of the AR value around the mean value of 2.25. It is worth noting that the environment around the NPs can also affect the linewidth but its effect is reported to be significant only for NPs larger than 100 nm [154], a size well above that of the AuNPs of our arrays.

Moving to the ultrafast transient optical response (Fig. 2.4), the experimental spectral profiles are consistent with those reported in the literature for other AuNP systems [41, 155]. Thanks

to our simulations [Figs. 2.8, 2.9(c) and 2.10] that better account for the real morphology of our 3D NP array than a model considering only a single NP shape, we have been able to assign several characteristics observed in the experimental transient optical response to the effect of the distribution of the NP shape. In particular, the profile of the two positive wings is strongly related to the shape and to the shape distribution of the NPs, as expected from the observation of quite different behaviors in spherical and rodlike NPs [41, 152, 156].

The spectra shown in Fig. 2.10 are the result of the different optical dynamics of NPs with different ARs. In particular, the absorption bleaching relaxes more rapidly for larger ARs as can be seen in Fig. 2.11. As a result of the simulation, the shape averaging is able to qualitatively reproduce the observed blue shift of the negative minimum with increasing time.

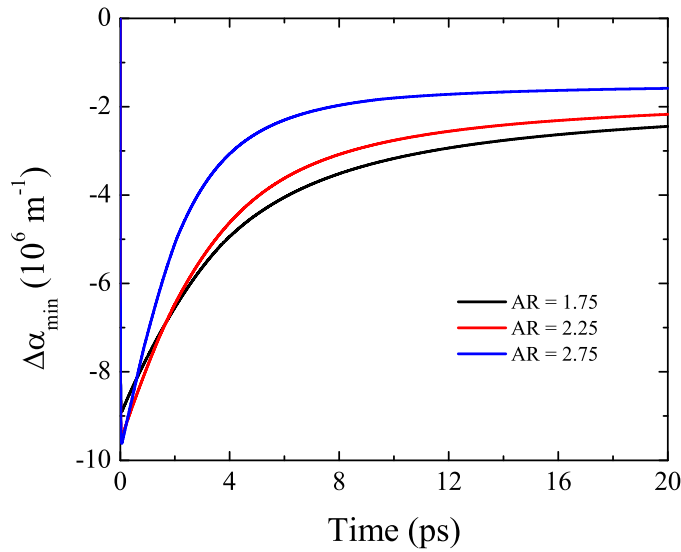


Figure 2.11 – Time evolution of the negative minimum of the absorption modification corresponding to the plasmon bleaching, as calculated for three NPs with AR = 1.75 (black), 2.25 (red), and 2.75 (blue), respectively.

The theoretical analysis of the temporal response of different ARs shows that carriers and lattice temperatures vary with different characteristic times for different ARs, as shown in Figs. 2.12(a) and 2.12(b), respectively. The curves are calculated by accounting for the different values of the absorption cross section at the pump laser wavelength for the different ARs, then resulting in a higher power absorbed for larger ARs. Figure 2.12(a) shows that the electron temperature relaxation time is slightly longer for larger ARs, a feature that, however, cannot explain the observed blueshift of the minimum negative absorption variation for increasing delay time. The different absorbed energy for varying AR could account for the different relaxation times of T_e displayed in Fig. 2.12(a), as it affects the initial maximum electron temperature reached and, as a result, the electron gas heat capacity. However, additional calculations (not shown) performed for different ARs but with the same volume density of absorbed energy exhibit the same behaviors. The proper interpretation lies rather in the dynamics of the lattice temperature: due to lower surface-to-volume ratio, larger AR NPs exhibit a slower heat release to the surrounding medium through the interface; T_l then reaches higher values for higher ARs, as shown in Fig. 2.12(b), which slows down the relaxation dynamics of T_e . The effect of the different C_e values when accounting

for the different pump energy absorbed just reinforces the trend within the first picoseconds after excitation, during which T_e is still significantly higher than T_l .

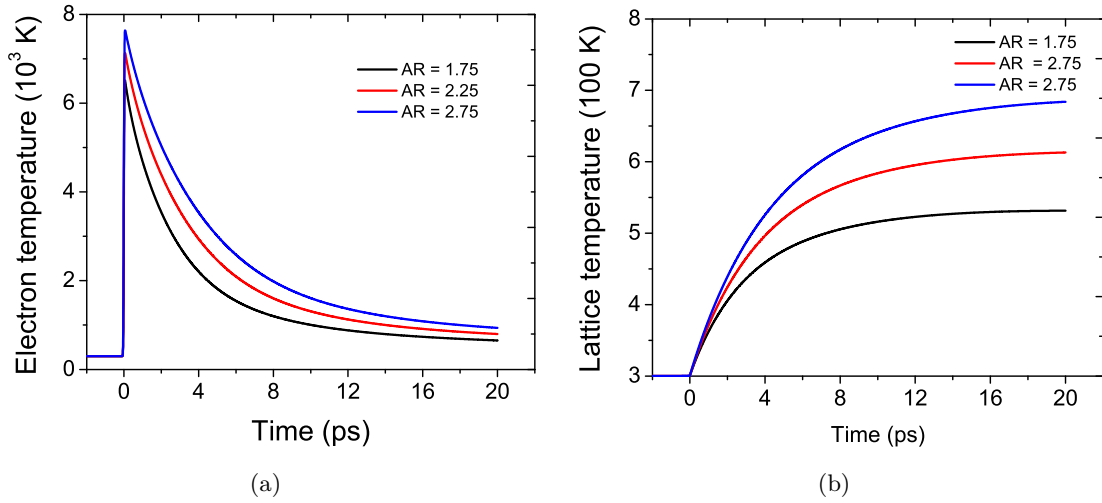


Figure 2.12 – Time evolution of the electron (a) and metal lattice (b) temperatures, as calculated by the 3TM for three NPs with AR = 1.75 (black), 2.25 (red), and 2.75 (blue).

We further observe that, while the dynamics of T_e and T_l of course do not depend on the probe photon energy, the dynamics of the transient absorption does. Although there exists of course a link between the relaxation dynamics of the temperatures and the dynamics of the optical signal, this link is not straightforward. The complex dynamics of the electron distribution, the electron scattering rate and the transition probabilities for the different photon energies have to be considered to interpret the transient signal [72]. Then, we cannot base the interpretation of the dynamics of the optical signal solely on the knowledge of the dynamics of the electron and metal lattice temperatures.

In order to better understand the origin of the AR-dependent relaxation time, we have extracted from the calculated dynamics an effective characteristic relaxation time, even if for some photon energies close to the plasmon mode this is somehow arbitrary as the sign of the transient absorption changes along time. The results are displayed in Fig. 2.13. First, one can observe that the relaxation time increases as the probe photon energy gets closer to the LSPR spectral range for both NP shapes. In addition, at low (<2.2 eV) and high (>2.8 eV) photon energies the relaxation times for the two ARs are rather close to each other, especially in the red part of the spectrum. Nevertheless, for AR = 1.75, the relaxation time is slightly higher than for AR = 2.75. This small homogeneous discrepancy can be ascribed to the dynamics of the intraband transition (Drude) contribution to the dielectric function. Indeed, the dominant term in the conduction electron scattering rate involved in this contribution is the one stemming from electron-phonon collisions, which is proportional to the metal lattice temperature [99]. As the dynamics of T_l is faster for high AR than for low AR [see the slopes of the curves in Fig. 2.12(b)], the dynamics of the Drude contribution is also faster, which explains the small, almost spectrally independent, discrepancy background, between the two curves of Fig. 2.13. In contrast, a large difference in relaxation times is superimposed on this background in the range from ~ 2.2 to ~ 2.8 eV where the relaxation is slower. This interval is close to the interband transition threshold associated with the L point of the Brillouin zone (the transitions close to the X point, starting from 1.8 eV, almost do not

contribute to the transient signal [40]). The vertical dashed lines on Fig. 2.13 denote the position of the LSPR, which roughly corresponds to the negative minimum in the transient differential absorption. In this region, the relaxation time for $AR = 1.75$ is significantly larger than for $AR = 2.75$. Beyond ~ 2.45 eV, the gap decreases progressively with increasing photon energy towards the blue end of the LSPR, beyond which only the small and almost spectrally independent contribution mentioned above remains. This difference, as well as the general increase of the relaxation time when approaching the LSPR spectral range for each AR, can be only attributed to the coupling of the LSPR with interband transitions: as the LSPR for low ARs lies at higher photon energy than for large ARs, this coupling is stronger and results in slower dynamics. This explains the amplified blue-shift when mixing different ARs, corroborating to what was shown in Fig. 2.11. The slowing down of the relaxation due to coupling of the LSPR with interband transitions was already demonstrated by the team of J.-Y. Bigot [157].

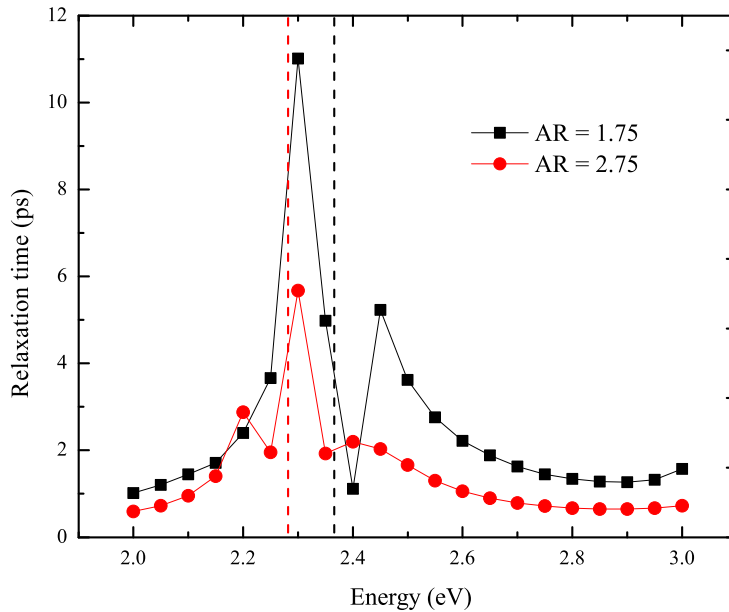


Figure 2.13 – Effective relaxation time of the transient optical signal as a function of probe photon energy, as extracted from the dynamics calculated for two NPs with $AR = 1.75$ (black) and 2.75 (red), respectively. The dashed vertical lines denote the spectral location of the corresponding LSPR mode.

We can then conclude that the blueshift observed when accounting for the shape distribution can be ascribed to the slowing down of the relaxation, in the vicinity of the LSPR, with decreasing AR. This trend cannot be simply interpreted in terms of temperature dynamics, but rather by invoking the stronger coupling of the plasmon resonance with interband transitions.

Finally, in Fig. 2.14, we show the position of both the experimental and theoretical negative minima of the transient absorbance as a function of the pump-probe delay time. Experimentally, the minimum reaches the energy value of 2.33 eV in about 20 ps and then remains at a constant energy. The shift depends on the pump pulse intensity: at higher intensities we observe stronger shifts of the minimum position and longer times are needed to reach the final value. Small differences (~ 10 meV) have been observed in the final value of the energy of the minimum, depending on the pump power. As mentioned above, the quantitative behaviors depend on the real shape

distribution that is certainly different from the one used in the model. The steeper profile of the calculated blue shift hence reflects the semi-arbitrary choice of the shape distribution in the model. We point out once more, however, that the simulations clearly indicate that the blue shift stems from the presence of a shape distribution in the AuNP array. Let us notice that this blue shift cannot be ascribed to the initial nonthermal nature of the electron distribution, as this regime lasts for about 1 ps only and the blue-shift extends over several ps (Fig. 2.14). The higher position of the theoretical points relative to the experimental ones indicates that the real NP shape distribution, partly dictated by the NW shape, is weighted towards higher ARs than that the arbitrary one used in the simulation.

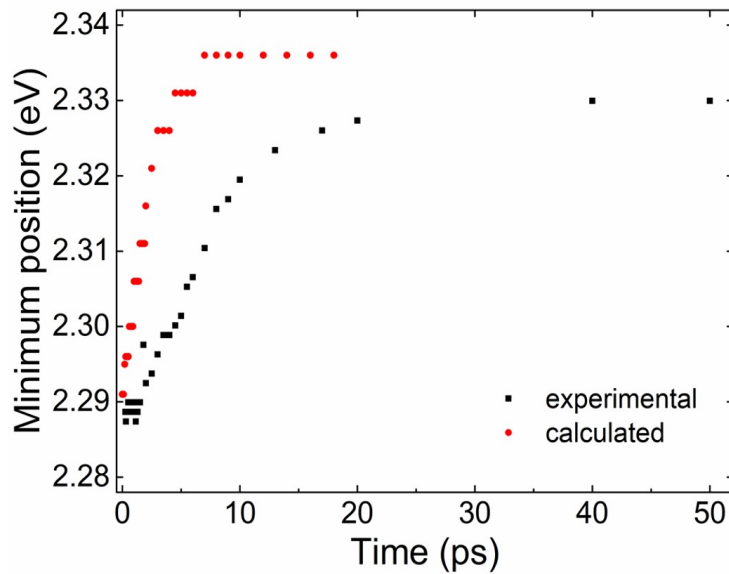


Figure 2.14 – Position of the main minimum in the ΔA measurements (black squares) and in the $\Delta\alpha$ calculation (red dots) as a function of the delay time between pump and probe pulses.

As a last remark, the measured e-ph scattering time constant of 0.95 ps [see Fig. 2.5(b)] agrees with that expected considering the NP size [148]. Indeed, the electron-phonon coupling constant is affected by the NP size only for sizes below 5 nm, while the NP shape has no effect on this time constant [149].

2.6 Summary

Au-decorated SiO₂ NW arrays have been fabricated on quartz substrates by our partners in Rome, starting from Si NWs. They have investigated the optical properties of the AuNPs covering the NW surface in both the stationary and dynamic regimes by the means of absorption and transient absorption spectroscopies, respectively. By developing a two-step, three-temperature model, we have been able to reproduce the stationary spectrum as well as the qualitative spectral dependence of the transient absorption profile obtained from the experiment. Indeed, using an arbitrary set of AuNPs with different aspect ratios, we have demonstrated that the width of the experimental spectra, the blue-shift of the absorption bleaching along the relaxation and the asymmetry between the two positive wings of the absorption variation spectrum can all be attributed to the nonuniform shape distribution of the AuNPs in the sample. We have observed that the temporal

behavior of the carrier and lattice temperatures alone is not sufficient to explain the experimental features and in particular the blue-shift. The latter can be interpreted by invoking the stronger coupling of the plasmon resonance with interband transitions in nanoparticles with smaller aspect ratio. This has an AR-dependent effect on the carrier relaxation dynamics that gives rise to the observed blue-shift with increasing delay time. The stationary and transient features observed in the plasmon resonance of our system suggest that in presence of a shape distribution of metal nanoparticles, the effects relying on their properties should be properly weighed. This is an important point to be kept in mind when designing sensors or catalysts based on a dewetting technique that, in turn, is a much easier and quicker technology if compared to the use of monodispersed, separately prepared nanoparticles. In particular for catalysts, where hot electrons play a crucial role [158], the different contributions to carrier cooling due to different shapes must be taken into account, as pointed out in the present work. Finally, we notice that the use of nanowires as substrates, where the nanoparticle coarsening occurs, introduces constraints on the atom diffusion on the NW sidewalls that influences the final result in terms of shape and size. Tuning the metal film thickness, the annealing temperature and duration, metal NPs with variable shape can be obtained with designed plasmon relaxation characteristics.

Chapter 3

Ultrafast transient optical response of nonspherical gold and core-shell, gold-silver nanoparticles

Contents

3.1	Introduction	51
3.2	Synthesis of the nanoparticles	53
3.2.1	Gold nanorods	53
3.2.2	Silver coating	53
3.3	Experimental study	55
3.3.1	Stationary regime optical response of the nanoparticles	55
3.3.2	Pump-probe investigation results	57
3.4	Theoretical analysis	64
3.4.1	Modeling the stationary optical response of the nanoparticles	65
3.4.2	Modeling the ultrafast transient optical response of the nanoparticles	69
3.5	Discussion	75
3.6	Summary	79

3.1 Introduction

In the preceding chapter, we have studied both the stationary and transient optical responses of anisotropic AuNPs whose short axis polarization LSPR was engulfed by their long axis counterpart, leading to an apparent single plasmon band in the spectrum. This was due to the oscillator strength difference and the spectral proximity of the two modes. However, the LSPR of metallic nanoparticles (NPs) can be tailored by controlling their morphology and composition [4, 7, 53, 54, 159] so that multiple modes can appear. Rod-like metallic nanostructures which possess two LSPRs that correspond to a field polarization along their longitudinal axis (LgSPR) and transverse axis (TrSPR) [160] are the best examples that have been exploited for different purposes. Owing to the tunability of their LgSPR within the visible and near-infrared spectral regions [160] as well as their

biocompatibility, gold nanorods (AuNRs) have appeared frequently in biochemical applications [16], plasmon-enhanced fluorescence [22] and photothermal therapy [28, 29, 161] studies. On the other hand, the field intensity enhancement factor of Ag can be up to 6.8 times greater than that of its Au counterpart [54]; this enables Ag nanostructures to be more preferable for fluorescence and Raman signal enhancement. Unfortunately, its lower stability makes Ag difficult to prepare into perfect nonspherical NPs, like silver nanorod (AgNR) for example. However, thanks to the facile surface functionalization of AuNRs [7, 55, 162], Ag can be deposited onto them, resulting in AuNR-core and Ag-shell hybrid bimetallic nanostructures, AuNR@Ag [7, 53–57]. By varying the Ag:Au molar ratio the shape and size of AuNR@Ag NPs can be controlled. These NPs have drawn a tremendous attention in the community of plasmonics since their optical properties cannot be tuned only by their shape and size, but also by tweaking their equivalent Ag:Au molar ratio (indicated by "eq" in the sample name). This allows one to easily obtain an anisotropic AuNR@Ag NP whose optical properties are more and more dominated by that of Ag [163] just by increasing the eq value. These NPs have already been successfully applied in numerous disciplines in the stationary regime, some of which are Raman signal enhancement [164, 165], biomedicine [14, 15], sensing [166], colorimetric assay of visual readout [167] and electromagnetic field transmission antenna [7]. In the transient regime, the sensitivity of their acoustic vibration modes (phonon dynamics) [168] to the amount of a material being deposited onto the surface of the Au-core have been a promising prospect for applications in mass sensing, i.e., as a nano-balance [59–62]. Despite the variety of spectral and temporal features that can be observed in such kind of nanostructures, a limited number of works have been devoted to the transient electron dynamics of anisotropic bimetallic NPs so far, all of them being mainly experimental. Holly F. Zarick *et al.* [63] have studied the electron dynamics in both cubic and pyramidal Au-core Ag-shell bimetallic nanostructures. Kuai Yu *et al.* [57] have demonstrated that some of the resonance modes of the AuNR@Ag samples of small Ag-shell thickness (2 nm and 4 nm) that are hidden in the stationary regime spectra can be uncovered by ultrafast transient spectroscopic experiments.

This chapter is devoted to the experimental and theoretical study of the stationary and transient optical responses of AuNR@Ag NPs. Their dependence on the Ag shell thickness will be particularly investigated. The anisotropic NPs have been synthesized according to a procedure reported earlier [53], which allows to systematically control the Ag shell thickness. The Ag deposition is dominant along the transverse dimension of the AuNR leading to cuboid shaped AuNR@Ag NPs. Samples of average Ag-shell thicknesses of up to 12.4 nm along the longitudinal dimensions and 18.2 nm along the transverse dimensions have been prepared. The stationary regime extinction spectra of the samples demonstrate multiple plasmonic resonance modes that are highly dictated by the amount of Ag deposited on the AuNR-core. The main contributors to these resonances (depending on the Ag thickness) will be discussed based on the calculations using the BEM. Near field maps taken at each resonance mode of the AuNR@Ag sample of the thickest Ag shell (eq = 8) have been calculated. Ultrafast transient spectroscopy experiments have also been carried out on the samples. The transient spectral signature of the high Ag thickness samples presents a surprising additional bleaching peak compared with what is expected from the number of LSPR modes. The main contributors to the transient spectral signature will be discussed and the origin of this unexpected additional peak will be determined theoretically. Besides, the electron-phonon (e-ph) relaxation time will be studied depending on the excitation wavelength and power.

3.2 Synthesis of the nanoparticles

The NP synthesis and characterization were performed by our collaborators (Cyrille Hamon, Doru Constantin and Claire Goldman) in the Laboratoire de Physique des Solides (LPS) in Orsay. Details about the synthesis procedure and the reactants used can be found in Appendix B.

3.2.1 Gold nanorods

The synthesized AuNR suspensions were stable for months. As estimated from TEM images, the obtained colloidal AuNRs have a mean length and diameter of 47.6 ± 4.7 nm and 15.8 ± 3.3 nm, respectively. The TEM image and the histogram depicting the corresponding size distribution are shown in Fig. 3.1.

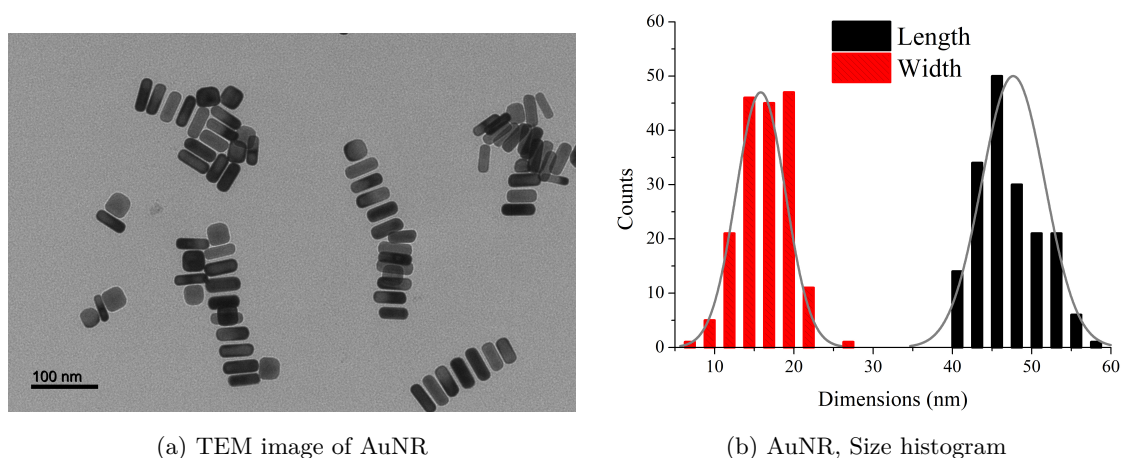


Figure 3.1 – (a) TEM image of the AuNRs and (b) its size distribution analysis from the TEM image. The black histogram corresponds to the longitudinal dimension (length) while the red histogram is for the transverse dimension (diameter).

3.2.2 Silver coating

The overgrowth of AuNR with Ag was performed according to the recently published protocols [7, 53, 162]. The scheme in Fig. 3.2 summarizes the overgrowth process. As shown in the TEM images (see Fig. 3.3), the NPs grow into cuboid shape as the Ag-shell thickness increases [7, 53].

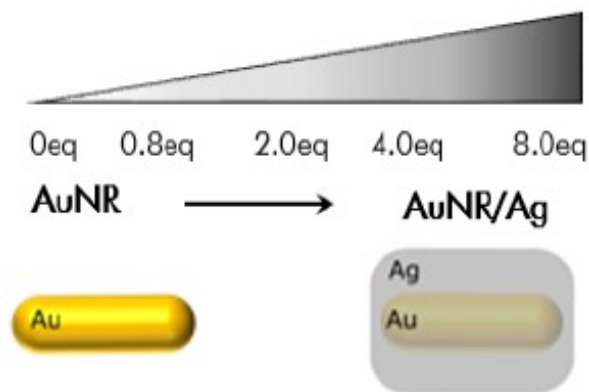


Figure 3.2 – A cartoon showing the Ag overgrowth process.

The average dimensions of the NPs (Table 3.1) determined by the TEM analysis show that in this process of synthesis the Ag growth along the transverse dimension is dominant over the longitudinal one [7, 53]. This is the reason for the NPs to grow into the cuboid shape. In addition to this, the increase in the Ag-shell thickness makes the cuboidal NPs to possess sharper edges and corners than the thin Ag-shell samples [7, 53]. The negative value in the second column of Table 3.1 indicates that the tips of the AuNR-core have not been covered completely (for AuNR@Ag 0.8eq sample) when the Ag:Au molar ratio was 0.8 (refer to the second column in Table 3.1).

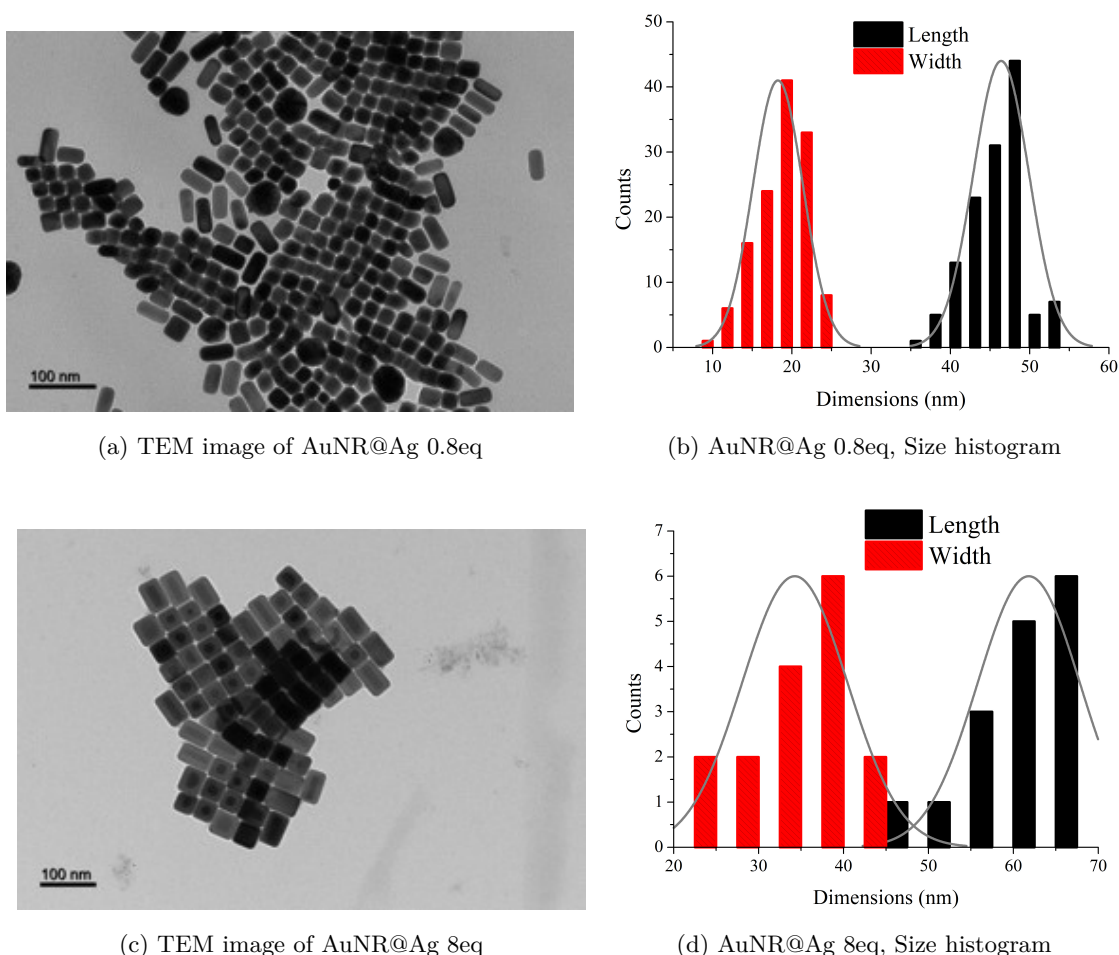


Figure 3.3 – TEM images of AuNR@Ag samples with (a) the thinnest Ag-shell (AuNR@Ag 0.8eq) and (c) the thickest Ag-shell (AuNR@Ag 8eq). The size distribution analysis of the TEM images for the two extreme samples (b) AuNR@Ag 0.8eq and (d) AuNR@Ag 8eq that correspond to their longitudinal dimension (black histogram) and transverse dimension (red histogram) are also shown.

eq (Ag:Au)	Longitudinal dimensions		Lateral dimensions	
	Total length (nm)	Ag thickness (nm)	Total length (nm)	Ag thickness (nm)
0	47.6	0	15.8	0
0.8	46.5	-1.1	18.2	2.4
2	53.3	5.7	28.5	12.7
4	57.8	10.2	32.5	16.7
8	60.0	12.4	34.0	18.2

Table 3.1 – Dimensions of the cuboidal AuNR-Ag bimetallic NPs estimated from the analysis of their TEM images.

3.3 Experimental study

3.3.1 Stationary regime optical response of the nanoparticles

The stationary regime extinction spectra of the colloidal samples were measured using a Cary 5000 UV-VIS-NIR spectrometer (Agilent). The double beam functionality of the instrument was used by initially determining the balance between the reference beam and the sample beam. This was performed by using pure water in a 1 mm glass cuvette (without the sample) in both the front beam (at the sample holder) and the rear beam (the reference holder). Once the baseline was determined in this way, the extinction measurements of the samples were done by using pure water as a reference in the rear sample holder. The obtained stationary regime spectra are presented in Fig. 3.4.

The AuNR solution presents two resonances that correspond to the transverse (TrSPR) and longitudinal (LgSPR) field polarizations at 515 nm and 680 nm, respectively. The Ag deposition leads to the appearance of additional peaks. All the bimetallic NP samples have four dominant resonance peaks labeled in the literature [7, 54] as 1, 2, 3, and 4 from lower to higher photon energy, according to the sequence of their appearance in the spectrum. However, the AuNR@Ag 2eq sample has got five peaks (see the red arrows in Fig. 3.4). Therefore, we will use a new labeling to identify each peak. The longitudinal mode will be labeled by L and the transverse modes will be represented by T. To be specific, L_0 and T_0 will represent the longitudinal and transverse dipolar plasmon modes, respectively, while the T_1 , T_2 and T_3 will denote the higher order modes. The four known peaks in the literature [7, 54] are therefore indicated by L_0 , T_1 , T_2 and T_3 . In these literature, the T_1 mode is considered to be a dipolar mode that originates from the dipolar mode of a cuboid shaped pure silver NP [169]. However, in this work we will not refer to it as a dipolar mode since a FDTD simulation of the charge distribution in the core-shell hybrid NPs reported in Ref. [7] demonstrates that this mode is not associated with a purely dipolar pattern due to the presence of mirror charges at the Au/Ag interface [see Fig. 3.5(a)]. The presence of the mirror charges make the T_1 mode to be a hybrid mode which is made of a dipole at the outer silver/air interfaces and an inverse dipole at the inner Au/Ag interfaces, which then results in the addition of a dipole and a quadrupole [see Fig. 3.5(b)]. The relative weights of the 2-pole and 4-pole evolve with the silver thickness. So, in the bimetallic objects, it is rather a hybrid multipolar mode.

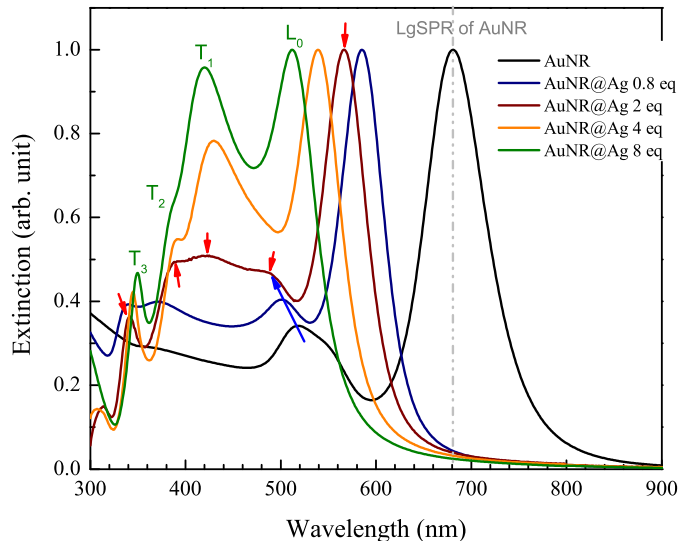


Figure 3.4 – Stationary regime extinction spectra of free AuNRs and of the AuNR@Ag NPs in water. The data are normalized by their respective maximum values. The L and T labels indicated on the AuNR@Ag 8eq resonances represent the longitudinal and transverse modes, respectively. Subscripts of L and T denote the mode types that are present for each field polarization: 0 subscript denotes a dipolar mode while the subscripts 1, 2 and 3 represent the higher order modes. Unlike the others, the AuNR@Ag 2eq sample presents five resonances which are indicated here with the red arrows. The blue arrow indicates the progressive blue shift of the T_0 TrSPR mode of the AuNR-core as the Ag:Au ratio increases.

Table 3.2 reports the observed LSPR mode positions. We represent the fifth peak that appears in between L_0 and T_1 of the AuNR@Ag 2eq sample as T_0 (see the third column in Table 3.2) for reasons that will be discussed later.

Sample name	L_0	T_0	T_1	T_2	T_3
AuNR	680 nm	515 nm	—	—	—
AuNR@Ag 0.8eq	586 nm	500 nm	—	371 nm	335 nm
AuNR@Ag 2eq	567 nm	494 nm	423 nm	388 nm	341 nm
AuNR@Ag 4eq	539 nm	—	428 nm	391 nm	345 nm
AuNR@Ag 8eq	513 nm	—	419 nm	386 nm	350 nm

Table 3.2 – Spectral positions of the resonant modes of the anisotropic AuNR@Ag nanoparticles depending on the Ag:Au molar ratio (eq) value.

As depicted in Fig. 3.4, the relative oscillator strength of the transverse T_1 , T_2 , and T_3 modes increases with the Ag shell thickness. The number of resonance modes appearing also evolves with the amount of Ag. Hence, it becomes difficult to correspondingly assign the labelings of the higher order modes. For example, the T_2 mode of AuNR@Ag 0.8 eq in Table 3.2 could also be assigned to T_1 . We have denoted it as T_2 because it resides in the spectral zone of T_2 modes of the other hybrid samples and it is very far away (in the spectrum) from the L_0 mode. So, we would like to stress that the subscripts of T (1, 2, and 3) are there to sequentially indicate the spectral locations of the modes from the L_0 mode towards the UV.

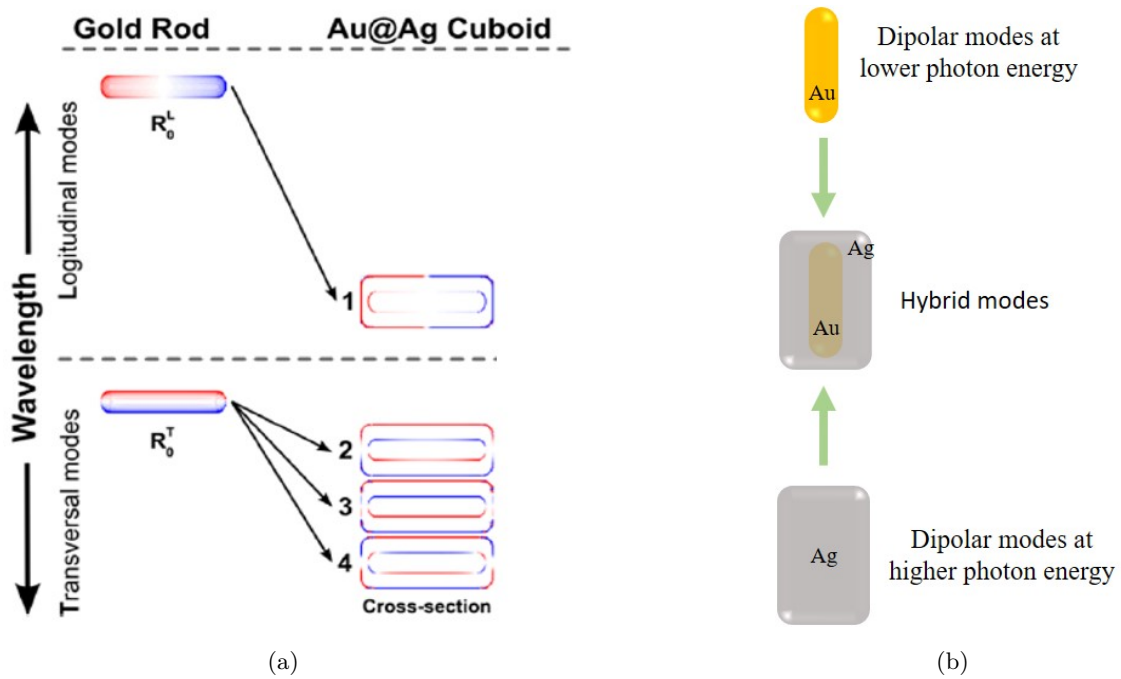


Figure 3.5 – (a) Surface charge distribution of AuNR (left) and AuNR@Ag cuboid (right) as calculated via FDTD (from Ref. [7]). R_0^L and R_0^T correspond to the longitudinal and transverse modes of a bare AuNR, respectively. The longitudinal dipolar mode, L_0 of the AuNR@Ag cuboid is indexed to 1 (it has in-phase charge distribution at both interfaces) while its transverse modes, T_1 , T_2 and T_3 have been indexed to 2, 3, and 4, respectively (they exhibit a mirror charge distribution). (b) A scheme summarizing the possible spectral locations and types of the resonance modes depending on the NP type.

It can be seen that the overgrowth of the AuNR with Ag results in a blue-shift of both the initial L_0 and T_0 resonances and a significant narrowing of the L_0 mode, called "plasmonic focusing", compared to the LgSPR of the bare AuNRs (see Fig. 3.4 and Table 3.2). The higher order plasmonic modes, T_2 and T_3 , show a slight red-shift as the Ag deposition increases. The blue-shift of the L_0 mode arises from both aspect ratio (AR) reduction due to the dominant growth of Ag along the lateral dimension over the longitudinal one, and the increase in the optical effect of Ag coating, the refractive index of which is lower than 1 for wavelengths larger than ~ 315 nm. [54]. The blue-shift of the T_0 mode is mainly attributed to the increased Ag coating [7, 54].

3.3.2 Pump-probe investigation results

The pump-probe experiments were done together with our colleagues (Stefano Turchini, Valentina Utrio Lanfaloni, Lorenzo Di Mario, Alessandra Paladini, Daniele Catone, Patrick O’Keeffe and Faustino Martelli) at the Istituto di Struttura della Materia (ISM), CNR, Rome, in the group of ultrafast processes in materials (FLASHit). Details on the pump-probe experiment setup have been presented in chapter 2 (see Fig. 2.3). The pump energy can be changed according to our need thanks to the optical parametric amplifier component of the setup. Transient absorbance measurements have then been done on the samples with different pump wavelengths and powers. For each experiment, the incident pump beam is maintained at a transverse size of about $400 \mu\text{m}$, pulse duration of about 50 fs and repetition rate of 1 kHz.

3.3.2.1 Transient regime spectral signature of the nanoparticles

As has been presented in the first chapter, the transient optical response of plasmonic NPs originates from the series of fast energy exchanges that they undergo upon their interaction with a laser pulse. In this section, we present the time and spectrum dependent optical response of a monometallic AuNR and that of the AuNR@Ag samples (depending on their Ag-shell thickness) after being irradiated by a femtosecond laser pulse of fluence $446 \mu\text{J}/\text{cm}^2$ at 380 nm.

The transient spectral profile of the bare AuNRs is similar to what has been reported before in the colloidal solution form and for a single AuNR [40, 72, 170]. The transient signature shows alternative induced absorption and transparency features that are due to the modification of the dielectric function of the AuNR subsequent to its pump pulse absorption [40]. These features emanate from the addition of the transient responses of the two LSPR modes associated with the AuNR, namely, TrSPR and LgSPR (see the black curve in Fig. 3.4). As a result, two plasmonic bleaching signals can be observed both around the TrSPR and LgSPR, each with one negative peak at the LSPR mode and two positive peaks in the red and blue wings of this mode [see Fig. 3.6(b) and (c)]. The central peak results from the superimposition of two positive signals contributed by the transient responses from the two plasmon modes of the AuNR. In the work of Xiaoli Wang [40, 72], it has been demonstrated that the relaxation dynamics varies with probe photon energy which results in the spectral shift of the observed local maxima and/or minima. This behavior can be observed readily in Fig. 3.6(c) where the bleaching feature around the TrSPR blue shifts as a function of delay time.

As could be expected based on the number of modes appearing in their stationary regime spectrum [Fig. 3.4], the transient signatures of AuNR@Ag 0.8eq [Fig. 3.7(b) and (c)] and AuNR@Ag 2eq [Fig. 3.8(b) and (c)] bimetallic samples, which have thinner Ag shells, demonstrate four and five plasmonic bleaching features, respectively. However, for the thicker Ag shell samples AuNR@Ag 4eq [Fig. 3.9(b) and (c)] and AuNR@Ag 8eq [Fig. 3.10(b) and (c)], that is not the case: In addition to the bleaching peaks that can be associated to the stationary regime plasmonic modes, a weak fifth negative peak can be observed between the bleaching features appearing around their T_1 and L_0 resonances [see the green arrows in Figs. 3.9(c) and 3.10(c)]. This feature was hidden in the stationary regime (Fig. 3.4) due to the influence of the Ag shell, but revealed in the transient regime thanks to the narrow spectral band in which the transient differential signal experiences sign changes [57].

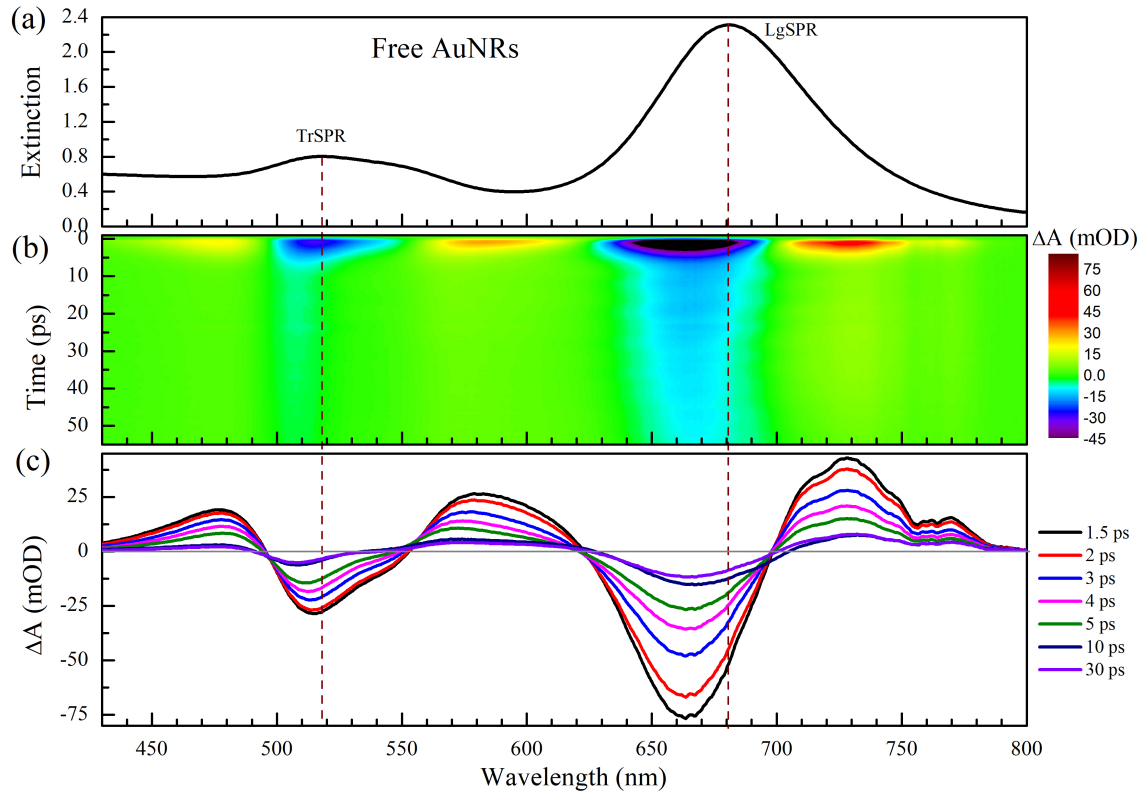


Figure 3.6 – (a) Extinction of the AuNR sample determined by UV-VIS spectrophotometry exhibiting the TrSPR and LgSPR bands. (b) Color chart of the time and spectral dependence of the absorbance variation (in mOD) of the AuNRs measured via pump-probe spectroscopy. (c) Spectral dependence of the differential absorbance at different delay times as extracted from (b). The vertical dashed lines indicate the spectral position of the two plasmon resonance modes of the AuNRs.

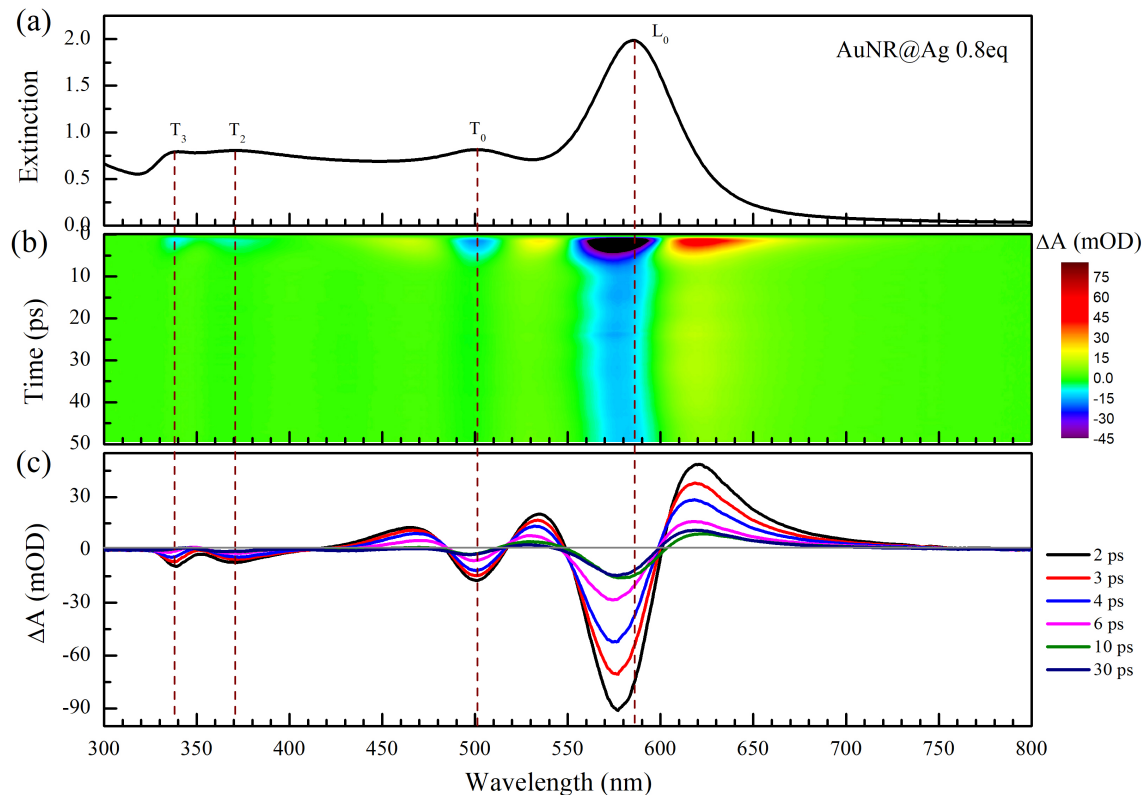


Figure 3.7 – Same as Fig. 3.6 but for AuNR@Ag 0.8eq.

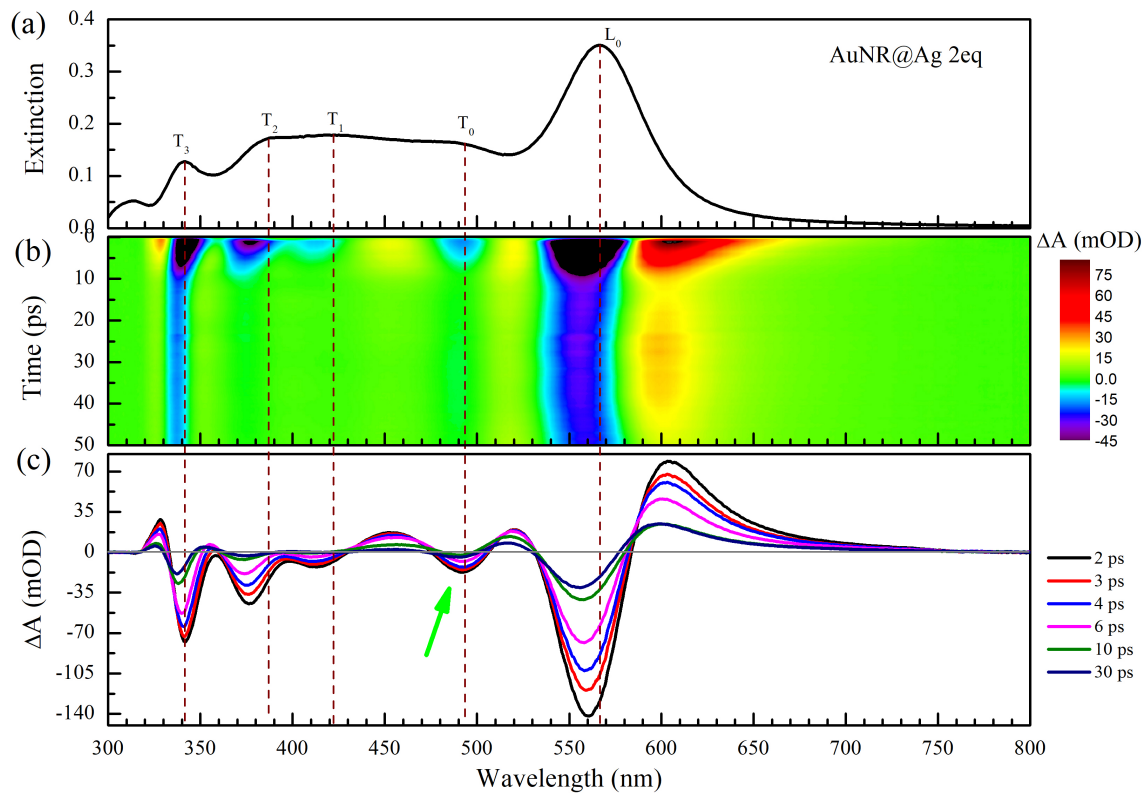


Figure 3.8 – Same as Fig. 3.6 but for AuNR@Ag 2eq. The green arrow in (c) shows the bleaching peak formed around the T_0 mode.

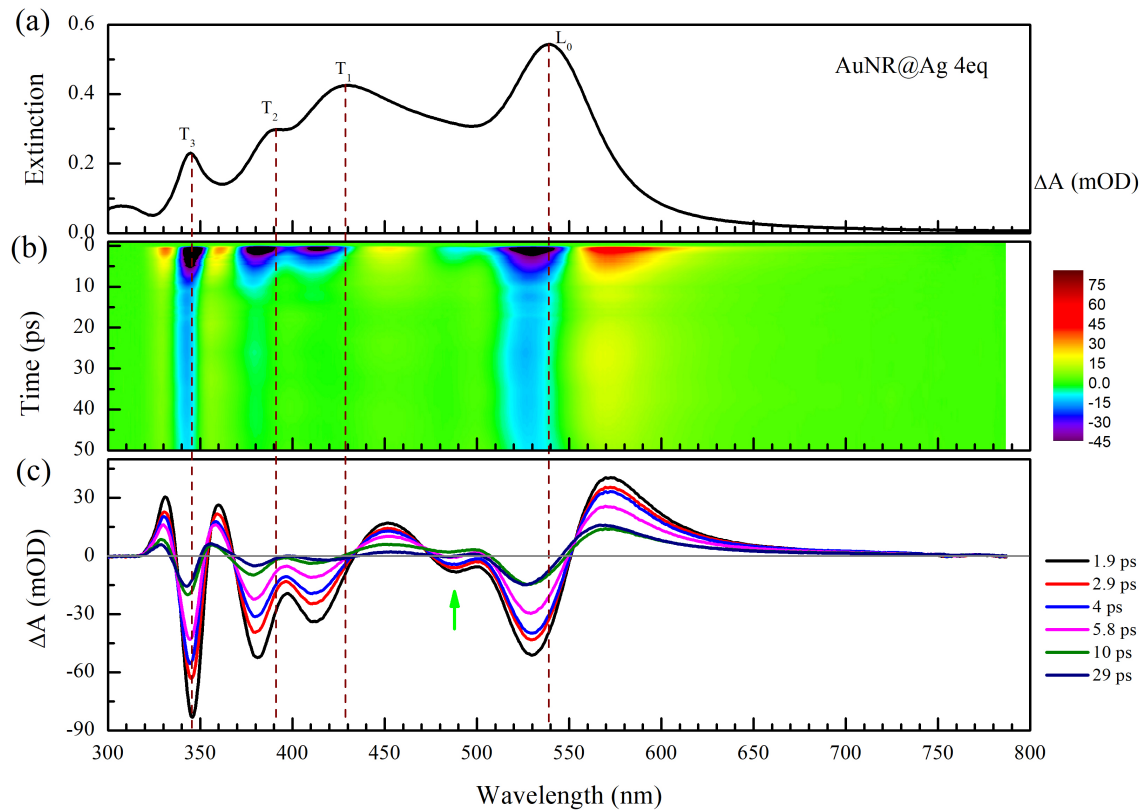


Figure 3.9 – Same as Fig. 3.6 but for AuNR@Ag 4eq. The green arrow in (c) indicates the fifth bleaching peak associated with the weak T_0 mode which is hidden in the T_1 band in (a).

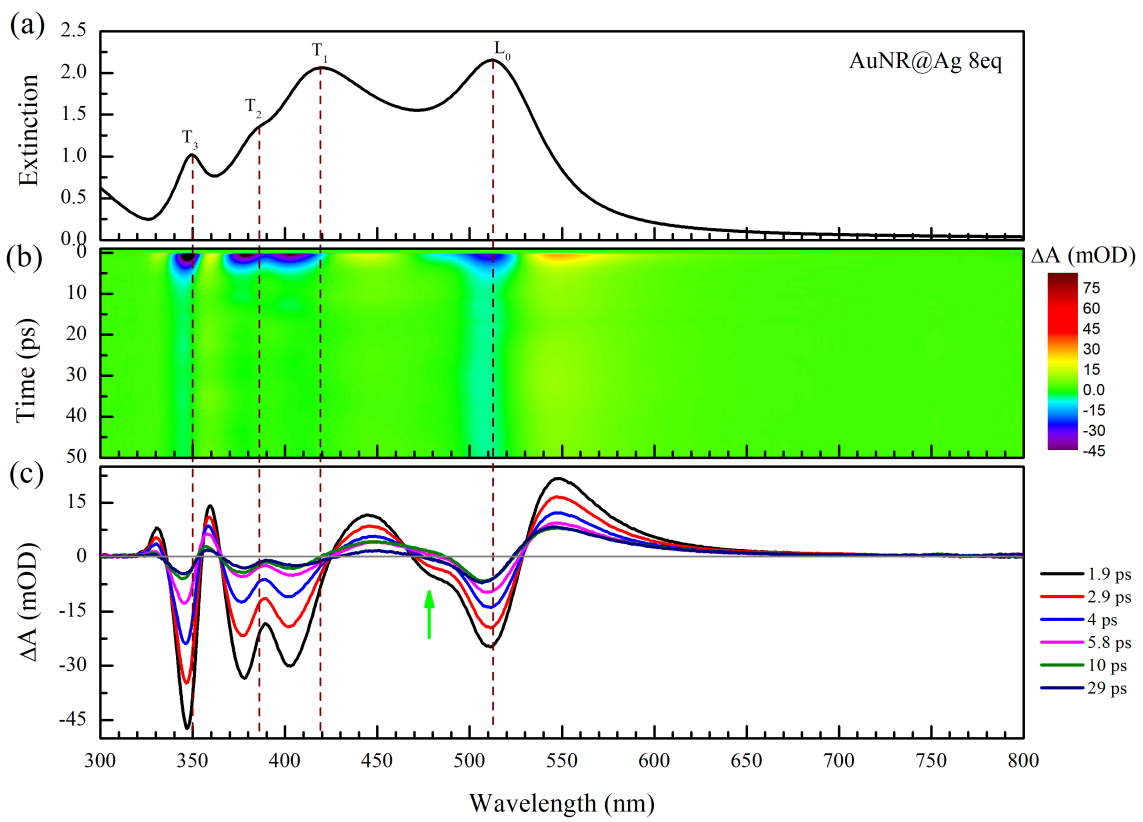


Figure 3.10 – Same as Fig. 3.9 but for AuNR@Ag 8eq.

3.3.2.2 Electron-phonon relaxation time in the nanoparticles

In the preceding section, we have studied the Ag-shell thickness dependent spectral signatures of the core-shell hybrid NPs by pumping them at 380 nm by a $446 \mu\text{J}/\text{cm}^2$ laser pulse. The results show that the spectral features are strongly influenced by the Ag shell size. In addition, the electron-electron (e-e) and electron-phonon (e-ph) scattering processes that happen during the rapid energy exchanges may also vary with NP size as the pump-induced perturbation of the electron distribution near the Fermi level differ according to the NPs [148, 171]. Hence, studying the rate of these process also appears relevant.

The transient intensity probe signal at wavelengths of interest have been fitted directly using an analytical expression which is based on the assumption that each collision (scattering) process can be assigned a characteristic rise or relaxation time. It gives the estimated rise time τ_1 of the signal following the excitation, e-ph relaxation time τ_2 and ph-ph relaxation times τ_3 (details about the equation can be found in Appendix C). Some examples of the fitting results are displayed in Fig. 3.11 for the two extreme samples (AuNR@Ag 0.8eq and AuNR@Ag 8eq). The poor fitting of the dynamics in the longer delay times of the AuNR@Ag 8eq NP is due to the oscillatory behavior of the experimental data stemming from the laser-induced acoustic vibrations of the NPs. We have detected both the breathing and extensional vibration modes in these NPs that depend on their size. The analysis of this phenomenon is left for a future work. Here, we will focus on the study of the e-ph relaxation dynamics (which occurs just before the acoustic phonon vibration regime) in the bimetallic nanoparticles and its dependence on different parameters. The e-ph characteristic time of free AuNRs in a colloidal ensemble or as a single NP has already been studied earlier [72, 170].

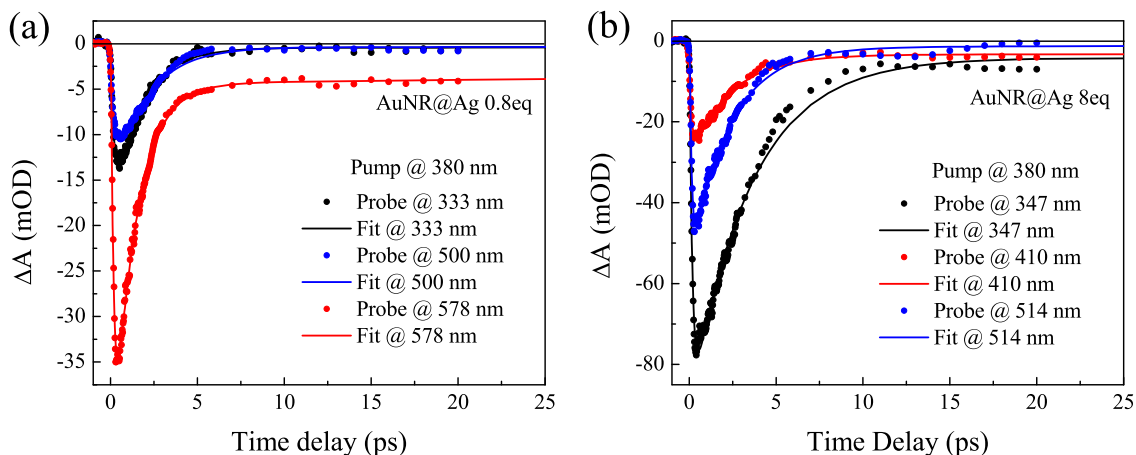


Figure 3.11 – Ultrafast dynamics of the pump-induced variation of the sample absorbance. Symbols: experimental transient data at different probe wavelengths for pump fluence of $56 \mu\text{J}/\text{cm}^2$. Full lines: fitting data by taking both the rise time, τ_1 , and relaxation times, τ_2 and τ_3 into account. (a) For AuNR@Ag 0.8eq and (b) for AuNR@Ag 8eq.

The e-ph characteristic time depends on different parameters, such as the NP size and shape, its absorption cross-section and the pump power. In addition, the extraction of the relaxation times from the signal decay reveals different values depending on the probe wavelength [40]. This underlines the fact that we don't monitor the e-ph relaxation directly but its influence on the probe signal. Then, we should call τ_2 and τ_3 the characteristic decay times of the fast and slow components of the relaxation, rather than e-ph and ph-ph relaxation times. This makes the study of

the e-ph scattering time of NPs complex. In the present work, pump power dependent pump-probe measurements have been done on each sample to further examine its electron dynamics. We also intend to see the effects that pumping in the UV or visible spectral region bring about on the dynamics. Hence, two pump wavelengths were chosen for this study. First, 380 nm pump wavelength was selected as being close enough to most of the plasmonic resonance modes that reside in this spectral zone. The samples have also been irradiated at a pump wavelength close to their respective longitudinal dipolar resonance mode L_0 (see Table 3.2). The difference between both cases affect not only the value of the absorption cross-section but also the degree of involvement of interband transitions.

In Fig. 3.12, the pump energy dependent e-ph relaxation time (τ_2) representing the decay time of the different bleaching peaks is shown for the four AuNR@Ag samples. The e-ph relaxation time increases with pump energy for all samples regardless of the irradiation wavelength. Indeed, a higher absorbed power results in a higher electron gas temperature, and then in a higher electron gas heat capacity. The decay of the bleaching peaks of the AuNR@Ag samples from 0.8 to 4 eq, Ag/Au ratio is slower when the NPs are pumped around their respective L_0 modes than when pumped at shorter wavelength (380 nm) for a given pulse energy [see the connected blue symbols in Figs. 3.12(a), (b) and (c)]. In this case, the NPs absorb more energy from the excitation pulse (see Fig. 3.4) since the pump wavelength and the maximum of their L_0 mode almost overlap, which results in the increase of the electron gas temperature. Nevertheless, this trend tends to decrease for almost all probe wavelengths as the Ag thickness increases [in Figs. 3.12(b) and (c) some connected red symbols mix up with the blue connected symbol] and even almost gets inverted for the thicker Ag shell [Fig. 3.12(d)]. This slowing down of the signal relaxation when increasing the amount of Ag in the bimetallic NPs has been attributed to the growing contribution of the excitation of the interband electron transitions of Ag (in the UV) in Ref. [63].

To go deeper into the relaxation time investigation, it would be necessary to rule out the influence of the pump energy input in the NPs, which depends on pump power, and wavelength (through the NP absorption cross-section). For this, the extrapolation of the data of Fig. 3.12 down to zero excitation energy is required [148, 171]. As can be guessed all curves converge toward about $\tau_2^0 \simeq 1$ ps, which roughly matches the usual findings in the literature. Note that a rigorous extrapolation would require a large number of data points. In addition, it would be interesting to analyze the evolution of τ_2 with probe photon energy from one sample to another, as was done previously in the team [40, 95]. For this, a large number of signal decay fits should be performed as in Fig. 3.11.

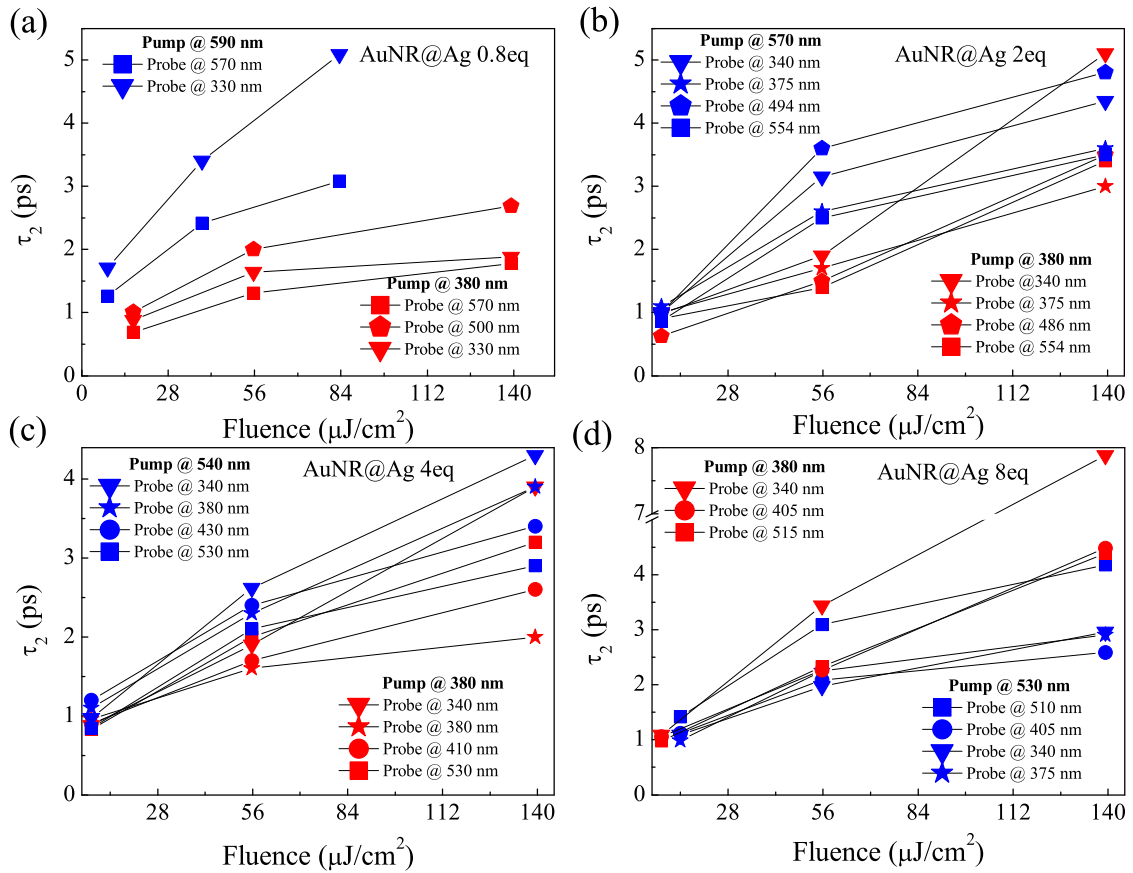


Figure 3.12 – Pump energy dependent e-ph relaxation time representing the recovery lifetime of the different bleaching peaks. The connected blue and red symbols in each panel represent the pump power dependent e-ph relaxation time (ps) of each sample pumped at 380 nm and at their respective dipolar LgSPR, L_0 . Panel (a) for AuNR@Ag 0.8 eq, (b) for AuNR@Ag 2eq, (c) for AuNR@Ag 4eq and (d) for AuNR@Ag 8eq.

3.4 Theoretical analysis

The theoretical modeling is based on the boundary element method (BEM) using a Matlab[®] toolbox called Metallic NanoParticle BEM (MNPBEM) [130]. As its name suggests, this toolbox is well suited for calculating the optical properties such as near field enhancement, absorption, scattering and extinction cross-sections of metallic NPs of arbitrary shape and composition with sizes ranging from a few nanometers to a few hundreds of nanometers, and for frequencies in the optical and near-infrared regime. As has been described in chapter 1, dielectric functions used in the calculations are obtained from the fitting of the experimental bulk dielectric functions of Ag [84] and Au [85]. The interband contributions of the X and L points of the Brillouin zone were considered for fitting the experimental Au data while only the L point interband transition contribution was considered for the experimental Ag data. The Drude term has also been accounted for in both cases (see chapter 1).

3.4.1 Modeling the stationary optical response of the nanoparticles

The bare AuNR was represented by a hemisphere-capped cylinder as the TEM image [Fig. 3.1(a)] suggests [7, 53]. The AR of the AuNR was varied to match the experimental LSPR. To do so, the average transverse dimension (15.8 nm) obtained from the TEM analysis in section 3.2 was kept constant and the longitudinal dimension was varied. The perfect match parameter was obtained when the longitudinal dimension is 45.8 nm (AR = 2.9). This longitudinal dimension and the AR are very close to the average values that was determined by TEM analysis: 47.6 nm and 3.0, respectively. The two dipolar modes that correspond to the LgSPR and TrSPR are reproduced (Fig. 3.13). Their overall spectral broadening as well as their relative oscillator strength weights in the experimental data can be attributed to the NR shape and size distribution in the sample. The shoulder in the experimental TrSPR band (indicated by the green arrow in Fig. 3.13) stems from the presence of small rounded cuboids of gold in the AuNR solution [see the TEM image in Fig. fig3:AuNR(a)] that have LSPR mode at the spectral position indicated by the green arrow in Fig. 3.13. Figures 3.14(a) and (b) depict the near field modulus ($\sqrt{\mathbf{E} \cdot \mathbf{E}}$) of the bare AuNR, retrieved at its resonant wavelengths LgSPR (680 nm) and TrSPR (514 nm). The well-known high field enhancement at the NR tips, associated with the LgSPR, can be observed.

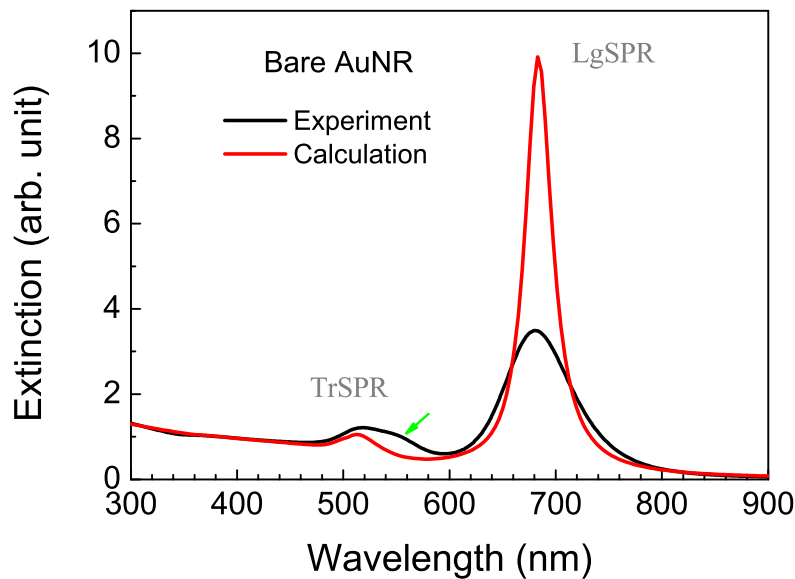


Figure 3.13 – Stationary optical response of the bare AuNRs. Black: experimental extinction of the AuNR solution. Red: extinction cross-section of a AuNR with AR = 2.9 calculated by the BEM. Both data are normalized by their respective values at 384 nm. The green arrow points at a shoulder in the TrSPR band of the experimental data, originating from a small population rounded cuboids of gold in the solution.

The bimetallic hybrid samples were modeled as a hemisphere-capped cylinder AuNR core and a cuboid-shaped Ag shell, i.e, the Ag shell has a square-based rectangular parallelepiped shape with base-side length W and height L [see Fig. 3.15(a)]. Two parameters were adjusted in the simulation to fit the experimental stationary regime spectra, namely, parameters of the Ag shell (W and L) and its degree of rounding [53]. The values obtained are reported in Table 3.3. They are very close to the average dimensions obtained for each sample by the TEM image analysis (compare the values in Table 3.3 with the ones reported in Table 3.1). Figure 3.16 displays the

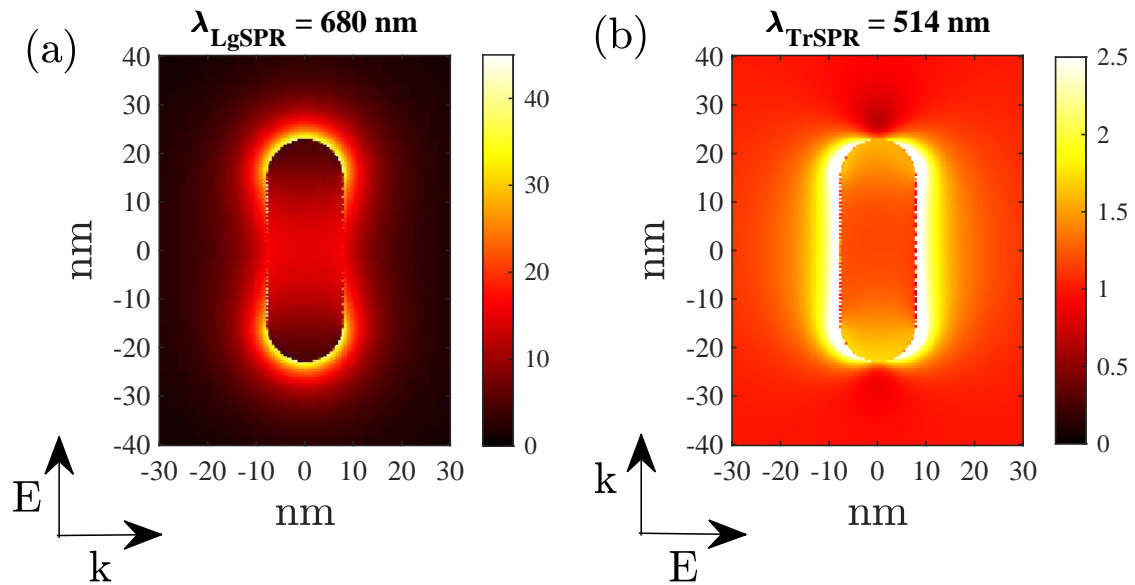


Figure 3.14 – Near field map (modulus of the field) of the bare AuNR determined by the BEM: taken (a) at its longitudinal resonance (680 nm, \mathbf{E} parallel to the NR) and (b) at its transverse resonance (514 nm, \mathbf{E} perpendicular to the NR).

simulated extinction spectra together with the experimental ones. All the dominant resonances that have been observed in the experimental spectra are also present in the ones theoretically determined. As for the bare AuNRs, we have to keep in mind that the actual samples exhibit a certain NP size and shape distribution, which explains that the mode peaks are broader and less peaked than the simulated spectra with a simple NP morphology. The modeled data for the hybrid NPs present multiple small shoulders in the blue and red spectral regions of the T_2 and T_3 resonances, respectively. This can be seen readily from the plots in Figs. 3.16(c) and (d) for the thick Ag samples.

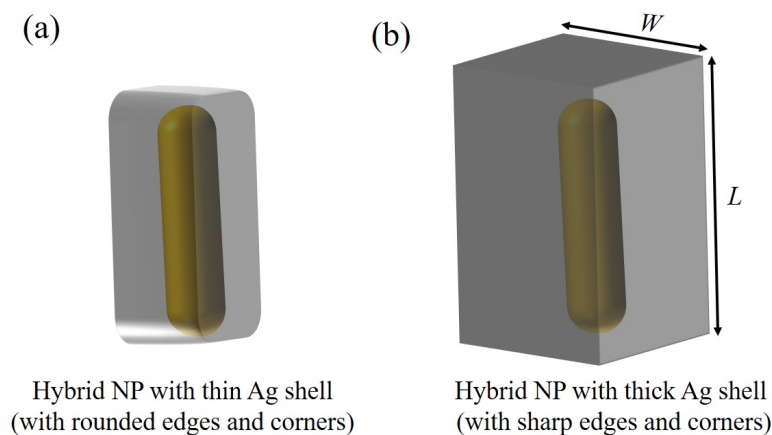


Figure 3.15 – Schematic representation of the AuNR@Ag NPs with (a) thin Ag shell and (b) thick Ag shell. The degree of rounding of the edges and corners can be seen.

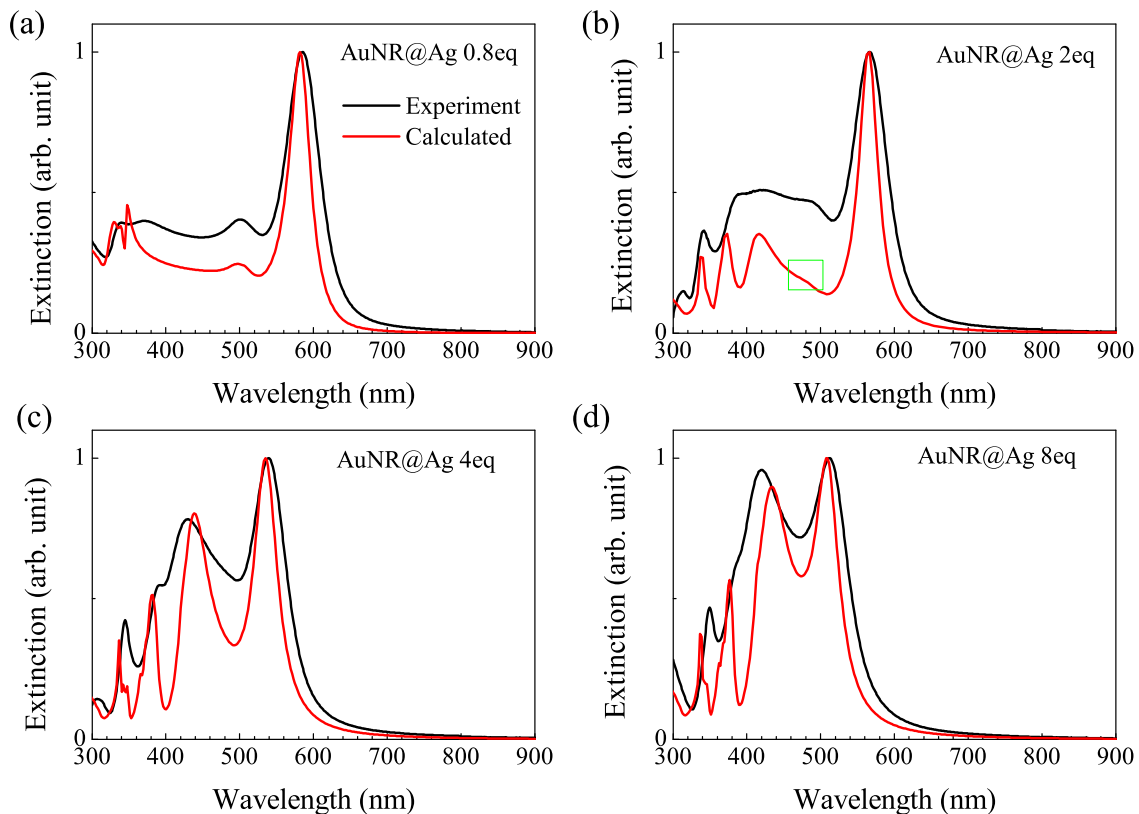


Figure 3.16 – Modeling the stationary optical response of the AuNR@Ag NPs using the BEM. From (a) to (d), the black curves denote the experimental extinction data while the red ones represent the modeled data. Both the experimental and the calculated data are normalized against their respective maximum value which is at the L_0 mode. The green square highlights the presence of a weak mode in that region.

The rounding value, p , is a dimensionless parameter of values between 0 and 1, in a super-ellipsoid equation which can be used to control the sharpness of the edges and the corners of a cuboid model [163]. $p = 0$ corresponds to a nanocuboid with sharp edges and corners while $p = 1$ produces a shape that is similar to an ellipsoid. So, in the simulation, lowering of the rounding values with the increase of Ag thickness is consistent with what can be seen in the TEM images of the AuNR@Ag samples [compare Figs. 3.1(a), 3.3(a) and (c)]. As the Ag deposition is increased, the NPs grow into cuboids whose edges and corners get sharper and sharper (see Fig. 3.15 above and the last column in Table 3.3). The influence of the sharp corners and edges on the resonance modes of AuNR@Ag NPs has been well explained by Michael B. Cortie *et al.* in Ref. [163]. The rounding plays a major role in shaping the modes appearing in the higher photon energies by turning them on or off. As can be seen in Fig. 3.17, the sharper the NP's edges and corners become, the higher the number of resonance modes are (especially in the higher photon energy) and the overall spectrum gets stretched out. This means that these multimodes do exist in the spectra of the samples with high p values but have been squeezed together into different bundled modes with a few number of peaks appearing [163]. These multimodes cannot be observed in the experimental spectra of colloidal ensembles due to the blending of the individual peaks because of its inhomogeneity. The irregularity of the higher photon energy resonances of the modeled

eq (Ag:Au)	Longitudinal dimension		Lateral dimension		Rounding
	L (nm)	Ag thickness (nm)	W (nm)	Ag thickness (nm)	p
0	45.8	0	15.8	0	—
0.8	44.6	-1.2	18.2	2.4	0.50
2	49.8	10.0	25.8	4.0	0.22
4	54.2	8.3	34.3	18.5	0.15
8	57.4	11.6	36.8	21.0	0.15

Table 3.3 – Dimensions of the cuboid-shaped AuNR@Ag bimetallic NPs obtained by adjusting the BEM simulation as to match the experimental stationary optical spectra.

stationary regime data (the red curves in Fig. 3.16) can be attributed to the the influence of these multimodal resonances.

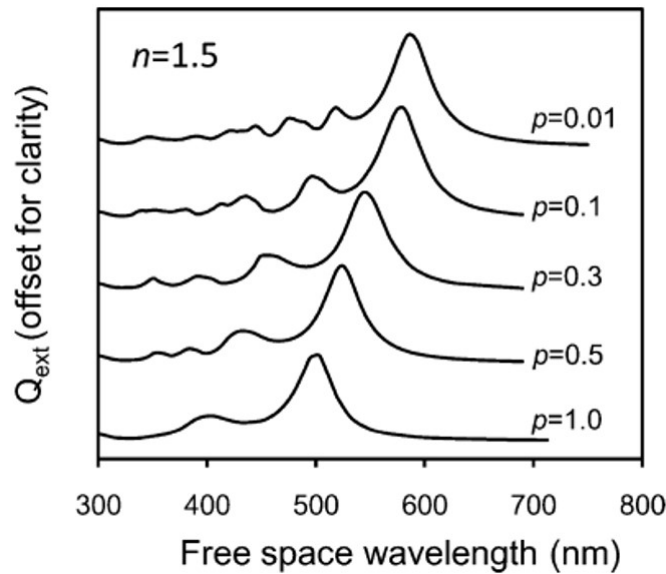


Figure 3.17 – Effect of the rounding of a silver nanocuboid as calculated using the DDA taken from Ref. [163]. p is a parameter in a super-ellipsoid equation which can be used to control the sharpness of the edges and the corners of a cuboid model. $p = 0.01$ corresponds to a nanocuboid with sharp edges and corners while $p = 1$ produces a shape that is similar to an ellipsoid.

Furthermore, we have modeled the field distribution around the dominant resonances (L_0 at 515 nm, T_1 at 427 nm, T_2 at 378 nm and T_3 at 341 nm) of the AuNR@Ag 8eq sample to observe the changes that the Ag overgrowth brings about compared to the field distribution of the bare AuNR [Fig. 3.14]. The near field map of the AuNR@Ag 8eq sample simulated around its four resonances are shown in Fig. 3.18. For the transverse excitation [(b) to (d)], the field map shows that a strong field (hot spot) can be induced at the Au/Ag interface around the spectral positions of modes appearing in the higher photon energy (compare the panels in Fig. 3.18). The transverse polarization modes are associated with bright regions along the NP interfaces. Besides, for the higher mode energies, the field spreading decreases and its intensity becomes more localized. The degree of brightness at the interface increases as we go deep into the spectral region of lower

wavelength [compare panels (b), (c) and (d) in Fig. 3.18]. The reason for this will be discussed later in this chapter.

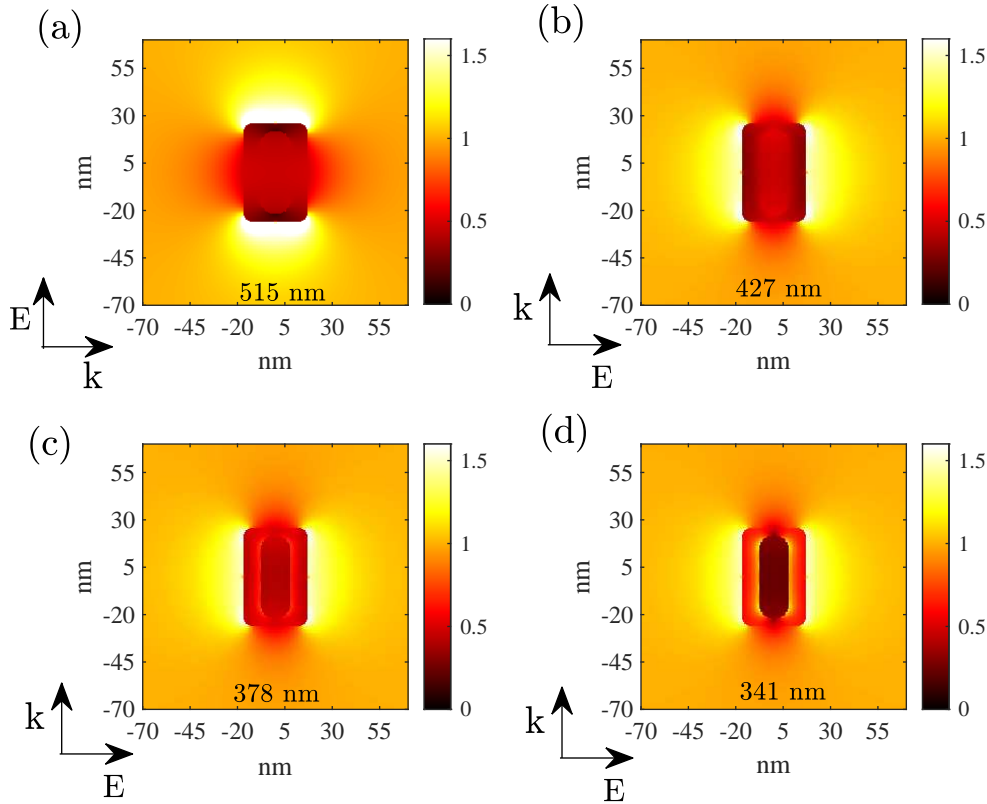


Figure 3.18 – Modulus of the near field of AuNR@Ag 8eq NP taken (a) around its longitudinal resonance mode [515 nm] and around its transverse resonance modes [(b) 427 nm, (c) 378 nm and (d) 341 nm], as determined by the BEM.

3.4.2 Modeling the ultrafast transient optical response of the nanoparticles

We have modeled the stationary optical response of the samples and obtained satisfying representations of their spectra. This has allowed us to determine the theoretical morphological parameters (dimensions and rounding) of the NPs that can now be used to model their transient response. So, in this section, we calculate the ultrafast transient dielectric function of the NPs and use it to model the time-dependent extinction cross-sections of the NPs. For this, the optical parameters of the pump laser are chosen to be identical to the experimental ones (§3.3.2). Just like as in the experiment (§3.4.1), an excitation fluence of $446 \mu\text{J}/\text{cm}^2$ was used and all the laser parameters were kept the same [transverse beam size is $400 \mu\text{m}$ (waist $w = 200 \mu\text{m}$) and pulse duration $\Delta t = 50 \text{ fs}$] for the study of the transient spectral signature of the NPs. Assuming a Gaussian pulse, the laser power absorbed by each NP was calculated from their absorption cross-section σ_{abs} at 380 nm by the following relation:

$$P_{abs} = \frac{\sigma_{abs} I_0}{V} \quad (3.1)$$

where V is volume of the NP and $I_0 = \frac{1}{\Phi\sqrt{2\pi}} \frac{2E}{\pi w^2}$ is the laser peak intensity, where $\Phi = \frac{\Delta t}{\sqrt{\ln(256)}}$ and E is the excitation energy [38].

As we intend to simulate the transient signal within a time range spanning over a several picoseconds while disregarding the initial athermal regime [40, 50], the 3TM has been selected to model the thermal dynamics inside and around the NPs (the details are available in Chapter 1). Indeed, this approach accounts for the heat release from the NP to its environment (water in our case). In addition, we have taken the dependence of the e-e and e-ph scattering rates on the electron gas internal energy and lattice temperature into account. The coupled nonlinear equations of the 3TM were solved via a numerical finite element method (FEM) optimized in a commercial software (COMSOL) as any analytical solving is excluded due to the complex morphology of the bare AuNR and AuNR@Ag NPs. A perfect contact at the interfaces and purely diffusive thermal transport into the host medium were considered [72]. This provides us with the time evolution of the electron (T_e) and lattice (T_l) temperatures in the NPs as well as the topography of the host medium temperature.

Modeling of the thermal dynamics in and around the AuNR@Ag NPs was carried out by considering each bimetallic system as a single homogeneous cuboid NP. A more rigorous approach would have consisted in accounting for the thermal resistance at the Au/Ag interface and the difference in the e-ph coupling constants, heat capacities and thermal conductivities of the two metals, which would have induced a discontinuity in the thermal dynamics at the boundary [172]. However, for the case of an Au/Ag interface, it has been shown by Bekir Sami Yilbas [173] that the short-pulse induced dynamics of both T_e and T_l are smooth (i.e., without discontinuities at the interface). Therefore, the influence of the Au/Ag thermal resistance is insignificant. This stems from the similarity between the thermal properties of Au and Ag as shown in Table 3.4. This supports our simplified approach which amounts to consider the bimetallic AuNR@Ag NP model as a homogeneous single cuboid.

Thermal parameter	Unit	Au	Ag
Lattice heat capacity, C_l	$\text{J m}^{-3} \text{K}^{-1}$	3.0×10^6	3.5×10^6
e-ph coupling constant, G_{e-ph}	$\text{J ps}^{-1} \text{m}^{-3} \text{K}^{-1}$	$(3 \pm 5) \times 10^4$	$(3.5 \pm 0.5) \times 10^4$
Electron gas heat capacity, C_e	$\text{J m}^{-3} \text{K}^{-1}$	$\gamma T_e, \gamma = 66$	$\gamma T_e, \gamma = 65$

Table 3.4 – Thermal properties of bulk Ag and Au at ambient temperature (300 K) as reported in Ref. [174].

In this way, the time evolution of both T_e and T_l inside the NPs, as well as the one of the thermal topography around (in the host medium) have been determined. These values have been used to calculate the transient variation of the dielectric function of Au and Ag in the NPs. The transient modification of the intraband susceptibility has been added to the interband one, determined through Lindhard's theory and Rosei model by considering a local parabolic band structure around the L and X points of the Brillouin zone for Au and at L point for Ag [see Chapter 1]. Once the time evolution of the dielectric function is calculated, the subsequent time evolution of the optical properties of the NPs (extinction, scattering and absorption cross-sections) is determined using the BEM.

The volume of the NPs that interact with the pump pulse is calculated according to their geometry. The AuNR posses a hemispherical-capped cylinder shape and its volume can be determined via Eq. 3.2 where D and L are its diameter and length, respectively, while the AuNR@Ag bimetallic NPs are considered as simple cuboids as explained above (the rounding is neglected for evaluating the NP volume).

$$V_{AuNR} = \pi \left(\frac{D}{2} \right)^2 \left[L - \frac{D}{3} \right]. \quad (3.2)$$

The calculated transient response spectrum of a bare AuNR in water is shown in Fig. 3.19. Two bleaching peaks can be seen just like as in the experimental data of the colloidal AuNR in Fig. 3.6(c). Let's note that our intention is to demonstrate the overall transient spectral dynamics both for the monometallic and bimetallic samples rather than reproducing quantitatively the experimental data, which would be rather meaningless owing to the size and shape distributions. The calculated change of the transient extinction cross-section, $\Delta\sigma_{ext}(\omega, t) = \sigma_{ext}(\omega, t) - \sigma_{ext}(\omega, 0)$, is plotted in Fig. 3.19. In order to be able to compare the spectral dynamics around the TrSPR with the one determined experimentally, we have also zoomed into that spectral zone [see the inset in Fig. 3.19(b)]. Indeed, the oscillator strength of the TrSPR is very small compared to that of the LgSPR [Fig. 3.19(a)] and therefore the close up helps to see the dynamics and spectral features occurring around the TrSPR. The bleaching signal around the TrSPR blue shifts with the delay time as has been observed in the experimental data [Fig. 3.6(c)].

Figures 3.20, 3.21, 3.22 and 3.23 depict the calculated transient optical responses of the AuNR@Ag 0.8eq, AuNR@Ag 2eq, AuNR@Ag 4eq and AuNR@Ag 8eq NPs, respectively. The data display the same number of dominant plasmonic bleaching peaks as has been observed in the experimental ones for each sample. Except the AuNR@Ag 0.8eq sample, which has got four bleaching peaks like its experimental counterpart [compare Fig. 3.20(b) with Fig. 3.7(c)], all the other samples have five [compare Fig. 3.21(b) with Fig. 3.8(c), Fig. 3.22(b) with Fig. 3.9(c) and Fig. 3.23(b) with Fig. 3.10(c)]. For each sample, the spectral positions of the bleaching peaks of the calculated data agree very well with the experimental ones. While for the bare AuNR the experimental and simulated spectral signatures are similar over the whole spectral region of interest, their agreement for the AuNR@Ag samples is less obvious in the higher photon energy range. Multiple spikes can be observed in the simulated differential cross-section for the bimetallic samples. The spikes get stronger for the larger Ag-shell thickness NPs [see Figs. 3.20(b), 3.21(b), 3.22(b) and 3.23(b)]. As has been discussed before, this is due to the presence of the multimodes, in the simulated data, in this spectral zone (§3.4.1) which bundle together to form each peak and are amplified by the transient response. The oscillator strength weight of the positive peaks in this spectral zone are somehow overestimated compared to what can be seen in the experimental data. This overestimation has the same origin as the difference in the sharpness of the spectral features observed in the stationary regime (compare the red and black curves in Fig. 3.16). Again, the theoretical calculation considers only a single NP which means, the NP shape and size distributions of the experimental sample are not accounted for. These distributions result in the blurring of the spectral variations measured as compared with the spikes in the simulated signal.

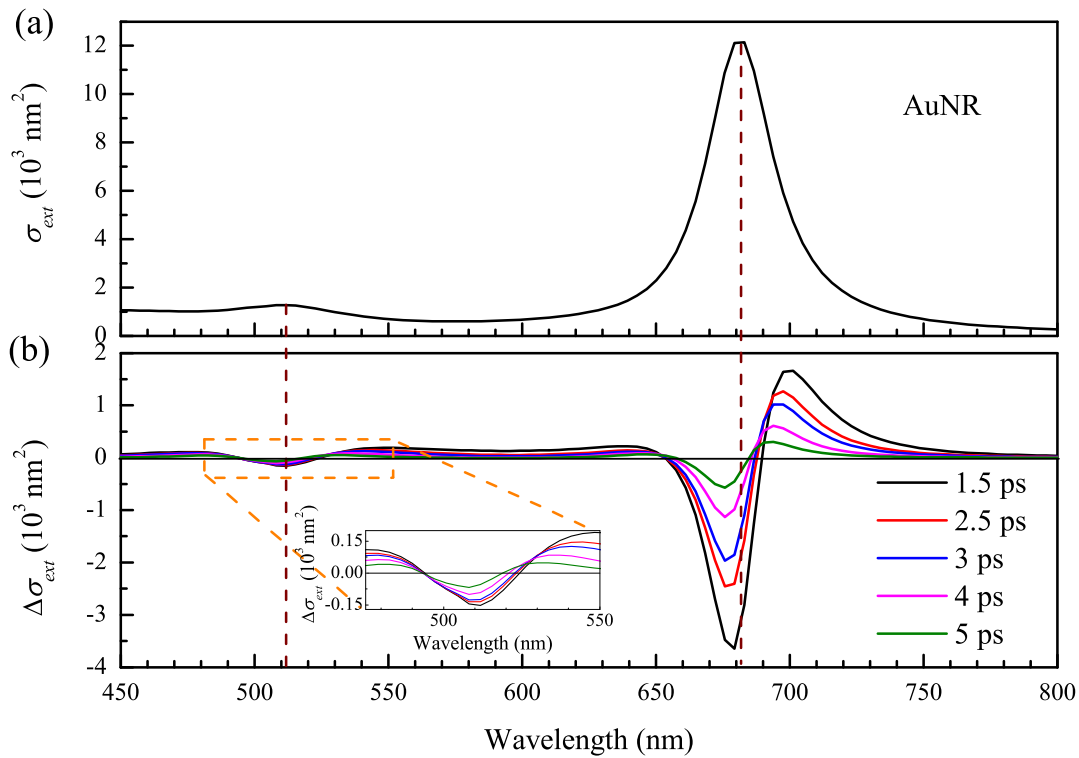


Figure 3.19 – (a) Calculated stationary regime extinction cross-section of a bare AuNR with $AR = 2.9$. (b) Its simulated transient optical response (variation of the time dependent extinction cross-section from the stationary one) at different delay times after 50-fs pump pulse absorption. The inset shows the dynamics around the TrSPR mode. The vertical dashed lines indicate the spectral positions of the LgSPR and TrSPR of the AuNR in the stationary regime.

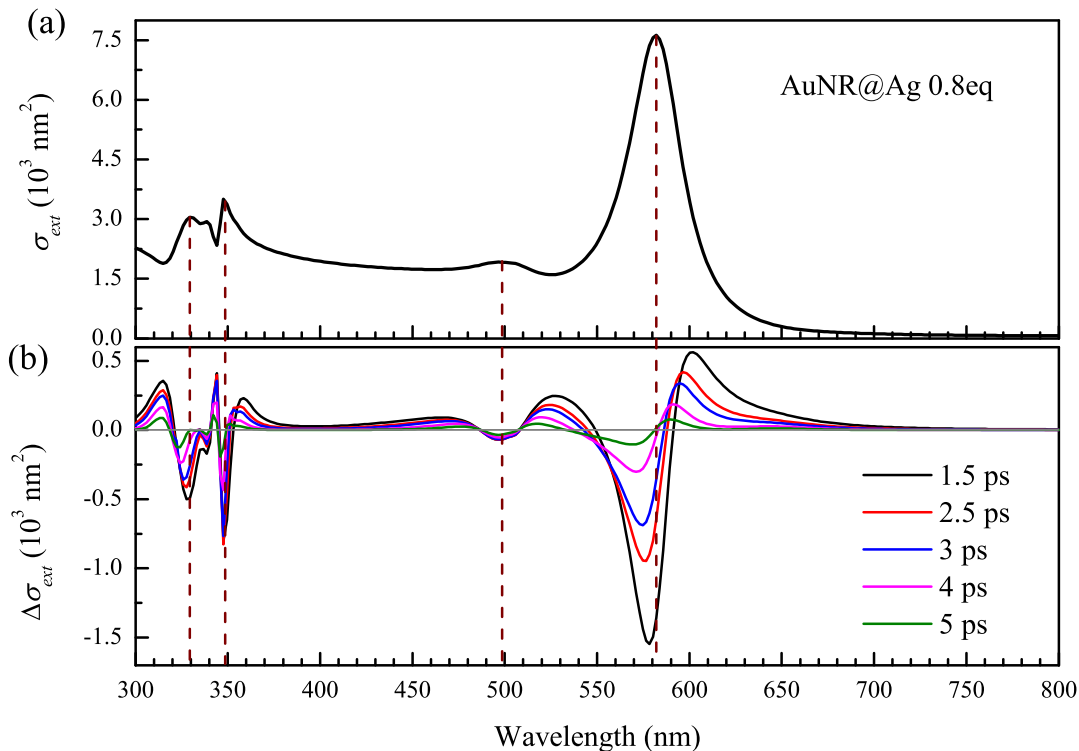


Figure 3.20 – Same as Fig. 3.19 but for AuNR@Ag 0.8eq.

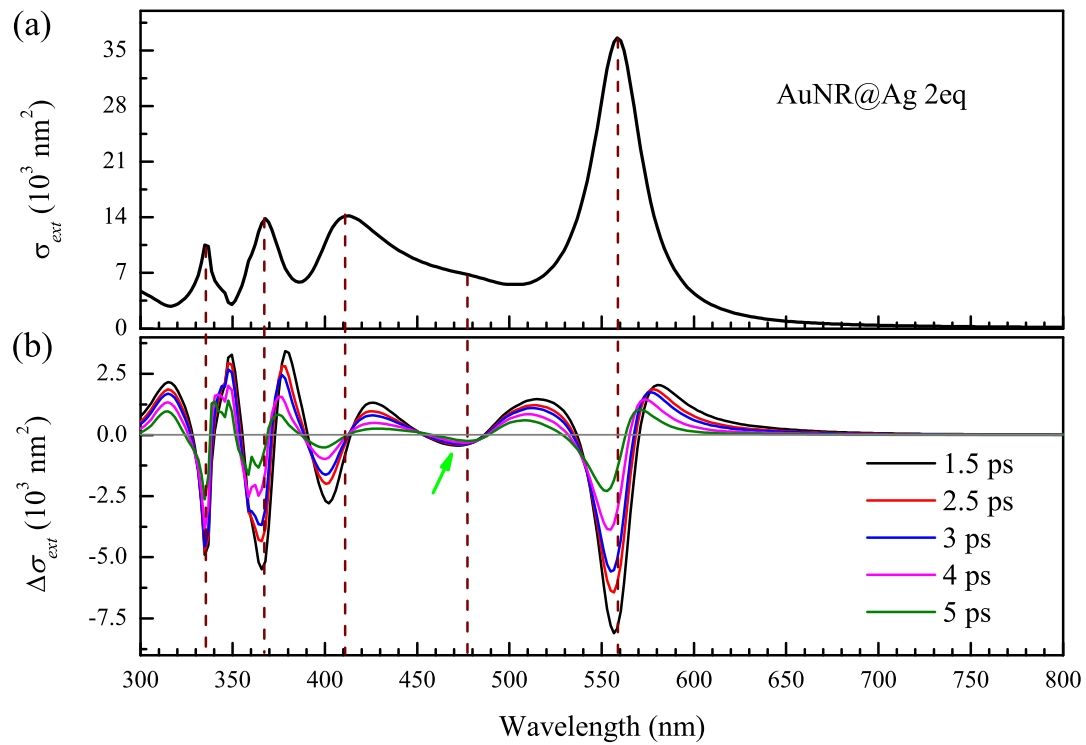


Figure 3.21 – Same as Fig. 3.19 but for AuNR@Ag 2eq. The green arrow in (c) shows the bleaching peak formed around the T_0 mode.

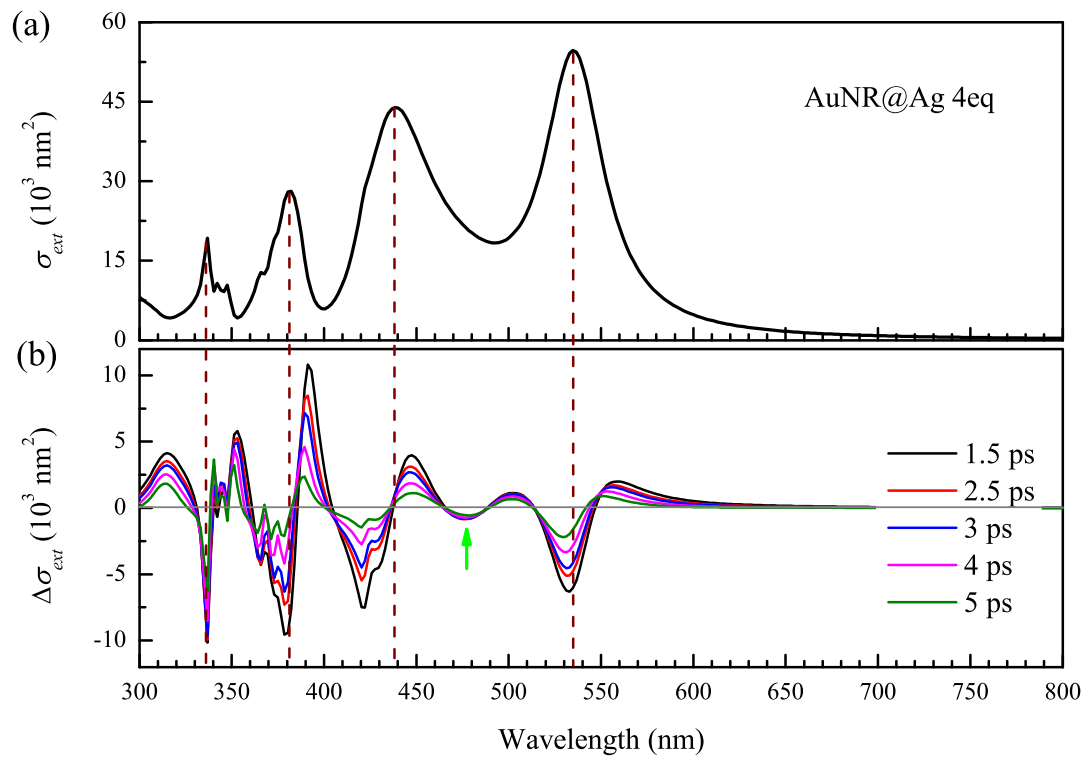


Figure 3.22 – Same as Fig. 3.19 but for AuNR@Ag 4eq. The green arrow in (b) indicates the fifth bleaching peak associated with the very weak T_0 mode.

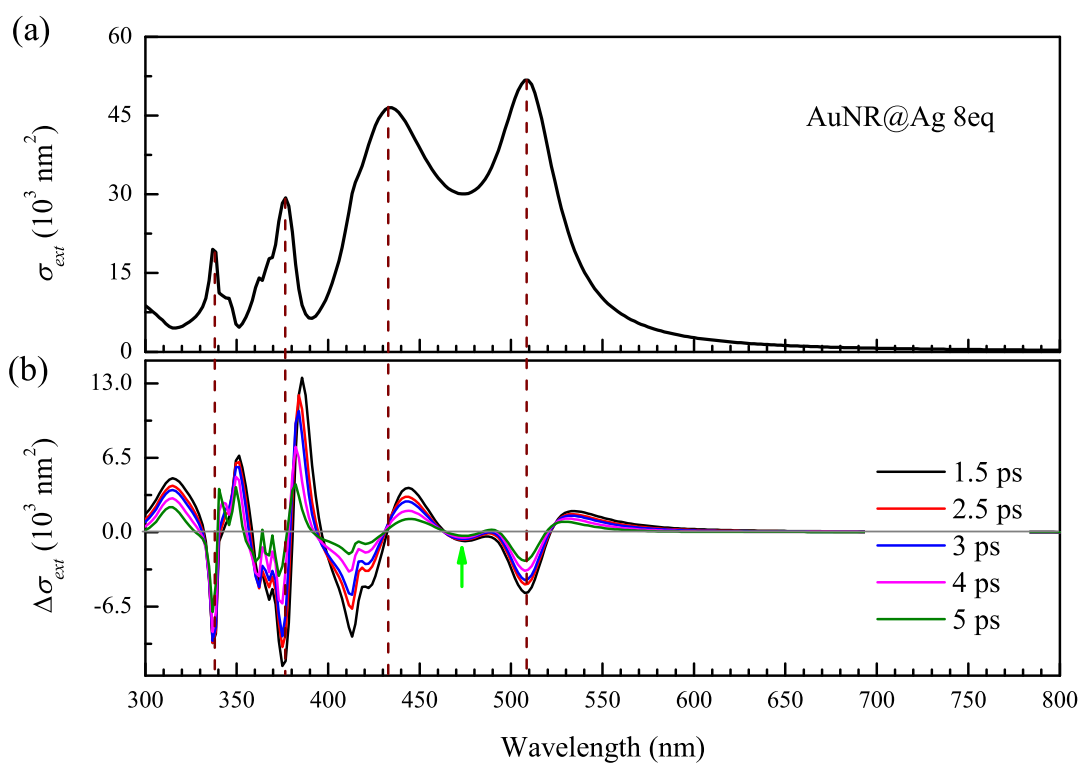


Figure 3.23 – Same as Fig. 3.22 but for AuNR@Ag 8eq.

3.5 Discussion

Let us break down the main contributors to the observed spectra of the AuNR@Ag samples both in the stationary and transient regimes. In particular, the relative influences of light scattering and absorption are examined. We focus on the two extreme samples: the thin Ag shell NP, AuNR@Ag 0.8eq, and the thick Ag shell NP, AuNR@Ag 8eq.

Figure 3.24 presents the extinction, absorption and scattering cross-sections of these two samples in the stationary regime. The contribution of scattering to the extinction spectrum of the AuNR@Ag 0.8eq sample is almost negligible [see the wine color curves in Fig. 3.24(a)]. For the thick Ag shell, both effects (scattering and absorption) play equitable roles [see the wine and olive curves in Fig. 3.24(b)]. Absorption dominates in the transverse polarization (TrPol) while scattering dominates in the longitudinal polarization (LgPol). It is known that the former pronounces in NPs of small size while the latter overtakes in the big ones. Thus, since the AuNR@Ag samples that are in consideration here are of cuboid shape with bigger longitudinal dimensions ($AR > 1$), dominance of the scattering effect over the absorption in this dimension is not surprising. They show independent dominance for the different light polarization directions but contribute equally to the general spectral profile of the extinction cross-section of the AuNR@Ag NPs. This leads to the choice of extinction cross-section over either of them to theoretically fit the experimental data (Fig. 3.16).

Though they are weak and a few in number for the thin Ag shell NP [Fig. 3.24(c)], the higher order modes are also present (at high photon energy) in the LgPol mode for both the thin and thick Ag shell NPs [see the dash-dotted lines in Figs. 3.24(c) and (d)]. They are more resonant in the LgPol for the large Ag shell thickness sample [Fig. 3.24(d)] than for the thin Ag shell. This could be due to the high abundance of the higher order multimodes in the thick Ag shell NP compared to the thin Ag shell one.

Let us now switch to the ultrafast transient optical response of the samples, as modeled by our approach described earlier. Figures 3.25 and 3.26 exhibit the pump-induced variation of the extinction, absorption and scattering cross-sections at a delay time $t = 2.5$ ps. Consistent with what we have discussed above regarding the NP size effect in the formation of the spectra in the stationary regime, the main contributor to the transient spectral signature of the thin Ag shell NP comes from the absorption process [compare the curves in Fig. 3.25(d)]. Indeed, the overall size of the AuNR@Ag 0.8eq NP is smaller than the one of the other bimetallic NPs, and therefore the contribution of scattering to the global transient extinction is small. In addition, the own optical response of the Ag shell in the spectral zone of the LgSPR is negligible. The T_0 mode bleaching peak of the AuNR@Ag 0.8eq NP is very close to that of its L_0 mode and its oscillator strength has not been reduced much compared to the bleaching peak of the TrSPR of the bare AuNR [Fig. 3.19(b)]. We can notice also the blue shift induced by the coupling of the optical response of the AuNR core with that of the thin Ag shell.

The role of absorption in dictating the LgPol mode fades and scattering takes over (see Fig. 3.26) as the Ag shell thickness increases [compare the red and blue lines in Fig. 3.26(d)]. However, the TrPol component of the transient absorption [the violet curve in Fig. 3.26(b)] plays a crucial role in the formation of the 5th bleaching peak identified in the transient spectral signature of the 2eq to 8eq NPs [see the green arrows in Figs. 3.21(b), 3.22(b) and 3.23(b)]. This bleaching peak

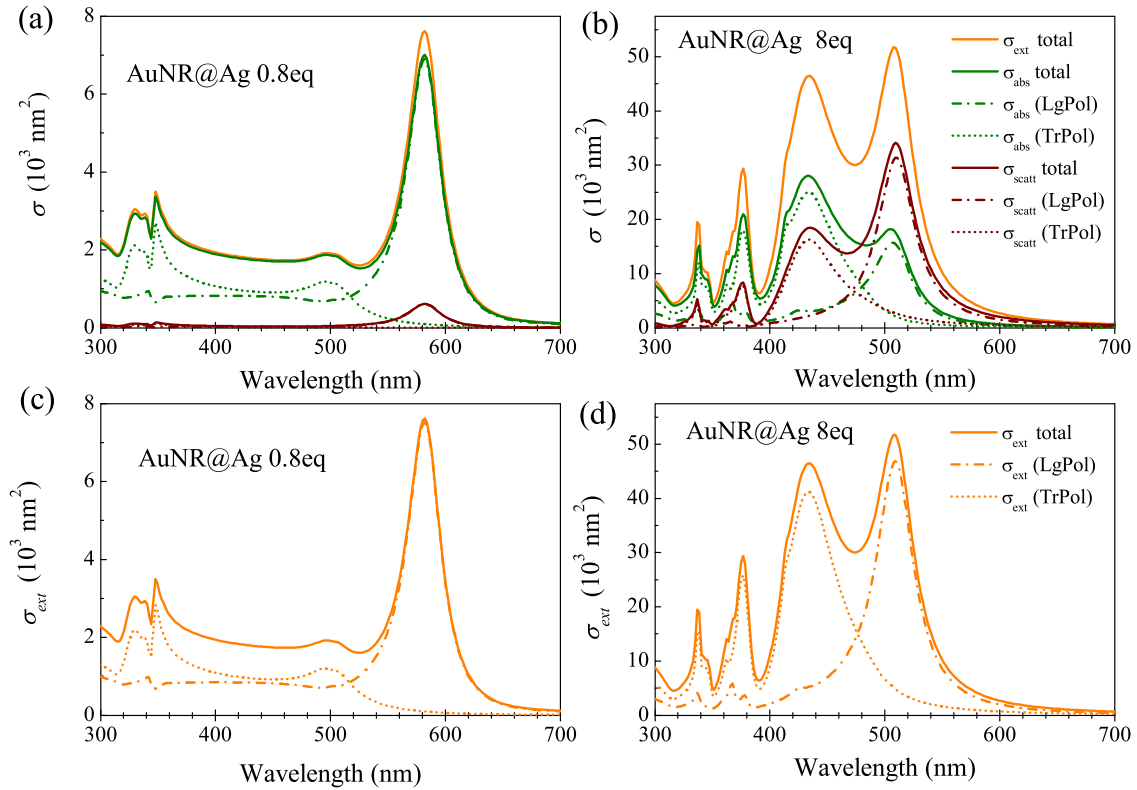


Figure 3.24 – Break down of the calculated extinction cross-section of the AuNR@Ag NPs into its contributing components for the two extreme samples AuNR@Ag 0.8eq (thin Ag shell) and AuNR@Ag 8eq (thick Ag shell). The top panels show the effects of scattering and absorption cross-sections for (a) AuNR@Ag 0.8eq and (b) AuNR@Ag 8eq. The orange colored full lines are the total extinction cross-section curves while the olive and wine colored full lines represent the absorption and scattering cross-sections, respectively. The longitudinal, LgPol (dash-dotted curve), and transverse, TrPol (dotted curve), polarization excitation contributions to the absorption (olive color) and the scattering (wine color) cross-sections are also shown in the top panels. The bottom two panels depict the overall polarization dependent contributions to the total extinction cross-section (c) for AuNR@Ag 0.8eq and (d) for AuNR@Ag 8eq.

is formed in between the bleaching peaks of the L_0 and T_1 modes which have both been detected experimentally in the stationary regime (see Fig. 3.4) and reproduced theoretically [Fig. 3.16(d)]. This, together with the transverse absorption origin of the transient signal, means that the TrSPR of the AuNR core is responsible for its formation but is hidden in the stationary regime spectra because of the large influence of Ag in this spectral zone. As in the stationary regime analysis above, both scattering and absorption cross-sections contribute (almost equally) for the formation of the overall transient spectral signature of the extinction cross-section. Absorption is mainly responsible for the features in the spectral range of the TrSPR modes while scattering is dominant in the LgSPR range [compare the curves in Fig. 3.26(d)]. In addition, both contributions compete around the L_0 mode (opposite signs) at this delay time, whereas they cumulate in the range of the transverse modes (at higher photon energy).

This leads us to argue that the mode appearing adjacent to the L_0 peak (in its blue wing) in Fig. 3.4 for the thin Ag-shell samples (the one labeled as T_0 for AuNR@Ag 0.8eq and AuNR@Ag

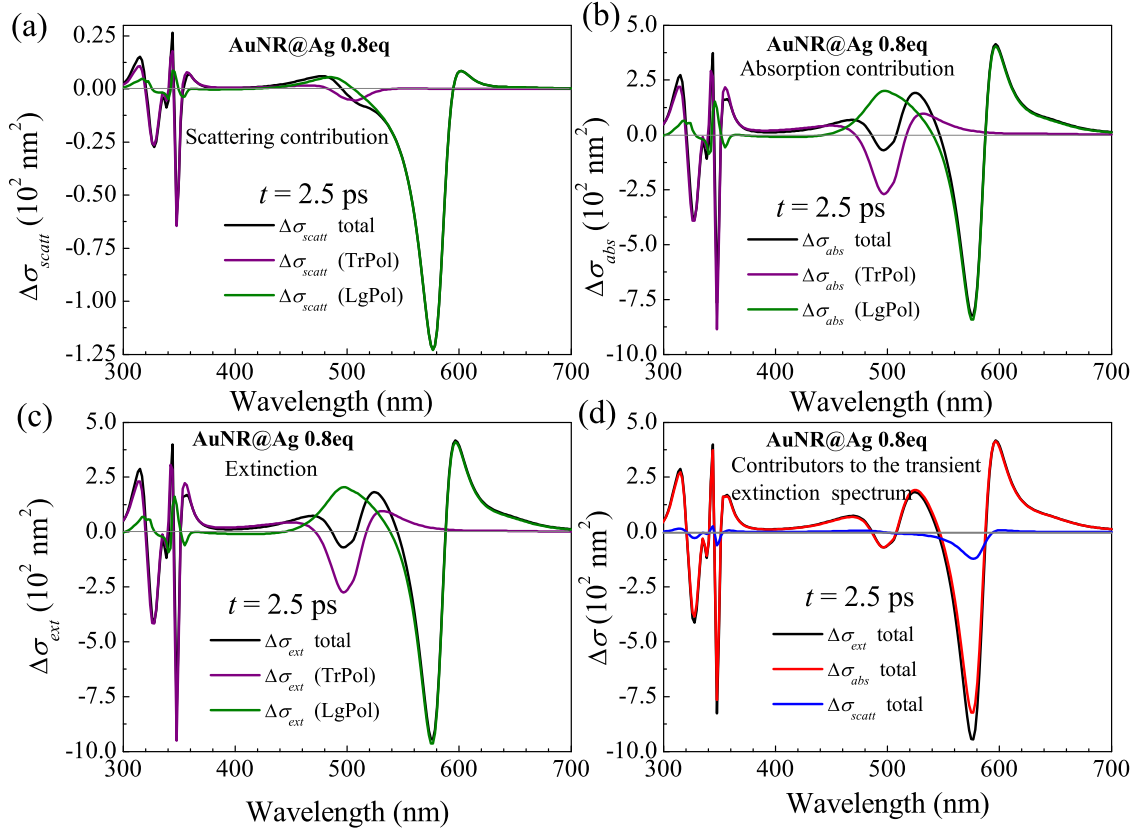


Figure 3.25 – Contributors to the transient extinction cross-section of the AuNR@Ag 0.8eq (thin Ag-shell) sample at 2.5 ps delay. The scattering [the black line in (a)] and absorption [the black line in (b)] cross-section contributions to the transient extinction [the black line in (c)] spectral signature are also shown. The purple and olive colored lines in (a), (b) and (c) correspond to the transverse- (TrPol) and longitudinal-polarization (LgPol) excitation components of the corresponding optical properties. The blue and red colored lines in panel (d) are the scattering and absorption contributors to the total extinction (black line).

2eq in Table 3.2) is actually the TrSPR mode of the AuNR evolving as the Ag shell grows. This means that the T_0 mode can still be observed in the stationary regime in the early stage of the overgrowth. The blue arrow in Fig. 3.4 indicates the progressive blue shift of the T_0 resonance mode as the Ag shell thickness increases. Meanwhile, its relative oscillating strength decreases due to (i) the blue-shift, which reinforces the coupling of the TrSPR with interband transitions of Au (known to quench the LSPR), (ii) the increasing relative weight of the other TrSPR modes, resulting from the coupling of the two metals, and (iii) the increasing wave energy absorption by the Ag shell. The T_0 mode still appears as a fifth dominant resonance for the AuNR@Ag 2eq sample, as a shoulder in the red spectral part of its T_1 mode. It no more has the strength to stand against the influence of other modes in the high Ag thickness samples, AuNR@Ag 4eq and 8eq, and therefore it contributes just to the broadening of their T_1 mode, resulting in the sloppy nature of the peak in its red spectral part (see the T_1 mode of the AuNR@Ag 4eq and 8eq samples in Fig. 3.4).

So, the T_0 mode, which was shielded by the influence of the Ag shell thickness in the stationary regime, has forced itself into appearance in the transient regime [57]. As stated in §3.3.2.1, this

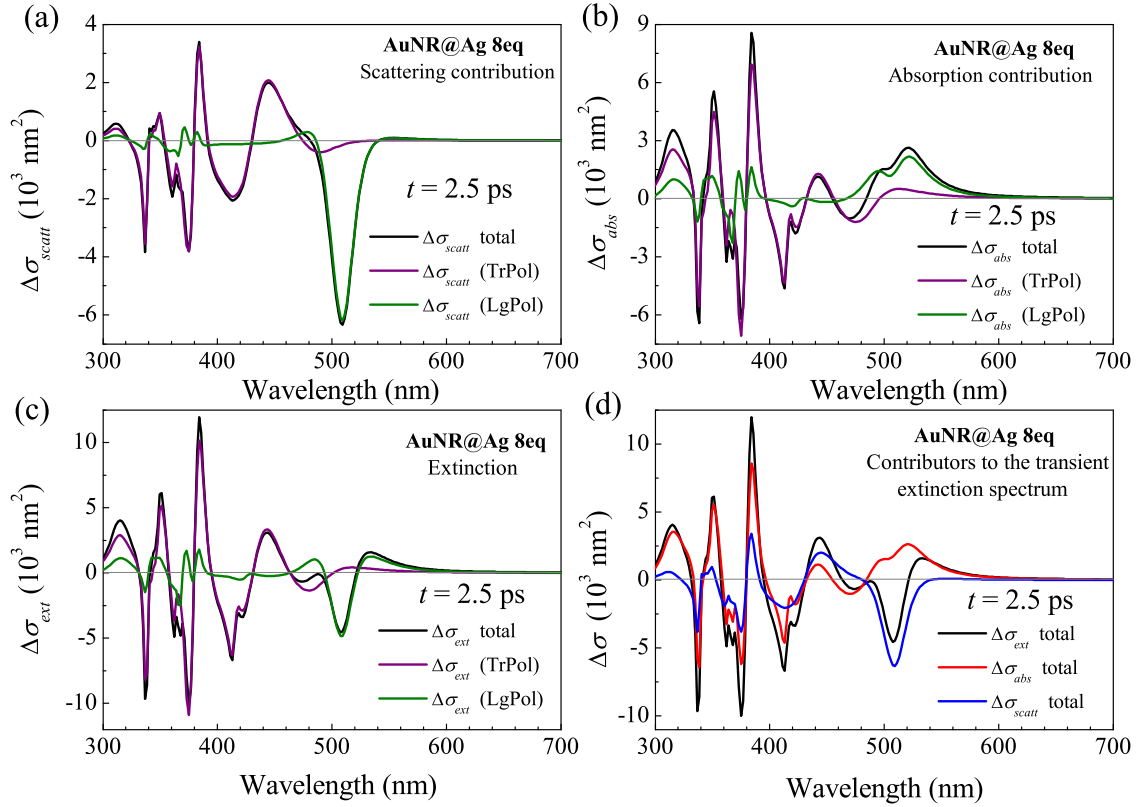


Figure 3.26 – Same as Fig. 3.25 but for AuNR@Ag 8eq (thick Ag shell).

highlights the fact that the influence of small spectral variations of the dielectric function cannot be readily observed in the stationary regime but their influence can be amplified in the transient optical response. The latter can then be exploited as a sensitive mean to reveal resonance modes, despite its complex spectral signature.

Let us now discuss the physical origin of what we have observed in the calculated near field topography of the AuNR@Ag 8eq sample (Fig. 3.18). For this, the real and imaginary parts of the dielectric function of Au and Ag are reported in Fig. 3.27. The phenomenon happening at the Au/Ag interface for the transverse excitation modes has already been analyzed in the work of Moritz Tebbe *et al.* [7]. There exists a significant difference in damping, ε_2 [Fig. 3.27(a)], and polarizability, ε_1 [Fig. 3.27(b)], of Au and Ag where Au dominates in both cases, everywhere above 350 nm wavelength. The transverse modes form in this spectral region where the interband transitions of Au and intraband transitions of Ag overlap [~ 326 nm - 515 nm] as shown in Fig. 3.27(a). This allows the Au core to have a retarded plasmonic oscillation compared to the Ag shell [7], leading to the creation of opposite interface charges (mirror charges) as can be seen on Fig. 3.5(a) reported from Ref. [7]. The Ag shell acts as an antenna transmitting its electromagnetic field to the Au core [see Fig. 3.5(a)]. Hence, the transverse modes T_1 to T_3 [427 nm, 378 nm and 341 nm in Figs. 3.18(b), (c) and (d), respectively] exhibit opposite charges at the outer and inner NP interfaces due to the above-mentioned reason. These modes then correspond to multipoles [that are clearly identified in Fig. 3.27(a)]. Due to the NP edge and corner rounding, they can also be excited by LgPol-state light, as revealed by Fig. 3.24. Generally, the dielectric function of Au fulfills the non-radiative (absorption) condition [175,176], i.e, the real part of the Au dielectric function is negative, and has a smaller absolute value than the dielectric function of the

environment (water in our case, $\epsilon_w = 1.77$). With increasing photon energy, especially above the interband transition threshold, it even falls below the non-radiative condition. Hence, the induced mirror charges get stronger at higher photon energies [7]. This is the reason for the increase in brightness of the field at the inner interface for the lower wavelengths as revealed in Fig. 3.18. The longitudinal L_0 mode of the AuNR@Ag 8eq NP in Fig. 3.18(a) does not experience this effect since it lies far (to the red spectral region, Fig. 3.4) from the T modes. It rather exhibits the same charge distribution (in-phase) at the Au/Ag interface and at the outer NP surface [Fig. 3.5(a)], which maintains it as a dipolar mode.

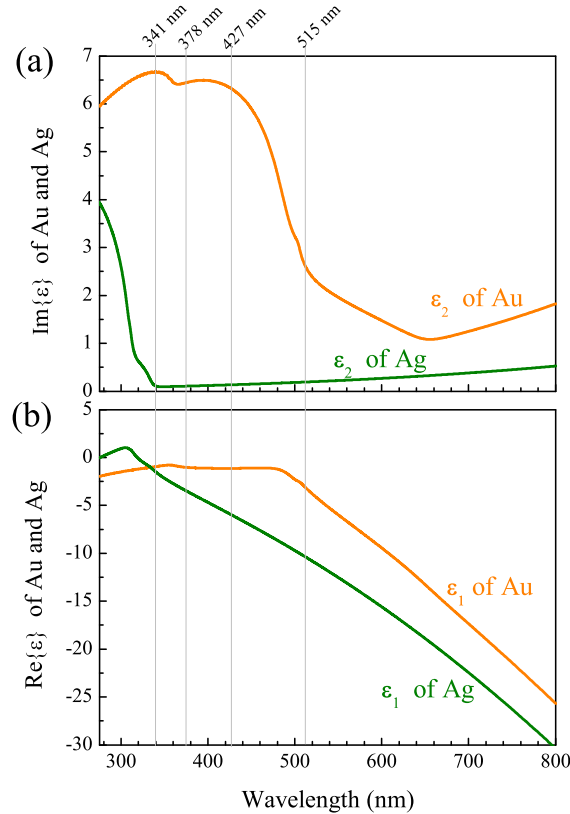


Figure 3.27 – (a) Imaginary and (b) real parts of the complex dielectric functions of Au and Ag plotted together. The vertical gray lines indicate the spectral positions of the four dominant resonances as modeled for the AuNR@Ag 8eq sample.

3.6 Summary

AuNRs were synthesized by seed mediated process and an Ag shell was epitaxially grown on top of them. The synthesis allows for more Ag mass to be deposited along the sides of the AuNRs than on their tips leading to cuboid shaped AuNR@Ag NPs. The Ag-shell thickness dependent optical response of the samples has been studied both in the stationary and transient regimes. Multiple plasmonic resonance modes have been observed in the stationary regime extinction spectra of the samples which are highly dictated by the amount of Ag deposited on the AuNR core. The spectral positions of the two dipolar modes (T_0 and L_0) are strongly influenced by the Ag-shell deposition (they blue-shift as the Ag-shell thickness increases) due to the influence of the optical properties of Ag on its Au counterpart. A BEM-based modeling of the NP stationary response has indicated

that the scattering effect is negligible for the smaller Ag-shell thickness NPs but both absorption and scattering cross-sections contribute almost equally to the extinction spectra of the thicker Ag-shell NPs. In addition to the stationary regime spectra of all the NPs, the near-field map inside and around the AuNR@Ag 8eq (the thick Ag-shell sample) has also been calculated using the BEM. The near-field maps taken at the successively increasing photon energies of the TrSPR modes show a bright region along the Au/Ag boundary the intensity of which increases. Mirror charges are created at the Au/Ag interface when the interband transitions of Au and intraband transitions of Ag overlap in the UV. The dominant absorptive nature of Au over Ag in this spectral zone leads to the transmission of the electromagnetic field from Ag to the Au core hence creating the mirror charges at the interface [7].

Transient regime calculations based on the 3TM have been performed for the further understanding of the experimental ultrafast transient signatures. A single homogeneous fictitious NP was used to represent bimetallic samples in the theoretical modeling of the transient response thanks to the similarity of the thermal properties of Au and Ag, and the epitaxial growth of Ag on Au, that allows to disregard the thermal resistance at the Au/Ag interface [173]. The experimental transient spectral signatures have been well reproduced theoretically except for the spikes appearing in the spectral zone of higher photon energy emanating from the influence of the multi-modes that reside in this zone [163]. The number of bleaching peaks that can be observed in the transient optical signature of plasmonic nanoparticles are usually equal to the number of resonance modes that can be observed in their stationary regime spectra [40]. However, an additional 5th bleaching peak was observed in the transient optical signatures of the thick Ag-shell AuNR@Ag samples. The theoretical modeling of the transient optical signatures of the NPs indicates that the transverse polarization component of the transient absorption is the main contributor for the formation of this fifth bleaching peak. It appears between the bleaching peaks of the L_0 and T_1 modes. Furthermore, its oscillator strength decreases with the increase of the Ag-shell thickness which becomes a clear indication that this signature is not related to Ag. Thus, these observations help us to conclude that the formation of this bleaching peak can be ascribed to a pure dipolar T_0 mode which evolves from the TrSPR dipolar mode of the bare AuNP with increasing Ag coating. It becomes hidden in the stationary regime spectra but is revealed by the ultrafast differential transient signal.

In this work, we have focused on the study of the optical extinction variation, mainly related to the electron dynamics. Beyond, these hybrid samples can be interestingly studied for their acoustic vibrations (phonon dynamics). They present vibration modes that are sensitive to the Ag shell mass that is being deposited on the Au core and hence can be used as nano-balances. Furthermore, they can be assembled into supercrystals [53] then allowing to modify or improve the optical properties through coupling, as highly spatially-organized metal nanorods are attractive for their strong, polarization-dependent plasmon properties.

Chapter 4

Ultrafast transient near field variation in and around a gold nanoparticle: investigation by FDTD

Contents

4.1 Introduction	81
4.2 Complex-conjugate pole-residue pair based (CCPRP) FDTD	83
4.2.1 Principle of the method	83
4.2.2 Validation of the end-to-end accuracy of the method	84
4.3 Modeling the ultrafast transient near-field	87
4.3.1 Transient dielectric function of the AuNP determined by the 3TM	87
4.3.2 Transient near field variation in and around the AuNP	89
4.4 Summary	95

4.1 Introduction

As we have seen in the first chapter, in the stationary regime there exist both numerical and analytic methods for calculating the near field enhancement inside and outside a plasmonic NP. This has allowed for the thorough study of the applications of the plasmonic near-field enhancement in the stationary regime. Finite Difference Time Domain (FDTD) method has been one of the mostly chosen numerical approaches for it provides the response of a system over a wide spectral range in a single simulation. Besides, many of the developments related to the ultrafast optical response of noble metal NPs, such as electron photoemission [47,48], photoluminescence [49], plasma generation around nanoparticle [50], nano-cavitation [51] or production of reactive oxygen species in aqueous media [52] depend on the near field enhancement in and/or around the nanostructures, which itself undergoes a transient variation. However, in most studies, the stationary near field is considered only in the analysis of these phenomena. Beyond, the ultrafast modulation of the

near field enhancement [68, 69] may be exploited to develop time resolved sensors, based on the same considerations as for the stationary plasmon enhanced fluorescence or SERS. The transient variation of the metal dielectric function following the ultrashort pulse absorption can be calculated via the two- or three-temperature model (see chapter 1) or a non-thermal approach [50]. At each time step of the calculation, it could be possible to determine the near field characteristics by using FDTD, provided the fine variations of the dielectric function are accurately accounted for in the latter. However, the FDTD simulation tools that are available by now are meant to simulate the optical response of dispersive materials by using phenomenological models based on fitting the permittivity data as the sum of multiple Debye, Drude and/or Lorentz pole pairs [177–180]. Unfortunately, catching the small variations of the plasmonic material optical properties along their dynamics cannot be achieved by these conventional phenomenological models with reasonable computational time. This may explain the absence, in the literature, of studies assessing numerically the ultrafast transient near field topography.

Modeling a transient dielectric function requires a very precise approach where some perturbative components should be added to the (non-perturbative) stationary description and the time dependent dielectric function variation has to remain stable along the whole dynamics, that is, has to present a sufficient regularity. This can be easily achieved by using the complex-conjugate pole-residue pair (CCPRP) [181] approach for fitting the dielectric function as has been proposed by Han *et al.* [181]. The dielectric function of arbitrary dispersive media is modeled by representing it as a sum of rational fractions. This method doesn't only lowers the number of pole pairs that are to be used in a simulation (and thus reduces the CPU time consumption and memory space) as compared to the phenomenological models evoked above, it also provides stable and smooth curves of the modeled data. We have implemented this approach for the relative dielectric function of gold, $\varepsilon_R(\omega)$, where ω is the wave angular frequency. A vector fitting technique [182] is employed to decompose the rational fraction into poles and residues which are then used in the FDTD simulation tool.

In this chapter, we will use the CCPRP based FDTD method that is customized by F. Mayran de Chamisso (a former student in the group) to account for the small variations of the dielectric function of plasmonic NPs in the transient regime. We first provide a simple method for checking the accuracy of the FDTD tool. The effective dielectric function "seen" by the FDTD algorithm, the value of which accounts for all the numerical errors due to the cumulated approximations, floating-point inaccuracies and effect of stray reflections at virtual sample boundaries, and after running for several 10k to 100k time steps, is recovered by Fast Fourier Transform and compared with the experimental data of the dielectric function of bulk gold. The resulting modulus error remains lower than 2.2% over the entire visible range.

This robust FDTD approach is then applied to calculate the ultrafast variation of the near field intensity enhancement in and around a spherical gold nanoparticle (AuNP) in air following the modulation of the metal electromagnetic properties induced by the absorption of a laser pulse. For this, the three-temperature model (3TM, see Chapter 1) has been integrated with the CCPRP based FDTD method. While the choice of the spherical shape does not fully illustrate the efficiency of FDTD, which potentially enables us to adapt to much more complex geometries, it is driven by the possibility of comparing our results with the ones provided by the Mie theory in order to validate our method. The stationary spectrum of $\varepsilon_R(\omega)$ is first fitted with a set of poles in

the CCPRP model. Then, the transient modulation of $\varepsilon_R(\omega)$ is calculated at different delay time steps t_D after pulse absorption by using the 3TM. This data is fitted for each delay time step with another set of poles and the field topography in the virtual sample is determined with the FDTD method by considering the total dielectric function at t_D . Then we consider the next delay time step, with a different dielectric function, and repeat the FDTD calculation. This approach is therefore limited to a "slow" variation of the dielectric function with respect to the time scale of the field oscillation (a few femtoseconds in the visible range). This perturbative modelling, consisting in adding some perturbative components to the non-perturbed stationary $\varepsilon_R(\omega)$, will be proven to be particularly stable over all time steps, as revealed by the smoothness of the curves obtained along time. By benefiting from a parallel FDTD simulator with GPU support, implementation of the CCPRP method and low-level C++ language optimization, we will show that this FDTD method is suited for modeling the ultrafast transient optical response of plasmonic nanostructures.

The spatial, temporal and spectral dependence of the field around the AuNP will be analyzed. We will show that the different contributions to the near field, propagating or not to the far field, exhibit different dynamics.

4.2 Complex-conjugate pole-residue pair based (CCPRP) FDTD

4.2.1 Principle of the method

We focus on a homogeneous, linear and isotropic non-magnetic material with arbitrary relative dielectric function, $\varepsilon_R = \varepsilon'_R + j\varepsilon''_R$ (where $j^2 = -1$) which can be written in terms of array, $[\omega_i, \varepsilon'_R(\omega_i), \varepsilon''_R(\omega_i)]$ with the angular frequency, ω_i , being sorted in ascending or descending order and $\varepsilon''_R(\omega_i) > 0$.

Han *et al.* [181] have demonstrated that for the same computing cost the CCPRP based FDTD method is more precise than phenomenological model based FDTD methods, like in the open source FDTD software MEEP [180] which uses a sum of Lorentzians. This is due to the difference that exists in the re-partitioning of the available degrees of freedom. Methods based on second order polynomials generally require more intermediate quantities to be stored during the FDTD computation than the methods which are based on first order polynomials. For example, the FDTD update equation provided in Ref. [183] requires the additional storage of the field \mathbf{E}^{n-1} computed at the preceding time step t_{n-1} (where t_n is the current FDTD time step of computation) which is not the case with Han's approach. We have then followed a method similar to the latter.

In the CCPRP approach, the relative permittivity, $\varepsilon_R(\omega)$, of an arbitrary dispersive material can be written as follows [184–186]:

$$\varepsilon_R(\omega) = \varepsilon_\infty + \sum_p^P \left(\frac{c_p}{j\omega - a_p} + \frac{c_p^*}{j\omega - a_p^*} \right) \quad (4.1)$$

where ε_∞ is the high-frequency limit of the function $\varepsilon_R(\omega)$. It is real since absorption tends to zero at high frequencies. Here, both a_p and c_p are complex numbers. The detailed procedure

for establishing the CCPRP based FDTD update equation has already been well described in Refs. [184–186].

To determine the coefficients ε_∞ , a_p and c_p in Eq. 4.1, we have used a vector fitting approach [182,185,187–189] which is based on converting the values of a measured (or a calculated) frequency-dependent dielectric function, $\varepsilon_M(\omega)$, into a sum of complex conjugate pole residues by iteratively refining the polynomial coefficients. In our case, 4 poles were enough to satisfactorily fit the experimental dielectric function data of bulk gold [85] using this technique as illustrated in Fig. 4.1(b). Gustavsen *et al.* in [182,188,189] have used the same approach in signal processing for the decomposition of the coefficients into CCPRPs. More examples of this approach can be found in the work of Han [184].

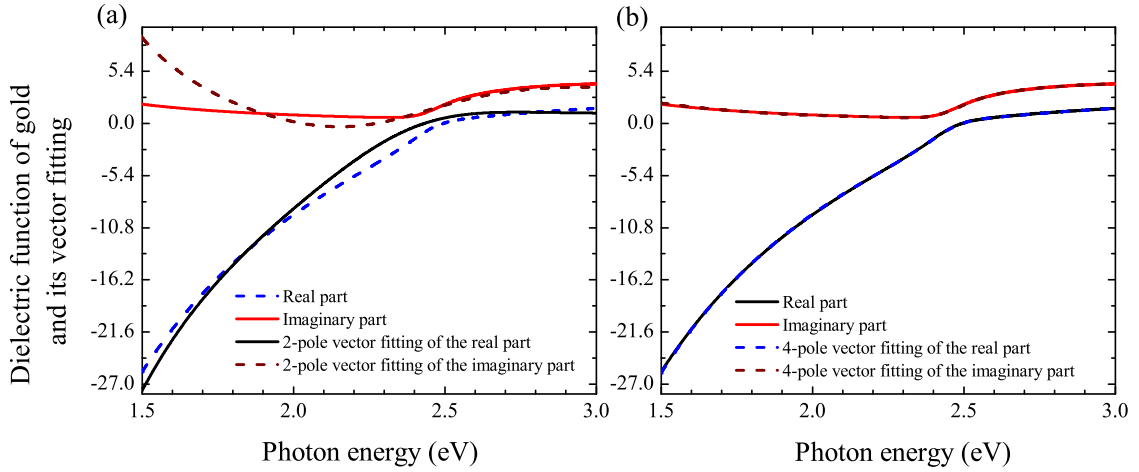


Figure 4.1 – Dielectric function of gold as a function of photon energy. Solid lines: experimental values obtained from [85]; dashed lines: curves fitted with the CCPRP method with (a) 2 and (b) 4 poles, obtained by the vector fitting.

Thus, by choosing only a spectral window $[\omega_1, \omega_2]$ within which we intend to perform the pole-residue decomposition, it is possible to model ε_R precisely. The poles obtained can be then injected into the constructed FDTD update equation for simulation [185,190].

4.2.2 Validation of the end-to-end accuracy of the method

Let us check the end-to-end accuracy of the whole FDTD tool. In theory, the dielectric function “seen” by the FDTD simulation must equal the input ε_R data, that is, the input parameters if the whole FDTD process is considered. However, in practice the one seen by the simulation contains all the numerical errors arising from accumulated approximations (floating-point inaccuracies, reflections at the boundaries and imperfect representation of the materials used to absorb residual waves). Our test method aims at showing that despite these numerical distortions along the whole computing process, the field propagation simulated corresponds to a medium having electromagnetic properties closely similar to the input ones.

Our checking method is based on the simulation flow chart depicted in Fig. 2(a) which is implemented for a layer of gold the dielectric function of which is taken as the one for bulk gold [85]. Let us note that this choice of the initial input dielectric function of the material is left

to the user. Here we have chosen the values of Ref. [186] as they are often used in the literature, but other values could have been selected either. This dielectric function data, ε_R^{meas} , is first modeled as a sum of complex-conjugate poles as shown in Fig. 1(b) [4 poles used for fitting $\varepsilon_R^{meas}(\omega)$]. Then, a simple FDTD simulation is run according to the layout shown in Fig. 2(b). From the field $\mathbf{E}(t)$ collected, the dielectric function seen by the wave during simulation, ε_R^{sim} , is recovered and compared to ε_R^{meas} . Let us now detail this procedure.

The gold layer is wide enough (140 px = 1400 nm in the x -direction) for any electromagnetic wave in the photon energy range considered to be almost completely absorbed when reaching the layer end. This hypothesis allows us to neglect the back-propagating wave due to reflection from the end side of the gold layer [Fig. 2(b)]. Perfectly Matched Layers (PMLs) [191,192] of thickness 160 nm are used in the $+x$ and $-x$ directions of the gold layer to absorb the reflected waves from the left gold-air interface and the fake fields which can possibly be generated because of some imprecise floating-point representations. Periodic boundary conditions are considered in the y and z directions. Field injection is done according to Ref. [193] with a broadband (1.5 to 3.5 eV) wave propagating along the x axis, with the $\mathbf{E}(t)$ polarization along the y axis and $\mathbf{H}(t)$ along the z axis (i.e., a TE-polarized wave). The injected field is formulated as the Fourier transform of a Gaussian around 3.5 eV. The field $\mathbf{E}(t_i)$ is retrieved at each simulation time step t_i for each of the first 20 pixels (px) along the x direction, effectively measuring the field propagated 200 nm into the gold layer. Then the Fourier transform of the field is computed to obtain $\mathbf{E}(\omega)$ from which the refractive index n ($n^2 = \varepsilon_R^{sim}$) seen by the wave after propagating 20 px into the gold layer is deduced as follows.

Considering the field propagation in the x direction [see Fig. 4.2(b)], at the material interface, the tangential component of the electric field \mathbf{E} as well as the normal component of the electric displacement field \mathbf{D} are continuous. Since, $n^2 = \varepsilon_R$ with $\text{Im}[n] > 0$, considering that the interface is located at $x = 0$, we get the following equation for the complex electric field within the gold layer, \mathbf{E}_{Au} :

$$\mathbf{E}_{Au}(x, \omega) = E \mathbf{e}_y = \frac{2}{1 + n(\omega)} E_0 \exp\left(j \frac{n(\omega)\omega}{c} x\right) \mathbf{e}_y \quad (4.2)$$

where E , c and ω are the complex field amplitude of \mathbf{E}_{Au} , speed of light in vacuum and angular frequency of the incident field, respectively. For the incoming incident field propagating in air, \mathbf{E}_{air} , we can write

$$\mathbf{E}_{air}(x, \omega) = E_a \mathbf{e}_y = E_0 \exp\left(j \frac{\omega}{c} x\right) \mathbf{e}_y \quad (4.3)$$

where E_a is the complex amplitude of the incident field propagating in air. The modulus of the complex amplitude in the gold layer relative to its counterpart in air is then

$$\left| \frac{E}{E_a} \right| = \left| \frac{2}{1 + n(\omega)} \right| \exp\left(\frac{-\text{Im}[n(\omega)]\omega}{c} x\right) \mathbf{e}_y. \quad (4.4)$$

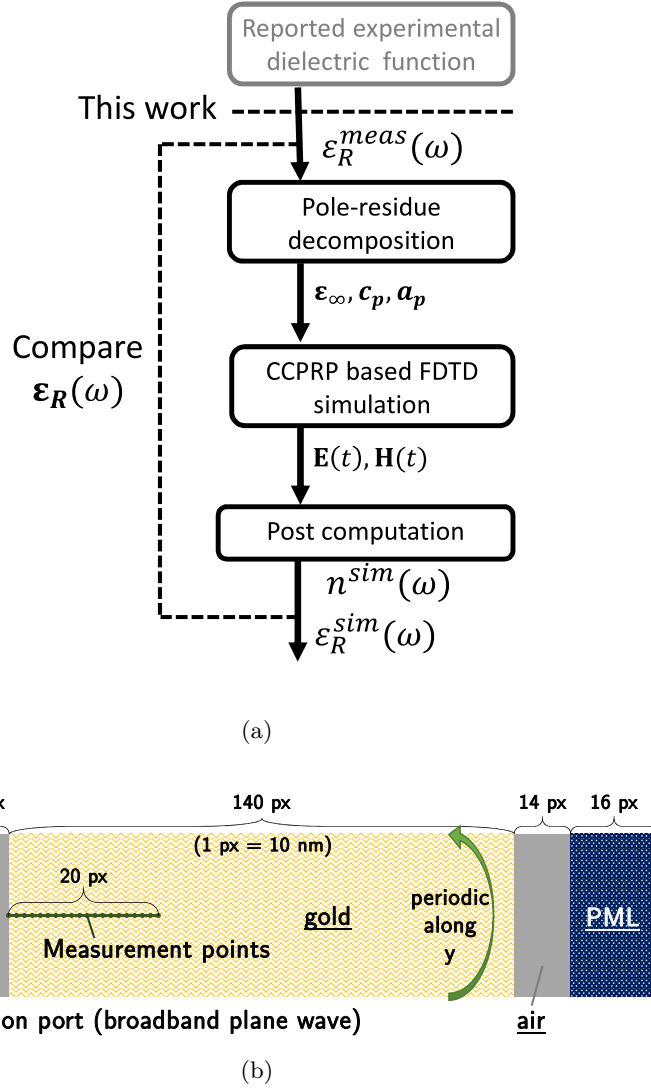


Figure 4.2 – The FDTD simulation used for checking the accuracy of the method on a thin gold layer:(a) flow chart of the modeling and (b) simulation layout. The dimensions used in the computational domain are represented as 1 px = 10 nm. PML: perfect matching layer.

The argument of the complex amplitude in the gold layer relative to its counterpart in air is

$$\arg\left(\frac{E}{E_a}\right) = \pi - \text{Arctan}\left[\frac{-\text{Im}[n(\omega)]}{1 + \text{Re}[n(\omega)]}\right] + \frac{\text{Re}[n(\omega) - 1]\omega}{c}x. \quad (4.5)$$

Eqs. 4.4 and 4.5 give us the optical response data that has been experienced by the electromagnetic wave while propagating through the gold layer. We can then extract the real and imaginary parts of the refractive index ($n^2 = \epsilon_R^{sim}$) from the slope of the argument (Eq. 4.5) and logarithm of the modulus (Eq. 4.4), respectively. Extraction of ϵ_R^{sim} is done by quadratically fitting lines to $\ln(|E/E_a|)$ and $\arg(E/E_a)$, which is more robust than simply measuring one single value of E at a given x and deducing n from it. Just like in Fig. 4.1 (b), the dielectric function theoretically “seen” by our FDTD approach ϵ_R^{sim} matches very well with the input one (corresponding to experimentally determined data ϵ_R^{meas}). The phase error as well as the absolute and relative errors

on the modulus of the simulated dielectric function are respectively displayed in Figs. 4.3(a), (b) and (c).

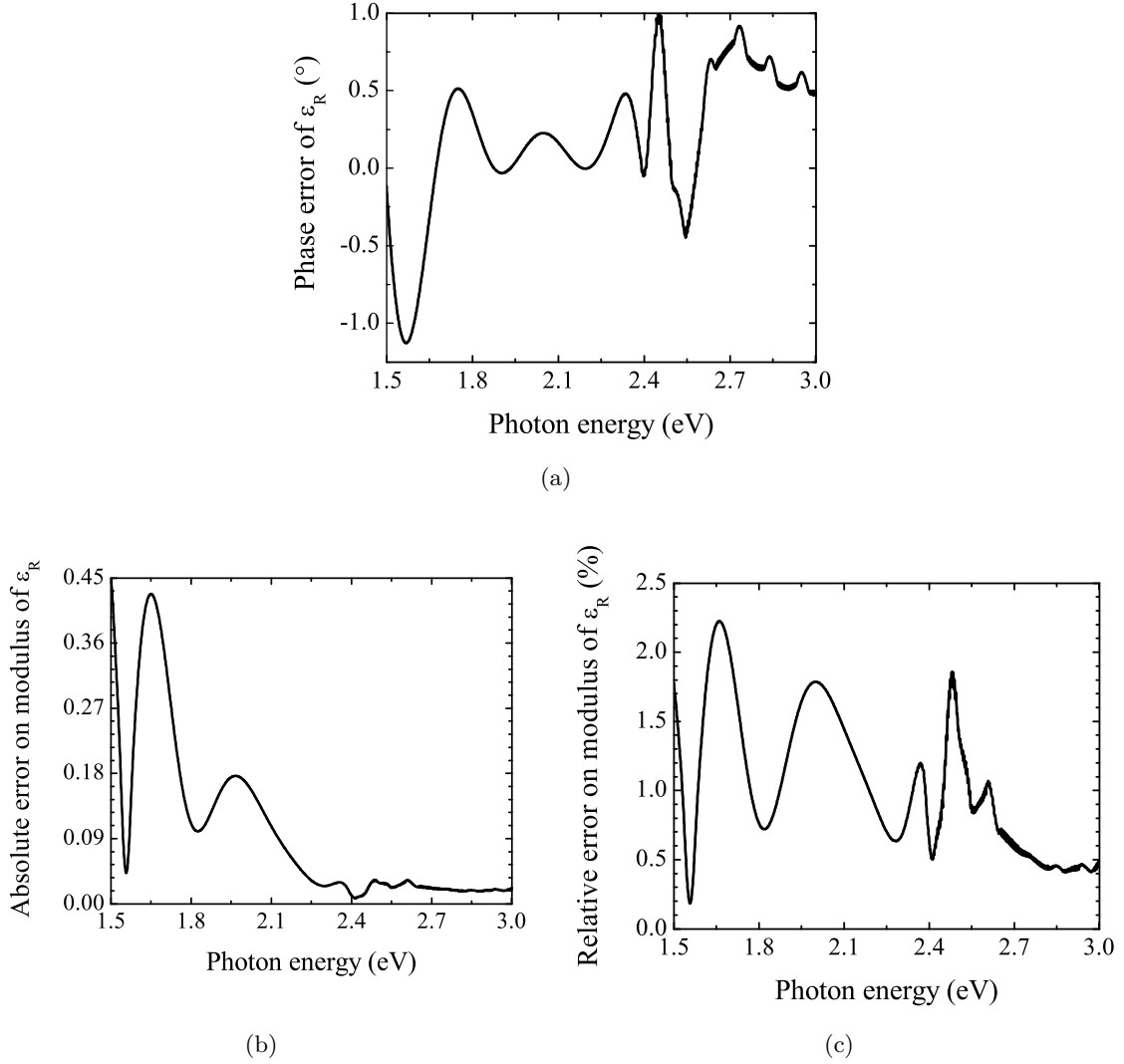


Figure 4.3 – Approximation errors between ϵ_R^{sim} and ϵ_R^{meas} : (a) the phase error, $arg(\epsilon_R^{sim}) - arg(\epsilon_R^{meas})$, (b) the absolute error on modulus, $\left| |\epsilon_R^{sim}| - |\epsilon_R^{meas}| \right|$ and (c) the relative error on modulus, $\left| \frac{|\epsilon_R^{sim}| - |\epsilon_R^{meas}|}{|\epsilon_R^{meas}|} \right|$.

The approximation errors show that the discrepancy is quite small. The modulus error remains lower than 2.2% over the entire visible range as shown in Fig. 3(c) while the phase difference remains within -1.1° and $+1.0^\circ$ [Fig. 4.3(a)]. Let us now use this powerful tool to investigate the ultrafast near-field response of an AuNP.

4.3 Modeling the ultrafast transient near-field

4.3.1 Transient dielectric function of the AuNP determined by the 3TM

The transient dielectric function of gold at each delay time t_D along and after light pulse absorption is determined by a method based on the 3TM. The data set obtained will enable us

later to determine the near field dynamics by using FDTD, as will be described in the next section. As has been precised in chapter 1, the 3TM is a prominent choice for the theoretical investigation of the ultrafast transient optical response of metal nanoparticles over “long” delays (t_D) after the absorption of an ultrashort laser pulse. The system we are considering here consists of a spherical AuNP of 20 nm diameter in air, illuminated by an ultrashort laser pulse with duration $\Delta t = 100$ fs and peak intensity $I_{00} = 5$ GW cm⁻². Following the pulse absorption, the respective temperatures of the electrons, metal lattice and host medium evolve, driven by energy exchanges which are described by the set of coupled differential equations 1.44 - 1.47 (Chapter 1). Knowing the source term (temporal profile of the instantaneous power absorbed from the light pulse) the time-dependent temperatures are calculated by numerically solving these 3TM equations. The electron gas temperature is then used to determine the evolution of the metal electron distribution after light pulse absorption. Finally, the spectrally- dependent transient variation of the complex dielectric function (Eq. 4.6), $\varepsilon(\omega, t_D)$, of the AuNP is computed. In this calculation, both the interband and intraband transition contributions to the dielectric function variations are accounted for (see Eq. 1.10 in Chapter 1):

$$\varepsilon(\omega, t_D) = \varepsilon_{st}^{ib}(\omega) + \Delta\varepsilon^{ib}(\omega, t_D) + \chi_{st}^D(\omega) + \Delta\chi^D(\omega, t_D) \quad (4.6)$$

where $\varepsilon_{st}^{ib}(\omega)$ and $\chi_{st}^D(\omega)$ are the interband and intraband (Drude susceptibility) parts of the stationary dielectric function of gold, respectively, while $\Delta\varepsilon^{ib}(\omega, t_D)$ and $\Delta\chi^D(\omega, t_D)$ are the respective transient variations of the interband and intraband contributions evaluated as described in Chapter 1 (§1.2.3). Details about the transient dielectric function modeling have been provided in previous papers [40, 41, 50]. The resulting relative variation of the transient dielectric function of the AuNP, $\Delta\varepsilon/\varepsilon = [\varepsilon(\omega, t_D) - \varepsilon_{st}(\omega)]/\varepsilon_{st}(\omega)$, where $\varepsilon_{st}(\omega)$ is the stationary total dielectric function, subsequent to the absorption of a laser pulse (524 nm wavelength) peaking at time $t_D = 0$ is reported on Fig. 4.4.

The overall behavior of $\Delta\varepsilon/\varepsilon$ is similar with the one reported in Ref. [72]. The imaginary part has an antisymmetric profile with negative and positive peaks in the red and blue spectral parts of the plasmon resonance, respectively [Fig. 4.4(b)]. The real part has a positive peak close to the resonance and is accompanied by two negative peaks in the blue and red wings of the resonance band [Fig. 4.4(d)]. The time-dependent dielectric function values of the AuNP obtained this way will now be used to simulate the corresponding ultrafast transient near field intensity.

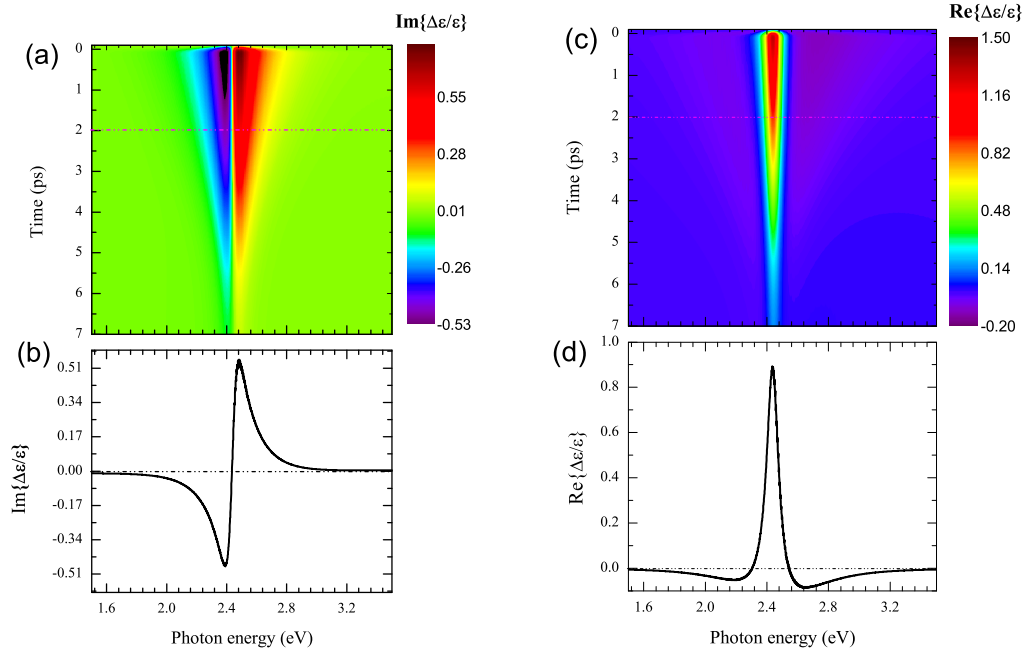


Figure 4.4 – (a) and (c): Optically induced transient relative change of the dielectric function of a 20 nm AuNP upon absorbing a 2.37 eV (524 nm) pump pulse (100 fs pulse duration, 5 GW cm^{-2} peak intensity). The vertical axis denotes the delay time, t_D , from -0.1 ps to 7 ps. (b) Spectral relative variation of the imaginary part of the dielectric function [taken along the dashed line in (a)]. In both the upper and the lower graphs, the horizontal axis denotes the photon energy ranging from 1.5 eV to 3.5 eV. (c) is the same as (a) while (d) is the same as (b) but for the real part of the transient dielectric function.

4.3.2 Transient near field variation in and around the AuNP

The modeling process, as schematized in Fig. 4.5(a): (1) begins with the calculation of the transient dielectric function at each delay time, t_D , following the procedure described above (§4.3.1) using the 3TM. Let us recall that t_D denotes the delay time separating the light pulse maximum and the further observation of the field properties. The transient (t_D dependent) dielectric function is plotted in Fig. 4.4. (2) Pole-residue decomposition (§4.2.2) is then carried out on the transient dielectric function. For this, the stationary regime dielectric function, $\epsilon_{st}^{ib}(\omega) + \chi_{st}^D(\omega)$, is first (vector) fitted. Then the transient contribution to the dielectric function, $\Delta\epsilon^{ib}(\omega, t_D) + \Delta\chi^D(\omega, t_D)$, is fitted separately at each t_D and added to the stationary component. In total, 8 poles are used at each t_D to model $\epsilon_R(\omega, t_D)$, distributed as 4 for the stationary regime modeling and 4 for the ultrafast part. This distribution of poles allows for a very fine modeling of the ultrafast variations while preserving a consistent stationary regime model [see Fig. 4.1(b)]. (3) Finally, the poles obtained for each t_D , resulting from the vector fitting, are then injected into a 3D-FDTD simulator from which the electric field $\mathbf{E}(t)$ is collected. The simulation gives the field inside and around the NP at each t_D . The overall detail on the 3D-FDTD simulation protocol as schematized in Fig. 4.5(b) is presented in the following paragraph.

The 3D-FDTD simulation setup embraces a 20 nm AuNP which is surrounded by air and a PML as shown in Fig. 4.5(b). An electromagnetic wave with Gaussian profile in the frequency domain propagates along the x -axis, with the \mathbf{E} polarization along the y -axis and \mathbf{H} along the z -axis. The same wave propagating in air (without AuNP) is used to normalize the field power

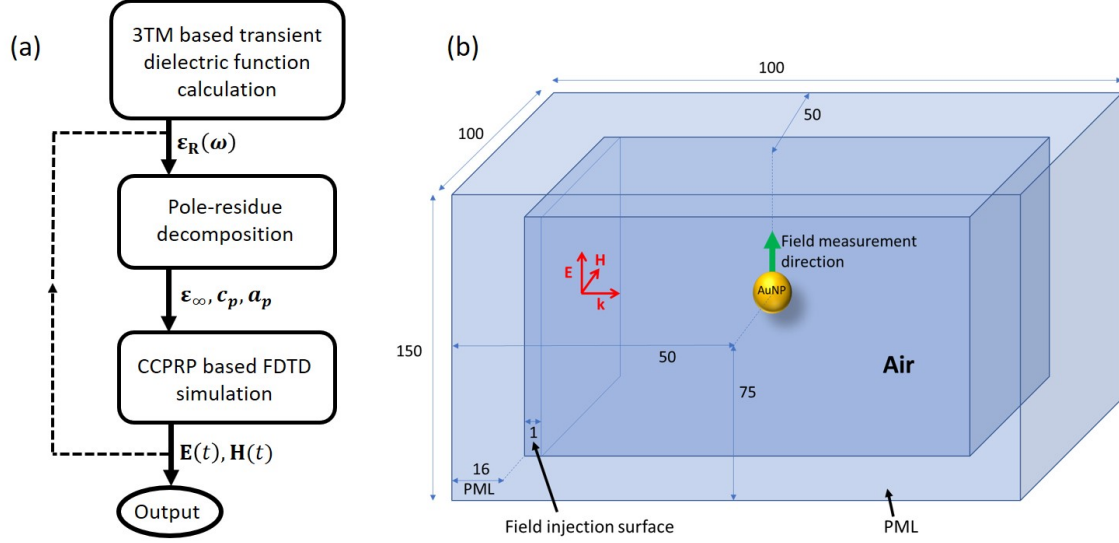


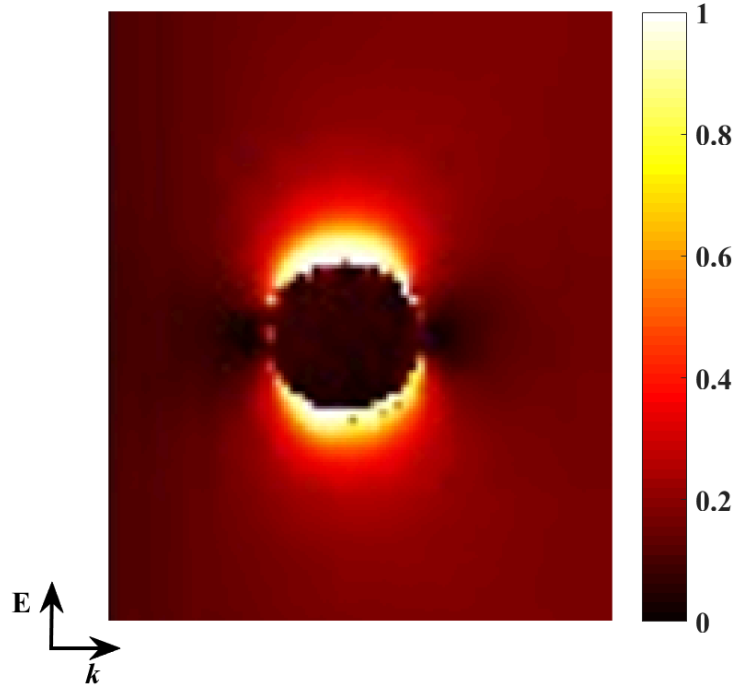
Figure 4.5 – (a) Sketch of the flow chart of the steps followed and (b) top view of the FDTD simulation layout to calculate the ultrafast variation of the near field enhancement around a 20 nm AuNP. The distances are given in pixels (1 px = 1 nm).

such that in the following $|\mathbf{E}|$ will denote the field enhancement (that is, the local field relative to the incoming field). The entire computational cell is made up of $100 \times 150 \times 100$ px where 1 px corresponds to 1 nm. The PML layer has a thickness of 16 px and the AuNP is represented with a diameter of 20 px while the remaining part of the computational domain is left to be air ($\epsilon_{air} = 1$). The field $\mathbf{E}(t)$ which is obtained by this way for both the stationary regime (before pump pulse absorption by the AuNP) and the transient one (along with and after pump pulse absorption) is then Fourier transformed to obtain the spectral components of the field, $\mathbf{E}(\omega, d, t_D)$, at a distance d away from the AuNP surface along the y -axis (field direction), which evolve with delay time. Note that t_D is not related to the time dependency of the FDTD simulation, t . Figure 4.6(a) is a time snapshot of a simulation with the same layout but replacing the wave source by a plane monochromatic wave at plasmon resonance. The figure displays the instantaneous electric field energy (normalized by the highest value) around the 20 nm AuNP in the stationary regime. In addition, the dependency of the field enhancement (at plasmon resonance) on the distance away from the nanoparticle [11] is depicted in Fig. 4.6(b). This result is all but surprising for a gold nanosphere the size of which is small against the wavelength of light (dipolar regime).

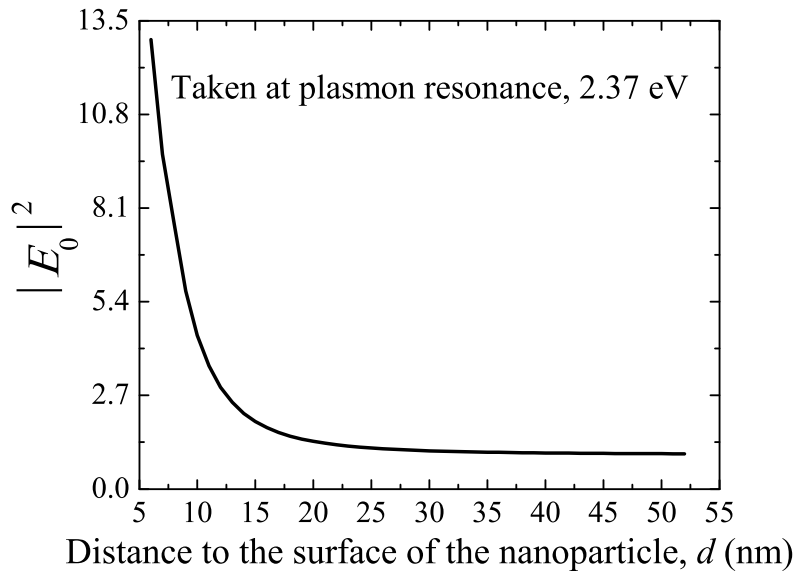
Let us move on to describing the transient optical response of the AuNP after absorbing the ultrashort laser pulse presented here through the rapid variation of the near field. For this purpose, we define the relative variation of the transient near-field intensity enhancement,

$$\frac{\Delta|\mathbf{E}|^2}{|\mathbf{E}_0|^2} = \frac{|\mathbf{E}|^2 - |\mathbf{E}_0|^2}{|\mathbf{E}_0|^2} \quad (4.7)$$

where $|\mathbf{E}|^2 = |\mathbf{E}(\omega, d, t_D)|^2$. $|\mathbf{E}_0|^2 = |\mathbf{E}(\omega, d, 0)|^2$ is the near field enhancement at a distance d when $t_D = 0$ (that is, identical to the one in the stationary regime). The variation defined in Eq. 4.7 will be referred to as the "transient near field intensity enhancement variation" (TNFIEV) hereafter.



(a)



(b)

Figure 4.6 – Stationary regime near-field properties in the close vicinity of a 20 nm spherical AuNP: (a) instantaneous electric field energy (normalized by the highest value) around the AuNP and (b) dependency of the near field enhancement on the distance away from the nanoparticle, as simulated via CCRPP-based FDTD, taken at the plasmon resonance frequency.

Figure 4.7 gives a side-by-side comparison of the TNFIEV that has been predicted by the FDTD simulation inside the nanoparticle (at the center) [Fig. 4.7(b)] with the one obtained using the well-known Mie theory (carried out at each delay time by using the transient dielectric function calculated in section 4.3.1) [Fig. 4.7(a)]. For the latter, 32 orders have been considered in the multipolar development. It can be observed that both spectral signatures are quite similar,

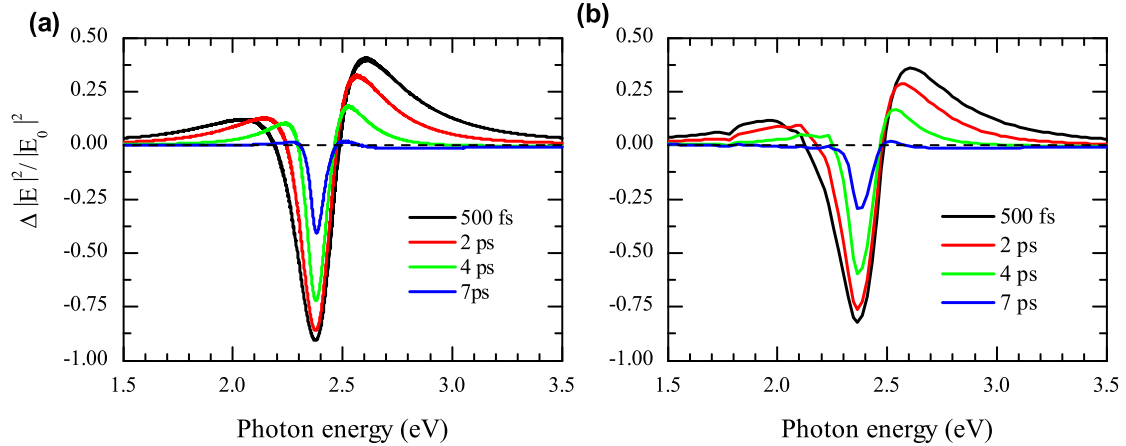


Figure 4.7 – Comparison of the transient near-field intensity enhancement variation (TNFIEV) of the 20 nm AuNP in air observed at its very center (a) calculated with the Mie theory and (b) obtained by our FDTD simulation, for different delay times (500 fs, 2 ps, 4 ps, and 7 ps) after irradiation with an ultrashort laser pulse having the same characteristics as in Fig. 4.4. Horizontal and vertical scales are identical.

depicting a typical feature of a plasmonic system with a single plasmon mode. They both show a single negative peak at the plasmon resonance energy and two positive peaks in the red and blue wings of the plasmon band. The signal is made up of two components, a symmetric one around the plasmon mode, typical of plasmon bleaching, and an antisymmetric one around an almost isosbestic point, accounting for a spectral shift of the interband transition threshold. The dynamics of the latter is faster than the one of the former. This signs the quenching, broadening and fast initial spectral shift of the resonance, induced by the Fermi smearing of the electron distribution, and the increase in the electron scattering rate, all driven by the dynamics of the electron and metal lattice temperatures [95, 99]. This comparability of the FDTD result with the analytical resolution of Maxwell’s equations (Mie theory), beyond the accuracy test described in section 4.2.2, is a confirmation of the validity of both the CCPRP-based approach and the present FDTD implementation. While comparing the results of FDTD calculation and Mie theory, however, a few discrepancies can be observed. The TNFIEV spectrum obtained via FDTD [Fig. 4.7(b)] is slightly broader and more damped than the one provided by Mie theory [Fig. 4.7(a)]. These differences may originate from the geometrical representation of the AuNP during the theoretical calculations. The Mie theory assumes a symmetrical, perfect sphere with homogeneous internal electromagnetic field while this is not the case for the FDTD simulation where the nanoparticle core is discretized into different elements. TNFIEV spectra simulated by the FDTD at positions different from the exact center of the nanoparticle but still within the particle (not shown here) have demonstrated the same feature as the one in Fig. 4.7(b) with almost no difference. Besides, the slight ripples observed in the curves of Fig. 4.7(b) may stem from numerical noise introduced by the Auxiliary Differential Equations in the FDTD, as well as from inaccuracies due to accumulating floating-point rounding errors.

The $|\mathbf{E}|^2$ spectral signature calculated at a distance d away from the AuNP resembles the near-field transmission spectra of a single AuNP measured by Okamoto *et. al.* [9] for different nanoparticle sizes. Indeed, the spectra are different from the ones that can be observed inside the

nanoparticle. They exhibit both an enhancement part (the effect of the LSPR) and an absorptive one, in the red and blue spectral regions, respectively (Fig. 4.8, red curve). The physical origin of this antisymmetric behavior of the spectra has already been well analyzed in the work of Okamoto both by analytical, extended Mie scattering theory and rigorous, Green dyadic method (GDM). The former has revealed that destructive and constructive interferences between the field retarded by the nanoparticle and the incoming field are respectively responsible for the attenuation and enhancement of the resulting local field, and then for the antisymmetric profile of the spectra. The GDM has confirmed this analysis, holding the respective contributions of interfering terms of different order in $1/d$ accountable for the local field spectral profile. The higher order (near-field) term gives a spectral peak in the red, while the lower order (propagating) term peaks in the blue of the spectral region [9]. The red-shift of the enhancement peak from the LSPR even gets reinforced in the case of transient regime because of the laser-induced ultrafast phenomena that have already been discussed earlier in this section (see the green arrows in Fig. 4.8).

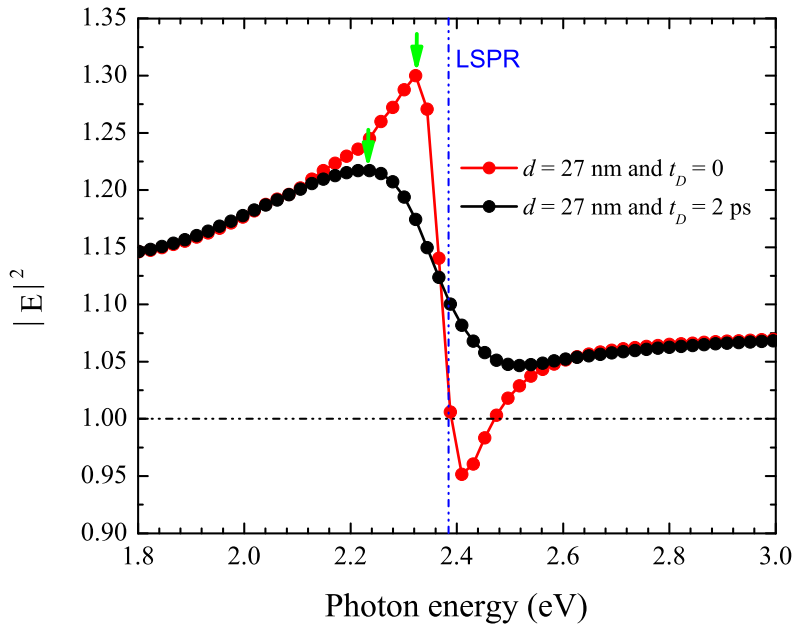


Figure 4.8 – Field intensity enhancement spectrum $|E|^2$ simulated by FDTD at $d = 27$ nm away from the AuNP in both the stationary (connected red dots) and transient (at 2 ps, connected black dots) regimes. The blue dash-dot vertical line indicates the stationary LSPR energy. The green arrows indicate the red-shift of the enhancement peak for both the stationary and transient near-field intensities.

The TNFIEV signal decreases along time, following the electron relaxation process triggered by the dynamics of the electron-phonon energy exchange and the heat release to the surrounding medium [40,41,50,95]. Let us recall that we are here interested in the transient relative variation of the near field in and around the NP rather than the near field itself, in order to illustrate the ability of our CCPRP-based FDTD approach to finely describe tiny changes of the dielectric function of materials, which is especially useful for ultrafast plasmonics. Outside the AuNP, the TNFIEV signal exhibits of course also a relaxation behavior after the initial excitation, as revealed by Fig. 4.9.

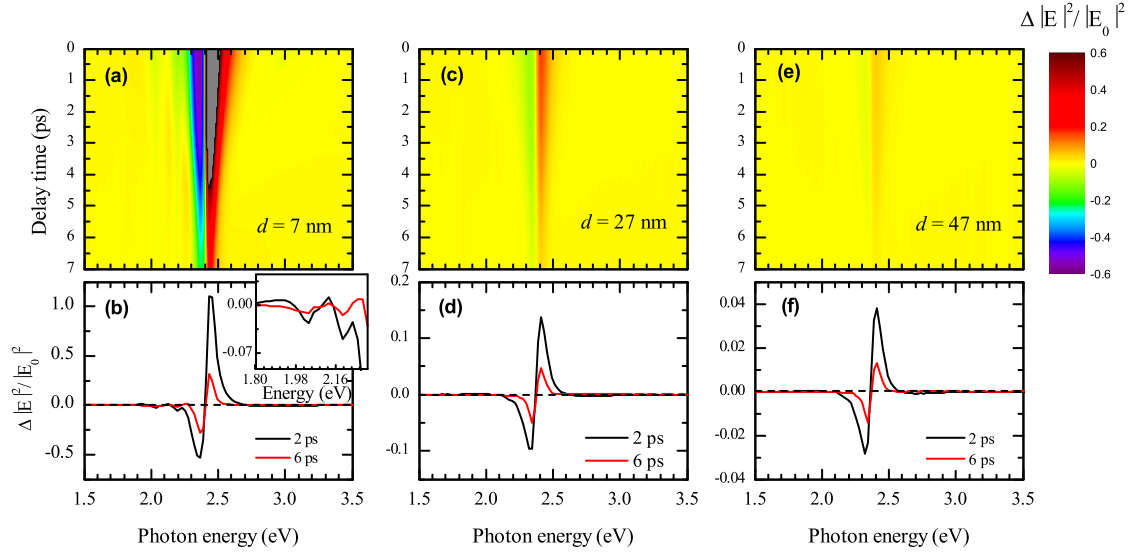


Figure 4.9 – Upper panel: color mapping of the time evolution (up to 7 ps) of the relative variation of the transient near-field intensity enhancement spectrum (from 1.5 to 3.5 eV) after initial pulsed excitation at three different distances, d , away from the AuNP surface along the y axis [(a) $d = 7$ nm, (c) $d = 27$ nm and (e) $d = 47$ nm] simulated by FDTD. The lower panel shows the relative variation of the near-field intensity enhancement observed at the delay times of 2 ps and 6 ps after the passage of the laser pulse, as are extracted from the upper panel plots [(b) from (a), (d) from (c) and (f) from (e)]. The inset in (b) shows a close-up of the additional artifact features that can be observed in the transient signal (numerical noise in the photon energy range from 1.9 eV to 2.2 eV) due to the proximity of the observation point to the AuNP surface and its pixelized interface with air.

More interestingly, a dependence on the distance away from the nanoparticle surface can be observed [Figs. 4.9(a) to (c)]. First, the TNFIEV signal decreases drastically as the observation point goes farther away from the nanoparticle. Indeed, the near field is composed of the radiative and reactive parts. The former can propagate into a far field while the latter is known for disappearing as an evanescent wave as the distance away from the field source is increased. Though the two parts of the near field are present in both the stationary and transient regimes, the weight of loss in the form of “reactive near field” in the two regimes is different due to the laser induced change of the dielectric function in the latter. This makes the TNFIEV change with the distance away from the AuNP. At closer distances, up to $d = 7$ nm away from the nanoparticle surface, additional features can be observed in the photon energy range from 1.9 eV to 2.2 eV. The inset in Fig. 4.9(b) shows this effect at $d = 7$ nm. This can be attributed to numerical artifacts due to the coarse space discretization in the FDTD. This feature disappears beyond $d = 7$ nm as the field propagates away from the AuNP [Figs. 4.9(c), (d), (e) and (f)]. In addition, it can be clearly observed that the spectral profile of the TNFIEV evolves with the distance from the NP [compare Fig. 4.7(b), Figs. 4.9(b), (d) and (f) at 2 ps delay]. Indeed, the symmetrical component progressively vanishes outside the NP and the two wings of the remaining antisymmetric component tend to balance exactly with increasing d .

4.4 Summary

We have exploited the fact that any physical dielectric function can be modeled by a rational fraction, equivalent to a sum of complex-conjugate pole-residue pairs. This approximation has been implemented in the frequency domain. We have provided a new method for checking the accuracy of a FDTD tool for materials with an arbitrary dielectric function. The dielectric function of bulk gold seen by the FDTD algorithm was recovered by Fast Fourier Transform and compared with the experimental data. The test simulation showed that a four-pole model is enough to get an accurate result. Beyond, it would also be possible to use the vector fitting technique for any anisotropic material (tensorial dielectric function) that can be approximated and FDTD-simulated using the method described in this chapter. However, introducing non-diagonal tensors in FDTD is not easy and requires further approximations, as mentioned in [194].

This CCPRP-based FDTD method was then used in coordination with the 3TM to study the ultrafast transient variation of the near-field intensity enhancement in and around a 20 nm AuNP. We have applied this FDTD method for the simplest case (a spherical NP); however, just like classical FDTD methods, our CCPRP-based FDTD tool can also be used to simulate the field topography with arbitrary NP shapes, groups or arrays of NPs, or plasmonic circuits, with the additional advantage for enabling the investigation of their ultrafast transient optical response while ensuring its regularity over the whole time range of investigation.

Let us summarize our main findings. The spectral signature of the near field determined outside the NP in the stationary regime resembles the one measured experimentally for a single NP. It exhibits an antisymmetric signature with an enhancement peak in the red and an absorptive peak in the blue parts of its LSPR, respectively due to the contributions from the near and the propagating fields. In the ultrafast transient regime, the NP properties evolve, triggered by the initial absorption of a light pulse. Inside the NP, the subsequent transient near field that the simulation predicts is similar to the one that can be derived from the Mie theory, validating our approach. Beyond, we have shown that the transient variation of the near field intensity relative to its stationary counterpart also changes with the distance from the NP, demonstrating the difference in the weight of the reactive near field loss in the two regimes.

This approach is particularly suited for determining numerically the variation of the near field topography induced by changes in the material dielectric function. It will then be particularly relevant in the analysis of the phenomena triggered by ultrashort laser pulses which are highly related to the near field enhancement in and around plasmonic nanostructures, such as electron photoemission, photoluminescence, production of reactive oxygen species, and photocatalysis [47, 49–52, 195].

Chapter 5

Plasmonic-photonic coupling: gold nanorods in a 1D microcavity

Contents

5.1 Introduction	97
5.2 The uncoupled sub-systems	98
5.2.1 Choosing a plasmonic nanocomposite layer	98
5.2.2 The 1D photonic crystal	100
5.3 Stationary regime optical response of the plasmonic-photonic hybrid microcavity	102
5.3.1 Coupling between the defect mode and the LgSPR	102
5.3.2 Coupling between the defect mode and the TrSPR	106
5.3.3 Absorbance of the hybrid cavity compared to that of a bare thin plasmonic film	107
5.4 Transient optical response of the hybrid structure	109
5.5 Summary	112

5.1 Introduction

In the stationary regime, coupling the LSPR of spherical NPs with a resonant mode of an electromagnetic cavity has demonstrated strong near-field enhancement and confinement as well as a strong absorbance of the hybrid structure [64, 65]. In the transient regime, our team has optimized the plasmonic-photonic coupling of such a hybrid structure and demonstrated an efficient signal modulation on a picosecond timescale [66, 67]. Indeed, the pump beam is trapped in the electromagnetic cavity which allows for large power to be absorbed by the NPs introduced into the defect layer of a dielectric photonic crystal. The subsequent ultrafast nonlinear response of the NPs then results in the strong modulation of both the near field around the NP, as has been discussed in the preceding chapter, and of the optical properties of the cavity. The latter has been assessed by pump-probe spectroscopy experiments. The modulation of the near-field intensity can be used to develop time-resolved sensors, based on the same considerations as for the stationary plasmon-enhanced fluorescence or SERS, for instance by associating such hybrid structures with

microfluidic technology. This potential application has triggered our interest for advancing the study of the ultrafast plasmonic-photonic coupling to a more complex configuration using parallel AuNRs rather than nanospheres. Indeed, the anisotropy of the optical response enables us to study light-polarization dependent optical functionalities. In this chapter, we will initiate the study of such complex plasmonic-photonic hybrid cavities for their ability to induce a controlled light-triggered ultrafast modulation of the near field.

Electron-beam lithography appears to be the most appropriate method for elaborating a monolayer of parallel and identical gold nanorods on a transparent oxide layer. Different plasmonic nanocomposite layers have been fabricated by e-beam lithography by our colleague (Sergei Kostcheev) from Université de Technologie de Troyes (UTT) and their LSPR has been studied. The elaborated plasmonic thin layers consist of parallel AuNRs on alumina (amorphous Al_2O_3). The samples differ in AuNR AR. The equivalent theoretical samples have been modeled by Yamaguchi's approach (see Chapter 1) by considering prolate AuNRs. A perfect fitting has been obtained between the different experimental and theoretical samples by varying the AR of the prolate AuNRs in the latter one. The sample with AR of 1.7 has then been chosen for the theoretical study of the plasmonic-photonic coupling. This fictitious nanocomposite layer has been sandwiched between two Bragg mirrors (1D photonic crystal) made up of alternating SiO_2 and TiO_2 dielectric materials in order to form a hybrid cavity. The polarization dependent optical response of this device has been studied both in the stationary and ultrafast transient regimes. These modeling steps will be now described in detail.

5.2 The uncoupled sub-systems

In this section the basic techniques that have been employed to model the ultimate plasmonic-photonic hybrid microcavity will be dealt with. The components that make up the device will be presented independently. The optical constants of the dielectric materials that we use in this theoretical study have been determined experimentally by our colleagues in UTT for this purpose. Refractive index of Al_2O_3 , TiO_2 and SiO_2 have been determined to be 1.63, 2.60 and 1.50, respectively. The stationary regime dielectric function values that we use here are the ones that have been fitted to the experimental data (see Chapter 1) of Edward D. Palik [85].

5.2.1 Choosing a plasmonic nanocomposite layer

As has been mentioned earlier, this last chapter is devoted to the theoretical investigation of the coupling between a defect mode of a 1D photonic crystal and nonspherical NPs. However, the choice of the dimensions for the theoretical representation of the AuNRs was based on a comparison with experimental results. Arrays of AuNRs of different AR, embedded in Al_2O_3 , were fabricated in UTT as shown in the SEM images on Fig. 5.1. The AR was varied by changing the length (L) of the AuNRs and while keeping their height (H) and width (W) constant at 30 nm. To avoid the inter-particle coupling, the arrays were fabricated in such a way that each NP is far enough (120 nm) away from the neighboring ones. The LSPR of each sample was determined after depositing a top layer of Al_2O_3 above the NPs. Since the size of these arrays is quite small, a $\times 50$ objective ($\text{NA} = 0.8$) was used for the signal acquisition. This allows to include the large angle scattered signals instead of the transmitted (collimated) ones only. The spectra are displayed in Fig. 5.2(a) along with the results obtained theoretically.

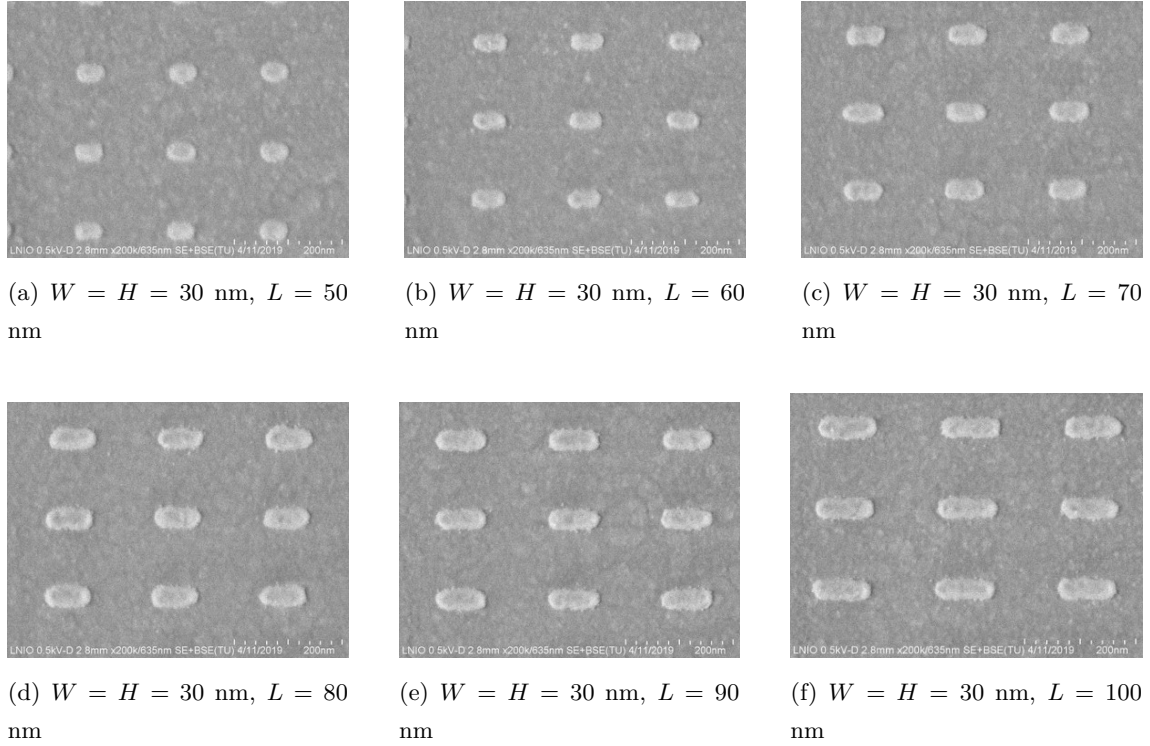


Figure 5.1 – SEM images of the samples fabricated in UTT by e-beam lithography: (a) AR = 1.7, (b) AR = 2.0, (c) AR = 2.3, (d) AR = 2.7, (e) AR = 3.0 and (f) AR = 3.3.

The fabricated plasmonic layers have been represented in our simulations by using the model proposed for 2D plasmonic nanocomposite layers (refer to Chapter 1) by Yamaguchi *et al.* [116]. Since this analytic approach is suited for spheroid-shaped NPs only, the AuNRs are represented by a prolate shape. The nanocomposite layer then consists of prolate AuNPs of diameter $D = 30$ nm (equivalent to $H = W = 30$ nm in the experimental samples) embedded in Al_2O_3 [Fig. 5.2(b)]. Just like in the experiment, the length of the prolate AuNRs has been varied in such a way that their LgSPR matches with that of the ones determined experimentally [see Fig. 5.2(a)]. The overall thickness of the fictitious samples is considered to be equal to the AuNR diameter D . The AuNRs are 120 nm apart from each 1st-neighbor NP in all directions (same as in the fabricated samples). The AuNR volume occupies only 0.1% of the modeled nanocomposite layers. This value of volume filling fraction (p) of AuNRs is half of the value that had been considered previously in Ref. [72] for spherical NPs. The LgSPR of AuNRs exhibits a higher oscillating strength than the LSPR mode of Au nanospheres with same volume. This may lead to vacuum Rabi splitting of the defect mode of the hybrid microcavity associated with the strong coupling regime. However, as will be shown bellow (§5.3.1.1), the $p = 0.001$ value lets the system well in the weak coupling regime.

The LSPR spectral locations determined experimentally and theoretically match exactly for almost the same L values [see the legend in Fig. 5.2(a)]. The spectra determined experimentally are quite broader than the theoretical ones. These differences can be due to some or all of the following reasons: (i) roughness of the fabricated AuNRs and/or the top and underlying Al_2O_3 layers; (ii) inhomogeneity of the lithography process. As the resist material may vary slightly from one experiment to the other (for example its thickness or the concentration of its constituents

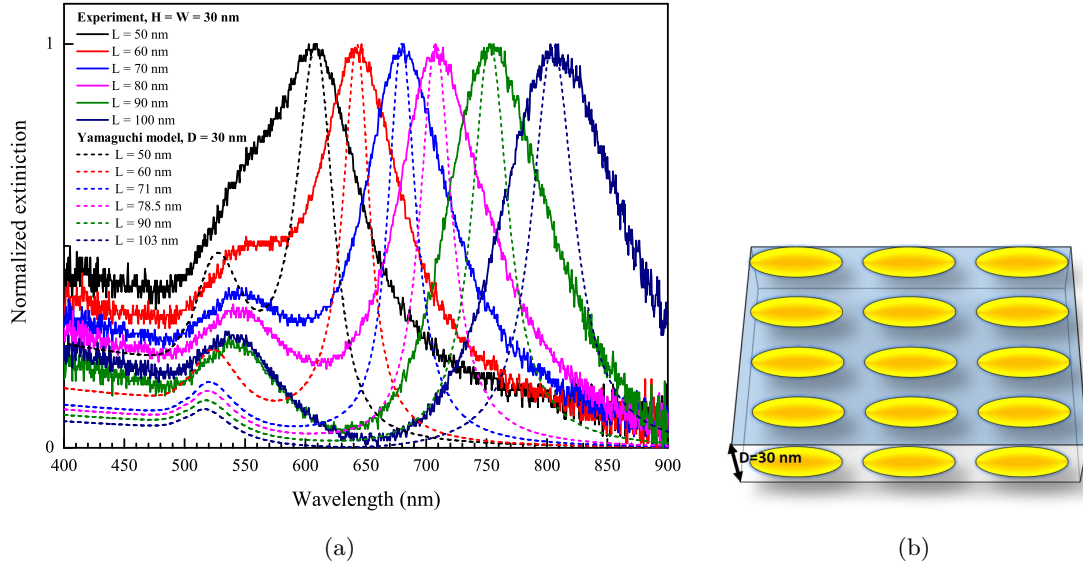


Figure 5.2 – (a) Normalized experimental extinction spectra (full lines) and the calculated absorption coefficient (dashed lines) as determined by using the Yamaguchi model of the samples with different AuNR ARs. (b) Sketch of the nanocomposite layer considered for calculation: array of prolate AuNRs ($D = 30$ nm and $L = 50$ nm) embedded in a Al_2O_3 layer. The total composite layer has a thickness $D = 30$ nm

might be different) this may affect the size and/or shape of the NPs during their fabrication (see Fig. 5.1); (iii) the size distribution of the AuNRs can also be affected by the variation of the exposure dose (amount of energy deposited per unit area) from one sample to the other; and (iv) acquisition of the experimental spectra using a large $\text{NA} = 0.8$ objective partly includes scattering while the calculated ones consider only the absorption coefficient.

For the theoretical work that we are dealing with in this chapter, the sample with the smallest $\text{AR} = 1.7$ ($D = 30$ nm and $L = 50$ nm) is chosen [black dashed line in Fig. 5.2(a)] owing to the spectral proximity of TrSPR and LgSPR modes, as will be explained later (§5.3.1).

5.2.2 The 1D photonic crystal

Photonic crystals (PC) are materials fabricated in such a way that two dielectric materials of different refractive indices are arranged in an alternate 1D, 2D or 3D periodic fashion [196]. This allows for destructive interferences between multiple reflected rays at the successive boundaries in a certain spectral range –called the photonic band gap– that cancel any transmitted rays. In this work, we are interested in 1D PCs consisting in a stack of high- and low-index transparent bilayers (Bragg mirrors). However, if this periodicity is disrupted, either by introducing another foreign material into the arrangement, or by changing the size of at least one of the dielectric materials that make up the PC, this results in the appearance of some permitted modes in the photonic band gap which are called the *defect modes*. Now, the two Bragg mirrors and the defect form a resonant cavity where the electromagnetic field spectral components corresponding to the defect modes are confined as a standing wave, with a high local field intensity. The modes appearing inside the photonic band gap are thus also called *cavity modes*.

A 1D PC has been designed by using the Transfer Matrix Method (TMM) according to the procedure described by E. Hecht [197]. This approach is based on storing the contribution of each

layer to the overall optical response of the PC into a single 2×2 matrix. Let us consider that our PC layers are identified by the label k ; hence, each layer is defined by:

$$M_k = \begin{pmatrix} \cos(\delta_k) & -j \frac{\sin(\delta_k)}{\eta_k} \\ -j \eta_k \sin(\delta_k) & \cos(\delta_k) \end{pmatrix} \quad (5.1)$$

where

$$\delta_k = \frac{2\pi}{\lambda} \tilde{n}_k d_k \cos(\theta_k). \quad (5.2)$$

d_k , $\tilde{n}_k = n_k + j\kappa_k$ are respectively the thickness and the complex optical index of the layer k and

$$\eta_k = \begin{cases} \tilde{n}_k \cos(\theta_k), & \text{for orthogonal (s) polarization and} \\ \frac{\tilde{n}_k}{\cos(\theta_k)}, & \text{for parallel (p) polarization to the plane of incidence.} \end{cases} \quad (5.3)$$

θ_k is the angle of refraction defined according to the Snell-Descartes law for refraction through an interface. Hence, the electric and magnetic fields inside the successive layers k and $k + 1$ are related through M_k (Eq. 5.1) as follows:

$$\begin{pmatrix} \mathbf{E}_k \\ \mathbf{B}_k \end{pmatrix} = M_k \begin{pmatrix} \mathbf{E}_{k+1} \\ \mathbf{B}_{k+1} \end{pmatrix}. \quad (5.4)$$

More details on the TMM can be found in Ref. [197]. In order to get the optical properties of the whole 1D-stack device, we need to calculate M_k for each layer and then perform a simple 2×2 matrix multiplication to obtain the total characteristic matrix of the entire PC

$$M = \prod_{k=1}^N M_k, \quad (5.5)$$

where N is its total number of layers.

A 1D PC made up of two Bragg mirrors sandwiching an Al_2O_3 defect layer has been designed. The Bragg mirrors have 5 bilayers on each side made up of SiO_2 and TiO_2 [see Fig. 5.3(a)]. Al_2O_3 ($n = 1.63$) was chosen since it has good thermal conductivity that can handle the photothermal effect of the AuNRs properly, by releasing heat efficiently. SiO_2 ($n = 1.5$) and TiO_2 ($n = 2.6$) were chosen as the constituents of the Bragg mirrors because of the index contrast that exists between the two, allowing for a sufficient reflectivity of Bragg mirrors. We chose the defect mode of the PC cavity (design wavelength λ_{des} at normal incidence) as to match the LgSPR (608 nm) of the chosen plasmonic nanocomposite layer [the black dashed line in Fig. 5.2(a)] so that an optimal coupling can be attained between the two (see details in §5.3.1). Hence, the thicknesses of the

layers forming the PC have been calculated as follows:

$$\begin{cases} d_L = \frac{\lambda_{des}}{4n_{SiO_2}} = 101.3 \text{ nm}, & \text{the thickest layer amongst the bilayers,} \\ d_H = \frac{\lambda_{des}}{4n_{TiO_2}} = 58.5 \text{ nm}, & \text{the thinnest layer amongst the bilayers and} \\ d_{defect} = \frac{\lambda_{des}}{2n_{Al_2O_3}} = 186.5 \text{ nm}, & \text{the defect layer.} \end{cases} \quad (5.6)$$

The subscripts L and H designate the low and high refractive indices values of SiO_2 and TiO_2 , respectively.

The design scheme and the transmittance for p-polarized light are displayed in Figs. 5.3(a) and (b), respectively. The design allows to have a defect mode transmittance close to 100% at $\lambda_{des} = 608 \text{ nm}$.

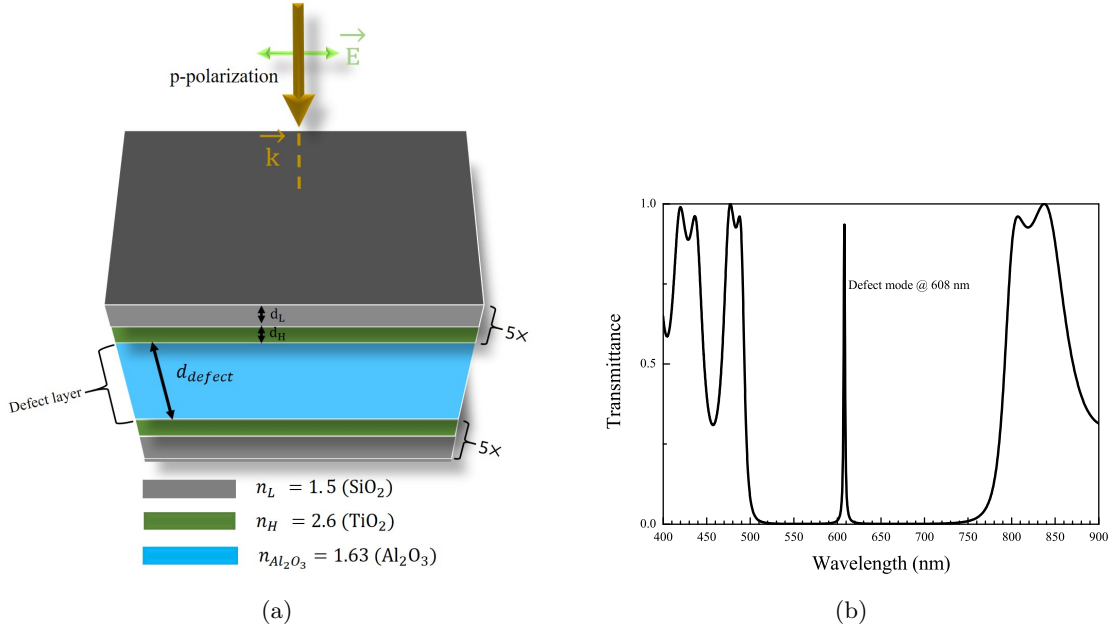


Figure 5.3 – (a) Schematic representation of a PC cavity obtained by sandwiching a Al_2O_3 layer between two Bragg mirrors, each of them being made of 5 bilayers of SiO_2 (L) and TiO_2 (H). (b) Transmittance of the PC cavity for p-polarized light.

5.3 Stationary regime optical response of the plasmonic-photonic hybrid microcavity

5.3.1 Coupling between the defect mode and the LgSPR

In the preceding section (§5.2.1), we have put some effort for stating (independently) the sub-systems that we intend to use for designing the hybrid plasmonic device. The λ_{des} of the host PC cavity was intentionally chosen to be 608 nm in order to obtain a good coupling between the defect mode and the LgSPR of the chosen plasmonic nanocomposite layer [black dashed line in Fig. 5.2(a) and Fig. 5.3(b)]. As shown in Fig. 5.4(a), the plasmonic nanocomposite layer [Fig. 5.2(b)] with $\lambda_{LgSPR} = 608 \text{ nm}$ and thickness 30 nm was inserted into the very middle of the Al_2O_3

defect layer of Fig. 5.3(a). The remaining Al_2O_3 spacers just above and below the plasmonic nanocomposite layer have equal thicknesses of 78.25 nm [see Fig. 5.4(a)]. The defect mode of the hybrid microcavity can be seen clearly at 608 nm [Fig. 5.4(c)].

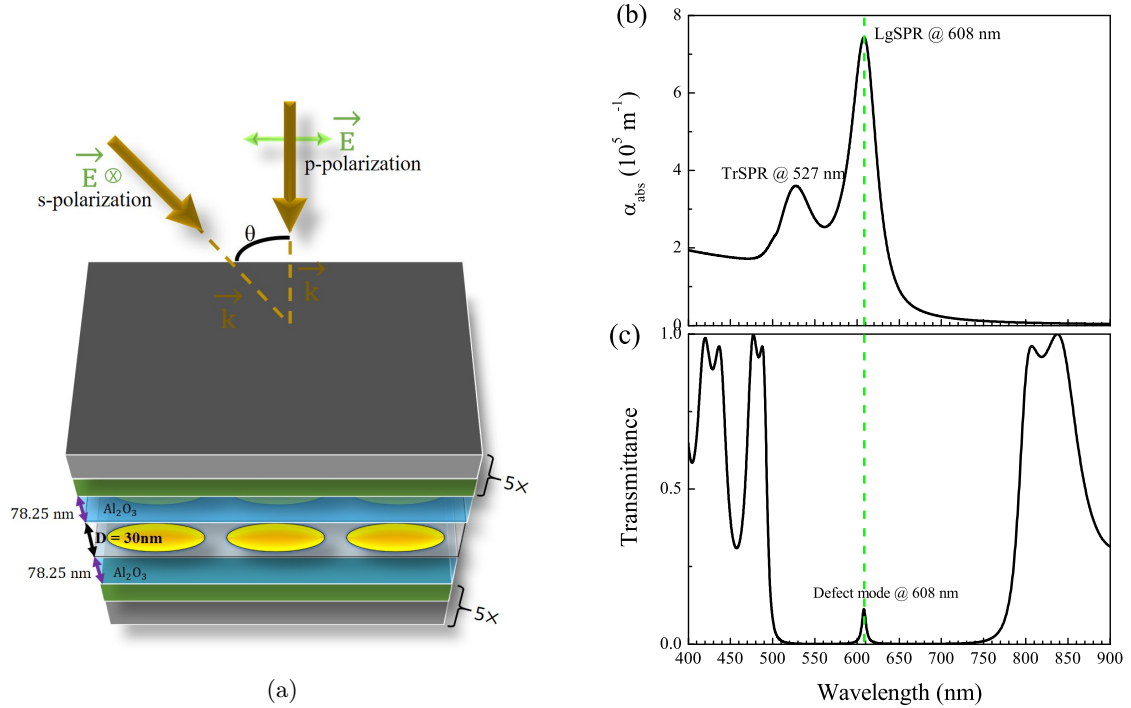


Figure 5.4 – (a) Schematic representation of the plasmonic-photonic hybrid structure. The *s*- and *p*- polarizations are also shown. (b) Stationary regime absorption coefficient of the free plasmonic nanocomposite layer as calculated by Yamaguchi model. (c) Stationary regime transmittance of the plasmonic-photonic hybrid device calculated by coordination of both the Yamaguchi model and the TMM for *p*-polarized light. The vertical line indicates the perfect spectral matching of the LgSPR of the free plasmonic layer and the defect mode of the PC.

The coupling modifies the optical characteristics of the PC. It has been shown that under such circumstances, absorbance of the hybrid nanostructure can be strongly enhanced compared to that of a nanocomposite layer that contains the same concentration of AuNPs [65, 72]. On the other hand, the introduction of the nanocomposite layer at the very middle of the host PC leads to a significant degradation of the quality factor of its defect mode [compare Figs. 5.4(c) and 5.3(b)]. The presence of the nanocomposite layer strongly absorbs the wave (plasmonic effect) around the spectral zone of the defect mode (608 nm), resulting in the significant reduction of its transmittance [72]. However, as shown in Fig. 5.5(c), despite the presence of the absorbing material the field intensity at the middle of the defect layer at 608 nm wavelength is enhanced by a factor ~ 15 . In Chapter 4 we have investigated the ultrafast transient near field variations of a plasmonic NP, which depends on both the wavelength and the distance from the NP, induced by the absorption of a subpicosecond laser pulse. Thus, this ultrafast modulation of the plasmonic near field in the nanocomposite material could be exploited in the hybrid plasmonic microcavity.

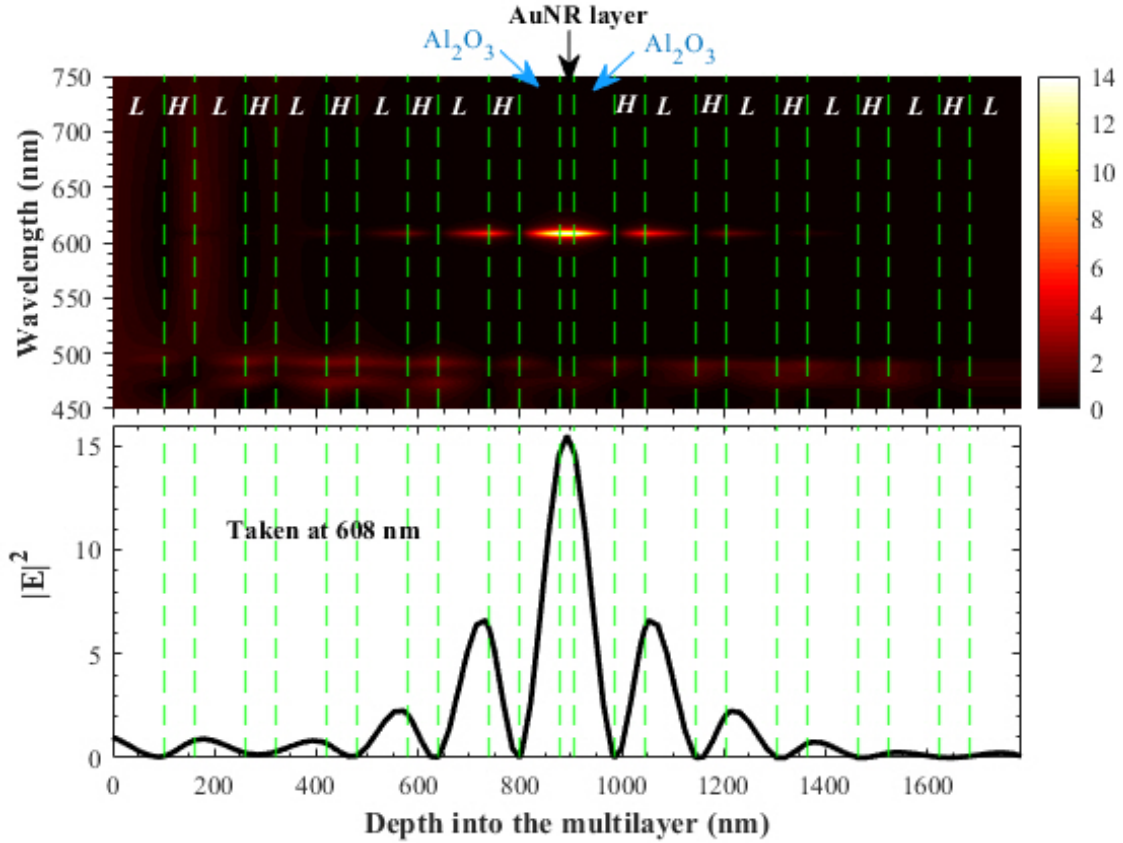


Figure 5.5 – Electric field intensity enhancement $|E|^2$ inside the plasmonic-photonic hybrid microcavity for p -polarized light in the stationary regime. The structure is designed such that the LgSPR of the plasmonic nanocomposite layer and the defect mode of the PC cavity are perfectly coupled at 608 nm. (a) Wavelength and position dependent $|E|^2$ distribution in the hybrid device. The arrows indicate the constituents of its defect layer: the plasmonic nanocomposite layer (with 0.1% Au) and the two Al_2O_3 layers. H and L designate the alternating high and low refractive index layers, respectively, that make up the Bragg mirrors. (b) $|E|^2$ distribution along the device taken at the LgSPR (608 nm) of the nanocomposite layer. The green vertical dashed lines indicate the interfaces between the H and L layers.

5.3.1.1 Monitoring the coupling regime: vacuum-field Rabi splitting

As has been demonstrated earlier in this section (§5.3.1), the coupling between the host PC defect mode and the LgSPR of the guest plasmonic nanocomposite layer ($p = 0.001$) exhibits a single transmittance inside the photonic band gap [see Fig. 5.4(c)]. This assumes that we are in the weak coupling regime. In the strong coupling regime, the two modes would hybridize to create two new eigenstates of mixed optical characteristics [198–203]. The newly created modes would point at angular frequencies detuned from the original resonance by $\pm\Omega$, the *vacuum-field Rabi splitting*. Though the TMM-based theoretical approach that we apply here could not reveal the strong coupling regime effects, it is important to predict ahead the filling fraction of Au in the nanocomposite layer for which the transition between the weak and strong coupling regimes should occur. So, in this section we present the tools that we have used to choose the value $p = 0.001$ ensuring the system to be well below the strong coupling regime values. This choice reduces the complexity of the system in consideration for this preliminary investigation. Indeed,

it enables us to track the modulation of a well defined single mode in the transient regime study of the plasmonic-photonic hybrid microcavity. Of course, it should be interesting to explore later its ultrafast transient response in the strong coupling regime.

Once the Full Width at Half Maximum (FWHM) of the bare PC cavity (Γ_{cav}) and of the LgSPR mode of the free plasmonic nanoparticle (Γ_{sp}) are known, the vacuum Rabi splitting can be analytically estimated. For the vacuum Rabi splitting of the hybrid mode in transmission, Ω is given by [200, 204]:

$$\Omega = \sqrt{\sqrt{\left(\frac{\alpha_0 \Gamma_{sp}}{2\pi n_{cav}}\right)^2 + \frac{\alpha_0 \Gamma_{sp}}{\pi n_{cav}} \Gamma_{sp} (\Gamma_{sp} + \Gamma_{cav})} - \Gamma_{sp}} \quad (5.7)$$

where n_{cav} is the refractive index of the background (Al_2O_3 in our case) and α_0 is the maximum of the absorption coefficient, α , of the thin plasmonic nanocomposite layer, which can be obtained from the Yamaguchi model in our study. The FWHM of the defect mode shown in Fig. 5.3(b) is obtained to be $\Gamma_{cav} = 1.7$ nm. The volume fraction dependent Γ_{sp} data of the LgSPR mode of the plasmonic nanocomposite layer, determined by fitting the $\alpha(\lambda)$ data to double Lorentzian peaks, is shown in Fig. 5.6(a). $\Gamma_{sp}^{0.001}$, the Γ_{sp} value at $p = 0.001$ [Fig. 5.4(b)], is found to be 38.8 nm.

As the p dependent Ω can be calculated by Eq. 5.7, the crossover from the weak- to strong-coupling regimes can be predicted using Eq. 5.8 since the coupling constant g and Ω are related as $\Omega = 2g$. Strong and weak interaction can occur between the LgSPR (λ_{sp}) and cavity (λ_{cav}) modes at a resonance ($\lambda_{sp} = \lambda_{cav} = \lambda_0$). Hence, in the picture of coupled oscillators, the resonance modes at λ_0 interacting are [204–206]:

$$\lambda - \lambda_0 = -j \left(\frac{\Gamma_{cav} + \Gamma_{sp}}{4} \right) \mp \sqrt{g^2 - \left(\frac{\Gamma_{sp} - \Gamma_{cav}}{4} \right)^2}. \quad (5.8)$$

As per Eq. 5.8, the requirement for the strong coupling is $g^2 > g_{co}^2 = (\Gamma_{sp}^{co} - \Gamma_{cav})^2/16$ and $g^2 \leq g_{co}^2$ for the weak coupling case, where Γ_{sp}^{co} is the FWHM at the crossover and g_{co} is the crossover constant. The strong coupling is manifested by the splitting of the resonance mode λ_0 into two new modes as depicted in Figs. 5.6(b). The splitting happens in the real part of $\lambda - \lambda_0$ of Eq. 5.8.

For the nanocomposite layer with $p = 0.001$, $(\Gamma_{sp}^{0.001} - \Gamma_{cav})^2/16 = 86.5 \text{ nm}^2$ which is below the crossover value of $g_{co}^2 = 89 \text{ nm}^2$. This shows that we are in the weak coupling regime and validates our modeling where a unique resonance mode is considered at $\lambda_{sp} = \lambda_{cav}$.

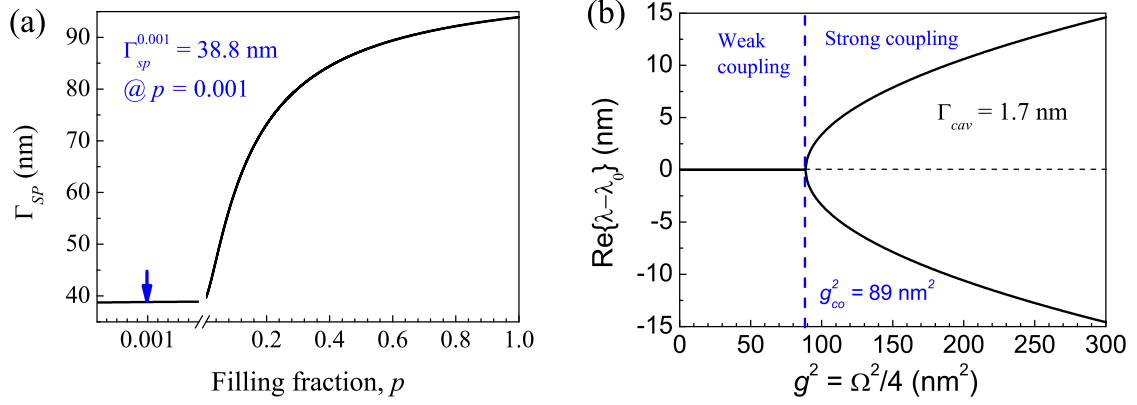


Figure 5.6 – (a) The filling fraction dependent FWHM, Γ_{sp} , of the LgSPR mode of the plasmonic nanocomposite layer determined by fitting its absorption coefficient α data to double Lorentzian peaks that correspond to its TrSPR and LgSPR modes. The blue arrow indicates the $\Gamma_{sp}^{0.001}$ value for $p = 0.001$. (b) Shows the crossover from the weak to the strong coupling regimes as a function of g^2 as calculated by Eq. 5.8. The blue dashed vertical line indicates the crossover point, $g_{co}^2 = 89 \text{ nm}^2$.

5.3.2 Coupling between the defect mode and the TrSPR

The defect mode of a PC cavity can be tuned in the spectrum (blue shifted) by changing the angle of incidence θ of the incoming light [see Fig. 5.4(a)] [66]. As has been stated in the previous section (§5.3.1), the design wavelength λ_{des} and the LgSPR of the guest plasmonic nanocomposite layer are chosen to match for the initial design of the hybrid PC cavity at normal incidence. On the other hand, the TrSPR mode of the plasmonic nanocomposite layer resides at a lower wavelength than that of its LgSPR mode. So, we just have to vary θ so that another plasmonic-photonic coupling can be achieved at the TrSPR mode. Fig. 5.7 shows this coupling which is attained at 527 nm for the angle of incidence of $\theta = 64^\circ$.

The quality factor of the hybrid cavity defect mode appearing at 527 nm (at 64° incidence) is larger than for the one appearing at $\lambda_{des} = 608 \text{ nm}$ (at normal incidence). Indeed, the plasmonic nanocomposite layer absorbs less at its TrSPR than at its LgSPR [see Fig. 5.4(b)]. Of course, it remains strongly quenched when compared to the defect mode of the uncoupled PC [Fig. 5.3(b)].

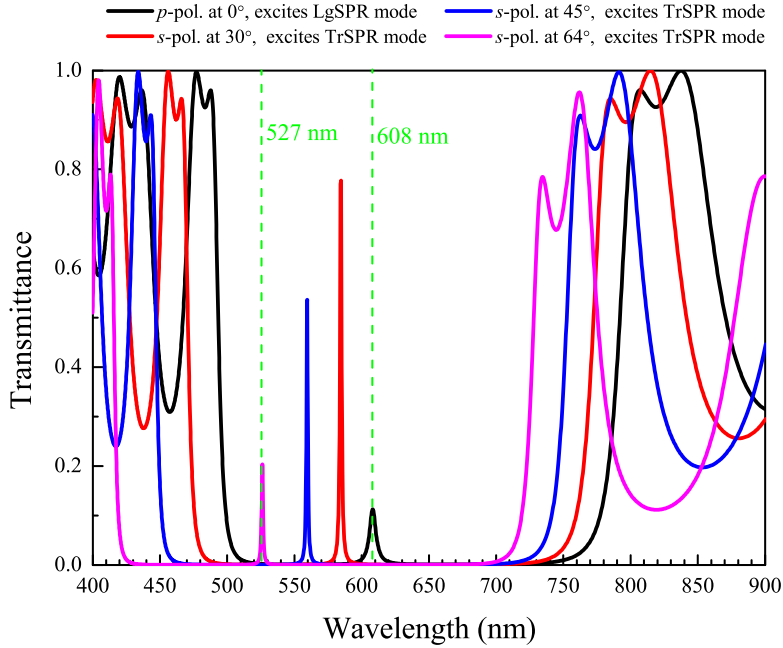


Figure 5.7 – Angle of incidence θ dependent transmittance spectra of the plasmonic-photonic hybrid cavity. The green vertical dashed lines indicate the spectral locations (527 nm and 608 nm) of the modes of the hybrid cavity as a result of the coupling between the guest plasmonic nanocomposite thin layer of 0.1% Au concentration and the defect mode of the host PC. They can be observed at $\theta = 64^\circ$ (s -polarization) and $\theta = 0^\circ$ (p -polarization), respectively.

5.3.3 Absorptance of the hybrid cavity compared to that of a bare thin plasmonic film

In the former sections, we have demonstrated that just by changing the incident light polarization, a satisfying coupling of the PC defect mode to either the LgSPR or the TrSPR modes of the parallel nanorods set in the middle of the cavity can be achieved. We have seen that the coupling significantly reduces the transmittance of the defect mode. In this section, we compare the absorptance of the hybrid cavity [Fig. 5.4(a)] with that of the bare nanocomposite film (Fig. 5.8). This bare thin film consists of a nanocomposite AuNR:Al₂O₃ layer ($p = 0.001$) sandwiched between two Al₂O₃ layers. The components have the same dimensions as the defect layer of the hybrid cavity.

The absorptance $A = 1 - T - R$, where T is the transmittance and R is the reflectance of either the hybrid or the bare thin film, has been calculated. The results are shown in Fig. 5.9. The red curves in Fig. 5.9 correspond to the absorptance calculated for s -polarized light at $\theta = 64^\circ$ angle of incidence while the black curves represent the calculations for the p -polarized light at normal incidence. It can be seen that the absorptance of the hybrid cavity is strongly enhanced compared to that of the bare thin layer in the both coupling cases. The absorptance magnitude maximum of the bare thin film at normal incidence (black dashed curve in Fig. 5.9) (at 608 nm) is larger than that of at $\theta = 64^\circ$ (at 527 nm), due to the balance of the LgSPR and TrSPR oscillating strengths. We can observe the opposite scenario for the hybrid cavity case where the absorptance at $\theta = 64^\circ$ incidence angle (red full line in Fig. 5.9) is larger than that at $\theta = 0^\circ$ (black full line in Fig. 5.9). The resonance widths of the two are also different (the red full line resonance is narrower

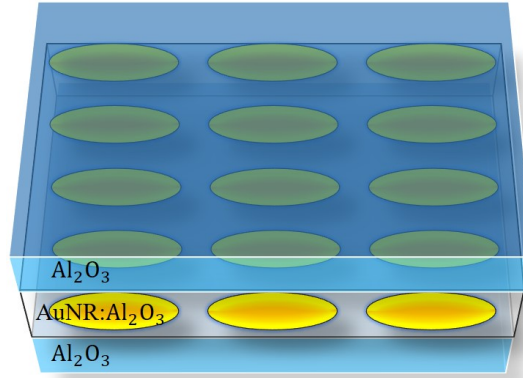


Figure 5.8 – Schematic representation of a bare thin film (equivalent to the defect layer of the hybrid cavity).

than the black full line). This result demonstrates that the plasmonic-photonic coupling in the hybrid cavity strongly modifies the absorption of light by the plasmonic NPs, by both enhancing the amount absorbed energy and tailoring the spectral profile. It had already been shown with spheres [65, 72].

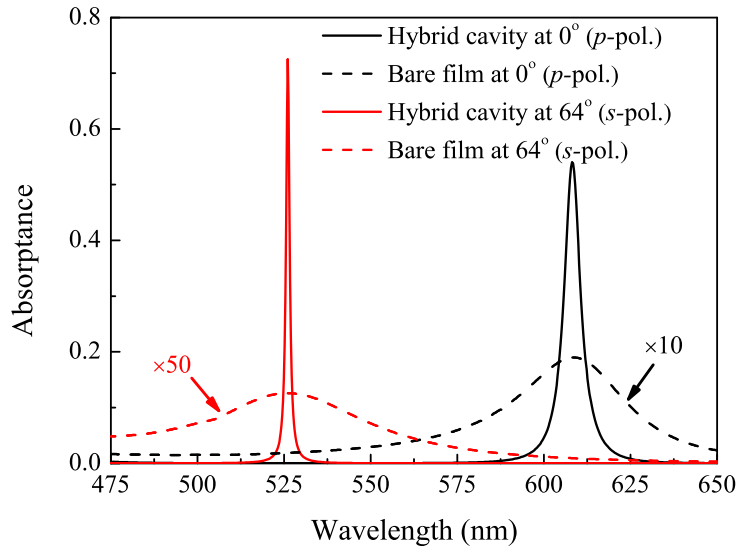


Figure 5.9 – Comparison of the absorbance of the hybrid cavity (full lines) and a thin bare nanocomposite film (dashed lines). The red and black curves correspond to the excitation of the TrSPR (*s*-pol. light at 64°) and LgSPR (*p*-pol. light at 0°) modes of the nanocomposite layer, respectively. The absorbance of the bare film is magnified 50 and 10 times for the TrSPR and LgSPR mode excitation, respectively.

In order to understand where the differences we have observed in Fig. 5.9 come from, we have plotted in Fig. 5.10 the absorbance corresponding to the two polarizations and angles of incidence considered here for both the bare film (a) and the hybrid cavity (b). Let us mention that in the case of *p*-pol. light at oblique incidence, the longitudinal excitation has been considered only (the vertical transverse one has been disregarded). As can be seen in Fig. 5.10(a), the absorbance of the bare cavity decreases with increasing angle of incidence for both polarizations. Indeed,

the reflectance is larger at 64° than at 0° (the Brewster angle for p -polarization at the air- Al_2O_3 interface is $\sim 58^\circ$), which then results in the overall reduction of the light energy which penetrates in the layer. Furthermore, at 64° incidence in the p -pol. state, only $\sim 20\%$ of the light energy is input in the LgSPR mode. For the hybrid cavity, the trend is very different [Fig. 5.10(b)]. The absorptances at the 64° incidence angle at 527 nm are now larger than the ones obtained at normal incidence at 608 nm for each polarization state. The transmittance balance between the two modes at the two angles is canceled by the large opposite balance in reflectance (not shown here).

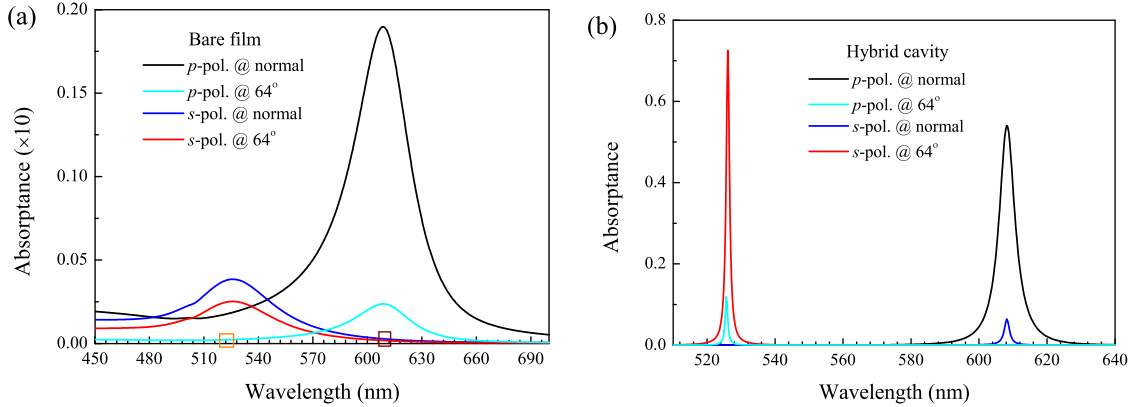


Figure 5.10 – Absorptance of (a) the bare thin plasmonic layer and (b) the hybrid cavity for the two polarizations at normal and $\theta = 64^\circ$ incidences. For the p -pol. light at 64° , the field component that excites the vertical TrSPR is disregarded. The orange and wine rectangles in (a) emphasize the small residual absorptance linked with the tails of the LgSPR and TrSPR at 527 and 608 nm, respectively.

The small absorptance of the hybrid cavity at 608 nm at normal incidence for the s -polarized light [the dark blue curve in Fig. 5.10(b)] stems from the small absorptance of the defect layer indicated by the wine rectangle in Fig. 5.10(a), which is a residue of the red tail of the TrSPR band. The $\sim 12\%$ absorptance of the hybrid cavity at 527 nm at 64° incidence for the p -polarization comes from the small residual absorptance from the blue tail of the LgSPR indicated by the orange rectangle in Fig. 5.10(a).

5.4 Transient optical response of the hybrid structure

The transient response investigation of the the hybrid device is carried out by three steps as schematized in Fig. 5.11. In the first step, the time dependent dielectric function $\varepsilon(\hbar\omega, t)$ is obtained by using the 3TM. As has been evoked in the preceding chapters and well detailed in the first chapter, the 3TM is well suited for the investigation of the optical dynamics of the plasmonic NPs over a "long" time. In the second step, the transient effective dielectric function $\varepsilon_{eff}(\hbar\omega, t)$ is obtained by using the Yamaguchi model for the AuNRs dispersed in Al_2O_3 as a 2D layer. Finally, in the third step, the nanocomposite medium obtained in the second step is introduced into the very middle of the 1D photonic crystal (Fig. 5.3) and the time dependent optical properties (transmittance, reflectance and absorbance) of the resulting hybrid device are calculated using the TMM.

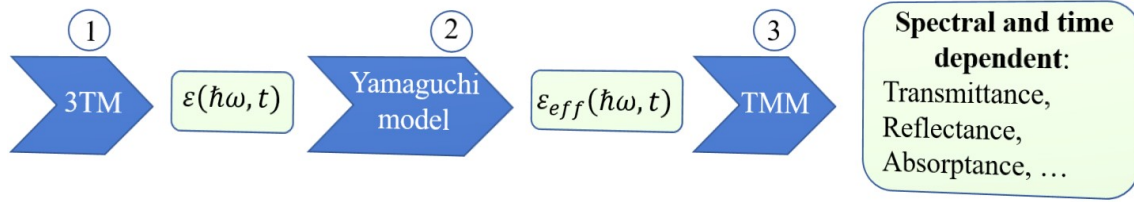


Figure 5.11 – Schematic representation of the calculation process for the transient optical response of the 1D plasmonic-photonic hybrid cavity.

A pump pulse of 100 fs is used to simulate the optical response. Two separate calculations are performed on the same hybrid structure [Fig. 5.4(a)] allowing for the investigation of the transient response depending on the laser pulse absorption at the TrSPR (527 nm) or the LgSPR (608 nm).

- **Case (1):** the structure is pumped at 527 nm in the s -polarization at 64° incidence and the spectral dependent ultrafast transient response of the hybrid structure is monitored by the probe beam parallel to the longitudinal axis of the AuNRs (p -polarization) at normal incidence.
- **Case (2):** this time, the p -polarized pump laser is injected at 608 nm at 0° incidence and the response is studied at 64° with the probe beam perpendicular to the AuNRs (s -polarization).

For both cases, the power absorbed (Eq. 3.1 in Chapter 3) by a NP is calculated from the absorption cross-section of the AuNR which is determined by the Gans-Mie theory (see Chapter 1). The laser peak intensity is considered to be 1 GW/cm^2 in both cases. Figure 5.12 depicts the spectral dependent transient relative variations of transmittance, $\Delta T/T$, of the hybrid structure for the two cases. The overall spectral profile and temporal dynamics of the signatures are similar to the ones observed in the works of X. Wang *et al.* [40,66,72] for spherical NPs sandwiched between two Bragg mirrors. The photo-induced $\Delta T/T$ profile is quite sharp as its main contributor is only the defect mode of the hybrid structure within the photonic band gap [72]. The signal profile has a strong symmetric positive peak around the LSPR that is surrounded by two negative peaks. This is due to the effect of plasmon bleaching that emanates from the transient response of the metal NPs as the surrounding medium is transparent. We also observe a slight blue-shift of the bleaching peak along the relaxation, a bit more pronounced in case (1) [Fig. 5.12(a)]. This difference may be due to the spectral sensitivity of the ultrafast modulation of the transmittance due to the dispersion and attenuation of the wave in the nanocomposite medium [66]. Though the peak power absorbed by the NPs in case (2) is the strongest (pumped at LgSPR), it can be observed in Fig. 5.12 that the pump induced modification of the transmittance for case (1) [Fig. 5.12(a)] is approximately twice as large as in case (2) [Fig. 5.12(b)]. This can be attributed to both the high value of the variation of the absorption coefficient $\Delta\alpha_{eff}$ of the nanocomposite layer that is induced by the pump and the strong LSPR experienced by the probe in case (1) [66]. Figure 5.13 depicts the relative variation of the effective absorption coefficient, $\Delta\alpha_{eff}/\alpha_{eff}$, of the nanocomposite medium for the two cases 3 ps after the absorption of the 100-fs laser pulse. The $|\Delta\alpha_{eff}|$ value induced around 2.04 eV for case (1) is quite higher than that around 2.35 eV for case (2).

The modulation of the defect mode within the photonic band gap after the absorption of the 100-fs laser pulse is presented in Figs. 5.14 and 5.15 for cases (1) and (2), respectively. For both cases, the figures display the dynamics in the delay time range from -1 to 8 ps where the pump pulse peaks at $t = 0$. The photonic band gaps and the defect mode transmittance peak are clearly

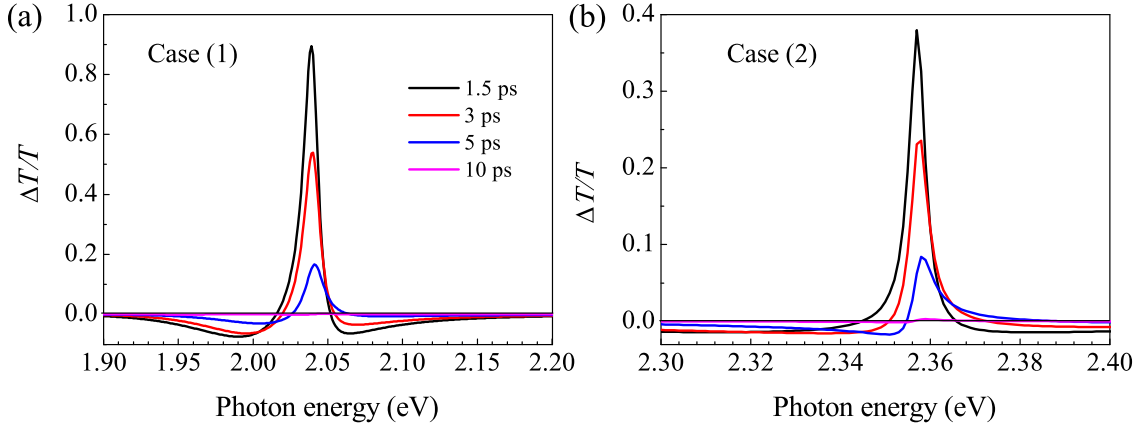


Figure 5.12 – Pump induced relative change of the transmittance of the hybrid structure after absorption of a 100-fs laser pulse: (a) Case (1), when pumped at TrSPR in s -polarization (527 nm, 2.35 eV) and probed with p -polarized light, and (b) Case (2), when pumped at LgSPR (608 nm, 2.04 eV) in p -polarization and probed with s -polarized light.

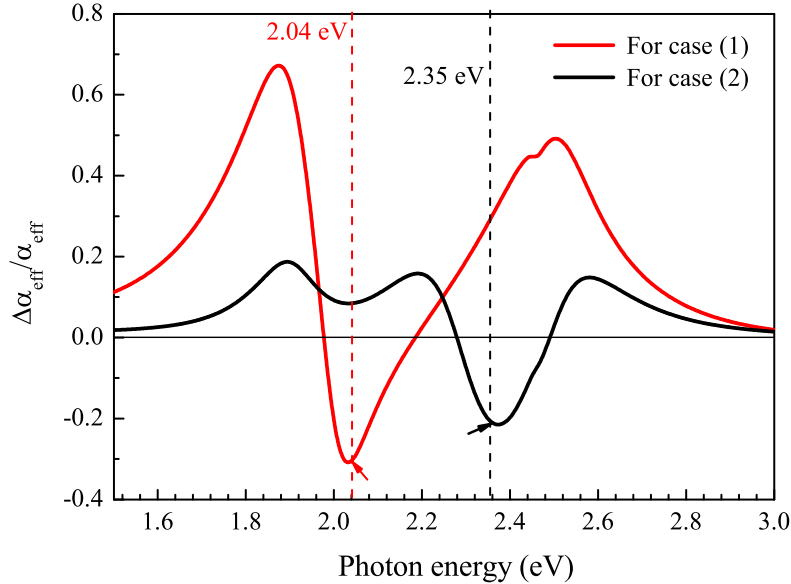


Figure 5.13 – Relative change of the absorption coefficient of the nanocomposite layer 3 ps after the absorption of a 100-fs laser pulse with $I_0 = 1 \text{ GW/cm}^2$. Red curve: for case (1), i.e, when pumped at TrSPR (547 nm, 2.35 eV) in s -polarization and probed with a light polarized parallel to the AuNRs. Black curve: for case (2), i.e, when pumped at LgSPR (608 nm, 2.04 eV) in p -polarization and probed with light polarized perpendicular to the AuNRs. The red and black arrows highlight the $\Delta\alpha_{\text{eff}}/\alpha_{\text{eff}}$ values at 2.04 eV and 2.35 eV, respectively.

visible on the figures. The two defect modes follow the same dynamics except from the difference in magnitude that we have discussed in the preceding paragraph. As expected, the defect mode transmittance abruptly reaches a maximum value just after $t = 0$ and then begins to decrease with time, relaxing back to the stationary situation.

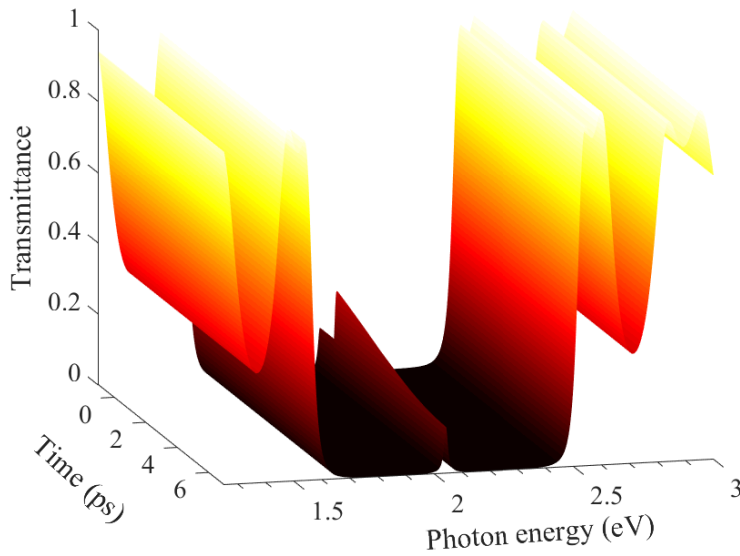


Figure 5.14 – Transient transmittance spectrum of the hybrid plasmonic-photonic cavity probed at normal incidence (excites the LgSPR of the AuNRs) after excitation by a 100-fs laser pulse at 527 nm (2.35 eV), case (1).

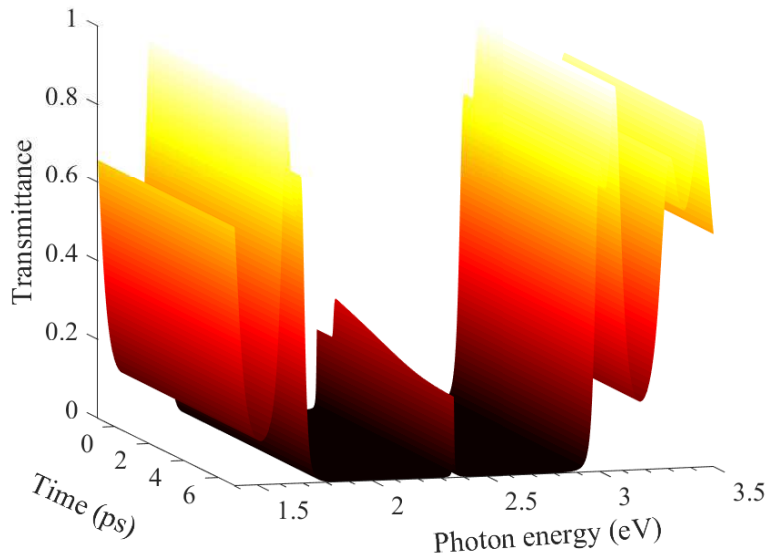


Figure 5.15 – Same as Fig. 5.14 but pumped at 608 nm (2.04 eV) and monitored by a *s*-polarized probe light at $\theta = 64^\circ$ exciting the TrSPR of the AuNRs, case (2).

5.5 Summary

We have studied theoretically the polarization-dependent coupling between the LSPR modes of a plasmonic thin layer of nanocomposite medium (made of AuNRs and Al_2O_3) and the defect mode of a 1D photonic crystal cavity both in the stationary and transient regimes. The parameters of the AuNRs were chosen by comparing the simulated LSPR characteristics of the nanocomposite medium with those measured in plasmonic structures fabricated by e-beam lithography. The choice

for this preliminary theoretical study was made with the future experimental work in mind. Indeed, the work requires the pump or the probe beam to be at oblique angle of incidence which would affect, in the experiment, the complete illumination of the sample compared to working at normal incidence. Hence, a plasmonic sample whose LgSPR and TrSPR are not spectrally decoupled much was chosen. The stationary regime TMM calculation has allowed us to obtain a perfect coupling between the LgSPR and TrSPR of the effective plasmonic medium and the defect mode of the 1D photonic crystal cavity at normal incidence and $\theta = 64^\circ$, respectively. The chosen filling fraction of Au in the nanocomposite medium allowed the coupling to remain in the weak regime, therefore ensuring a single defect mode in the photonic band gap of the hybrid cavity.

The 3TM, Yamaguchi model and TMM have been coordinated to simulate the polarization-dependent ultrafast transient optical response of the hybrid structure. The photo-induced modulation of its transmittance has been studied. It has been shown that the polarization-dependent response does not only depend on the pump power absorbed by the AuNRs but also on the spectral location where the dynamics is monitored. Indeed, the transient modulation of the plasmonic nanocomposite layer optical properties (dispersion and attenuation) varies strongly in the spectrum, hence affecting the overall optical dynamics of the hybrid device at different spectral locations [66].

In this work, we have presented only a few photonic functionalities that can be exploited in such kind of hybrid devices due to the time constraint of this Ph.D. work. For example, the electromagnetic fields from the pump and probe beams can be trapped inside the cavity and become intensified by the plasmonic effect of the NPs at the defect layer (see Fig. 5.5). So, the field inside the cavity will experience a strong ultrafast transient modulation under pump pulse excitation, as described in the preceding chapter. Thus, this modulation can be exploited for the realization of ultrafast local sensors, allowing for the time-resolved study of the optical response dynamics of objects in the vicinity of the plasmonic layer. This could be interestingly implemented in a microfluidic configuration.

Conclusion

This Ph.D. work was began with the aim of studying the ultrafast transient optical response of nonspherical noble metal nanoparticles owing to the role that it plays in many recent developments, some of them being part of our team research activities. The combination of metal NPs with other nanostructures or the design of bimetallic NPs may enable to tailor the plasmonic properties as to optimize these applications. Two kinds of hybrid plasmonic nanostructures have been studied both experimentally and theoretically: AuNP-decorated silica fibers and colloidal bimetallic core-shell (Au-Ag) NPs. The former provides macroporous framework that could enable for sensing fluidic environments while a rich LSPR feature can be observed in the latter over a broad spectral range spanning from the visible to the UV. The experimental dielectric function of the bulk gold and silver have been fitted with a very good precision, by considering both interband and intraband electron transition contributions. This work has focused on the ultrafast dynamics of the NPs over a "long" time and therefore the 3TM-based approach was used to calculate the transient thermal dynamics inside and around the NPs, accounting for the heat exchange with the surrounding medium while disregarding the initial athermal regime. We have also demonstrated that the ultrafast transient variation of the plasmonic near field in and around NPs can be theoretically assessed by coordinating the 3TM and a CCPRP-based FDTD method. Besides, we have carried out a preliminary study of the polarization-dependent ultrafast transient modification of the defect mode of a hybrid structure made of parallel AuNRs within a 1D photonic crystal cavity. In the following, the main results that have been obtained throughout this Ph.D. work will be presented.

We have experimentally studied the optical responses of Au-decorated SiO₂ fiber arrays and bimetallic AuNR@Ag/core@shell NP samples. The former exhibits a single resonance mode while the latter can have up to five LSPR modes depending on the amount of the Ag-shell deposited on the AuNR-core. In the transient regime, the Au-decorated SiO₂ NW sample has demonstrated a single bleaching peak around its LSPR which blue shifts with increasing delay time after initial excitation. The AuNR@Ag samples show different spectral signatures from one sample to another depending on the Ag-shell thickness. Multiple plasmonic resonance modes have been observed in the stationary regime extinction spectra which are highly dictated by the amount of Ag deposited on the AuNR core. The thicker Ag shell samples, which show 4 dominant LSPR modes in the stationary regime, exhibit 5 bleaching peaks in the transient regime. This new fifth mode is hidden in the stationary response but appears in the ultrafast differential transient signal. We have performed pump power dependent pump-probe measurements on each sample and observed that the fast relaxation component τ_2 of the signal dynamics converges toward zero excitation energy to about $\tau_2^0 \simeq 1$ ps for all AuNR@Ag samples, which roughly matches the usual findings from the literature. This relaxation time study could be further improved by recording more data

points. For our Au-decorated silica nanowire sample we obtained a value of $\tau_2^0 = 1.95$ ps which is in the range of the values that have already been reported for AuNPs of the same size. We have also studied the relaxation time of the AuNR@Ag NPs at two pump wavelengths. For thin Ag-shell NPs the global relaxation time is higher than that of thick Ag-shell samples for excitation around the L_0 mode. A reversed trend is observed for the excitation in the UV region of the TrSPR modes where the relaxation of the thicker Ag NPs gets slower.

We have used an arbitrary set of oblate AuNPs with different ARs for modeling the Au-decorated SiO_2 NW sample. We have demonstrated theoretically that the width of the experimental spectra, the blue-shift of the absorption bleaching along the relaxation and the asymmetry between the two positive wings of the absorption variation spectrum can all be attributed to the non-uniform shape distribution of the AuNPs in the sample. We have observed that the temporal behavior of the carrier and lattice temperatures alone is not sufficient to explain the details of the experimental features and in particular the blue-shift. The latter has been interpreted by invoking the stronger coupling of the plasmon resonance with interband transitions in nanoparticles with smaller aspect ratio. In addition, the modeled stationary spectra of the AuNR@Ag NPs have indicated that the scattering effect is negligible for the smaller Ag-shell thickness NPs but both absorption and scattering contribute almost equally to the extinction spectrum of the thicker Ag-shell NPs. The theoretical modeling of the transient optical signature of the AuNR@Ag NPs indicates that the transverse polarization component of the transient absorption is the main contributor for the formation of the unexpected fifth bleaching peak in the thick Ag-shell NPs. It is a pure dipolar T_0 mode which evolves from the TrSPR dipolar mode of the bare AuNP with increasing Ag coating which was shielded by the influence of the Ag shell in the stationary regime, but forced itself into appearance in the transient regime.

Furthermore, we have exploited the fact that any physical dielectric function can be modeled by a rational fraction, equivalent to a sum of complex-conjugate pole-residue pairs. The CCPRP-based FDTD tool that we have implemented shows a very good match between the experimental dielectric function and that retrieved from the simulation. The spectral signature of the near field determined by the CCPRP-based FDTD method for a Au nanosphere exhibits an antisymmetric profile with an enhancement peak in the red and an absorptive peak in the blue parts of its LSPR, respectively, due to the contributions from the near and the propagating fields. The simulated ultrafast transient variation of the near-field intensity enhancement inside the NP is similar to the one that can be derived from the Mie theory, validating our approach. Outside the NP, the transient variation of the near field intensity relative to its stationary counterpart also changes with the distance from the NP, demonstrating the difference in the weight of the reactive near field loss in the two regimes. This result appears to be particularly relevant for the analysis of the phenomena which are triggered in plasmonic nanostructures by ultrashort laser pulses. We have implemented this FDTD approach on a nanosphere to be able to compare the results obtained with that of the Mie theory. However, it could be used for the calculation of the ultrafast transient near field of NPs with various shape and composition. For instance, we could assess and exploit the transient near field around bimetallic AuNR@Ag NPs linked with their sharp and intense TrSPR mode variations in the UV. The great advantage of this FDTD method then lies in the improvement that it provides to the study of the developments which depend on the transient near field, like the pulse-induced electron photoemission from plasmonic nanostructures. To our knowledge, only

the stationary near field has been considered in the analysis of this phenomena up to now. Our approach should then be particularly suited for this study.

In the stationary regime, it has been shown that coupling the LSPR of nanospheres with a resonance mode of a photonic cavity enables for a strong enhancement of light absorption. Furthermore, it was demonstrated in our group that such coupling can lead to the strong ultrafast modulation of the defect mode of the hybrid device in the transient regime. The transient modulation magnitude of the optical properties of such a structure can be improved by using NPs with large LSPR oscillator strength. As nanorods have strong LgSPR mode and can also allow for polarization-dependent photonic functionalities, we have studied theoretically the coupling between the LSPR modes of a plasmonic thin layer made up of parallel gold nanorods and a defect mode of a 1D photonic crystal cavity, both in the stationary and transient regimes. The AuNR and photonic crystal characteristics have been chosen as to obtain a perfect coupling between the LgSPR and TrSPR of the effective plasmonic medium and the defect mode of the cavity at normal incidence and $\theta = 64^\circ$, respectively. The selected filling fraction of Au in the nanocomposite medium allowed the coupling to remain in the weak regime, therefore ensuring a single defect mode in the photonic band gap of the hybrid cavity. The relative transient change of absorbance for the LgSPR-defect mode coupling when pumped at TrSPR wavelength and $\theta = 64^\circ$ has been observed to be larger than the one for the TrSPR-defect mode coupling condition when is excited at LgSPR wavelength and normal incidence. This is mainly ascribed to the difference in the magnitude of the pump-induced absorption variation of the defect nanocomposite layer between the two excitation scenarios. The spectral-dependent transmittance modulation of the hybrid device has also been calculated for the two scenarios. This work unveils the new possibilities offered by the introduction of anisotropy into the optical properties of the hybrid cavity through the use of parallel nanorods rather than nanospheres. The control and signal pulses can now be manipulated independently via their polarization, wavelength and angle of incidence. Although this work still requires further parameter optimization, it should quickly lead to experimental investigations thanks to our partnership with UTT for sample elaboration.

Appendix A

Rosei Model

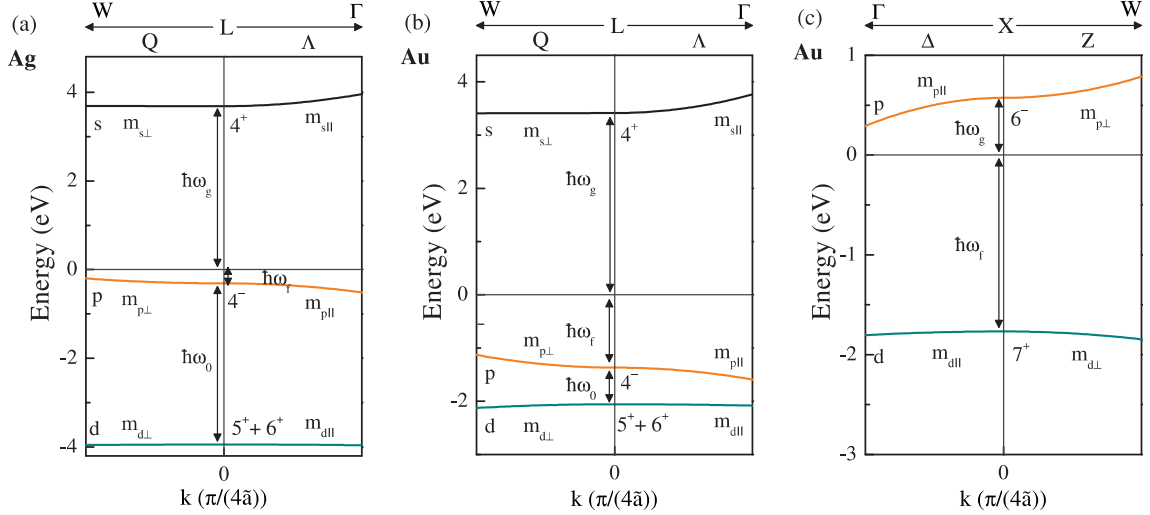


Figure A.1 – The parabolic band structure of Rosei model around the (a) L point of Ag and the (b) L & (c) X points of Au Brillouin zone, taken from Ref. [96]. The origin is taken to be the Fermi level E_F .

Fig. A.1 displays the assumed anisotropic parabolic bands in each direction around the symmetry points. According to the Rosei model, they can be described by their approximated effective masses. We define $m_{s\perp}$, $m_{s\parallel}$, $m_{p\perp}$, $m_{p\parallel}$, $m_{d\perp}$ and $m_{d\parallel}$ the positive effective masses in the bands sp and d , the symbol \parallel referring to the directions $L\text{-}\Gamma$ and $\Gamma\text{-}X$ while the symbol \perp to the directions $L\text{-}W$ and $X\text{-}W$ according to the electron wave vectors \mathbf{k}_{\parallel} and \mathbf{k}_{\perp} . Values of the effective masses for both Au and can be found in the thesis of T. Stoll [96]. All the notations of the different bands and points in the band structure are defined on Fig. A.1. Around the point L : the energy gap between d - and p bands, p -band and E_F , E_F and s -band are denoted by $\hbar\omega_0$, $\hbar\omega_f$ and $\hbar\omega_g$ respectively. Around the point X : the energy gap between d -band E_F is denoted by $\hbar\omega_f$ while the energy gap between p -band and E_F is represented by $\hbar\omega_g$ [96]. In these conditions, setting the origin of energies at E_F and the origin of wave vectors at point L and X , the d , p and s bands can

be described by the parabolic anisotropic dispersion relations [96]:

$$\begin{aligned}
\hbar\omega_d &= -\hbar\omega_f - \hbar\omega_0 - \frac{\hbar^2}{2m_{d\perp}}\mathbf{k}_\perp^2 - \frac{\hbar^2}{2m_{d\parallel}}\mathbf{k}_\parallel^2, \\
\hbar\omega_p &= -\hbar\omega_f + \frac{\hbar^2}{2m_{p\perp}}\mathbf{k}_\perp^2 - \frac{\hbar^2}{2m_{p\parallel}}\mathbf{k}_\parallel^2, \\
\hbar\omega_s &= \hbar\omega_g + \frac{\hbar^2}{2m_{s\perp}}\mathbf{k}_\perp^2 - \frac{\hbar^2}{2m_{s\parallel}}\mathbf{k}_\parallel^2.
\end{aligned} \tag{A.1}$$

The wave vector of a photon is negligible compared to the momentum of an electron, which makes the electron transition almost vertical. In addition, the transitions require the conservation of energy. So, Considering a photon with energy $\hbar\omega$ exciting an electron from an initial i band to a final f band, the energy conservation condition gives:

$$E_f(\mathbf{k}) = \hbar\omega + E_i(\mathbf{k}) \tag{A.2}$$

where E_i and E_f are the electron energy in bands i and f , respectively. The joint density of states (JDOS) for the transitions is then written as [72, 73, 96]:

$$J_{i-f}(\hbar\omega) = \int_{-\infty}^{+\infty} D_{i-f}(E, \hbar\omega) [1 - f(E + \hbar\omega)] dE, \tag{A.3}$$

where D_{i-f} is the energy-dependent joint density of states (EDJDOS) which can be written as follows for the $d \rightarrow p$ and $p \rightarrow s$ transitions [76, 96].

$$\begin{aligned}
D_{d-p}(E, \hbar\omega) &= \frac{F_{d-p}}{16\pi^2\hbar^2} \left[\frac{\hbar}{m_{p\perp}} [\hbar\omega - \hbar\omega_0 - \hbar\omega_f - (E - E_F)] - \frac{\hbar}{m_{d\perp}} [(E - E_F) + \hbar\omega_f] \right]^{-1/2}, \\
D_{p-s}(E, \hbar\omega) &= \frac{F_{p-s}}{16\pi^2\hbar^2} \left[\frac{\hbar}{m_{p\perp}} [(E - E_F) + \hbar\omega - \hbar\omega_g] - \frac{\hbar}{m_{s\perp}} [(E - E_F) + \hbar\omega_f] \right]^{-1/2},
\end{aligned} \tag{A.4}$$

the expressions being $E - E_F$ dependent. F_{i-f} in Eq. A.4 is defined as:

$$F_{i-f} = \sqrt{\frac{m_{i\perp} m_{f\parallel} m_{i\perp} m_{f\parallel}}{m_{i\perp} m_{f\parallel} + m_{i\parallel} m_{f\perp}}}. \tag{A.5}$$

In this work, we consider the E_F values of Ag and Au to be 5.53 eV and 5.49 eV respectively [96].

Considering that the d -band is completely filled while the s -band is empty, the JDOS equation for the specific cases of $d \rightarrow p$ and $p \rightarrow s$ transitions writes [96]:

$$\begin{aligned} J_{d-p}(\hbar\omega) &= \int_{-\infty}^{E_{max}} D_{d-p}(E, \hbar\omega) [1 - f(E)] dE , \\ J_{p-s}(\hbar\omega) &= \int_{E_{min}}^{\infty} D_{p-s}(E, \hbar\omega) [1 - f(E)] dE , \end{aligned} \quad (\text{A.6})$$

E_{max} and E_{min}) being:

$$E_{max} = E_F - \hbar\omega_f + \begin{cases} \frac{m_{d\parallel}}{m_{d\parallel} - m_{p\parallel}} (\hbar\omega - \hbar\omega_0) & \text{for } \hbar\omega < \hbar\omega_0 , \\ \frac{m_{d\perp}}{m_{d\perp} + m_{p\perp}} (\hbar\omega - \hbar\omega_0) & \text{for } \hbar\omega > \hbar\omega_0 , \end{cases} \quad (\text{A.7})$$

$$E_{min} = E_F - \hbar\omega_f + \begin{cases} \frac{m_{s\perp}}{m_{p\perp} - m_{s\perp}} (\hbar\omega_g + \hbar\omega_f - \hbar\omega_0) & \text{for } \hbar\omega < \hbar\omega_g + \hbar\omega_f , \\ \frac{m_{p\parallel}}{m_{p\parallel} + m_{s\parallel}} (\hbar\omega_g + \hbar\omega_f - \hbar\omega_0) & \text{for } \hbar\omega > \hbar\omega_g + \hbar\omega_f . \end{cases} \quad (\text{A.8})$$

Now, the Lindhard's theory of dielectric function can be used to obtain the imaginary part of the interband contribution to the dielectric function, ε_2^{ib} . So, the photon momentum is considered to be negligible compared to the electron one since, according to the Rosei model, we assume that only vertical transitions are possible around the L and X points. Hence, as per the Lindhard's theory, ε_2^{ib} is connected to JDOS as [72, 73, 96]:

$$\varepsilon_2^{ib}(\hbar\omega) \propto \frac{1}{\omega^2} |M^{i-f}|^2 J_{i-f}(\hbar\omega) , \quad (\text{A.9})$$

where M^{i-f} is the matrix element associated with the transition from i to f around the point L or X . It weights the oscillator strength of each transition. Thus, when the $d \rightarrow p$ and $p \rightarrow s$ transition are considered:

$$\varepsilon_2^{ib}(\hbar\omega) \propto \frac{1}{\omega^2} \left(|M^{d-p}|^2 J_{d-p}(\hbar\omega) + |M^{p-s}|^2 J_{p-s}(\hbar\omega) \right) . \quad (\text{A.10})$$

From the ε_2^{ib} , the real part ε_1^{ib} can be easily obtained by using the Eq. 1.8 in Chapter 1 (the Kramers-Kronig's relationship) as reported in the work of F. Castro & B. Nabet [207]. We calculate the ε_1^{ib} according to the method of Y. Guillet [73] which is based on the Hilbert's transform [207].

Appendix B

Synthesis of NPs and the reactants used

Reactants

All the reactants were purchased from Sigma Aldrich and used without further purification: Hexadecyltrimethylammonium bromide (CTAB, $\geq 99\%$), hexadecyltrimethylammonium chloride (CTAC, 25 wt % in H_2O), 5-bromosalicylic acid (90%), hydrogen tetrachloroaurate trihydrate ($\text{HAuCl}_4 \cdot 3\text{H}_2\text{O}$, $\geq 99.9\%$), silver nitrate (AgNO_3 , $\geq 99\%$), L-ascorbic acid (AA, $\geq 99\%$), sodium borohydride (NaBH_4 , 99%), and (1-mercaptoundec-11-yl)hexa(ethyleneglycol) (MUDOL, $> 99\%$). Water was purified by reverse osmosis with a resistivity ($> 15 \text{ M}\Omega \cdot \text{cm}$).

Synthesis of the AuNRs

The AuNRs were synthesized with seed-mediated process which involves a prereduction step with Salicylic acid ($\text{C}_7\text{H}_6\text{O}_3$) [53, 208, 209]. For the preparation of the seeds, 50 μL of a 0.025 M HAuCl_4 solution was added to 4.7 mL of 0.1 M CTAB solution at 30°C ; after mixing, 300 μL of a freshly prepared 0.01 M NaBH_4 solution was injected under vigorous stirring. The growth solution for the AuNR was constituted with 100 mL of 0.05 M of CTAB in which 90 mg of 5-bromosalicylic acid were dissolved. Then, 960 μL of 0.01 M AgNO_3 and 2 mL of 0.025 M HAuCl_4 solution were added to the mixture. The absorbance at 396 nm was monitored in a cuvette with 1 cm optical path length until it reached 0.65, indicating suitable prereduction conditions. Then 260 μL of 0.1 M AA solution was added under vigorous stirring, immediately followed by 160 μL of seed solution. The mixture was left undisturbed at 30°C for at least 4hs. The suspension was purified by 3 centrifugations (7100 g, 40 min) and pellet redispersion in a solution of 1 mM CTAC.

Synthesis of the AuNR@Ag NPs

The purified AuNR was centrifuged at 8500g for 30 min and redispersed in a 10 mM CTAC solution at a final gold concentration of 0.25 mM in all samples. The Ag:Au molar ratio equivalence (eq) was adjusted systematically as presented in Table 3.1 of Chapter 3. The molar ratio between

the Ag precursor and AA was fixed to 4 in all experiments. After mixing, the reaction vials were kept at 60°C during 3h to yield AuNR@Ag. After the synthesis, the excess reactants were purified by two centrifugation steps (7100 g, 40 min) and pellet redispersion in a solution of 1 mM CTAB at a final gold concentration of 0.25 mM in all samples.

Appendix C

Heaviside step function based equation for electron dynamics fitting

If the rise time τ_1 of the electron-phonon (e-ph) and phonon-phonon (ph-ph) scattering processes, e-ph relaxation times τ_2 and ph-ph relaxation times τ_3 at the specific probe energy are considered. The fitting equation can be written as:

$$\begin{aligned}
 f(t) = & A_1 \frac{\tau_2}{2(\tau_1 - \tau_2)} \exp\left(\frac{\sigma^2}{2\tau_1^2} - \frac{t-c}{\tau_1}\right) \left[1 + \operatorname{erf}\left(\frac{-c+t}{\sqrt{2}\sigma} - \frac{\sigma}{\sqrt{2}\tau_1}\right)\right] - \exp\left(\frac{\sigma^2}{2\tau_2^2} - \frac{t-c}{\tau_2}\right) \\
 & \left[1 + \operatorname{erf}\left(\frac{-c+t}{\sqrt{2}\sigma} - \frac{\sigma}{\sqrt{2}\tau_2}\right)\right] \\
 & + A_2 \frac{\tau_3}{2(\tau_1 - \tau_3)} \exp\left(\frac{\sigma^2}{2\tau_1^2} - \frac{t-c}{\tau_1}\right) \left[1 + \operatorname{erf}\left(\frac{-c+t}{\sqrt{2}\sigma} - \frac{\sigma}{\sqrt{2}\tau_1}\right)\right] - \exp\left(\frac{\sigma^2}{2\tau_3^2} - \frac{t-c}{\tau_3}\right) \\
 & \left[1 + \operatorname{erf}\left(\frac{-c+t}{\sqrt{3}\sigma} - \frac{\sigma}{\sqrt{2}\tau_3}\right)\right].
 \end{aligned} \tag{C.1}$$

where A_1 and A_2 represent the amplitudes that correspond to the e-ph and ph-ph scattering processes respectively. Equation C.1 considers a laser pulse of Gaussian profile centered at c and with standard deviation σ . Each term in Eq. C.1 is the result of a convolution product of a Gaussian laser profile $g(t)$ (Eq. C.3) and the kinetic profile $h(t)$ of a state created by a first order process (Eq.C.4). Equation C.4 is a product of the first order process and Heaviside step function whose value is zero when $t < c$ and 1 when $t > c$. The Heaviside function imposes a zero intensity before the arrival of the laser pulse and hence allows to describe the evolution of the physical processes by accounting for the laser duration. Therefore, the convolution product gives the characteristic times of the physical processes being studied without neglecting the laser pulse duration.

$$f(t) = g(t) * h(t) = \int_{-\infty}^{+\infty} g(u-t)f(u)du \tag{C.2}$$

$$g(t) = \frac{1}{\sigma\sqrt{2\pi}} e^{-\frac{t^2}{2\sigma^2}} \quad (\text{C.3})$$

$$h(t) = A \frac{\tau_2}{2(\tau_1 - \tau_2)} \left[\exp\left(-\frac{t-c}{2\tau_1}\right) - \exp\left(-\frac{t-c}{2\tau_2}\right) \right] * \theta(t-c) \quad (\text{C.4})$$

Bibliography

- [1] R. W. Wood, “On a remarkable case of uneven distribution of light in a diffraction grating spectrum,” *Proceedings of the Physical Society of London*, vol. 18, no. 1, p. 269, 1902.
- [2] G. Mie, “Beiträge zur Optik trüber Medien, speziell kolloidaler Metallösungen,” *Annalen der Physik*, vol. 330, no. 3, pp. 377–445, 1908.
- [3] S. A. Maier, *Plasmonics: fundamentals and applications*. Springer Science & Business Media, 2007.
- [4] L. M. Liz-Marzán, “Tailoring surface plasmons through the morphology and assembly of metal nanoparticles,” *Langmuir*, vol. 22, no. 1, pp. 32–41, 2006.
- [5] P. K. Jain, X. Huang, I. H. El-Sayed, and M. A. El-Sayed, “Review of some interesting surface plasmon resonance-enhanced properties of noble metal nanoparticles and their applications to biosystems,” *Plasmonics*, vol. 2, no. 3, pp. 107–118, 2007.
- [6] X. Wang, P. Gogol, E. Cambril, and B. Palpant, “Near- and far-field effects on the plasmon coupling in gold nanoparticle arrays,” *The Journal of Physical Chemistry C*, vol. 116, no. 46, pp. 24 741–24 747, 2012.
- [7] M. Tebbe, C. Kuttner, M. Mayer, M. Maennel, N. Pazos-Perez, T. A. König, and A. Fery, “Silver-overgrowth-induced changes in intrinsic optical properties of gold nanorods: From noninvasive monitoring of growth kinetics to tailoring internal mirror charges,” *The Journal of Physical Chemistry C*, vol. 119, no. 17, pp. 9513–9523, 2015.
- [8] P. A. Atanasov, N. N. Nedyalkov, T. Sakai, and M. Obara, “Localization of the electromagnetic field in the vicinity of gold nanoparticles: Surface modification of different substrates,” *Applied Surface Science*, vol. 254, no. 4, pp. 794–798, 2007.
- [9] K. Imura, T. Nagahara, and H. Okamoto, “Characteristic near-field spectra of single gold nanoparticles,” *Chemical Physics Letters*, vol. 400, no. 4-6, pp. 500–505, 2004.
- [10] G. Wiederrecht, “Near-field optical imaging of noble metal nanoparticles,” *The European Physical Journal-Applied Physics*, vol. 28, no. 1, pp. 3–18, 2004.
- [11] K. Tanabe, “Field enhancement around metal nanoparticles and nanoshells: a systematic investigation,” *The Journal of Physical Chemistry C*, vol. 112, no. 40, pp. 15 721–15 728, 2008.
- [12] R. Chakraborty, D. Leshem-Lev, and D. Fixler, “The scattering of gold nanorods in identification of macrophages,” in *Nanoscale Imaging, Sensing, and Actuation for Biomedical Applications XVI*, vol. 10891. International Society for Optics and Photonics, 2019, p. 108911A.

- [13] I. Fratoddi, I. Venditti, C. Battocchio, L. Carlini, S. Amatori, M. Porchia, F. Tisato, F. Bondino, E. Magnano, M. Pellei *et al.*, “Highly hydrophilic gold nanoparticles as carrier for anticancer copper (I) complexes: loading and release studies for biomedical applications,” *Nanomaterials*, vol. 9, no. 5, p. 772, 2019.
- [14] T. Kim, Q. Zhang, J. Li, L. Zhang, and J. V. Jokerst, “A gold/silver hybrid nanoparticle for treatment and photoacoustic imaging of bacterial infection,” *ACS Nano*, vol. 12, no. 6, pp. 5615–5625, 2018.
- [15] K. Eskandari, N. Mah-Heidari, M. Fasihi-Ramandi, M. Heiat, F. Dashtestani, M. Kamali, and D. Ashiani, “Gold-silver hybrid nanoparticles as a novel carrier for electrochemical study of redox protein,” *Journal of Applied Biotechnology Reports*, vol. 4, no. 4, pp. 695–699, 2017.
- [16] S. Carozza *et al.*, “Two-photon luminescence of gold nanorods: applications to single-particle tracking and spectroscopy,” Ph.D. dissertation, Leiden University, 2017.
- [17] C. Adura, S. Guerrero, E. Salas, L. Medel, A. Riveros, J. Mena, J. Arbiol, F. Albericio, E. Giralt, and M. J. Kogan, “Stable conjugates of peptides with gold nanorods for biomedical applications with reduced effects on cell viability,” *ACS Applied Materials & Interfaces*, vol. 5, no. 10, pp. 4076–4085, 2013.
- [18] X. Huang, S. Neretina, and M. A. El-Sayed, “Gold nanorods: from synthesis and properties to biological and biomedical applications,” *Advanced Materials*, vol. 21, no. 48, pp. 4880–4910, 2009.
- [19] G. Lin and M. Lewandowska, “Plasmon-enhanced fluorescence provided by silver nanoprisms for sensitive detection of sulfide,” *Sensors and Actuators B: Chemical*, vol. 292, pp. 241–246, 2019.
- [20] J. F. Li, C. Y. Li, and R. F. Aroca, “Plasmon-enhanced fluorescence spectroscopy,” *Chemical Society Reviews*, vol. 46, no. 13, pp. 3962–3979, 2017.
- [21] Y. Fu, J. Zhang, and J. R. Lakowicz, “Plasmon-enhanced fluorescence from single fluorophores end-linked to gold nanorods,” *Journal of the American Chemical Society*, vol. 132, no. 16, pp. 5540–5541, 2010.
- [22] T. Ming, L. Zhao, Z. Yang, H. Chen, L. Sun, J. Wang, and C. Yan, “Strong polarization dependence of plasmon-enhanced fluorescence on single gold nanorods,” *Nano Letters*, vol. 9, no. 11, pp. 3896–3903, 2009.
- [23] O. G. Tovmachenko, C. Graf, D. J. van den Heuvel, A. van Blaaderen, and H. C. Gerritsen, “Fluorescence enhancement by metal-core/silica-shell nanoparticles,” *Advanced Materials*, vol. 18, no. 1, pp. 91–95, 2006.
- [24] K. Aslan, J. R. Lakowicz, and C. D. Geddes, “Metal-enhanced fluorescence using anisotropic silver nanostructures: critical progress to date,” *Analytical and Bioanalytical Chemistry*, vol. 382, no. 4, pp. 926–933, 2005.
- [25] X. Wang, X. Bai, Z. Pang, J. Zhu, Y. Wu, H. Yang, Y. Qi, and X. Wen, “Surface-enhanced raman scattering by composite structure of gold nanocube-PMMA-gold film,” *Optical Materials Express*, vol. 9, no. 4, pp. 1872–1881, 2019.
- [26] B. Nikoobakht, J. Wang, and M. A. El-Sayed, “Surface-enhanced raman scattering of molecules adsorbed on gold nanorods: off-surface plasmon resonance condition,” *Chemical Physics Letters*, vol. 366, no. 1-2, pp. 17–23, 2002.

- [27] C. D. Keating, K. K. Kovaleski, and M. J. Natan, "Heightened electromagnetic fields between metal nanoparticles: surface enhanced raman scattering from metal- cytochrome c-metal sandwiches," *The Journal of Physical Chemistry B*, vol. 102, no. 47, pp. 9414–9425, 1998.
- [28] K. Ma, Y. Li, Z. Wang, Y. Chen, X. Zhang, C. Chen, H. Yu, J. Huang, Z. Yang, X. Wang *et al.*, "A core-shell gold nanorod@layered double hydroxide nanomaterial with high efficient photothermal conversion and its application in antibacterial and tumor therapy," *ACS Applied Materials & Interfaces*, 2019.
- [29] M. R. Ali, Y. Wu, and M. A. El-Sayed, "Gold-nanoparticle-assisted plasmonic photothermal therapy advances toward clinical application," *The Journal of Physical Chemistry C*, vol. 123, no. 25, pp. 15 375–15 393, 2019.
- [30] X. Huang and M. A. El-Sayed, "Gold nanoparticles: optical properties and implementations in cancer diagnosis and photothermal therapy," *Journal of Advanced Research*, vol. 1, no. 1, pp. 13–28, 2010.
- [31] H. Song, H. Ahn, T. Kim, Y. Lee, J.-r. Choi, and K. Kim, "Manipulation of light at the nanoscale for high-performance spectroscopic and optical applications," *Applied Spectroscopy Reviews*, vol. 54, no. 6, pp. 482–508, 2019.
- [32] M. A. Otte, M.-C. Estévez, D. Regatos, L. M. Lechuga, and B. Sepúlveda, "Guiding light in monolayers of sparse and random plasmonic meta-atoms," *ACS Nano*, vol. 5, no. 11, pp. 9179–9186, 2011.
- [33] S. A. Maier, P. G. Kik, and H. A. Atwater, "Optical pulse propagation in metal nanoparticle chain waveguides," *Physical Review B*, vol. 67, no. 20, p. 205402, 2003.
- [34] S. J. Tan, M. J. Campolongo, D. Luo, and W. Cheng, "Building plasmonic nanostructures with DNA," *Nature Nanotechnology*, vol. 6, no. 5, p. 268, 2011.
- [35] A. Block, M. Liebel, R. Yu, M. Spector, Y. Sivan, F. G. de Abajo, and N. F. van Hulst, "Tracking ultrafast hot-electron diffusion in space and time by ultrafast thermomodulation microscopy," *Science Advances*, vol. 5, no. 5, p. eaav8965, 2019.
- [36] N. Del Fatti, C. Voisin, M. Achermann, S. Tzortzakis, D. Christofilos, and F. Vallée, "Nonequilibrium electron dynamics in noble metals," *Physical Review B*, vol. 61, no. 24, p. 16956, 2000.
- [37] H. Inouye, K. Tanaka, I. Tanahashi, and K. Hirao, "Ultrafast dynamics of nonequilibrium electrons in a gold nanoparticle system," *Physical Review B*, vol. 57, no. 18, p. 11334, 1998.
- [38] B. Palpant, "Photothermal properties of gold nanoparticles," in *Gold nanoparticles for physics, biology and chemistry*, L. Catherine and P. Oliver, Eds. World Scientific, 2017.
- [39] M. G. Silva, D. C. Teles-Ferreira, C. Manzoni, L. Ganzer, L. Siman, C. R. Chaves, L. O. Ladeira, G. Cerullo, S. Longhi, S. De Silvestri *et al.*, "Ultrafast optical response of plasmonic structures beyond the perturbative regime: evidence of universal saturation dynamics," in *EPJ Web of Conferences*, vol. 205. EDP Sciences, 2019.
- [40] X. Wang, Y. Guillet, P. R. Selvakannan, H. Remita, and B. Palpant, "Broadband spectral signature of the ultrafast transient optical response of gold nanorods," *The Journal of Physical Chemistry C*, vol. 119, no. 13, pp. 7416–7427, 2015.
- [41] Y. Guillet, E. Charron, and B. Palpant, "Spectral dependence of the ultrafast optical response of nonspherical gold nanoparticles," *Physical Review B*, vol. 79, no. 19, p. 195432, 2009.

- [42] K.-H. Kim and S.-H. Choe, “Ultrafast nonlinear optical responses of dielectric composite materials containing metal nanoparticles with different sizes and shapes,” *Plasmonics*, vol. 12, no. 3, pp. 855–861, 2017.
- [43] Y. Takeda, O. A. Plaksin, and N. Kishimoto, “Dispersion of nonlinear dielectric function of Au nanoparticles in silica glass,” *Optics Express*, vol. 15, no. 10, pp. 6010–6018, 2007.
- [44] S. Link, C. Burda, M. Mohamed, B. Nikoobakht, and M. El-Sayed, “Femtosecond transient-absorption dynamics of colloidal gold nanorods: Shape independence of the electron-phonon relaxation time,” *Physical Review B*, vol. 61, no. 9, p. 6086, 2000.
- [45] V. Juvé, M. Scardamaglia, P. Maioli, A. Crut, S. Merabia, L. Joly, N. Del Fatti, and F. Vallée, “Cooling dynamics and thermal interface resistance of glass-embedded metal nanoparticles,” *Physical Review B*, vol. 80, no. 19, p. 195406, 2009.
- [46] N. Del Fatti and F. Vallee, “Ultrafast optical nonlinear properties of metal nanoparticles,” *Applied Physics B*, vol. 73, no. 4, pp. 383–390, 2001.
- [47] L. Douillard, F. Charra, C. Fiorini, P. M. Adam, R. Bachelot, S. Kostcheev, G. Lerondel, M. L. De La Chapelle, and P. Royer, “Optical properties of metal nanoparticles as probed by photoemission electron microscopy,” vol. 101, no. 8. AIP, 2007, p. 083518.
- [48] P. Lang, X. Song, B. Ji, H. Tao, Y. Dou, X. Gao, Z. Hao, and J. Lin, “Spatial- and energy-resolved photoemission electron from plasmonic nanoparticles in multiphoton regime,” *Optics Express*, vol. 27, no. 5, pp. 6878–6891, 2019.
- [49] T. Haug, P. Klemm, S. Bange, and J. M. Lupton, “Hot-electron intraband luminescence from single hot spots in noble-metal nanoparticle films,” *Physical Review Letters*, vol. 115, no. 6, p. 067403, 2015.
- [50] T. Labouret and B. Palpant, “Nonthermal model for ultrafast laser-induced plasma generation around a plasmonic nanorod,” *Physical Review B*, vol. 94, no. 24, p. 245426, 2016.
- [51] É. Boulais, R. Lachaine, and M. Meunier, “Plasma mediated off-resonance plasmonic enhanced ultrafast laser-induced nanocavitation,” *Nano Letters*, vol. 12, no. 9, pp. 4763–4769, 2012.
- [52] T. Labouret, J. F. Audibert, R. B. Pansu, and B. Palpant, “Plasmon-assisted production of reactive oxygen species by single gold nanorods,” *Small*, vol. 11, no. 35, pp. 4475–4479, 2015.
- [53] C. Hamon, C. Goldmann, and D. Constantin, “Controlling the symmetry of supercrystals formed by plasmonic core-shell nanorods with tunable cross-section,” *Nanoscale*, vol. 10, no. 38, pp. 18362–18369, 2018.
- [54] R. Jiang, H. Chen, L. Shao, Q. Li, and J. Wang, “Unraveling the evolution and nature of the plasmons in (Au core)–(Ag shell) nanorods,” *Advanced Materials*, vol. 24, no. 35, pp. OP200–OP207, 2012.
- [55] S. Hou, X. Hu, T. Wen, W. Liu, and X. Wu, “Core-shell noble metal nanostructures templated by gold nanorods,” *Advanced Materials*, vol. 25, no. 28, pp. 3857–3862, 2013.
- [56] G. Park, C. Lee, D. Seo, and H. Song, “Full-color tuning of surface plasmon resonance by compositional variation of Au@Ag core-shell nanocubes with sulfides,” *Langmuir*, vol. 28, no. 24, pp. 9003–9009, 2012.
- [57] K. Yu, G. You, L. Polavarapu, and Q.-H. Xu, “Bimetallic Au/Ag core-shell nanorods studied by ultrafast transient absorption spectroscopy under selective excitation,” *The Journal of Physical Chemistry C*, vol. 115, no. 29, pp. 14000–14005, 2011.

- [58] E. Cottancin, J. Lermé, M. Gaudry, M. Pellarin, J.-L. Vialle, M. Broyer, B. Prével, M. Treilleux, and P. Mélinon, “Size effects in the optical properties of Au_nAg_n embedded clusters,” *Physical Review B*, vol. 62, no. 8, p. 5179, 2000.
- [59] B. Dacosta Fernandes, M. Spuch-Calvar, H. Baida, M. Tréguer-Delapierre, J. Oberlé, P. Langot, and J. Burgin, “Acoustic vibrations of au nano-bipyramids and their modification under Ag deposition: a perspective for the development of nanobalances,” *ACS Nano*, vol. 7, no. 9, pp. 7630–7639, 2013.
- [60] A. Crut, P. Maioli, N. Del Fatti, and F. Vallée, “Time-domain investigation of the acoustic vibrations of metal nanoparticles: size and encapsulation effects,” *Ultrasonics*, vol. 56, pp. 98–108, 2015.
- [61] K. Yu, J. E. Sader, P. Zijlstra, M. Hong, Q.-H. Xu, and M. Orrit, “Probing silver deposition on single gold nanorods by their acoustic vibrations,” *Nano Letters*, vol. 14, no. 2, pp. 915–922, 2014.
- [62] M. F. Cardinal, D. Mongin, A. Crut, P. Maioli, B. Rodriguez-Gonzalez, J. Perez-Juste, L. M. Liz-Marzan, N. Del Fatti, and F. Vallée, “Acoustic vibrations in bimetallic Au@Pd core-shell nanorods,” *The Journal of Physical Chemistry Letters*, vol. 3, no. 5, pp. 613–619, 2012.
- [63] H. F. Zarick, A. Boulesbaa, E. M. Talbert, A. Poretzky, D. Geohegan, and R. Bardhan, “Ultrafast excited-state dynamics in shape-and composition-controlled gold-silver bimetallic nanostructures,” *The Journal of Physical Chemistry C*, vol. 121, no. 8, pp. 4540–4547, 2017.
- [64] M. Barth, S. Schietinger, S. Fischer, J. Becker, N. Nusse, T. Aichele, B. Löchel, C. Sonnichsen, and O. Benson, “Nanoassembled plasmonic-photonic hybrid cavity for tailored light-matter coupling,” *Nano Letters*, vol. 10, no. 3, pp. 891–895, 2010.
- [65] A. Jiménez-Solano, C. López-López, O. Sánchez-Sobrado, J. M. Luque, M. E. Calvo, C. Fernández-López, A. Sánchez-Iglesias, L. M. Liz-Marzán, and H. Míguez, “Integration of gold nanoparticles in optical resonators,” *Langmuir*, vol. 28, no. 24, pp. 9161–9167, 2012.
- [66] X. Wang and B. Palpant, “Large and ultrafast optical response of a one-dimensional plasmonic-photonic cavity,” *Plasmonics*, vol. 8, no. 4, pp. 1647–1653, 2013.
- [67] X. Wang, R. Morea, J. Gonzalo, and B. Palpant, “Coupling localized plasmonic and photonic modes tailors and boosts ultrafast light modulation by gold nanoparticles,” *Nano Letters*, vol. 15, no. 4, pp. 2633–2639, 2015.
- [68] M. Hensen, B. Huber, D. Friedrich, E. Krauss, S. Pres, P. Grimm, D. Fersch, J. Lüttig, V. Lisinetskii, B. Hecht, and T. Brixner, “Spatial variations in femtosecond field dynamics within a plasmonic nanoresonator mode,” *Nano Lett.*, vol. 19, no. 7, pp. 4651–4658, 2019.
- [69] A. N. Koya, B. Ji, Z. Hao, and J. Lin, “Coherent control of gap plasmons of a complex nanosystem by shaping driving femtosecond pulses,” *Plasmonics*, vol. 12, no. 6, pp. 1693–1699, 2017.
- [70] X. Hou, “Nano-objets photo-activés pour le ciblage cellulaire et l’hyperthermie,” Ph.D. dissertation, Université Paris-Saclay, 2019.
- [71] T. Labouret, “Irradiation laser ultrabrève de nanobâtonnets d’or individuels en milieu aqueux: photo-génération de phénomènes d’intérêt biomédical,” Ph.D. dissertation, Université Paris-Saclay, 2016.
- [72] X. Wang, “Photo-induced ultrafast optical and thermal responses of gold nanoparticles,” Ph.D. dissertation, Université Pierre et Marie Curie-Paris 6, 2013.

- [73] Y. Guillet, “Dynamique de la réponse optique non-linéaire ultra-rapide d’une assemblée de nanoparticules d’or,” Ph.D. dissertation, Université Pierre et Marie Curie-Paris 6, 2007.
- [74] T. Li and W. A. Schroeder, “Nonparametric modeling of face-centered cubic metal photocathodes,” *arXiv preprint arXiv:1704.05371*, 2017.
- [75] T.-S. Choy, J. Naset, S. Hershfield, C. Stanton, and J. Chen, *A database of Fermi surfaces in virtual reality modeling language*, 2000 (accessed October 11, 2019). [Online]. Available: <http://www.phys.ufl.edu/fermisurface/>
- [76] N. W. Ashcroft and N. D. Mermin, *Solid state physics*. Saunders college, Philadelphia, 1976.
- [77] X. Wang, D. M. Riffe, Y.-S. Lee, and M. Downer, “Time-resolved electron-temperature measurement in a highly excited gold target using femtosecond thermionic emission,” *Physical Review B*, vol. 50, no. 11, p. 8016, 1994.
- [78] D. M. Riffe, X. Wang, M. C. Downer, D. Fisher, T. Tajima, J. L. Erskine, and R. More, “Femtosecond thermionic emission from metals in the space-charge-limited regime,” *JOSA B*, vol. 10, no. 8, pp. 1424–1435, 1993.
- [79] Z. Lin, L. V. Zhigilei, and V. Celli, “Electron-phonon coupling and electron heat capacity of metals under conditions of strong electron-phonon nonequilibrium,” *Physical Review B*, vol. 77, no. 7, p. 075133, 2008.
- [80] A. M. Brown, R. Sundararaman, P. Narang, W. A. Goddard III, and H. A. Atwater, “Ab initio phonon coupling and optical response of hot electrons in plasmonic metals,” *Physical Review B*, vol. 94, no. 7, p. 075120, 2016.
- [81] J. M. Ziman, *Electrons and phonons: the theory of transport phenomena in solids*. Oxford University Press, 2001.
- [82] W. M. Haynes, *CRC handbook of chemistry and physics*. CRC Press, 2014.
- [83] C. F. Bohren and D. R. Huffman, *Absorption and scattering of light by small particles*. John Wiley & Sons, 2008.
- [84] P. B. Johnson and R.-W. Christy, “Optical constants of the noble metals,” *Physical Review B*, vol. 6, no. 12, p. 4370, 1972.
- [85] E. D. Palik, *Handbook of optical constants of solids*. Academic Press, 1998, vol. 3.
- [86] N. Blanchard, C. Smith, D. Martin, D. Hayton, T. Jenkins, and P. Weightman, “High-resolution measurements of the bulk dielectric constants of single crystal gold with application to reflection anisotropy spectroscopy,” *Physica Status Solidi (C)*, no. 8, pp. 2931–2937, 2003.
- [87] R. L. Olmon, B. Slovick, T. W. Johnson, D. Shelton, S.-H. Oh, G. D. Boreman, and M. B. Raschke, “Optical dielectric function of gold,” *Physical Review B*, vol. 86, no. 23, p. 235147, 2012.
- [88] H. U. Yang, J. D’Archangel, M. L. Sundheimer, E. Tucker, G. D. Boreman, and M. B. Raschke, “Optical dielectric function of silver,” *Physical Review B*, vol. 91, no. 23, p. 235137, 2015.
- [89] A. Marini, M. Conforti, G. Della Valle, H. W. Lee, T. X. Tran, W. Chang, M. A. Schmidt, S. Longhi, P. S. J. Russell, and F. Biancalana, “Thermo-modulational interband susceptibility and ultrafast temporal dynamics in nonlinear gold-based plasmonic devices,” *New Journal of Physics*, vol. 15, pp. 1367–2630, 2013.

- [90] R. Rosei, F. Antonangeli, and U. Grassano, "D bands position and width in gold from very low temperature thermomodulation measurements," *Surface Science*, vol. 37, pp. 689–699, 1973.
- [91] M. Guerrisi, R. Rosei, and P. Winsemius, "Splitting of the interband absorption edge in Au," *Physical Review B*, vol. 12, no. 2, p. 557, 1975.
- [92] R. Rosei, "Temperature modulation of the optical transitions involving the fermi surface in Ag: Theory," *Physical Review B*, vol. 10, no. 2, p. 474, 1974.
- [93] F. Antonangeli, E. Colavita, R. Rosei, and S. Salusti, "Optical gaps and interband matrix elements of silver as a function of temperature," *Il Nuovo Cimento B (1971-1996)*, vol. 24, no. 1, pp. 121–129, 1974.
- [94] J. Lindhard, "On the properties of a gas of charged particles," *Danske Matematisk-fysiske Meddeleiser*, vol. 28, no. 8, pp. 1–57, 1954.
- [95] L. Di Mario, T. O. Otomalo, D. Catone, P. O’Keeffe, L. Tian, S. Turchini, B. Palpant, and F. Martelli, "Time-dependent optical response of three-dimensional Au nanoparticle arrays formed on silica nanowires," *Physical Review B*, vol. 97, no. 11, p. 115448, 2018.
- [96] T. Stoll, "Ultrafast electronic, acoustic and thermal properties of metal nanoparticles and clusters," Ph.D. dissertation, Universit ´e Claude Bernard Lyon 1, 2014.
- [97] R. Gurzhi, "Mutual electron correlations in metal optics," *Sov. Phys. JETP*, vol. 8, no. 4, pp. 673–675, 1959.
- [98] C.-Y. Tsai, C.-Y. Tsai, C.-H. Chen, T.-L. Sung, T.-Y. Wu, and F.-P. Shih, "Theoretical model for intravalley and intervalley free-carrier absorption in semiconductor lasers: Beyond the classical Drude model," *IEEE Journal of Quantum Electronics*, vol. 34, no. 3, pp. 552–559, 1998.
- [99] T. Stoll, P. Maioli, A. Crut, N. Del Fatti, and F. Vallée, "Advances in femto-nano-optics: ultrafast nonlinearity of metal nanoparticles," *The European Physical Journal B*, vol. 87, no. 11, p. 260, 2014.
- [100] B. Palpant, B. Prével, J. Lermé, E. Cottancin, M. Pellarin, M. Treilleux, A. Perez, J. Vialle, and M. Broyer, "Optical properties of gold clusters in the size range 2–4 nm," *Physical Review B*, vol. 57, no. 3, p. 1963, 1998.
- [101] J. M. Ziman, *Principles of the theory of Solids*. Cambridge University Press, 1972.
- [102] O. Kvítek, J. Siegel, V. Hnatowicz, and V. Švorčík, "Noble metal nanostructures influence of structure and environment on their optical properties," *Journal of Nanomaterials*, vol. 2013, p. 111, 2013.
- [103] Y. R. Davletshin, A. Lombardi, M. F. Cardinal, V. Juvé, A. Crut, P. Maioli, L. M. Liz-Marzan, F. Vallée, N. D. Fatti, and J. C. Kumaradas, "A quantitative study of the environmental effects on the optical response of gold nanorods," *ACS Nano*, vol. 6, no. 9, pp. 8183–8193, 2012.
- [104] X. Huang, S. Neretina, and M. A. El-Sayed, "Gold nanorods: from synthesis and properties to biological and biomedical applications," *Advanced Materials*, vol. 21, no. 48, pp. 4880–4910, 2009.
- [105] C. L. Nehl, H. Liao, and J. H. Hafner, "Optical properties of star-shaped gold nanoparticles," *Nano Letters*, vol. 6, no. 4, pp. 683–688, 2006.

- [106] S. W. Prescott and P. Mulvaney, "Gold nanorod extinction spectra," *Journal of Applied Physics*, vol. 99, no. 12, p. 123504, 2006.
- [107] R. Gans, "Über die form ultramikroskopischer Goldteilchen," *Annalen der Physik*, vol. 342, no. 5, pp. 881–900, 1912.
- [108] D. Constantin, "Why the aspect ratio? shape equivalence for the extinction spectra of gold nanoparticles," *The European Physical Journal E*, vol. 38, no. 11, p. 116, 2015.
- [109] R. Gans, "Über die form ultramikroskopischer Silberteilchen," *Annalen der Physik*, vol. 352, no. 10, pp. 270–284, 1915.
- [110] S. Marhaba, "Effect of size, shape and environment on the optical response of metallic nanoparticles," in *Noble and precious metals-Properties, nanoscale effects and applications*. IntechOpen, 2017.
- [111] S. Eustis and M. A. El-Sayed, "Determination of the aspect ratio statistical distribution of gold nanorods in solution from a theoretical fit of the observed inhomogeneously broadened longitudinal plasmon resonance absorption spectrum," *Journal of Applied Physics*, vol. 100, no. 4, p. 044324, 2006.
- [112] Y. Hong, Y.-M. Huh, D. S. Yoon, and J. Yang, "Nanobiosensors based on localized surface plasmon resonance for biomarker detection," *Journal of Nanomaterials*, vol. 2012, p. 111, 2012.
- [113] O. Muskens, D. Christofilos, N. Del Fatti, and F. Vallée, "Optical response of a single noble metal nanoparticle," *Journal of Optics A: Pure and Applied Optics*, vol. 8, no. 4, p. S264, 2006.
- [114] J.-C. M. Garnett, "Colours in metal glasses and in metallic films," *Philosophical Transactions of the Royal Society of London. Series A, containing papers of a mathematical or physical character*, vol. 203, no. 359-371, pp. 385–420, 1904.
- [115] J.-C. M. Garnett, "Colours in metal glasses, in metallic films, and in metallic solutions," *Philosophical Transactions of the Royal Society of London. Series A, containing papers of a mathematical or physical character*, vol. 205, no. 387-401, pp. 237–288, 1906.
- [116] T. Yamaguchi, S. Yoshida, and A. Kinbara, "Optical effect of the substrate on the anomalous absorption of aggregated silver films," *Thin Solid Films*, vol. 21, no. 1, pp. 173–187, 1974.
- [117] M. Rashidi Huyeh, "Influence des effets thermiques sur la réponse optique de matériaux nanocomposites métal-diélectrique," Ph.D. dissertation, Université Pierre et Marie Curie-Paris 6, 2006.
- [118] V. A. Markel, "Introduction to the Maxwell Garnett approximation: tutorial," *JOSA A*, vol. 33, no. 7, pp. 1244–1256, 2016.
- [119] J. Toudert, D. Babonneau, L. Simonot, S. Camelio, and T. Girardeau, "Quantitative modelling of the surface plasmon resonances of metal nanoclusters sandwiched between dielectric layers: the influence of nanocluster size, shape and organization," *Nanotechnology*, vol. 19, no. 12, p. 125709, 2008.
- [120] M. L. Protopapa, "Surface plasmon resonance of metal nanoparticles sandwiched between dielectric layers: theoretical modelling," *Applied Optics*, vol. 48, no. 4, pp. 778–785, 2009.
- [121] V. Fedotov, V. Emel'yanov, K. MacDonald, and N. Zheludev, "Optical properties of closely packed nanoparticle films: spheroids and nanoshells," *Journal of Optics A: Pure and Applied Optics*, vol. 6, no. 2, p. 155, 2003.

- [122] S. Camelio, *Eclairage sur les propriétés optiques des matériaux nanostructurés*, Habilitation a Diriger des Recherches. Université de Poitiers, 2010.
- [123] E. M. Purcell and C. R. Pennypacker, “Scattering and absorption of light by nonspherical dielectric grains,” *The Astrophysical Journal*, vol. 186, pp. 705–714, 1973.
- [124] B. T. Draine and P. J. Flatau, “Discrete-dipole approximation for scattering calculations,” *JOSA A*, vol. 11, no. 4, pp. 1491–1499, 1994.
- [125] B. T. Draine and P. J. Flatau, “Discrete-dipole approximation for periodic targets: theory and tests,” *JOSA A*, vol. 25, no. 11, pp. 2693–2703, 2008.
- [126] P. Flatau and B. T. Draine, “Fast near field calculations in the discrete dipole approximation for regular rectilinear grids,” *Optics Express*, vol. 20, no. 2, pp. 1247–1252, 2012.
- [127] K. Yee, “Numerical solution of initial boundary value problems involving Maxwell’s equations in isotropic media,” *IEEE Transactions on Antennas and Propagation*, vol. 14, no. 3, pp. 302–307, 1966.
- [128] F. G. De Abajo and A. Howie, “Retarded field calculation of electron energy loss in inhomogeneous dielectrics,” *Physical Review B*, vol. 65, no. 11, p. 115418, 2002.
- [129] J.-W. Liaw, “Simulation of surface plasmon resonance of metallic nanoparticles by the boundary-element method,” *JOSA A*, vol. 23, no. 1, pp. 108–116, 2006.
- [130] U. Hohenester and A. Trügler, “MNPBEM—a matlab toolbox for the simulation of plasmonic nanoparticles,” *Computer Physics Communications*, vol. 183, no. 2, pp. 370–381, 2012.
- [131] C. Rockstuhl, M. G. Salt, and H. P. Herzig, “Application of the boundary-element method to the interaction of light with single and coupled metallic nanoparticles,” *JOSA A*, vol. 20, no. 10, pp. 1969–1973, 2003.
- [132] P. Waterman, “Matrix formulation of electromagnetic scattering,” *Proceedings of the IEEE*, vol. 53, no. 8, pp. 805–812, 1965.
- [133] L. Zhao, K. L. Kelly, and G. C. Schatz, “The extinction spectra of silver nanoparticle arrays: influence of array structure on plasmon resonance wavelength and width,” *The Journal of Physical Chemistry B*, vol. 107, no. 30, pp. 7343–7350, 2003.
- [134] M. I. Mishchenko, L. D. Travis, and D. W. Mackowski, “T-matrix computations of light scattering by nonspherical particles: a review,” *Journal of Quantitative Spectroscopy and Radiative Transfer*, vol. 55, no. 5, pp. 535–575, 1996.
- [135] V. Juvé, M. Scardamaglia, P. Maioli, A. Crut, S. Merabia, L. Joly, N. Del Fatti, and F. Vallée, “Cooling dynamics and thermal interface resistance of glass-embedded metal nanoparticles,” *Physical Review B*, vol. 80, no. 19, p. 195406, 2009.
- [136] F. Banfi, V. Juvé, D. Nardi, S. Dal Conte, C. Giannetti, G. Ferrini, N. Del Fatti, and F. Vallée, “Temperature dependence of the thermal boundary resistivity of glass-embedded metal nanoparticles,” *Applied Physics Letters*, vol. 100, no. 1, p. 011902, 2012.
- [137] G. V. Hartland, “Optical studies of dynamics in noble metal nanostructures,” *Chemical Reviews*, vol. 111, no. 6, pp. 3858–3887, 2011.
- [138] E. Galopin, J. Barbillat, Y. Coffinier, S. Szunerits, G. Patriarche, and R. Boukherroub, “Silicon nanowires coated with silver nanostructures as ultrasensitive interfaces for surface-enhanced Raman spectroscopy,” *ACS Applied Materials & Interfaces*, vol. 1, no. 7, pp. 1396–1403, 2009.

- [139] D. Naumenko, V. Zannier, V. Grillo, D. Cassese, G. Priante, S. Dal Zilio, S. Rubini, and M. Lazzarino, “Enhanced plasmonic properties of gold-catalysed semiconductor nanowires,” *Nanoscale*, vol. 6, no. 22, pp. 13 651–13 659, 2014.
- [140] N. D. Hoa, P. Van Tong, N. Van Duy, T. Dao, H. Chung, T. Nagao, N. Van Hieu *et al.*, “Effective decoration of Pd nanoparticles on the surface of SnO_2 nanowires for enhancement of CO gas-sensing performance,” *Journal of Hazardous Materials*, vol. 265, pp. 124–132, 2014.
- [141] M. S. Saha, R. Li, M. Cai, and X. Sun, “High electrocatalytic activity of platinum nanoparticles on SnO_2 nanowire-based electrodes,” *Electrochemical and Solid-State Letters*, vol. 10, no. 8, pp. B130–B133, 2007.
- [142] W. Dong, H. Huang, Y. Zhu, X. Li, X. Wang, C. Li, B. Chen, G. Wang, and Z. Shi, “Room-temperature solution synthesis of Ag nanoparticle functionalized molybdenum oxide nanowires and their catalytic applications,” *Nanotechnology*, vol. 23, no. 42, p. 425602, 2012.
- [143] W. H. Hung, M. Aykol, D. Valley, W. Hou, and S. B. Cronin, “Plasmon resonant enhancement of carbon monoxide catalysis,” *Nano Letters*, vol. 10, no. 4, pp. 1314–1318, 2010.
- [144] S. Navalon, M. de Miguel, R. Martin, M. Alvaro, and H. Garcia, “Enhancement of the catalytic activity of supported gold nanoparticles for the fenton reaction by light,” *Journal of the American Chemical Society*, vol. 133, no. 7, pp. 2218–2226, 2011.
- [145] A. Convertino, M. Cuscunà, F. Martelli, M. G. Manera, and R. Rella, “Silica nanowires decorated with metal nanoparticles for refractive index sensors: three-dimensional metal arrays and light trapping at plasmonic resonances,” *The Journal of Physical Chemistry C*, vol. 118, no. 1, pp. 685–690, 2013.
- [146] A. Convertino, M. Cuscuna, and F. Martelli, “Optical reflectivity from highly disordered Si nanowire films,” *Nanotechnology*, vol. 21, no. 35, p. 355701, 2010.
- [147] G. V. Hartland, “Coherent excitation of vibrational modes in metallic nanoparticles,” *Annu. Rev. Phys. Chem.*, vol. 57, pp. 403–430, 2006.
- [148] J. Hodak, I. Martini, and G. V. Hartland, “Ultrafast study of electron–phonon coupling in colloidal gold particles,” *Chemical Physics Letters*, vol. 284, no. 1-2, pp. 135–141, 1998.
- [149] A. Arbouet, C. Voisin, D. Christofilos, P. Langot, N. Del Fatti, F. Vallée, J. Lermé, G. Celep, E. Cottancin, M. Gaudry, M. Pellarin, M. Broyer, M. P. Maillard, Pileni, and M. Treguer, “Electron-phonon scattering in metal clusters,” *Physical Review Letters*, vol. 90, no. 17, p. 177401, 2003.
- [150] N. P. Bansal and R. H. Doremus, *Handbook of glass properties*. Elsevier, 2013.
- [151] R. Guereca, H. Richardson, J. Gordon, J. Walker, and J. Cooper, “Thermophysical properties of selected gases below 300 k,” Bureau of Mines, Amarillo, Tex. Helium Research Center, Tech. Rep., 1965.
- [152] Y. Guillet, M. Rashidi-Huyeh, and B. Palpant, “Influence of laser pulse characteristics on the hot electron contribution to the third-order nonlinear optical response of gold nanoparticles,” *Physical Review B*, vol. 79, no. 4, p. 045410, 2009.
- [153] S. Link, M. Mohamed, and M. El-Sayed, “Simulation of the optical absorption spectra of gold nanorods as a function of their aspect ratio and the effect of the medium dielectric constant,” *The Journal of Physical Chemistry B*, vol. 103, no. 16, pp. 3073–3077, 1999.

- [154] A. Wokaun, J. Gordon, and P. Liao, "Radiation damping in surface-enhanced raman scattering," *Physical Review Letters*, vol. 48, no. 14, p. 957, 1982.
- [155] M. Perner, P. Bost, U. Lemmer, G. Von Plessen, J. Feldmann, U. Becker, M. Mennig, M. Schmitt, and H. Schmidt, "Optically induced damping of the surface plasmon resonance in gold colloids," *Physical Review Letters*, vol. 78, no. 11, p. 2192, 1997.
- [156] H. Baida, D. Mongin, D. Christofilos, G. Bachelier, A. Crut, P. Maioli, N. Del Fatti, and F. Vallée, "Ultrafast nonlinear optical response of a single gold nanorod near its surface plasmon resonance," *Physical Review Letters*, vol. 107, no. 5, p. 057402, 2011.
- [157] J.-Y. Bigot, V. Halté, J.-C. Merle, and A. Daunois, "Electron dynamics in metallic nanoparticles," *Chemical Physics*, vol. 251, no. 1-3, pp. 181–203, 2000.
- [158] S. Mukherjee, F. Libisch, N. Large, O. Neumann, L. V. Brown, J. Cheng, J. B. Lassiter, E. A. Carter, P. Nordlander, and N. J. Halas, "Hot electrons do the impossible: plasmon-induced dissociation of H_2 on Au," *Nano Letters*, vol. 13, no. 1, pp. 240–247, 2012.
- [159] I. Haidar, A. Day, P. Decorse, S. Lau-Truong, A. Chevillot-Biraud, J. Aubard, N. Félidj, and L. Boubekeur-Lecaque, "Tailoring the shape of anisotropic core-shell Au-Ag nanoparticles in dimethyl sulfoxide," *Chemistry of Materials*, vol. 31, no. 8, pp. 2741–2749, 2019.
- [160] S. Link and M. El-Sayed, "Simulation of the optical absorption spectra of gold nanorods as a function of their aspect ratio and the effect of the medium dielectric constant," *The Journal of Physical Chemistry B*, vol. 109, no. 20, pp. 10 531–10 532, 2005.
- [161] X. Huang, I. H. El-Sayed, W. Qian, and M. A. El-Sayed, "Cancer cell imaging and photothermal therapy in the near-infrared region by using gold nanorods," *Journal of the American Chemical Society*, vol. 128, no. 6, pp. 2115–2120, 2006.
- [162] S. Gomez-Grana, B. Goris, T. Altantzis, C. Fernandez-Lopez, E. Carbo-Argibay, A. Guerrero-Martínez, N. Almora-Barrios, N. Lopez, I. Pastoriza-Santos, J. Perez-Juste *et al.*, "Au@Ag nanoparticles: halides stabilize {100} facets," *The Journal of Physical Chemistry Letters*, vol. 4, no. 13, pp. 2209–2216, 2013.
- [163] M. B. Cortie, F. Liu, M. D. Arnold, and Y. Niidome, "Multimode resonances in silver nanocuboids," *Langmuir*, vol. 28, no. 24, pp. 9103–9112, 2012.
- [164] A.-M. Hada, M. Potara, S. Suarasan, A. Vulpoi, T. Nagy-Simon, E. Licarete, and S. Astilean, "Fabrication of gold-silver core-shell nanoparticles for performing as ultrabright sers-nanotags inside human ovarian cancer cells," *Nanotechnology*, vol. 30, no. 31, p. 315701, 2019.
- [165] L. Wu, Z. Wang, S. Zong, Z. Huang, P. Zhang, and Y. Cui, "A SERS-based immunoassay with highly increased sensitivity using gold/silver core-shell nanorods," *Biosensors and Bioelectronics*, vol. 38, no. 1, pp. 94–99, 2012.
- [166] X. Yang, Y. Wang, Y. Liu, and X. Jiang, "A sensitive hydrogen peroxide and glucose biosensor based on gold/silver core-shell nanorods," *Electrochimica Acta*, vol. 108, pp. 39–44, 2013.
- [167] Z. Gao, K. Deng, X.-D. Wang, M. Miro, and D. Tang, "High-resolution colorimetric assay for rapid visual readout of phosphatase activity based on gold/silver core/shell nanorod," *ACS Applied Materials & Interfaces*, vol. 6, no. 20, pp. 18 243–18 250, 2014.
- [168] M. Hu, X. Wang, G. V. Hartland, P. Mulvaney, J. P. Juste, and J. E. Sader, "Vibrational response of nanorods to ultrafast laser induced heating: theoretical and experimental analysis," *Journal of the American Chemical Society*, vol. 125, no. 48, pp. 14 925–14 933, 2003.

- [169] R. Kodiyath, S. T. Malak, Z. A. Combs, T. Koenig, M. A. Mahmoud, M. A. El-Sayed, and V. V. Tsukruk, "Assemblies of silver nanocubes for highly sensitive sers chemical vapor detection," *Journal of Materials Chemistry A*, vol. 1, no. 8, pp. 2777–2788, 2013.
- [170] H. Baida, D. Mongin, D. Christofilos, G. Bachelier, A. Crut, P. Maioli, N. Del Fatti, and F. Vallée, "Ultrafast nonlinear optical response of a single gold nanorod near its surface plasmon resonance," *Physical Review Letters*, vol. 107, no. 5, p. 057402, 2011.
- [171] D. Mongin, P. Maioli, J. Burgin, P. Langot, E. Cottancin, S. D'addato, B. Canut, M. Treguer, A. Crut, F. Vallée *et al.*, "Ultrafast electron-lattice thermalization in copper and other noble metal nanoparticles," *Journal of Physics: Condensed Matter*, vol. 31, no. 8, p. 084001, 2019.
- [172] B. S. Yilbas, "Laser short-pulse heating of gold–copper two-layer assembly: thermo-elasto-plastic analysis," *Japanese Journal of Applied Physics*, vol. 41, no. 8R, p. 5226, 2002.
- [173] B. S. Yilbas, "Laser short-pulse heating of gold–silver assembly: entropy generation due to heat and electricity flows in electron subsystem," *Numerical Heat Transfer, Part A: Applications*, vol. 49, no. 9, pp. 873–891, 2006.
- [174] M. Perner, "Optische Untersuchung der Elektronen-und Gitterdynamik in Edelmetall-Nanopartikeln," Ph.D. dissertation, Ludwig-Maximilians-Universität München, 1999.
- [175] W.-S. Chang, B. Willingham, L. S. Slaughter, S. Dominguez-Medina, P. Swanglap, and S. Link, "Radiative and nonradiative properties of single plasmonic nanoparticles and their assemblies," *Accounts of Chemical Research*, vol. 45, no. 11, pp. 1936–1945, 2012.
- [176] H. Raether, "Surface plasmons on smooth surfaces," in *Surface plasmons on smooth and rough surfaces and on gratings*. Springer, 1988, pp. 4–39.
- [177] F. Hao and P. Nordlander, "Efficient dielectric function for FDTD simulation of the optical properties of silver and gold nanoparticles," *Chemical Physics Letters*, vol. 446, no. 1-3, pp. 115–118, 2007.
- [178] A. D. Rakić, A. B. Djurišić, J. M. Elazar, and M. L. Majewski, "Optical properties of metallic films for vertical-cavity optoelectronic devices," *Applied Optics*, vol. 37, no. 22, pp. 5271–5283, 1998.
- [179] A. Vial and T. Laroche, "Comparison of gold and silver dispersion laws suitable for FDTD simulations," *Applied physics B*, vol. 93, no. 1, pp. 139–143, 2008.
- [180] A. F. Oskooi, D. Roundy, M. Ibanescu, P. Bermel, J. D. Joannopoulos, and S. G. Johnson, "MEEP: a flexible free-software package for electromagnetic simulations by the FDTD method," *Computer Physics Communications*, vol. 181, no. 3, pp. 687–702, 2010.
- [181] M. Han, R. W. Dutton, and S. Fan, "Model dispersive media in finite-difference time-domain method with complex-conjugate pole-residue pairs," *IEEE Microwave and Wireless Components Letters*, vol. 16, no. 3, pp. 119–121, 2006.
- [182] E. Richards, "Applications of vector fitting in the solution of electromagnetic field interactions," Ph.D. dissertation, Arizona State University, 2014.
- [183] A. Deinega and S. John, "Effective optical response of silicon to sunlight in the finite-difference time-domain method," *Optics Letters*, vol. 37, no. 1, pp. 112–114, 2012.
- [184] L. Han, "Simulation of optical devices and circuits using time domain methods," Ph.D. dissertation, McMaster University, 2012.

- [185] H. Lin, M. F. Pantoja, L. D. Angulo, J. Alvarez, R. G. Martin, and S. G. Garcia, “FDTD modeling of graphene devices using complex conjugate dispersion material model,” *IEEE Microwave and Wireless Components Letters*, vol. 22, no. 12, pp. 612–614, 2012.
- [186] M. A. Alsunaidi and A. A. Al-Jabr, “A general ADE-FDTD algorithm for the simulation of dispersive structures,” *IEEE Photonics Technology Letters*, vol. 21, no. 12, pp. 817–819, 2009.
- [187] D. Deschrijver, M. Mrozowski, T. Dhaene, and D. De Zutter, “Macromodeling of multiport systems using a fast implementation of the vector fitting method,” *IEEE Microwave and Wireless Components Letters*, vol. 18, no. 6, pp. 383–385, 2008.
- [188] B. Gustavsen, “Improving the pole relocating properties of vector fitting,” *IEEE Transactions on Power Delivery*, vol. 21, no. 3, pp. 1587–1592, 2006.
- [189] B. Gustavsen and A. Semlyen, “Rational approximation of frequency domain responses by vector fitting,” *IEEE Transactions on Power Delivery*, vol. 14, no. 3, pp. 1052–1061, 1999.
- [190] L. Han, D. Zhou, K. Li, X. Li, and W.-P. Huang, “A rational-fraction dispersion model for efficient simulation of dispersive material in FDTD method,” *Journal of Lightwave Technology*, vol. 30, no. 13, pp. 2216–2225, 2012.
- [191] J. P. Berenger, “A perfectly matched layer for the absorption of electromagnetic waves,” *Journal of Computational Physics*, vol. 114, no. 2, pp. 185–200, 1994.
- [192] J.-P. Berenger, “Three-dimensional perfectly matched layer for the absorption of electromagnetic waves,” *Journal of Computational Physics*, vol. 127, no. 2, pp. 363–379, 1996.
- [193] A. Taflove, S. C. Hagness, and M. Picket-May, “Computational electromagnetics: the finite-difference time-domain method,” in *The electrical engineering handbook*, W.-K. Chen, Ed., 2005.
- [194] A. F. Oskooi, C. Kottke, and S. G. Johnson, “Accurate finite-difference time-domain simulation of anisotropic media by subpixel smoothing,” *Optics Letters*, vol. 34, no. 18, pp. 2778–2780, 2009.
- [195] P. Zilio, M. Dipalo, F. Tantussi, G. C. Messina, and F. De Angelis, “Hot electrons in water: Injection and ponderomotive acceleration by means of plasmonic nanoelectrodes,” *Light Sci. Appl.*, vol. 6, no. 6, p. e17002, 2017.
- [196] S. G. Johnson, A. Mekis, S. Fan, and J. D. Joannopoulos, “Molding the flow of light,” *Computing in Science & Engineering*, vol. 3, no. 6, p. 38, 2001.
- [197] E. Hecht, *Optics*. Pearson Education, 2005.
- [198] Y. Zhu, D. J. Gauthier, S. Morin, Q. Wu, H. Carmichael, and T. Mossberg, “Vacuum Rabi splitting as a feature of linear-dispersion theory: Analysis and experimental observations,” *Physical Review Letters*, vol. 64, no. 21, p. 2499, 1990.
- [199] R. Ameling and H. Giessen, “Microcavity plasmonics: strong coupling of photonic cavities and plasmons,” *Laser & Photonics Reviews*, vol. 7, no. 2, pp. 141–169, 2013.
- [200] J. P. Long and B. Simpkins, “Coherent coupling between a molecular vibration and Fabry–Perot optical cavity to give hybridized states in the strong coupling limit,” *ACS Photonics*, vol. 2, no. 1, pp. 130–136, 2014.
- [201] B. Simpkins, K. P. Fears, W. J. Dressick, B. T. Spann, A. D. Dunkelberger, and J. C. Owrutsky, “Spanning strong to weak normal mode coupling between vibrational and Fabry–

- Perot cavity modes through tuning of vibrational absorption strength,” *ACS Photonics*, vol. 2, no. 10, pp. 1460–1467, 2015.
- [202] X. Shi, K. Ueno, T. Oshikiri, Q. Sun, K. Sasaki, and H. Misawa, “Enhanced water splitting under modal strong coupling conditions,” *Nature Nanotechnology*, vol. 13, p. 1, 2018.
- [203] X. Yu, Y. Yuan, J. Xu, K.-T. Yong, J. Qu, and J. Song, “Strong coupling in microcavity structures: Principle, design, and practical application,” *Laser & Photonics Reviews*, vol. 13, no. 1, p. 1800219, 2019.
- [204] V. Savona, L. Andreani, P. Schwendimann, and A. Quattropani, “Quantum well excitons in semiconductor microcavities: Unified treatment of weak and strong coupling regimes,” *Solid State Communications*, vol. 93, no. 9, pp. 733–739, 1995.
- [205] J. P. Reithmaier, G. Şek, A. Löffler, C. Hofmann, S. Kuhn, S. Reitzenstein, L. V. Keldysh, V. D. Kulakovskii, T. L. Reinecke, and A. Forchel, “Strong coupling in a single quantum dot–semiconductor microcavity system,” *Nature*, vol. 432, no. 7014, p. 197, 2004.
- [206] L. C. Andreani, G. Panzarini, and J.-M. Gérard, “Strong-coupling regime for quantum boxes in pillar microcavities: Theory,” *Physical Review B*, vol. 60, no. 19, p. 13276, 1999.
- [207] F. Castro and B. Nabet, “Numerical computation of the complex dielectric permittivity using Hilbert transform and FFT techniques,” *Journal of the Franklin Institute*, vol. 336, no. 1, pp. 53–64, 1999.
- [208] L. Scarabelli, M. Grzelczak, and L. M. Liz-Marzan, “Tuning gold nanorod synthesis through prereduction with salicylic acid,” *Chemistry of Materials*, vol. 25, no. 21, pp. 4232–4238, 2013.
- [209] X. Ye, L. Jin, H. Caglayan, J. Chen, G. Xing, C. Zheng, V. Doan-Nguyen, Y. Kang, N. Engheta, C. R. Kagan, and C. B. Murray, “Improved size-tunable synthesis of monodisperse gold nanorods through the use of aromatic additives,” *ACS Nano*, vol. 6, no. 3, pp. 2804–2817, 2012.

Titre : Réponse optique ultrarapide de nanoparticules plasmoniques complexes

Mots clés : plasmonique, nanoparticules, ultrarapide, champ proche

Résumé : Les propriétés remarquables associées à la résonance plasmon localisée (LSPR) dans les nanoparticules (NP) de métaux nobles font de la plasmonique un sujet aux applications multiples. Lorsque les NP sont éclairées par des impulsions laser ultracourtes, une dynamique rapide d'échanges d'énergie conduit à la variation ultrarapide de leurs propriétés optiques, accompagnée d'autres effets comme la photoluminescence, l'échauffement hyperlocalisé, la photoémission électronique, la production de radicaux libres, la nano-cavitation. La conception de nanostructures hybrides complexes permet d'adapter les propriétés plasmoniques pour optimiser les applications. Nous avons étudié certaines nanostructures hybrides par spectroscopie d'absorption pompe-sonde large bande et une modélisation dédiée : fibres de silice décorées de NP d'or, NP cœurs-coquilles Au-Ag. Leurs réponses optiques stationnaire et transitoire sont analysées en fonction de la morphologie des NP. Dans les développements évoqués ci-dessus, l'exal-

tation de champ proche autour des NP plasmoniques joue un rôle clé. Cependant, l'étude de la modulation transitoire du champ proche est limitée par l'incapacité des outils numériques usuels à saisir de faibles variations de la permittivité des NP. Nous mettons en œuvre une méthode FDTD basée sur les paires pole-résidu complexes-conjugués pour pouvoir simuler l'évolution temporelle de la topographie du champ proche plasmonique. Au-delà, le mode LSPR peut être couplé à un mode photonique dans une cavité hybride pour concevoir des fonctionnalités photoniques optiquement contrôlées. Le couplage d'un réseau 2D de nanobâtonnets d'or parallèles avec le mode de défaut d'une cavité d'un cristal photonique 1D est étudié théoriquement. L'anisotropie optique permet de jouer avec plusieurs degrés de liberté comme la polarisation du champ. La modulation ultrarapide de la réponse optique prédite dans de telles nanostructures hybrides ouvre la possibilité de leur optimisation future pour la conception de capteurs résolus en temps.

Title : Ultrafast optical response of complex plasmonic nanoparticles

Keywords : plasmonics, nanoparticles, ultrafast, near-field

Abstract : The remarkable properties associated with the localized plasmon resonance (LSPR) in noble metal nanoparticles (NPs) make plasmonics an important topic with multiple applications. When NPs are illuminated by ultrashort laser pulses they undergo a rapid dynamics of energy exchanges which leads to the ultrafast variation of their optical properties, associated with other effects such as broadband photoluminescence, hyperlocalized heat release, electron photoemission, production of reactive oxygen species and nano-cavitation. The design of complex hybrid nanostructures can enable us to tailor the plasmonic properties as to optimize the applications. We have studied some hybrid nanostructures by broadband pump-probe absorption spectroscopy and a dedicated modeling : AuNP-decorated silica fibers and core-shell Au-Ag NPs. Their stationary and transient optical responses are analyzed depending on the NP morphology.

In the developments evoked above, the enhanced

near field around plasmonic NPs plays a key role. However, the study of the ultrafast transient modulation of the near field is limited by the inability of the conventional numerical tools to catch the small variations of the NP permittivity. Here, a complex-conjugate pole-residue pair based FDTD method is successfully implemented to simulate the time-dependence of the plasmonic near-field topography. Beyond, the LSPR mode can be resonantly coupled with a photonic mode in a hybrid microcavity for conceiving optically-controlled photonic functionalities. The coupling of a 2D array of parallel gold nanorods with the defect mode of a 1D photonic crystal cavity is investigated theoretically. The optical anisotropy enables us to play with several degrees of freedom like field polarization. The ultrafast modulation of the optical response that is predicted in such hybrid nanostructures opens the possibility of their future optimization for designing time-resolved sensors.

